РОССИЙСКАЯ АКАДЕМИЯ НАУК

Институт проблем безопасного развития атомной энергетики

ТРУДЫ ИБРАЭ

Под общей редакцией члена-корреспондента РАН
Л. А. Большова

Выпуск 5

МОДЕЛИ ВЫХОДА ПРОДУКТОВ ДЕЛЕНИЯ ИЗ ОБЛУЧЕННОГО ТОПЛИВА

(на английском языке)

MODELS FOR FISSION PRODUCTS RELEASE FROM IRRADIATED UO_2 FUEL

(in English)

Научный редактор
профессор, доктор физико-математических наук
Р. В. Арутюнян

Москва Наука 2008

УДК 621.039
ББК 31.4
Т78

Рецензенты:
Doctor *R. Dubourg* (IRSN, France),
доктор физико-математических наук *В.Ф. Стрижов*

Труды ИБРАЭ РАН / под общ. ред. чл.-кор. РАН Л. А. Большова ; Ин-т проблем безопасного развития атомной энергетики РАН. — М. : Наука, 2007— .
Вып. 5 : Модели выхода продуктов деления из облученного топлива / науч. ред. Р. В. Арутюнян. — 2008. — 157 с. : ил. — ISBN 978-5-02-036951-1 (в пер.).

Представлены ключевые модели кода MFPR, основанные на детальном описании поведения продуктов деления (ПД) в топливных зернах и на их границах, а также верификация моделей на базе аналитических экспериментов в различных условиях (стационарное облучение, переходные режимы и высокотемпературный отжиг). Показано, что микроскопические дефекты кристаллической структуры UO_2 могут существенно влиять на выход газовых ПД из топлива. Кроме того, представлено механистическое описание поведения химически активных ПД. Оно основано на самосогласованном рассмотрении процессов диффузии ПД в зернах и их испарения в условиях термодинамического равновесия в многофазной и мнокомпонентной системе на границах зерен, а также в применении к окисленному топливу. Приведены примеры применения кода к интегральным экспериментам, проводимым в условиях окисляющей или редуцирующей атмосферы, а также в условиях тяжелых аварий на АЭС.

Для студентов, аспирантов и специалистов в области материаловедения ядерных реакторов и анализа безопасности АЭС.

Proceedings of IBRAE RAS / Ed. by L.A. Bolshov ; Nuclear Safety Institute (IBRAE) RAS. — Moscow : Nauka, 2007— .
Issue 5 : Models for Fission Products Release from Irradiated UO_2 Fuel / Ed. by R.V. Arutyunyan. — 2008. — 157 p. : ill. — ISBN 978-5-02-036951-1 (bound).

The main models of the mechanistic code MFPR are described. Exhaustive description of fission-gas behaviour in grain and out of grain is given in relation with individual validation results on analytical experiments under various conditions (steady irradiation, transient, post-irradiation annealing). It is shown that microscopic defects in the UO_2 crystal structure can strongly influence fission-gas transport out of grains and release from fuel pellets. The mechanistic description of chemically-active-elements behaviour is also presented. It is based on complex association of diffusion-vaporization mechanism involving multi-phase and multi-component thermo-chemical equilibrium at the grain boundary with accurate calculation of fuel oxidation. Examples of application to integral experiments performed at high temperatures in oxidising and oxidising/reducing gas atmospheres, show the possibilities of the code in the frame of severe-accident interpretation.

The assumed target for the issue are students and specialists in nuclear materials research and NPP safety analysis.

ISBN 978-5-02-036951-1

CONTENTS

Foreword

Any model that attempts a realistic description of fission-gas release and fuel swelling as a function of fuel-fabrication variables and in a wide range of reactor operating conditions must treat them as coupled phenomena and must include various mechanisms influencing fission-gas behaviour. The most advanced mechanistic codes FASTGRASS [1] and VICTORIA [2] present various detailed models for evolution of intragranular bubbles formed from the solid solution of gas atoms in the UO_2 matrix under irradiation conditions, however, they are essentially based on consideration of the equilibrium state of the bubbles. Such an approach radically simplifies the theory, since in this case the defect structure of the crystal (including point defects, such as vacancies and interstitials, and extended defects, such as dislocations) is almost completely excluded from consideration. Such simplification is well grounded only in steady-state irradiation conditions (except of high burnups) which can be relatively well described, however, by a simple parametric Booth model or other semi-empirical correlation models. So, in these simple situations, the advantage of the mechanistic approach is not so visible.

Under transient and/or annealing conditions the approximation of equilibrium bubbles is not anymore valid, and interactions of bubbles with point defects and dislocations become essential. Lacking mechanistic description of real defects (vacancies, interstitials and dislocations) and their interactions with bubbles, various artificial mechanisms were introduced in the codes, in order to simulate more complicated regimes. These artificial mechanisms require «effective» parameters, which introduce strong uncertainties in the code predictions, and, as a result, the advantage of the mechanistic approach is essentially lost. Trying to avoid any artificial tuning and introduction of artificial mechanisms was important reason for development of the code MFPR (**M**odule for **F**ission **P**roducts **R**elease) [3, 4].

This code self-consistently describes evolution of various defects and their interactions with gas atoms and bubbles migrating out of grains, and new parameters characterizing the crystal defect structure also arise. However, being physically grounded, these microscopic parameters can be fixed from the analysis of available experimental data and then used without any artificial tuning in further calculations. This is the main goal of this mechanistic approach performed in collaboration between the Nuclear Safety Institute (IBRAE) of Russian Academy of Sciences and the French «Institut de Radioprotection et de Sûreté Nucléaire» (IRSN), where the code is used to better understand the results of the experiments performed in the context of radiological consequences of accidents (e. g., [5]). In particular, this approach will help in developing appropriate models for evaluating the risk of fission-product release in the event of a severe accident or designing basis accident in a LWR.

In addition, as shown by many observations and interpretations, the release of various chemically-active fission products (FP) strongly depends on formation of separate phases, mainly at grain boundaries, and thermal behaviour of these phases in various gas atmospheres that determine the fuel oxygen potential and thus the stability of the different phases. The MFPR module includes modelling of chemical effects on the behaviour of FP within irradiated oxide fuel at high temperatures in the interval 500–3000 K. The «U – FP – O» system is considered as a multi-phase system consisting of multi-component phases. Within the fuel matrix, the fission products migrate as atoms to the gas bubbles and solid phase precipitates at grain faces, and their mobility depends in particular on the extent of fuel oxidation characterized by the stoichiometry deviation. The release rate is thus proportional to partial pressures of FP vapours determined by chemical states of condensed FP species, and the major mechanism for release of the fission products is their vaporization at the gas/solid interface. In connection with that description, a model for fuel oxidation in steam/air mixtures was also developed.

This collection of papers will describe, for an intact fuel geometry, the main models of the MFPR code both for fission gases and chemically-active elements and will give results of validation of individual models against separate-effects experiments and more global validation against integral experiments (e. g., the French VERCORS tests [6]).

Acknowledgments

The work on development of new advanced models for the MFPR code was supported by IRSN, Cadarache (France) under the Contract on the mechanistic code MFPR development; personal support and collaboration of Drs. R. Dubourg, P. Giordano and M. Kissane (IRSN) are greatly acknowledged.

M.S. Veshchunov

References

1. Rest *J., Zawadzki S.A.* FASTGRASS: A Mechanistic Model for the Prediction of Xe, I, Cs, Te, Ba and Sr release from Nuclear Fuel under Normal and Severe-Accident Conditions. NUREG/CR-5840 TI92 040783. 1994.
2. *Heames T.J., Williams D.A., Bixler N.E., Grimley A.J., Wheatley C.J., Johns N.A., Domogala P., Dickson L.W., Alexander C.A., Osborn-Lee I., Zawadzki S., Rest J., Mason A., Lee R.Y.* VICTORIA: A Mechanistic Model of Radionuclide Behaviour in the Reactor Coolant System under Severe Accident Conditions. NUREG/CR-5545. 1992.
3. *Veshchunov M.S., Ozrin V.D., Shestak V.E., Tarasov V.I., Dubourg R., Nicaise G.* // Nucl. Eng. Des. 2006. Vol. 236. P. 179–200.
4. *Veshchunov M.S., Dubourg R., Ozrin V.D., Shestak V.E., Tarasov V.I.* // J. Nucl. Mater. 2007. Vol. 362. P. 327–335.
5. *Dubourg R., Faure-Geors H., Nicais G., Barachin M.* // Nucl. Eng. Des. 2005. Vol. 235. P. 2183.
6. *Ducros G., Malgouyres P.P., Kissane M., Boulaud D., Durin M.* // Nucl. Eng. Des. 2001. Vol. 208. P. 191.

Modelling of Fission Products Transport in UO_2 Fuel

V.D. Ozrin, V.I. Tarasov

Introduction

In this paper a general formulation of a model describing the fission-product (FP) accumulation, transport and release from solid UO_2 fuel under both irradiation and post-irradiation conditions is presented. The model is underlying for MFPR code, which has been developed for the last decade in the framework of IRSN—IBRAE (NSI) RAS collaboration. The intragranular transport problem is considered separately for two subsystems: the noble FP (gas atoms dissolved in the matrix and filling the grain bubbles) and chemically active FP (elements and chemical compounds formed by these elements). We restrict ourselves with presentation of the basic objects the model deals with, main assumptions and simplifications related to their properties, interactions and transport. Also the framework of the MFPR numerical algorithm is outlined. However, the model for chemically active fission-product elements is considered more explicitly including formation of separate solid phases at the grain boundaries and gaseous compounds in the grain face bubbles. The separate models simulating specific effects under different regimes are described in detail in the accompanying papers of this issue.

1. Main physical processes

Due to fission processes, a wide spectrum of fission product elements is created in the UO_2 matrix, the most important being combined into 15 element groups: Cs, Ce, I, Eu, Mo, Nd, Ru, Nb, Ba, Sb, Sr, Te, Zr, Xe, La. Typical abundance ratios for these elements per fission [1] are shown in Table 1.

Table 1. Abundance of fission- product elements used in MFPR module

FP element	*Fission yield*	*FP element*	*Fission yield*
Cs	0.182	Ce	0.154
I	0.011	Eu	0.002
Mo	0.248	Nd	0.303
Ru	0.142	Nb	0.008
Ba	0.084	Sb	0.0003
Sr	0.078	Te	0.026
Zr	0.326	Xe	0.241
La	0.065		

It is assumed that FP elements exist in the UO_2 matrix in atomic form. All impurity atoms formed due to fission processes migrate diffusively within the matrix, in particular, to grain boundary. In this way, atoms can be captured by intragranular gas bubbles which also can migrate to grain boundaries. Competing processes are irradiation-induced and thermal re-solution of atoms from the bubbles. It is assumed that intragranular bubbles are filled up by noble gases only.

Chemical interactions between the FP elements and the dissolved oxygen result in formation of separate phases in solid precipitates on the grain boundaries and vaporization to the intergranular gas bubbles. These processes affect significantly the release rates of all FP elements including noble gases.

Intergranular bubbles are represented by two groups: bubbles on grain faces (GF) and on grain edges (GE). The GF bubble growth progresses up to the grain surface saturation, when interlinkage of the GF bubble and formation of grain face channels to the grain edges and corners occur. Growth of the GE bubbles leads to their interconnection by tunnels and formation of an open porosity structure.

In the MFPR model, the process of FP release from solid fuel is divided into two consecutive stages:

- intragranular FP transport from the bulk to the grain boundary accompanied by formation of solid precipitates and gaseous species in the intergranular bubbles,
- accumulation of FP-bearing gases in the intergranular bubbles, and release to the open porosity through the system of bubbles on the grain boundaries and the network of channels and tunnels.

The model currently ignores the transport delay in the FP releases to the gap related to the gas transfer through the channel network and through the open porosity.

2. Intragranular transport of FP elements

In the transport problem, a fuel grain is considered, for simplicity, as an isotropic sphere. The problem is formulated separately (and in different manners) for two subsystems: the noble gas atoms (Xe, Kr) dissolved in the matrix and filling the grain bubbles, and atoms of chemically active element and molecules of compounds formed by these elements.

2.1. Diffusion and release of chemically active FP elements

According to experimental data [2] and thermo-chemical calculations [3–7], the major considered phases in the irradiated UO_2 are the «fuel—FP» solid solution, the metal phase, the oxide phase of complex ternary compounds, the solid phase of CsI and the gas phase. Zirconium and rare earth elements are partially or completely miscible with uranium dioxide to form a solid solution. The relatively low solubility of cesium, barium and strontium results in precipitating the majority of barium in the form of uranates, zirconates and molybdates as a multi-component «*grey*» phase, which also includes ternary compounds. Solubility of the metals Mo and Ru and their oxides in solid UO_2 is extremely low. These metals (along with Tc, Rh, Pd) are present in the metallic («*white*») inclusions. Within the fuel matrix the fission products migrate as atoms [8] to the grain boundary where they can form compounds in gas bubbles or condensed precipitates. Chemical composition of fuel along with the diffusivities of FP elements depends significantly on the extent of fuel oxidation.

In the MFPR chemical model [9, 10], irradiated oxide fuel including fission products and dissolved oxygen is considered as a multiphase system consisting of multi-component phases. The model for releases of the chemically active FP elements from solid fuel implemented in the current MFPR version is based on the following assumptions:

- In the system «UO_2—FP elements—Oxygen», the following phases are considered: solid solution (SS) of FP elements and oxygen in UO_2 matrix, separate solid phases—precipitates (SP) that is the metal phase, «grey» phase of complex ternary compounds, the phase of condensed CsI(c), and the gas phase including molecular oxygen, noble gases and FP element-bearing vapors. The role of the gas phase plays the system of the GF bubbles. Chemical interactions with the intragranular bubbles, as well as changes in chemical states of gaseous FP within the GE bubbles and in the open pores are ignored.

- Fission product elements migrate within the UO_2 matrix in the atomic form. Since the coefficient of solid state diffusion of oxygen is significantly higher than that of the fission product elements, the dissolved oxygen has a spatially homogeneous concentration.
- Separate solid phases are formed at the gas/solid interface. It is assumed that existence of these phases is determined by thermodynamic conditions only. Any kinetic limitations on formation of solid phases are not taken into account. Diffusion of fission-product elements within these phases is ignored.
- The gas phase is in the equilibrium state, and it is in equilibrium with the SP phases and with the boundary layer of the SS phase.

Detailed description of the phase composition and the approach to calculating chemical equilibrium is given in the Appendix.

To formulate the transport problem, the complex system is separated into two subsystems. That is (1) solid solution (SS) of FP elements and atomic oxygen dissolved in the UO_2 matrix, and (2) the subsystem «solid precipitates—gas phase» (SP/G). Concentration profiles of FP elements in SS are described by the diffusion equation:

$$\frac{\partial}{\partial t} Y_1^{(i)} = B_i + r^{-2} \frac{\partial}{\partial r}\left(D_i r^2 \frac{\partial}{\partial r} Y_1^{(i)} \right), \qquad (1)$$

where $Y_1^{(i)}$ is the local volume concentration of the i-th element in solid solution, the subscripts enumerate the subsystems, B_i is the rate of generation of the i-th element due to fission, D_i is the diffusion coefficient.

To introduce analogous equation for oxygen it is needed, first of all, to define what part of total oxygen can be considered as dissolved or «free» and can participate in the diffusion process. In pure non-stoichiometric urania, UO_{2+x}, the molar concentration of the dissolved oxygen coincides, by definition, with the stoichiometric deviation, x, the chemical potential of the dissolved oxygen is a relatively well defined function of temperature and x given by Lindemer and Besmann [11], and the diffusion equation is written for the dissolved oxygen concentration defined as $Y^{(ox)} = x \cdot Y^{(\mathrm{UO_2})}$. The same approach could be used for a more complicated system of irradiated fuel with solid solution of FP elements and oxygen in solid UO_2. However, in this case, in contrast to pure UO_{2+x}, there are no enough experimental data and no corresponding models for oxygen potential as a function of T, the dissolved oxygen concentration, x, and concentrations of all other FP elements. To overcome this problem it is assumed that in solid solution there is local chemical equilibrium described in the same way as that for liquid solution:

$$\begin{aligned} \mu_{\mathrm{ZrO_2(c)}} &= \mu_{\mathrm{Zr(c)}} + 2\mu_{\mathrm{O(c)}}, \\ \mu_{\mathrm{MoO_2(c)}} &= \mu_{\mathrm{Mo(c)}} + 2\mu_{\mathrm{O(c)}}, \qquad (2) \\ \mu_{\mathrm{LaO_{3/2}(c)}} &= \mu_{\mathrm{La(c)}} + \tfrac{3}{2}\mu_{\mathrm{O(c)}}, \quad \ldots \end{aligned}$$

where $\mu_{\mathrm{O(c)}}$ is the chemical potential of the dissolved oxygen, chemical potentials depend on concentrations which are functions of coordinates and time. According to these assumptions, total local concentrations of oxygen and FP elements can be written respectively in the form

$$Y_1^{(ox,tot)}(r,t) = Y_1^{(ox,f)}(r,t) + Y_1^{(ox,b)}(r,t), \qquad (3)$$

$$Y_1^{(ox,b)}(r,t) = \sum_i b_{i,ox} Y_1^{(i,o)}(r,t), \qquad (4)$$

and

$$Y_1^{(i)}(r,t) = Y_1^{(i,m)}(r,t) + Y_1^{(i,o)}(r,t), \qquad (5)$$

where $Y_1^{(ox,f)}$ and $Y_1^{(ox,b)}$ are concentrations of dissolved or «free» and «bonded» oxygen, respectively, the sum in the second equation is over all «virtual» oxides in solid solution with the concentrations $Y_1^{(i,o)}$, $Y_1^{(i,m)}$ is the concentration of the «metallic» form of element «I», and $b_{i,ox}$ is the stoichiometric coefficient defining the number of oxygen atoms in the molecule. Concentrations of «virtual» oxides and, thus, distribution of oxygen between «free» and «bonded» states can be found from equations of local chemical equilibrium (2).

In accordance with decomposition represented by Eqs. (4), total diffusion flux of oxygen consists of the «free» oxygen flux with the coefficient D_{ox} and the fluxes of «bonded» oxygen accompanying diffusion of each FP element with the diffusion mobility specific for this element. This is an additional model assumption about synchronization or adopting of the «bonded» oxygen motion to motion of the corresponding FP element. Hence, the diffusion equation for oxygen is of the form

$$\partial Y_1^{(ox,tot)}(r,t)\big/\partial t = D_{ox}\Delta Y_1^{(ox,f)}(r,t) + \sum_i D_i b_{i,ox}\Delta Y_1^{(i)}(r,t) + B_{ox}, \qquad (6)$$

where B_{ox} is the rate of oxygen liberation due to fission. In the case of external fuel oxidation/reduction this term includes an additional source/sink for oxygen.

It should be emphasized that the discussed approach realized in Eqs. (3)–(6) can exist only if there is a significant difference (in orders of magnitude) between the diffusion coefficients of oxygen and atoms of FP elements, namely $D_i << D_{ox}$, which, in general, provides relatively well defined decomposition to the «bonded» fraction rapidly adopting to slow FP motion and the remaining, fast diffusing «free» fraction. In particular, according to MFPR data for 2000 K $D_{ox}/<D> \sim 10^5–10^9$, where $<D>$ is an average FP diffusion coefficient. Therefore, instead of Eq. (6), asymptotics of this equation at $D_{ox}/<D> \to \infty$ can be used, which is given by

$$\nabla Y_1^{(ox,f)}(r,t) = 0\,, \qquad (7)$$

that has a simple and evident physical meaning: in the time scale of (slow) FP diffusion the concentration of free oxygen in solid solution is independent of coordinates.

Note that Eqs. (2) defining local equilibrium are used only to find the «free» fraction of oxygen. Due to condition (7) and some specific peculiarities of the system this problem can be additionally simplified. It can be analytically shown that there are no need to solve Eqs. (2) for each spatial point (or each spatial mesh): true relation between the oxygen fractions can be found if solid solution is considered as a homogeneous system (with the same number of FP and O atoms as that in the initial, inhomogeneous system), and to solve Eqs. (3) for such system.

Conservation of the FP elements in the gas/solid system is governed by the equation

$$N_1^{(i)} + N_2^{(i)} = N_{\mathrm{tot}}^{(\mathrm{i})}\,, \qquad (8)$$

where $N_1^{(i)}$, $N_2^{(i)}$ and $N_{\mathrm{tot}}^{(i)}$ are the total number of moles of the element «*i*» per grain in the subsystems SS and SP/G, and in the full system, respectively. This equation can be rewritten in the differential form as

$$\begin{aligned} &\frac{d}{dt}N_2^{(i)} = V_{gr}F_{gb}^{(i)}\,, \\ &F_{gb}^{(i)} = -\frac{6D_i}{d_{gr}}\left[\frac{\partial}{\partial r}Y_1^{(i)}\right]_{r=d_{gr}/2}, \end{aligned} \qquad (9)$$

where d_{gr} is the grain diameter. Integration of these equations yields changes in elemental composition of the subsystem SP/G. Since, as assumed, solid precipitates and the gas phase are in chemical equilibrium, distribution of the FP elements between chemical states within the subsystem SP/G is a well-defined function of the values $N_2^{(i)}$, temperature and the gas phase volume, V_{gas}.

In turn, knowledge of the chemical composition of the subsystem SP/G allows formulating the conditions of the equilibrium at the interface between the subsystems in the standard form of equalities for chemical potentials:

$$\begin{aligned} &\mu_{\mathrm{O(c)}}\Big|_{\mathrm{r=d_{gr}/2}} = \tfrac{1}{2}\mu_{\mathrm{O_2(g)}}, \quad \mu_{\mathrm{Zr(c)}}\Big|_{\mathrm{r=d_{gr}/2}} = \mu_{\mathrm{Zr(g)}}, \\ &\mu_{\mathrm{Mo(c)}}\Big|_{\mathrm{r=d_{gr}/2}} = \mu_{\mathrm{Mo(g)}}, \quad \mu_{\mathrm{La(c)}}\Big|_{\mathrm{r=d_{gr}/2}} = \mu_{\mathrm{La(g)}}, \quad \ldots \end{aligned} \qquad (10)$$

Solution of Eqs. (10) with respect to boundary composition of the SS phase is given by

$$Y_1^{(i)}\Big|_{r=d_{gr}/2} = V_{gr}^{-1}\bar{f}^{(i)}(N_2^{(1)},...,N_2^{(n_e)};V_{\text{gas}}), \quad (11)$$

where n_e is the total number of elements in the system. These equations provide the boundary conditions for the diffusion problem (1). To simplify the problem and to decrease the computation time, the current implementation of the model uses the quasi-asymptotic approximation based on the calculation of the total equilibrium in the full «SS & SP & Gas phase» system. That approach yields

$$Y_1^{(i)}\Big|_{r=d_{gr}/2} \cong V_{gr}^{-1} f^{(i)}(N_{tot}^{(1)},...,N_{tot}^{(n_e)};V_{\text{gas}}), \quad (12)$$

and thus, the approximate boundary conditions are determined by total amount of elements in the system and the temperature.

Thus, simultaneous solution of Eqs. (1)–(5) and (7)–(11) yields the space-time dependent distribution of the FP elements between chemical states. Note, this distribution is calculated self-consistently with the external fuel oxidation.

Due to interface equilibrium, the elemental fluxes to the grain boundary, $F_{gb}^{(i)}$, can be represented in terms of the fluxes of chemical components of the «SP & Gas phase» subsystem,

$$F_{gb}^{(i)} = \sum_j b_{ji} F_{\text{gas}}^{(j)} + \sum_j b_{ji} F_{\text{cond}}^{(j)}, \quad (13)$$

where the stoichiometric coefficients b_{ji} define number of atoms of the type «*i*» participating in formation of the molecule «*j*», the sums are over the gaseous and condensed species, respectively. The expression for the fluxes of the FP-bearing gaseous species is used in the problem of the following migration of the FP elements in the form of gaseous compounds to open porosity discussed below.

2.2. Transport of fission gas

The present version of the MFPR code includes two macro-models for intragranular transport of the fission product Xe: bi- and multi-modal models. The most detailed approach to describe the intragranular Xe gas-bubble system is the multi-modal model, formulated in terms of the distribution function for the bubble sizes.

In the bi-modal approach similar to that of the VICTORIA and FASTGRASS codes, the effects related to a finite width of the bubble size distribution are ignored. The basic space-time dependent variables are the volume concentrations of gas atoms C_g and bubbles C_b, the average number of gas atoms within a bubble N_b, and the average bubble volume V_b. Additionally, MFPR includes self-consistent consideration of point (vacancies and interstitials) and extended defects (vacancy and dislocation loops, dislocation network), which mutually interact with each other and with gas bubbles and as-fabricated pores during their evolution under irradiation or annealing conditions. Details of such an approach will be presented in papers of this Collection on pp. 47 and 58.

Transport equations for C_g and concentration of atoms-in-bubbles $Y_b = N_b C_b$ can be written as

$$\frac{\partial C_g}{\partial t} = D_g \Delta C_g - F_{g\to b} - F_{g\to d} + \kappa G, \quad (14)$$

$$\frac{\partial Y_b}{\partial t} = \nabla\left(D_b \nabla Y_b\right) - \omega_{bmg} Y_b + F_{g\to b} - F_{b\to d}, \quad (15)$$

where

$$F_{g\to b} = k_{gg} F_n C_g^2 + k_{gb}\left(C_g - C_g^{eq}\right)C_b - bGY_b, \quad (16)$$

$$k_{xy} = 4\pi(D_x + D_y)(R_x + R_y), \quad x, y = g, b. \quad (17)$$

Different terms in the right hand side of these equations correspond to the following physical effects, each being characterized by a particular kinetic parameter:

- Diffusion (D_g and D_b are the diffusivities of gas atoms and bubbles, respectively);
- Gas atom generation by fission (G is the fission rate and $\kappa = 0.241$ is the probability of Xe formation by fission);
- Bubble biased migration (ω_{bmg}) along the temperature gradient;
- Bubble nucleation (with the nucleation rate F_n);
- Gas atom capture by bubbles (R_g is the gas-atom radius and R_b is the bubble radius in the capture kernel k_{gb});
- Thermal re-solution (C_g^{eq} is the equilibrium gas concentration);
- Radiation induced re-solution (b is the re-solution probability factor).

Modelling of these effects as well as sweeping of gas and bubbles by climbing dislocations ($F_{g\to d}$ and $F_{b\to d}$) is described in papers of this Collection on pp. 47 and 87. Superposition of these effects (along with the Van-der-Waals equation for the gas state) determines, in particular, the intragranular bubbles concentration C_b and mean radius R_b, as well as gas release to the grain faces.

In growing grains, the boundary conditions for Eqs. (3)—(5) are set at moving grain boundaries:

$$\begin{gathered}\left.\frac{\partial C_g}{\partial r}\right|_{r=0}=0,\\ \left.C_g\right|_{r=R_{gr}(t)}=C_\delta,\\ \left.\frac{\partial Y_b}{\partial r}\right|_{r=0}=0,\\ \left.Y_b\right|_{r=R_{gr}(t)}=0. \qquad (18)\end{gathered}$$

Additionally, sweeping of intragranular bubbles by moving grain boundaries takes place. The MFPR model for the grain growth with the retarding effect of attached bubbles is presented in paper of this Collection on p. 109.

2.3. Intergranular FP transport

Since the GF bubbles are filled up by a multi-component gas mixture including Xe and FP-bearing molecules, total flux density of molecules (number of molecules/sec/m^2) from the grain and the grain boundary takes the form of sum over all types of gaseous species:

$$F_{\mathrm{tot}}=\sum_i F_{\mathrm{gas}}^{(i)}+F_{\mathrm{gb}}^{(\mathrm{Xe})}, \qquad (19)$$

where $F_{\mathrm{gas}}^{(i)}$ is the flux density of the i-th gaseous compound of a chemically active FP elements discussed in the previous Section, $F_{\mathrm{gb}}^{(\mathrm{Xe})}$ is the flux density of Xe. As has been explained above, the chemically active FP elements are partially trapped in the solid precipitates. This part does not contribute the total gaseous flux F_{tot}, that determines eventually the FP release to the open porosity.

The intergranular FP transport is described in terms of volume concentrations of the gas components contained in the GF and GE bubbles denoted by $Y_f^{(i)}$ and $Y_e^{(i)}$, respectively. Total volume concentration of gas molecules composing bubbles is defined as a sum over all gas components:

$$Y_x=\sum_i Y_x^{(i)}, \qquad x=f,e, \qquad (20)$$

that is related to the corresponding bubble concentrations by

$$Y_f=C_fN_f, \qquad Y_e=C_eN_e, \qquad (21)$$

where N_f and N_e are the average numbers of gas molecules in a GF and GE bubble, respectively. The volume concentration of bubbles C_i can be represented in terms of the grain volume V_{gr}, and the factors determining the grain geometry:

$$C_f=\frac{N_{bpf}N_{fpgr}}{V_{gr}}, \quad C_e=\frac{N_{epgr}}{V_{gr}}, \qquad (22)$$

where the factors $N_{fpgr} = 7$ and $N_{epgr} = 12$ are respectively the numbers of faces and edges per grain. The surface ρ_f and volume C_f concentrations of the GF bubbles are related by $C_f = 3X_f/d_{gr}$. Evolution of these concentrations caused by the coalescence effects determines the factor N_{bpf}. The bubble radii and volumes are related by $V_i = 4\pi f_i R_i^3/3$, $i = f, e$, where f_i are the shape factors accounting for non-spherical form of intragranular bubbles.

The equations governing the chemically active FP transport from the system of GF and GE bubbles to the open porosity are formulated basing on a percolation type approach close to that developed by White and Tucker [12]. In the case of grain face bubbles, the rate equation takes the form

$$\frac{d}{dt} Y_f^{(i)} = F_{\text{gas}}^{(i)} \theta_f, \quad \theta_f \equiv \theta(A^* - \varphi), \qquad (23)$$

where $\theta(x)$ is the Heaviside step function, the constant A^* is set equal to 0.5 [13] and φ is the projected area coverage of the grain face by the GF bubbles given by

$$\varphi_f = \pi\,(R_f \sin\theta_f)^2 \rho_f, \qquad (24)$$

ρ_f being the surface concentration of GF bubbles (number of bubbles per unit surface area). Note that the projected area coverage along with the face bubble concentrations and radius depends on time due to the coalescence effects. The critical area coverage of the grain face determines the onset of formation of the interconnected channels from GF bubbles to the grain edges, when the critical value is exceeded.

The rate equations for the concentration of a gas component in the GE bubbles are of the form

$$\frac{d}{dt} Y_e^{(i)} = F_{\text{gas}}^{(i)} \left(1 - \theta_f\right) \theta_e, \qquad (25)$$

where

$$\theta_e \equiv \theta(L_{\text{edge}} - 2R_e N_{\text{bpe}}), \qquad (26)$$

L_{edge} is the average edge length, R_e is the radius of edge bubble, and N_{bpe} is the number of edge bubbles per a grain edge. Saturation of the grain edge porosity takes place when these bubbles are just touching each other, that is $2R_e N_{\text{bpe}} = L_{\text{edge}}$ [12]. This is the critical point for formation of the long-range interconnection of GE and GC bubbles to the open porosity.

Finally, the release rate of the i-th gas component is determined by

$$\frac{d}{dt} Y_{\text{out}}^{(i)} = F_{\text{gas}}^{(i)} \left(1 - \theta_f\right)\left(1 - \theta_e\right), \qquad (27)$$

where $Y_{\text{out}}^{(i)}$ is the concentration of the gas component released from the fuel. The release rate of the FP element «*ie*» can be represented in terms of the stoichiometric coefficients by a relationship:

$$\frac{d}{dt} Y_{\text{out}}^{(ie)} = \sum_j b_{j,ie} \frac{d}{dt} Y_{\text{out}}^{(j)}, \qquad (28)$$

where $Y_{\text{out}}^{(ie)}$ is the concentration of the FP element «*ie*» released from the fuel. Total number of the released atoms of the element «*ie*» is given by $\overline{Y}_{\text{out}}^{(ie)} = V_{\text{fuel}} Y_{\text{out}}^{(ie)}$.

The MFPR code includes an improved model for the transport of Xe atoms that self-consistently takes into account the effects of atom diffusion along the grain surface and irradiation re-solution from intergranular bubbles presented in papers of this Collection on pp. 17 and 25.

Conclusions

Models of fission product accumulation, transport and release from solid UO_2 fuel are presented. The model for transport of chemically active fission product elements includes intragranular diffusion accompanied by formation of separate solid phases at the grain boundaries and gaseous compounds in the grain face bubbles. The model for transport of noble gases includes their intragranular diffusion both in atomic form and within intragranular bubbles, the interactions with point and extended crystal defects being taken into account. The model for intergranular transport describes formation of long-range interconnection of intergranular porosity with the open porosity and fission-product release from the fuel. The considered models have been implemented in the MFPR code.

APPENDIX. Thermo-chemical equilibrium in the multi-phase system

The principal phases that appeared in the irradiated UO_2 and are considered in the model are the following:

- ***The fuel-FP oxide solid-solution*** that includes, apart from UO_2 and dissolved oxygen: caesium Cs(c), alkaline earth metals Ba(c) and Sr(c) and their oxides BaO(c), SrO(c), zirconium and niobium in the forms Zr(c), ZrO_2(c), Nb(c), NbO(c), NbO_2(c), rare earth elements La(c), Ce(c), Eu(c), Nd(c), and their oxides $LaO_{3/2}$(c), $CeO_{3/2}$(c), CeO_2(c), $EuO_{3/2}$(c), EuO(c), $NdO_{3/2}$(c), metalloid Sb(s) and $SbO_{3/2}$(c), noble metals Mo(s), Ru(s) and their oxides MoO_2(c), RuO_2(c).
- ***The metal phase*** composed of Mo(c) and Ru(c).
- ***The phase of complex ternary compounds (grey phase)*** including molybdates, zirconates and uranates of Ba, Sr and Cs in the form: $BaUO_4$(c), $SrUO_4$(c), Cs_2UO_4(c), $BaMoO_4$(c), $SrMoO_4$(c), Cs_2MoO_4(c), $BaZrO_3$(c), $SrZrO_3$(c) and Cs_2ZrO_3(c).
- ***The separate solid-phase*** of CsI(c).
- ***The gas phase*** with the main components: Xe(g), Te(g), I(g), Cs(g), CsI(g), Cs_2MoO_4(g), MoO_3(g), $(MoO_3)_2$(g), $(MoO_3)_3$(g), RuO(g), RuO_2(g), RuO_3(g), Ba(g), Sr(g), ZrO(g), LaO(g), CeO(g), NdO(g), NbO(g), O_2(g). Total list of gases includes 58 species.

Thermo-chemical equilibrium in the system determines partitioning of elements between allowed compounds, solid phases and the gas phase. In the MFPR model, chemical equilibrium is treated in the framework of the equilibrium constant method based on the mass action law and discussed, for instance, in [3, 5, 6, 14]. It is worth noting that following Ref. [15], oxides of trivalent elements such as La, Nd, Ce and Eu presented in the solid solution are here interpreted as the $MeO_{1.5}$ form rather than the Me_2O_3 form.

The equilibrium composition of the phases is treated in terms of semi-ideal chemical model in which phenomenological solid solubilities of FP elements [16] are used, and the chemical potential of dissolved oxygen is described by the Lindemer — Besmann correlation [11].

A general approach to description of the «UO_2—FP—O» system used in the MFPR model is formulated as follows [14].

The thermo-chemical equilibrium in the multiphase system with n_p phases that consist of n_s species composed of n_e elements, is considered. It is supposed that the system includes all simple (mono-atomic) substances and $n_s \geq n_e$. Each species is to be a component of only one phase. Therefore, for atomic molybdenum, ruthenium and antimony two condensed states are considered, that is Mo(s) and Mo(c), Ru(s) and Ru(c), Sb(s) and Sb(c), which are the constituents of solid solution (SS) and metal phase (MPh), respectively.

The reaction of formation of each species Si from the «basic» components can be written as

$$S_i = \sum_{j=1}^{n_e} b_{ij} S_j , \quad i = 1, \ldots n_s , \qquad (A.1)$$

where b_{ij} are the stoichiometric coefficients.

For equilibrium in the reactions of formation, Eq. (A.1), the mass action law yields:

$$A_i = K_i \prod_{j=1}^{n_e} \left(A_j \right)^{b_{ij}} , \qquad (A.2)$$

where A_i is the activity of the i-th species. For the gaseous species A_i coincides with the partial pressure in atm:

$$A_i = P_i . \qquad (A.3)$$

It is assumed that the partial pressures are related to moles by the ideal gas law:

$$P_i = N_i \frac{RT}{p_0 V_{\text{gas}}} , \qquad (A.4)$$

where N_i is the number of moles of the species «i», T is the temperature in K, R is the universal gas constant, V_{gas} is the volume of the gas phase, $p_0 = 1.01325 \cdot 10^5$ kg/(m·s^2·atm).

In the case of condensed species, except dissolved oxygen, the activity is given by

$$A_i = \gamma_i X_i , \qquad (A.5)$$

where γ_i is the activity coefficient, X_i is the mole fraction of the species «i» defined as

$$X_i = N_i / M^{(p)} , \quad M^{(p)} = \sum_k N_k , \qquad (A.6)$$

where $M^{(p)}$ is the sum of moles in the condensed phase «p» that includes this species.

There are no reliable experimental data and well established models for the activities of the majority of species in the considered system. In the current MFPR model the activity coefficients γ_i are set equal to 1 for almost all species. Exception is made for the following low soluble elements: condensed cesium, Cs(c), metals Mo, Ru and Sb, and alkaline earth elements Ba and Sr. The noble metals are known to be practically immiscible with UO_2. On the other hand, in the presence of the metallic phase the activity coefficients of these species in the phase SS can be estimated as an inverse maximal solid solubility. Therefore, in accordance with estimates presented in [16] the activity coefficients for Mo(s) and MoO_2(c) are estimated as 10^5. The same values of the activity coefficients are ascribed to the pairs Ru(s) and RuO_2(c), Sb(s) and $SbO_{3/2}$(c). In analogy to metals and basing on data for maximal solid solubilities [16], the activity coefficient of Cs(c) is set equal to 10^3, for barium (and BaO(c)) $\gamma = 10^3$, and for strontium (and SrO(c)) $\gamma = 10^2$.

Additionally, the activity coefficient for the cesium molybdate is $\gamma(Cs_2MoO_4) = 10^2$. Although enhancing of the cesium molybdate activity cannot yet be well grounded by theoretical or experimental arguments, the reasons for such setting follow from the results of modelling of integral tests with a wide range of physical conditions including temperature regimes and oxidation/reduction environment.

In the MFPR chemistry model, the stoichiometry deviation x in UO_{2+x} is interpreted as a «mole fraction» (negative for hypostoichiometry) of the oxygen dissolved in the matrix, while the number of 'moles' of the dissolved oxygen is related to the stoichiometric deviation by

$$N_{\mathrm{O(c)}} = xN_{\mathrm{UO_2}} \,. \qquad \text{(A.7)}$$

In the equilibrium state, the partial pressure of the gaseous-molecular oxygen is related to the stoichiometry deviation by the equation

$$P_{\mathrm{O_2}} = \overline{P}_{\mathrm{O_2}}(x,T) \,, \qquad \text{(A.8)}$$

while the activity of the dissolved oxygen is defined as

$$A_{\mathrm{O(c)}} = \sqrt{\overline{P}_{\mathrm{O_2}}(x,T)} \,. \qquad \text{(A.9)}$$

The function $\overline{P}_{\mathrm{O_2}}(x,T)$ is described in literature in detail. In the current version of the MFPR module, the well-known correlation proposed by Lindemer and Besmann [11] is used.

The equilibrium constant K_i in the mass action equation (A.2) is related to the Gibbs free energy of formation of the species «i» by

$$K_i = \exp\left(-\Delta_f G_i^0 \big/ RT\right) \,, \qquad \text{(A.10)}$$

$$\Delta_f G_i^0 = G_i^0 - \sum_{j=1}^{n_e} b_{ij} G_j^0 \,, \qquad \text{(A.11)}$$

where G^0_j is the chemical potential or the Gibbs free energy per mole of pure species in the standard state.

The equilibrium state of the considered system is determined by the solution of the mass action equations which satisfy the mass balance constraints given by

$$E_i^{\mathrm{tot}} = \sum_{j=1}^{n_s} N_j \, b_{ji} \,, \qquad \text{(A.12)}$$

and obeyed the additional condition

$$N_i \ge 0. \qquad \text{(A.13)}$$

Here, E_i^{tot} is the total number of moles of the element «i» in the system, b_{ij} are stoichiometry coefficients introduced in Eq. (A.2). As mentioned above, the condition, Eq. (A.13), is allowed to be violated only for oxygen dissolved in the matrix because the oxygen 'moles' defined by Eq. (A.7) can be negative in the case of hypostoichiometry.

References

1. *Degaltzev Yu.G., Ponomarev-Stepnoj N.N., Kuznetzov V.F.* Behaviour of high-temperature nuclear fuel under irradiation. Moscow: Energoatomizdat, 1987 (in Russian).
2. *Kleykamp H.* The chemical state of the fission products in oxide fuels // J. Nucl. Mater. 1985. 131. P. 221–246.
3. *Imoto S.* Chemical state of fission products in irradiated UO_2 // Ibid. 1986. Vol. 140. P. 19–27.
4. *Cordfunke E.H.P., Konings R.J.M.* Chemical interactions in water-cooled nuclear fuel: a thermochemical approach // Ibid. 1988. Vol. 152. P. 301–309.
5. *Ball R.G.J., Burns W.G., Henshaw J., Mignanelli M.A., Potter P.E.* The chemical constitution of the fuel-clad gap in oxide fuel pins for nuclear reactors // Ibid. 1989. Vol. 167. P. 191–204.
6. *Cordfunke E.H.P., Konings R.J.M.* The release of fission products from degraded UO_2 fuel: thermochemical aspects // Ibid. 1999. Vol. 201. P. 57–69.
7. *Moriyama K., Furuya H.* Thermochemical prediction of chemical form distributions of fission products in LWR oxide fuels irradiated to high burnup // J. Nucl. Sci. and Techn. 1997. Vol. 34. P. 900–908.
8. *Grimmes R.W., Catlow C.R.A.* The stability of fission products in uranium dioxide // Phil. Trans. R. Soc. London, 1991. Vol. A335. P. 609–634.
9. *Veshchunov M.S., Ozrin V.D., Shestak V.E., Tarasov V.I., Dubourg R., Nicaise G.* Development of mechanistic code MFPR for modelling fission product release from irradiated UO_2 fuel // Nuclear Engineering and Design. 2006. Vol. 206. P. 179–200.
10. *Veshchunov M.S., Dubourg R., Ozrin V.D., Shestak V.E., Tarasov V.I.* Mechanistic modelling of urania fuel evolution and fission product migration during irradiation and heating // J. Nucl. Mater. 2007. Vol. 362. P. 327–335.
11. *Lindemer T.B., Besmann T.M.* . Chemical thermodynamic representation of $<UO_{2\pm x}>$ // Ibid. 1985. Vol. 130. P. 473–488.
12. *White R.J., Tucker M.O.* A new fission-gas release model // Ibid. 1983. Vol. 118. P. 1–38.
13. *Heames T.J.* et. al. VICTORIA: A Mechanistic Model of Radionuclide Behavior in the Reactor Coolant System Under Severe Accident Conditions. — NUREG/CR-5545 SAND90-0756. 1992. Rev. 1 R3, R4.
14. *Baibuz A.B., Zitserman V.U., Golubushkin L.M., Chernov U.G.* Chemical Equilibrium in Nonideal Systems. Moscow: Institute of High Temperatures 1985. (in Russian).
15. *Wang W.E., Olander D.R., Lindemer T.B.*. Vaporisation thermodynamics of urania-neodymium mixed oxides // J. Nucl. Mater. 1994. Vol. 211. P. 85–94.
16. *Kleykamp H.* The solubility of selected fission products in UO_2 and (U, Pu)O_2 // J. Nucl. Mater. 1993. Vol. 206. P. 82–86.

Model for Grain-Face Diffusion Transport in UO$_2$ Fuel
Part 1. Model Formulation

M.S. Veshchunov, A.V. Berdyshev

Introduction

In the majority of currently existing models for fission-product (FP) release from UO$_2$ fuel, it is assumed that during steady-state reactor operation the grain boundary bubbles increase in size until they touch allowing FP release to the open porosity [1–4]. The grain boundary bubbles appear to be relatively immobile, particularly at temperatures below about 1900 K [5], and it is usually assumed that gas release occurs only on interlinking. The time for the «grain-face porosity saturation» to occur corresponds to an incubation time period of bubble growth [2]. It is generally accepted now that the grain-face porosity saturates at the fractional coverage of the grain boundaries occupied by bubbles ≈ 50 %, and commencement of gas release from grain faces to edges (and further through the edge tunnels outside the grain) is usually associated with the formation of the open porosity network at this coverage [1–4].

However, in tests [6, 7] this conclusion was not confirmed. In these tests the 3 and 4 BWR cycle specimens with ≈ 2.4 and 2.9 % burnup, respectively, were taken from the outer pellet region (between rim and middle), and the fractional coverage of grain faces by bubbles was evaluated from SEM photographs as ≈ 6 and 10 % [7], respectively, see Fig. 1, panels *a* and *b*.

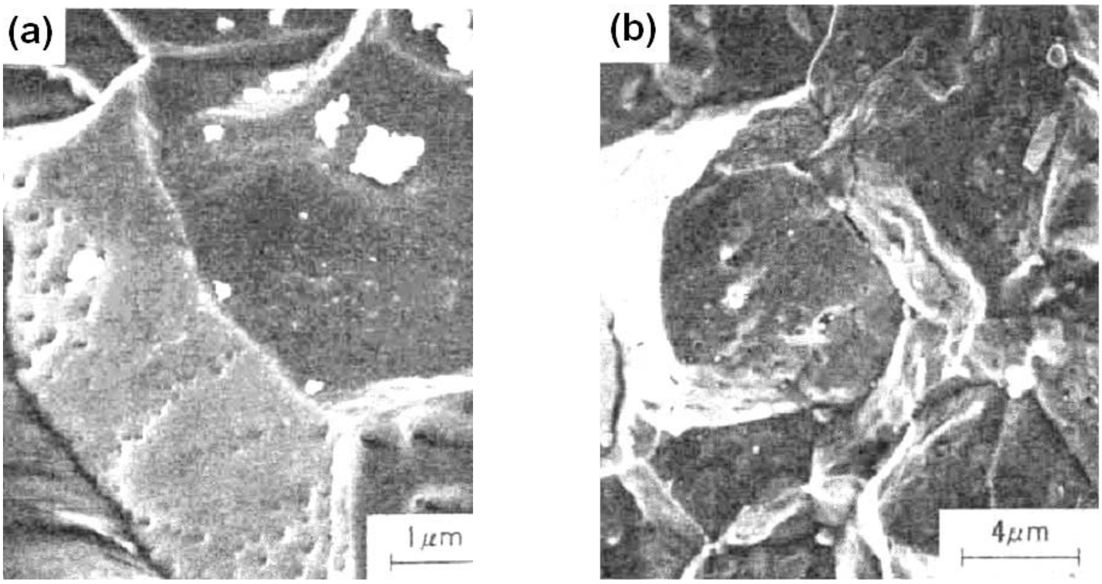

Fig. 1. Scanning electron micrographs of fuel fracture surface from Ref. [6]:
(a) 2 cycle as-irradiated specimen, (b) 4 cycle as-irradiated specimen

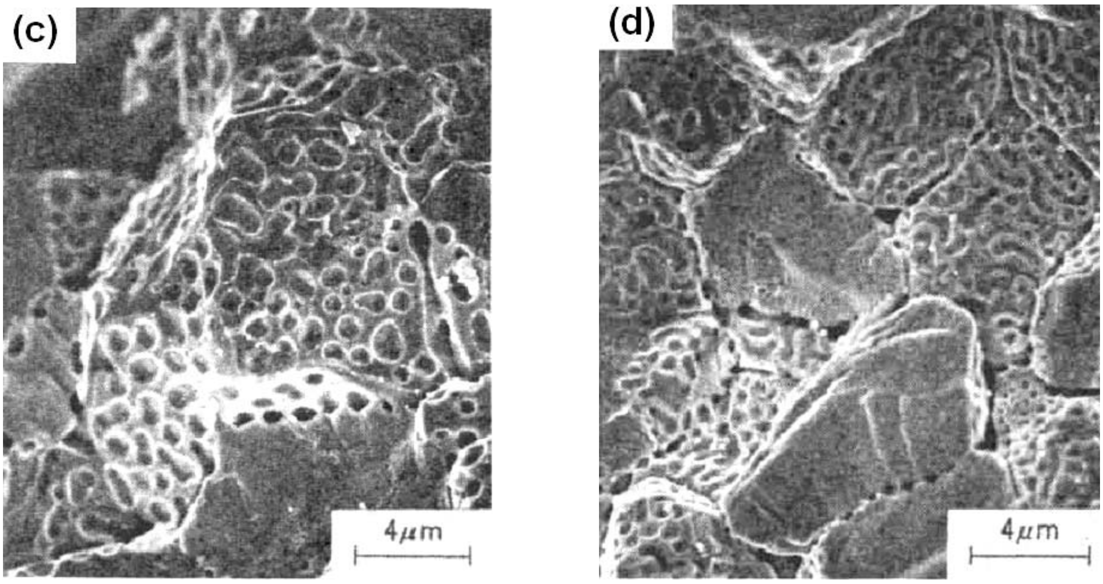

Fig. 1. Scanning electron micrographs of fuel fracture surface from Ref. [6]:
(c) 4 cycle specimen heated up to 1800 °C, (d) 2 cycle specimen annealed 5 h at 1800 °C

Despite such low values of the grain-face coverage, significant fractional fission gas release (up to 20–30 %) during their base irradiation was measured by pin puncture tests from these specimens, Fig. 2. Therefore, a noticeable gas release from these fuel samples occurred at coverage far below the saturation value ≈ 50 % and without visible bubble interlinking on the grain faces. The irradiation temperature at the location of the specimens was not directly measured, but might be evaluated as ~ 1100–1300 ºC from the maximum linear heat generation rates (see below).

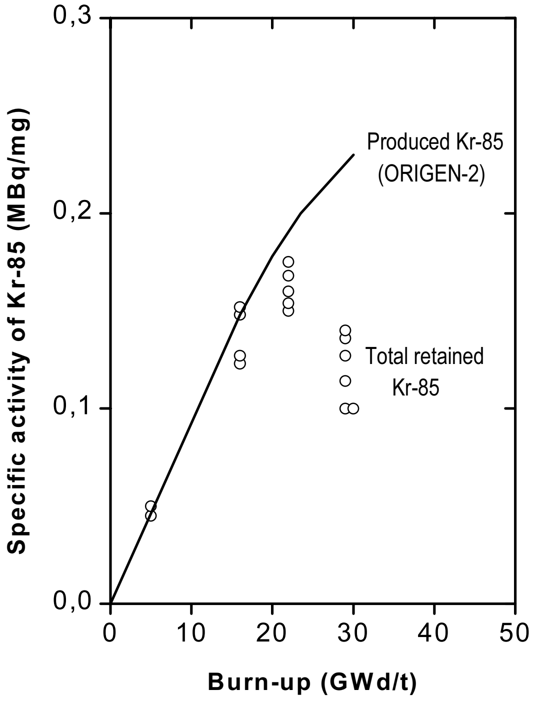

Fig. 2. ^{85}Kr concentrations in UO$_2$ as a function of burn-up measured in Ref. [6]

On the other hand, a significant burst release observed in these tests during post-irradiation annealing at 1600–1800 °C was invariably associated in [6, 7] with the coverage of about 40–50 % attained under various burnups and heating conditions, Fig. 1, panels *c* and *d*. Hence, interlinking of grain-face bubbles at the threshold value of the coverage ≈ 50 % considered in the models [1–4] might be responsible for the secondary burst release observed in the annealing stage of the tests [6, 7].

Therefore, from these tests it can be generally concluded that at low irradiation temperatures (≤ 1250 °C) the formation of the open porosity network can be significantly delayed, but this does not prevent an earlier commencement of gas release. To explain this effect one should additionally consider an input in the total gas release of the diffusion transport of gas atoms along grain faces in presence of grain boundary traps (bubbles). This diffusion transport becomes dominant in the lack of interlinking of grain-face bubbles. Usually the diffusion process is considered only in evaluation of the grain-face bubble size [8–11] and/or estimation of the incubation period for saturation coverage [1, 2], since it is assumed that practically all gas diffused from grains to grain boundaries is collected by the growing grain-face bubbles and only a negligible part is transported to grain edges (before interlinking of grain bubbles). This assumption was seemingly supported by the theoretical analysis [11] that shown that the sink strength of the grain-face periphery (edges) becomes (after some initial time interval) negligibly small in comparison with the total sink strength of the growing grain-face bubbles. A similar conclusion was later derived in [12].

However, these results can be strongly violated if one additionally takes into account resolution of gas atoms from face bubbles back to the grain matrix (not considered in [11]), that may essentially redistribute the diffusion flux from grains among different sinks on grain faces.

Indeed, as shown in [13] re-dissolved atoms are knocked some distance δ into the grain from the grain boundary, whence they may proceed to diffuse again. The built-up concentration barrier c_δ of the re-solution layer reduces the diffusion flux from the grain Φ_{dif}, on the one hand, and determines the net flux of atoms deposited on the grain boundary $\Phi_\delta \approx Dc_\delta/\delta$, on the other hand [13]. This flux Φ_δ should counterbalance the resolution flux back into the grain Φ_{res} and, in accordance with the flux matches $\Phi_{dif} + \Phi_{res} = \Phi_\delta$ (see below), may essentially exceed the «source term» from the grain Φ_{dif}. Namely this flux Φ_δ should be redistributed among various grain-face sinks (bubbles and edges) rather than the source term flux Φ_{dif}.

Neglecting such an effect in Ref. [11] resulted in underestimation of the grain boundary diffusion flux to edges. On the other hand, gas atom resolution from grain faces was taken into account in some other papers (e. g., see [1, 8, 13]), however the grain-face diffusion transport to edges was not included in consideration. The simultaneous consideration of various processes on grain-faces (atom diffusion, trapping by and resolution from the grain boundary bubbles) was proposed for the first time in [14] in order to reconcile various approaches. However, some simplifications of the model adopted for numerical analysis of coupled equations for intra- and inter-granular transport apparently prevented the author [14] from important conclusions concerning essential role of atomic grain-face transport to edges in the course of face bubbles growth. For this reason, in the subsequent paper [12] the author concluded that the contribution of grain boundary diffusion to fission gas release on the pellet scale is strongly inhibited as soon as the aerial coverage of the grain boundary traps is about 1 %, and consequently a simplified or alternative model for the inter-granular behavior of fission products (FP) was further developed.

In papers [15, 16] an essential role of the grain-face diffusion transport in the gas release mechanism was highlighted, in order to explain the above mentioned [6, 7] and some other observations. For this purpose a completely self-consistent scheme for analysis of diffusion and resolution processes in the grain and grain faces was considered. In particular, it was shown that «circulation» of gas atoms collected by growing intergranular bubbles from the grain face and then returned back (by the resolution process) into the grain matrix, made bubbles much less effective sinks for gas atoms in the course of their growth saturation (i. e. approaching a balance among absorbed and re-emitted atoms) and thus continuously increased a fraction of the source term flux from grain bulk eventually transported to edges. Specifically, this leads to a natural conclusion that in the limiting case of the complete balance between absorbed and re-emitted atoms and cessation of the face bubble growth (before their interlinking), 100 % of the source term flux will be transported to grain edges via grain-face diffusion process.

1. Model description

1.1. Extra-granular porosity geometry

From geometrical point of view, the UO_2 grains can be considered as truncated octahedrons or tetrakaidecahedrons (TDK) [1]. The TDK has 14 faces, six of which are square and eight hexagonal, 36 edges and 24 corners. When packed together an array of TDKs can fill all available space in a solid and thus represents an appropriate basic building block. The meeting point of each grain face is shared by two grains, each grain edge — by three grains, and each grain corner — by four grains. Hence, on average each grain has $N_{fpgr} = 7$ faces, $N_{epgr} = 12$ edges and $N_{cpgr} = 6$ corners.

Three intergranular bubble types are considered in MFPR:

1) the grain face bubbles uniformly covering the bubble faces with the surface concentration ρ_f;
2) the edge bubbles located at grain edges (one bubble per edge), and
3) the corner bubbles located at the grain corners (one bubble per corner).

Generally, the bubbles are of non-spherical shape with volume V calculated by multiplication of the volume of a sphere with the same curvature radius by a correction factor f, which depends on the semidihedral angle θ:

$$V_i = \frac{4}{3}\pi R_i^3 f_i(\theta_i) , \qquad (1)$$

where R_i is the bubble curvature radius, subscript i specifying bubble type.

The curvature radii for all bubble types are calculated assuming their equilibration:

$$\left(\frac{2\gamma}{R_b} + p_h\right) V_b f_b\left(\theta\right) = N_b k_B T . \qquad (2)$$

Grain face lenticular bubbles are formed by intersection of two spherical surfaces of radius R_f and hence have a circular projection. The projected circular radius is $R_f \sin\theta$, the correction factor for the volume is [17]

$$f_f(\theta) = 1 - \frac{3}{2} k_f + \frac{1}{2} k_f^3 , \qquad (3)$$

where $k_f = \cos\theta_f = \cos 50^\circ \approx 0.64$.

Following model [17], the edge bubbles were considered as cigar-shaped formed by intersection of three spherical surfaces. The length of an edge bubble is connected with its radius of curvature by the relationship

$$l_e = 2R_e\sqrt{1 - \frac{4k_e^2}{3}} , \qquad (4)$$

where $k_e = 1/2$. The volume correction factor is calculated as

$$f_e = \frac{3}{2\pi}\left[\pi - 2\arcsin\left(\frac{1}{2\sqrt{1-k_e^2}}\right) + \frac{k_e^2}{3}\sqrt{3-4k_e^2} - k_e\left(3-k_e^2\right)\arccos\left(\frac{k_e}{\sqrt{3\left(1-k_e^2\right)}}\right)\right] \approx 0.16 . \qquad (5)$$

The FP release to open porosity is associated with formation of the interconnected channels at grain-face periphery when the growing edge and corner bubbles begin touching each other.

The corner bubbles with the shape constructed by intersection of four spherical surfaces [17], with a reasonable accuracy can be considered as spherical ones.

1.2. The mean field model for gas atoms in the grain face

The model considers the evolution of gas atom concentration at the grain faces in the framework of the mean field approximation taking into account irradiation induced resolution of the gas atoms from grain face and edge bubbles, which returns a part of the atoms absorbed by these bubbles back into the grain matrix. Under steady state conditions the total gas atom flux Φ_δ per one grain (the number of gas atoms per one grain transported to the intergranular space per second) is a sum of diffusion and irradiation induced resolution fluxes, Φ_{dif} and Φ_{res} :

$$\Phi_\delta = \Phi_{\text{dif}} + \Phi_{\text{res}}. \qquad (6)$$

As shown in [13] re-dissolved atoms are knocked some distance δ into the grain from the grain boundary, whence they may proceed to diffuse again. This process results in a built-up concentration barrier c_δ of the resolution layer, which can be estimated from relation

$$\Phi_\delta \approx D_g c_\delta / \delta. \qquad (7)$$

Therefore, the concentration c_δ turns out as a natural boundary condition at the resolution layer boundary δ, as recommended by Turnbull [8] instead of zero boundary condition in the simplified model with no resolution effect taken into account.

The resolution flux is calculated as

$$\Phi_{\text{res}} = \omega_f Y_f + \omega_e Y_e + \omega_c Y_c, \qquad (8)$$

where $Y_{f,e,c}$ are the total numbers of gas atoms per one grain within face, edge or corner bubbles and $\omega_{f,e,c}$ are the kinetic parameters of irradiation induced resolution. Namely the flux Φ_δ should be redistributed among various grain-face sinks (bubbles and edges) rather than the source term flux Φ_{dif}.

These considerations imply that the gas atoms knocked out from the bubbles are homogeneously redistributed in vicinity of the grain boundary due to diffusion in the lateral directions, and then are deposited on the grain boundary contributing to the total intragranular gas transport. The characteristic time τ^* for the diffusion homogenization of gas atom concentration in the lateral direction can be estimated as R_s^2/D_g, where R_s is the mean interbubble distance and D_g is the gas atom diffusion coefficient. Using typical value for $D_g \approx 10^{-16}$–10^{-15} cm^2/s under irradiation with fission rate $G \approx 10^{13}$ cm^{-3}s^{-1} at 1000-1300 K and $R_s \approx 0.1$ μm, one obtains $\tau^* \approx 10^5$–10^6 s, i. e. the diffusion flux from the grain to the grain faces can be considered as uniform (in the lateral direction) after a relatively short initial interval of steady irradiation. Therefore, the mean field approach seems to be well-grounded for the grain-face bubbles that almost uniformly cover the grain faces due to their large number (10^2–10^3 per face).

However, the approach is doubtful considering the edge and corner bubbles located at the periphery of the grain face. Indeed, after delivery of the (uniform) diffusion flux to the grain face, a part of this flux is absorbed by the face bubbles, whereas a remaining part diffuses along the surface concentration gradient and sinks into the grain face periphery, i.e., is absorbed by the edge and corner bubbles. Therefore, only a part of atoms knocked out from the face bubbles eventually return back to these bubbles. This redistribution effect is properly described by the MFPR model. On the other hand, majority of atoms knocked out from the peripheral bubbles eventually return back to these bubbles since being deposited on the grain-face in the vicinity of the grain face periphery, they continue to move along the concentration gradient (directed to the grain-face periphery) sinking again into the edge without losses to the face bubbles. Therefore, one suggests that the gas atoms knocked out from the peripheral bubbles due to collisions with the fission fragments tend to return back to the bubbles rather than to contribute to the mean field concentration. This implies that in the mean field approach the irradiation induced resolution from the periphery bubbles should be essentially suppressed by an additional factor introduced in the subsequent paper of this Collection on p. 25.

1.3. Coverage factors

The part $\Phi_\delta^{(f,e,c)}$ of the above introduced flux Φ_δ, which is directly captured by the face, edge or corner bubbles, is calculated as $\Phi_\delta \varphi_{f,e,c}$, where

$$\varphi_{f,e,c} = S_{f,e,c}\rho_{f,e,c}, \qquad (9)$$

where $S_{f,e,c}$ and $\rho_{f,e,c}$ are the area of the bubble projection on the grain surface and the bubble surface density, respectively.

For the grain face bubble the area is calculated as $S_f = \pi\left(\sin\theta_f R_f\right)^2$. The surface density of these bubbles was measured in several independent tests (e.g., [7, 18, 19]) and turned out to vary in the range 10^{11}–10^{13} m^{-2}.

The analysis of the available data demonstrates that ρ_f can be fairly well approximated in a wide temperature interval 800–1900 °C by the formula

$$\rho_f = \min\left\{\rho_0 \exp\left(T_0/T\right), \rho_{\max}\right\}, \qquad (10)$$

where $\rho_{\max} = 10^{13}$ m^{-2}, $\rho_0 = 3.67\cdot10^8$ m^{-2}, $T_0 = 13140$ K.

Simplified evaluation of projection area for edge and corner bubbles will be presented in the subsequent paper of this Collection on p. 25.

1.4. Sink strengths

Owing to an extremely high ratio of the gas atom diffusion coefficients on grain faces D_f and in the grain matrix D_g, which is usually believed to be of the same order of magnitude as that for the uranium self-diffusion coefficients, $D_f/D_g \sim 10^5$ [20], one can apply results of the steady-state consideration of the grain-face diffusion problem [11] to calculate the face bubbles and edges sink strengths in the mean field approximation:

$$\left(k_f R_s\right)^2 = \frac{8\left(1-\varphi_f\right)}{-\left(1-\varphi_f\right)\left(3-\varphi_f\right) - 2\ln\varphi_f}, \qquad (11)$$

$$\left(k_e R_{\text{face}}\right)^2 = 2k_f R_{\text{face}} \frac{I_1\left(k_f R_{\text{face}}\right)}{I_2\left(k_f R_{\text{face}}\right)}, \qquad (12)$$

where $R_{\text{face}} = d_{gr}\big/\sqrt{N_{fpg}} = d_{gr}\big/\sqrt{14}$ is the effective radius of the grain face, R_s is the radius of a concentric sink-free region which surrounds each face bubble in the plane of the grain boundary, $\varphi_f = \left(R_{\text{face}}/R_s\right)$ is the grain-face coverage.

The values k_f^2 and k_e^2 determine the relative sinks of the surface diffusion flux: a part $k_f^2\big/\left(k_f^2 + k_e^2\right)$ of the flux sinks to the face bubbles (and then is partially ejected back into the grain), while the reminder $k_e^2\big/\left(k_f^2 + k_e^2\right)$ sinks to the edges.

Note, that it follows from Eq. (11) that $k_f R_s > 1$, provided $\varphi_f > 0.01$. Taking into account that $R_{\text{face}} >> R_s$ this implies that $k_f R_{\text{face}} > 1$. Therefore, taking into account that $I_1(x)\big/I_2(x) \to 1$, for the large x values one deduces that $k_e/k_f \approx \sqrt{2/k_f R_{\text{face}}} << 1$. It is just that strong inequality that prevented authors of papers [11, 12] from conclusion concerning the important role of the atomic grain-face transport to edges in the course of grain-face bubble growth.

1.5. Transport equations

Equations for number of gas atoms in face and edge bubbles, Y_f and Y_e , per one grain take the form

$$\frac{d}{dt}Y_f = \varphi_f\Phi_\delta + \left(1-\varphi_f-\varphi_e-\varphi_c\right)\Phi_\delta\frac{k_f^2}{k_f^2+k_e^2} - \omega_f Y_f,$$
$$\frac{d}{dt}Y_e = \varphi_e\Phi_\delta + \eta_e\left(1-\varphi_f-\varphi_e-\varphi_c\right)\Phi_\delta\frac{k_e^2}{k_f^2+k_e^2} - \omega_e Y_e, \qquad (13)$$
$$\frac{d}{dt}Y_c = \varphi_c\Phi_\delta + \eta_c\left(1-\varphi_f-\varphi_e-\varphi_c\right)\Phi_\delta\frac{k_e^2}{k_f^2+k_e^2} - \omega_c Y_c,$$

where relative parts η_e and η_c of the total flux out of grain face to edge and corner bubbles, respectively, for simplicity are assumed to be equal to the relative numbers of corresponding bubbles on an edge: $\eta_e = N_{bpe}/(N_{bpe} + 1)$ and $\eta_c = 1 - \eta_e$ (where N_{bpe} is the number of edge bubbles per edge).

The first terms in the r.h.s. of the equations describe the part of the total gas flux that is directly captured by the bubbles. The second terms describe the diffusion transport along the grain faces, redistributed in accordance to the sink strengths. The third terms describe the loss of the gas atoms due to irradiation induced resolution.

The system Eq. (13) describes evolution of extragranular porosity up to the moment when corresponding saturation conditions are attained. The grain-face saturation by fission gas is supposed to be attained when the projected area coverage of the grain face by bubbles φ_f exceeds the critical value $\varphi_f^{\text{crit}} = 0.5$.

1.6. Preliminary validation

Preliminary validation of the model after its implementation in the MFPR code against various tests [6, 7, 18, 21] confirmed that a noticeable gas release from these fuel samples might occur at coverage 6–10 %, i. e. far below the saturation value ≈ 50 % and without visible bubble interlinking on the grain faces, see [15, 16]. More detailed validation of the further developed model will be presented in the subsequent paper of this Collection on p. 25.

1.7. Discussion of tests with MOX fuel

In the MOX MIMAS AUC fuel irradiated in PWR rods (where the centre-line temperatures as calculated lie in the range from 1000 to 1200 °C) there is no evidence of inter-granular bubbles [22]. In order to explain high release values and decrease of the gas content in the U-rich matrix measured in the central part of the pellet, assumption is made in [22] that in MOX fuel, there is a strong enhancement of the kinetic of xenon migration in the grain boundaries. This assumption is based on the experiments on interdiffusion of PuO_2 in UO_2 [23] which show that the cation diffusion coefficients in grain boundary is much higher (about 2 orders of magnitude) in the presence of Pu. As xenon diffusion is related to cation diffusion, it was assumed a similar evolution of the Xe diffusion coefficients.

For modelling of the MOX fuel irradiated in PWR rods in which there is no evidence of inter-granular bubbles despite fission gas release is relatively high, the new model for gas transport on grain boundaries becomes especially important. This model allows explanation of gas release without interconnection of bubbles (as observed in the above described tests with UO_2 fuel [6, 7]), and thus, after certain modifications can be applied to the MOX fuel.

Conclusions

The advanced model for the grain-face transport of gas atoms self-consistently takes into account the effects of atom diffusion along the grain surface and irradiation-induced re-solution from intergranular bubbles. It is shown that «circulation» of gas atoms collected by growing intergranular bubbles from the grain face and then returned back (by the re-solution process) into the grain matrix, makes intergranular bubbles much less effective sinks for gas atoms, since it decreases their growth (i.e. approaching a balance among absorbed and re-emitted atoms) and thus continuously increases a fraction of the source term flux (i.e. diffusion flux from grain to grain faces) eventually transported to grain edges. In particular, this allows prediction of a noticeable gas release from fuel when the grain-face coverage is far below the saturation value ≈ 50 % determining onset of grain-face-bubble interlinking.

References

1. *White R.J., Tucker M.O.*/ J. Nucl. Mater. 1983. Vol. 118. P. 1.
2. *Beere W., Reynolds G.L.*/ Ibid. 1973. Vol. 47. P. 51.
3. *Dollins C.C., Nichols F.A.*// Ibid. 1976. Vol. 91. P. 143.
4. *Heames T.J.* et al. VICTORIA: A Mechanistic Model of Radionuclide Behaviour in the Reactor Coolant System under Severe Accident Conditions. NUREG/CR-5545. 1992.
5. *Hastings I.J.* // J. Nucl. Mater. 1974. Vol. 54. 138.
6. *Une K., Kashibe S.* // J. Nucl. Sci. Technol. 1990. Vol. 27. P. 1002.
7. *Kashibe S., Une K.*// Ibid. 1991. Vol. 28. P. 1090.
8. *Turnbull J.A.* // J. Nucl. Mater. 1974. Vol. 50. P. 62.
9. *Turnbull J.A., Tucker M.O.*// Philos. Mag. 1974. Vol. 30. P. 47.
10. *Wood M.H.* // J. Nucl. Mater. 1983. Vol. 119. P. 67.
11. *Matthews J.R., Wood M.H.*// Ibid. 1980. Vol. 91. P 241.
12. *Van Uffelen P.* Assessing the contribution of grain boundary diffusion to fission gas release in nuclear fuel // Enlarged Halden Programme Group Meeting. Loen, Norway, 1999.
13. *Speight M.V.* // Nucl. Sci. Engrg. 1969. Vol. 37. P. 180.
14. *Van Uffelen P.* Development of a new fission gas release and fuel swelling model // Enlarged Halden Programme Group Meeting. Lillehammer, Norway, 1998. HPR-349.
15. *Veshchunov M.S., Berdyshev A.V., Tarasov V.I.* Development of Fission Gas Bubble Models for UO2 Fuel in Framework of MFPR Code. — (Preprint / Nuclear Safety Institute (IBRAE) RAS, no IBRAE-2000-08). Moscow: NSI (IBRAE) RAS, 2000.
16. *Berdyshev A.V., Veshchunov M.S.* Modelling of grain face diffusion transport and swelling in uo2 fuel. (Preprint / Nuclear Safety Institute (IBRAE) RAS, no IBRAE-2002-14). Moscow: NSI (IBRAE) RAS, 2002.
17. *Clemm P.J. Fisher J.C.* // Acta Metall. 1955. Vol. 3. P. 70.
18. *Pati S.R., Dapt M.J., O'Boyle D.R.*// J. Nucl. Mater. 1974. Vol. 50. P. 227.
19. *Walker C.T., Knappik P., Mogensen M.*// Ibid. 1988. Vol. 160. P. 10.
20. *Alcock G.B., Hawkins R.J., Hills A.W.D., McNamara P.* // IAEA. Symp. Thermodynamics. Vienna, 1965. — Paper SM-66/36. P. 57.
21. *Zimmermann H.* // J. Nucl. Mater. 1978. Vol. 75. P. 54.
22. *Guerin Y., Noirot J., Lispaux D., Struzik C., Garcia P., Blainpain P., Chigne G.* Microstructure evolution and in-reactor behaviour of MOX fuel // Proc. Int. Top. Meet. LWR Fuel Performance April 10–13, 2000; Park City, Utah, USA. P. 706–719.
23. *Mendez S.* Etude de l'interdiffusion U–Pu applique au combustible MOX // Thesis Universite Aix-Marseille. 1995.

Model for Grain-Face Diffusion Transport in UO_2 Fuel Part 2. Model Improvement and Validation

V.I. Tarasov, M.S. Veshchunov

Introduction

An advanced model for the grain-face transport of gas atoms has been suggested in paper of this Collection (see p. 17) that self-consistently takes into account the effects of atom diffusion along the grain surface and irradiation-induced re-solution from intergranular bubbles. It is shown that «circulation» of gas atoms collected by growing intergranular bubbles from the grain face and then returned back (by the re-solution process) into the grain matrix makes intergranular bubbles much less effective sinks for gas atoms and thus increases a fraction of the diffusion flux from the grain directly transported to the grain edges. In particular, this mechanism allowed explanation of the observed in the experiment [1, 2] a noticeable gas release from fuel even when the grain-face coverage is far below the saturation value $\varphi \approx 50\,\%$, which was associated in the standard approaches with the grain-face-bubble interlinkage and the onset of fission product release [3-6].

Further development of the model is described in this paper that relates to revision of the intergranular bubble nomenclature, their shape, sizes and concentration, more detailed consideration of the applicability of the mean field approach for the «circulated» gas atoms and improvement of the model for the irradiation induced re-solution of gas atoms from the bubbles. The modified model has been implemented into the MFPR code [7] and fitted to experimental data [1, 2]. The results of the model validation are also given in the article.

1. Model description

1.1. Extra-granular porosity geometry

From geometrical point of view, the UO_2 grain can be considered the tetrakaidecahedron, the number of faces, edges and corners per one grain being 7, 12 and 6. The volume V of the tetrakaidecahedron is calculated as

$$V = 8\sqrt{2}L_{\mathrm{edge}}^3, \qquad (1)$$

where L_{edge} is the grain edge length. For simplicity, the fuel grains are assumed to be of spherical form. So, equating the sphere volume with the value given by Eq. (1) one derives that

$$L_{\mathrm{edge}} = \sqrt[3]{\frac{\pi}{48\sqrt{2}}}d_{gr} = \beta_e d_{gr} \approx 0.359 d_{gr}, \qquad (2)$$

where d_{gr} is the grain diameter, so the typical value for L_{edge} is 3-4 μm.

In the original model paper of this Collection (see p. 17) there are three types of intergranular bubbles: grain face, edge and corner ones. The corner bubbles are considered as the spherical ones. The grain face bubbles are considered of the lenticular shape formed by intersection of two spherical surfaces of radius Rf, the semi-dihedral angle θf is supposed to be equal to 50°. The edge bubbles are considered as cigar-shaped formed by intersection of three spherical surfaces. The length le and the volume Ve of an edge bubble is connected with its radius of curvature by the relationship [8]

$$l_e = 2R_e\sqrt{1-\frac{4k_e^2}{3}}\ , \tag{3}$$

$$V_e = 2R_e^3\left[\pi - 2\arcsin\left(\frac{1}{2\sqrt{1-k_e^2}}\right) + \frac{k_e^2}{3}\sqrt{3-4k_e^2} - k_e\left(3-k_e^2\right)\arccos\left(\frac{k_e}{\sqrt{3\left(1-k_e^2\right)}}\right)\right], \tag{4}$$

where $k_e = \cos\theta_e = 1/2$. If to approximate the shape of the edge bubble by a cylinder with length l_e and diameter d_e then equating the volumes, one easily evaluates that

$$\frac{l_e}{d_e} = \sqrt{\frac{3}{2f_e}}\left(1-\frac{4k_e^2}{3}\right)^{3/2} \approx 2.3, \tag{5}$$

indicating that the longitudinal and transversal bubble sizes are of the same order of magnitude.

The FP release to open porosity is associated with formation of the interconnected channels at grain face periphery when the growing edge and corner bubbles begin touching each other. Under simplifying assumption that there are one grain edge bubble and one corner bubble per each edge, the formation of the channels commences when $R_e \sim R_c \sim L_{\text{edge}}/2$. In view of estimates, Eqs. (2) and (5), this means that the commencement of the FP release is possible if the sizes of the edge and corner bubbles are ~1 μm.

However this conclusion is not confirmed by the experiment [1, 2], which demonstrates much less bubble sizes (e.g., see Fig. 1 from paper on p. 17). So, the only way to eliminate this discrepancy is to suppose that there is much more than one bubble per each grain edge. In this connection, the complicated modelling of the edge bubbles shape seems to be unjustified taking into account the target model accuracy, so it is natural to simplify the consideration suggesting that the shape of the edge bubbles is the spherical one (that is the same as for the corner bubbles). At last, it is natural to suppose that edge and corner bubbles capture the diffusion flux in proportionally to their sizes. This implies that the sizes of both types of the bubbles are comparable to each other and therefore, will be further considered as indistinguishable. Therefore, in the modified model of intergranular transport the peripheral porosity is represented only by spherical edge bubbles, their number per edge being the MFPR free parameter.

1.2. Mode for irradiation induced resolution

1.2.1. Track length

According to the Nelson's model [9] the resolution rate does not depend on the size of small (van der Waals) bubbles. For larger spherical bubbles only a fraction of gas atoms within a critical distance from the bubble surface δ may escape. Therefore the resolution kinetic parameter is calculated as

$$\omega_{rsi}^{\text{Nelson}}(R_b) = G b_0 \cdot \begin{cases} 1 & \text{for} \quad y = \delta/R_b \ge 1, \\ 3y\left(1-y+y^2/3\right) & \text{for} \quad y = \delta/R_b < 1, \end{cases} \tag{6}$$

where G is the fission rate, $b_0 = 2\cdot10^{-23}$ cm^3 is the resolution constant. Supposing that the minimal energy that a struck gas atom must receive to be trapped by surrounding lattice is 300 eV, the value of δ can be estimated as 1.0–1.5 nm [9]. In the VICTORIA [6] and FASTGRASS [10] codes the modified model was implemented that introduced, instead of δ, the average distance λ which an ejected atom travels in the bubble. So for the spherical bubbles one gets

$$\omega_{rsi}(R_b) = G\,b_0 \cdot \begin{cases} 1 & \text{for} \quad z = \lambda / 2R_b \geq 1, \\ \frac{1}{2} z\left(3 - z^2\right) & \text{for} \quad z = \lambda / 2R_b < 1. \end{cases} \tag{7}$$

As seen both formulas coincide for small bubbles; whereas for large bubbles they coincide asymptotically, provided $\lambda = 4\,\delta$, in a reasonable agreement with the VICTORIA's value $\lambda = 5$ nm.

However these parameters cannot be considered as universal ones applicable to all bubbles. Indeed, the energy loss of the struck atom is determined by the number of collisions it has before it escapes the bubble. Therefore, the track length increases with the increase of inter-atomic distance within the bubble, which, in turn, increases with the bubble size. The universal scaling of the track length is determined by the formula

$$\lambda = 1/n\sigma, \tag{8}$$

where n is the (number) density of the media and σ is the effective cross-section of the collisions. The above mentioned parameter λ (hereafter referred to as λ_{vdW}) was introduced in Ref. 9 for the small van der Waals bubbles for which $n = 1/B_{\mathrm{Xe}}$, where B_{Xe} is the van der Waals constant for xenon. Therefore, one evaluates σ value as $B_{\mathrm{Xe}}/\lambda_{vdW}$ and derives an approximate relation between the basic scale parameters of the model:

$$\lambda = \frac{\lambda_{vdW}}{nB_{\mathrm{Xe}}} = \frac{\lambda_{vdW}V_b}{B_{\mathrm{Xe}}N_b}, \tag{9}$$

where λ_{vdW} can be considered as a model free parameter (Nelson's estimate is ~5 nm), V_b and N_b are the bubble volume and number of atoms in the bubble. The rhs of Eq. (9) can be written in form $V_b/N_b\sigma$, which does not explicitly refer to properties of van der Waals bubbles, σ being considered as the fitting parameter. However we prefer to deal with the form Eq. (9), which deals with more tangible variables.

In particular for the large grain face bubbles obeying the ideal gas law with the equilibrium pressure $p = 2\gamma/R_b$, where γ is the surface tension, Eq. (9) reduces to

$$\lambda = \lambda_{vdW}\frac{kTR_b}{2\gamma B_{\mathrm{Xe}}}. \tag{10}$$

For instance, in the case of $R_b = 10^{-7}$ m and $T = 1200$ K one gets $\lambda \approx 40$ nm, that is 8 times greater than for the van der Waals bubbles. Also, it is seen from this equation that for the large bubbles the ratio λ/R_b depends on temperature only.

1.2.2. Resolution from non-spherical bubbles

The above Eqs. (6) and (7) were derived for spherical bubbles, for which the shapes correspond to the minimal surface area at fixed bubble volume and therefore to the minimal resolution intensity. For lenticular bubbles the relative bubble volume, from which atoms can escape, increases owing to the bubble specific geometry, therefore resolution kinetic coefficient should be modified. For large bubbles ($R_b >> \lambda$) Eq. (7) can be rewritten in the form

$$\omega_{rsi}(R_b) = G\,b_0\frac{3\lambda}{4R_b} = G\,b_0\frac{S_b}{V_b}\frac{\lambda}{4},$$

so, that taking into account the well-known equations for the volume V_b and surface S_b of a lenticular bubble:

$$V_b = \frac{4\pi}{3}\left(1 - \frac{3}{2}\cos\theta + \frac{1}{2}\cos^3\theta\right)R_b^3 = \frac{4\pi}{3}\left(1 - \cos\theta\right)\left(1 - \frac{1}{2}\cos\theta - \frac{1}{2}\cos^2\theta\right)R_b^3,$$
$$S_b = 4\pi R_b^2\left(1 - \cos\theta\right),$$

where θ is semi-dihedral angle, one derives that

$$\omega_{rsi}\left(R_b\right)=\frac{3\lambda G b_0}{4R_b\left(1-\frac{1}{2}\cos\theta-\frac{1}{2}\cos^2\theta\right)}=\frac{\omega_{rsi}^{spherical}\left(R_b\right)}{1-\frac{1}{2}\cos\theta-\frac{1}{2}\cos^2\theta}. \tag{11}$$

It is seen from Eq. (11) that the angle factor is always greater than 1. In particular, for the face bubbles with θ = 50° consideration of the bubble shape correction results in increase of the resolution intensity by a factor of 2.1 comparing with the spherical bubble with the same curvature radius R_b.

1.2.3. Restrictions for applicability of the mean field approach

As explained in the paper on p. 17, the atoms knocked out from the edge bubbles due to collisions with the fission fragments move in the strong concentration gradient in the vicinity of the grain face periphery. Therefore, in contrast to the grain face bubbles, the gas atoms knocked out from the edge bubbles tend to return back to the bubbles rather than to contribute to the mean field concentration. As a result, this reverse flux essentially compensates the irradiation induced resolution flux. To simulate this effect, the irradiation induced resolution from the edge bubbles is supposed to be partially suppressed. The new fitting parameter — suppression factor, σ_b, is introduced so the expression for the irradiation induced resolution kinetic parameter is modified as

$$\omega_{res}(R_b)=\frac{G b_0\sigma_b}{\left(1-\frac{1}{2}\cos\theta-\frac{1}{2}\cos^2\theta\right)}\begin{cases}1 & \text{for } \lambda\geq 2R_b,\\ \frac{\lambda}{4R_b}\left(3-\frac{\lambda^2}{4R_b^2}\right) & \text{for } \lambda< 2R_b,\end{cases} \tag{12}$$

where the track length is given by Eq. (9).

1.3. Coverage factors

The coverage factors, φ_f and φ_e, for the face and edge bubbles are defined as

$$\varphi_{f,e}=S_{f,e}\rho_{f,e}, \tag{13}$$

where $S_{f,e}$ and $\rho_{f,e}$ are the area of the bubble projection on the grain surface and the bubble surface density, respectively. The coverage factor for the grain face bubbles is straightforwardly calculated, see paper on p. 17. To estimate S_e one takes into account that each edge bubble is shared by three grains. Therefore, the bubble projection within one grain has the shape of ellipse with the semi-major and semi-minor axes R_e and $\sqrt{3}R_e/2$, respectively, so that the projection area is evaluated as

$$S_e\approx\pi\left(\sqrt{3}/2\right)R_e^2\approx 0.866\pi R_e^2. \tag{14}$$

As for the surface density of the edge bubbles, lacking detailed systematic data it is assumed that the mean distance Lee between the edge bubble is proportional to the mean distance between face bubbles:

$$L_{ee}=2\zeta_e R_s, \tag{15}$$

where $R_s=\left(\pi\rho_f\right)^{-1/2}$ is the radius of sink-free region and ζ_e is the MFPR free parameter. Therefore, the surface density ρ_e of the edge bubbles can be calculated as

$$\rho_e=\frac{3N_{epg}L_{edge}}{2\zeta_e R_s\pi d_{dr}^2}=\frac{18\beta_e\left(\pi\rho_f\right)^{1/2}}{\pi\zeta_e d_{gr}},$$

where the coefficient $\beta_e\approx 0.359$ was introduced in Eq. (2).

So, the formulas for the coverage factors of grain face and edge bubbles take the form:

$$\varphi_f=\pi\rho_f\left(R_f\sin\theta_f\right)^2,$$
$$\varphi_e=\frac{18\sqrt{3\pi}\beta_e\rho_f^{1/2}R_e^2}{\zeta_e d_{gr}}\approx 9.92\frac{\rho_f^{1/2}R_e^2}{\zeta_e d_{gr}}. \tag{16}$$

1.4. Transport equations

Time evolution of concentrations of gas atoms in face, edge and corner bubbles, Y_f, Y_e and Y_c, is described by a system of differential equations given in paper on p. 17. In accordance with the above described modifications, it can be represented in the following form:

$$\begin{aligned}\frac{d}{dt}Y_f &= -a_f\omega_f Y_f + a_e\omega_e Y_e + a_e\Phi_{dif},\\ \frac{d}{dt}Y_e &= a_f\omega_f Y_f - a_e\omega_e Y_e + a_f\Phi_{dif},\end{aligned} \tag{17}$$

where

$$a_f \equiv \frac{\varphi_e k_f^2 + \left(1-\varphi_f\right)k_e^2}{k_f^2 + k_e^2},$$

$$a_e \equiv \frac{\left(1-\varphi_e\right)k_f^2 + \varphi_f k_e^2}{k_f^2 + k_e^2},$$

Φ_{dif} being the source term (number of atoms diffused from the grains during a second per unit volume); note the condition $a_f + a_e = 1$.

The system Eq. (17) describes evolution of extra-granular porosity up to the moment when corresponding saturation conditions are attained. The grain-face saturation by fission gas is supposed to be attained when the projected area coverage of the grain face by bubbles φ_f exceeds the critical value $\varphi_f^{crit} = 0.5$. The grain edge porosity saturation takes place when these bubbles are just touching each other; with Eq. (15) taken into account this is equivalent to condition

$$R_e = \zeta_e R_s = \zeta_e\left(\pi\rho_f\right)^{-1/2}. \tag{18}$$

2. Model validation

2.1. Tests of Kashibe and Une

There are several experimental works where microscopic behaviour of intergranular bubbles was observed directly [1, 11]. As above mentioned, in [1] the specimens were taken from UO$_2$ pellets irradiated in commercial BWR (burn-up: 6~28 GWd/t) at a point between the fuel rim and middle. Grain face bubble concentration and fractional coverage were examined by scanning electron microscope fractography. The grain sizes of the fuel and irradiation rate were approximately equal to 9 μm and $1.8\cdot 10^{19}$ m^{-3}s^{-1}, correspondingly. In the lack of temperature measurements in these tests, one can evaluate the irradiation temperature at the location of the specimens as ~ 1500 K basing on the correlation between the linear heat generation rate (between 300 and 370 W/cm) and fuel temperature profiles [12].

As above explained, the new model has three unknown dimensionless parameters: the factor σ_b for resolution suppression from edge bubbles, Eq. (12), the track length λ_{vdW}, Eq. (9), and the ratio ζ_e of the average distance between edge bubbles to that between face bubbles, Eq. (15). Variation of these parameters has revealed that λ_{vdW} had a weak effect on the model predictions so it was fixed at the value of 5 nm, which is the center of the interval 4-6 nm followed from the Nelson's estimate (see subsection 1.2.1). Other parameters were chosen to provide the correct commencement of Xe fractional release in Zimmerman's test (see below, subsection 2.3) and bubble size to the end of the irradiation cycle 4 in the test of Une and Kashibe (burn-up: 28 GWd/t). The found values are $\zeta_e = 0.1$, $\sigma_b = 0.2$.

In Table 1 the calculated grain-face bubble characteristics: the coverage factor φ_f, the Xe fractional release f_{Xe}, the surface concentration of the grain-face bubbles ρ_b, and the mean diameters of intergranular bubbles d_f and d_e are compared with experimental data.

Table 1. Characteristics of the grain-face bubbles in simulation of the Kashibe—Une tests

	φ_f (%)	f_{Xe} (%)	ρ_f (m^{-2})	d_f (nm)	d_e (nm)
Model	4.9	44	$2.1\cdot10^{12}$	219	39
Experiment	10.1	30-50	$1.6\cdot10^{12}$	229	–

As seen, on the whole the model adequately describes the experimental data with some underestimation of the grain-face coverage and the small overestimation of the face bubble concentration. However, it should be noted that the data of Refs. [1, 2] are quite widely scattered from grain to grain and the measured values may be considered only as estimations. In particular, the experimental data are mutually inconsistent; indeed, the theoretical coverage calculated from the measured mean bubble radius and concentration:

$$\varphi = \pi R_f^2 C_f = 3.14\cdot\left(229\cdot10^{-9}/2\right)^2\cdot1.6\cdot10^{12}\cdot100\% \approx 6.6\%,$$

which is less than 10.1 % given in [2], cf. Table 1. This value is in a better agreement with the model prediction ≈ 4.9 %.

2.2. Tests of Pati et al.

In experiment [11] by Pati et al. the UO_2 fuel irradiated to a burn-up of $2\cdot10^{26}$ m^{-3} with fission rate $\approx 2.6\cdot10^{19}$ s^{-1}m^{-3} was examined by transmission and scanning electron microscopy and replication metallography. In these tests gas release was not measured, however, the fission gas distribution on the grain boundaries was characterized as a function of irradiation temperature 750–1350 °C. In Fig. 1 the temperature dependences of volume concentration C_f (upper panel) and radius R_f (lower panel) of intergranular bubbles are compared with experimental data.

As seen the MFPR correlation correctly describe the temperature dependence of the concentration of the grain face bubbles at high temperatures while overestimates the experiment for temperatures below ~1250 K. In fact, the concentration is calculated using simple correlation:

$$C_f = \min\left(C_{\text{cutoff}}, C_0\exp\left(-T_0/T\right)\right). \qquad (19)$$

whereas C_{cutoff} is the cut-off density, which was set equal to 10^{13} m^{-2} in the original model to fit the Pati's data. However, this restriction is inconsistent with other data. For instance Kashibe and Une cited the concentrations up to $6\cdot10^{13}$ m^{-2}. For this reason, in present version parameter C_{cutoff} was increased up to 10^{13} m^{-2}.

As for bubble radii, MFPR results underestimate the experimental ones by a factor of ~ 2. However note, that Pati's data [11] are in strong contradiction with measurements of Kashibe and Une who cited the surface concentrations up to $6\cdot10^{13}$ m^{-2} (at temperature 1400–1600 K) that correspond to the volume concentration of $2\cdot10^{19}$ m^{-2}, more that an order of magnitude higher than presented in Fig. 1. Also, there is a disagreement between the measured bubble radii. Indeed, the value of Kashibe and Une was 229/2 ≈ 115 nm at $T = 1523$ K (cf. Table 1) that is three times less than Pati's value whereas the inverse ratio takes place for the burn-ups (3.3 % for the test of Kashibe and Une and 0.8 % for Pati test.). So in our simulations we give the preference to more recent (and apparently more precise) experimental data [1, 2].

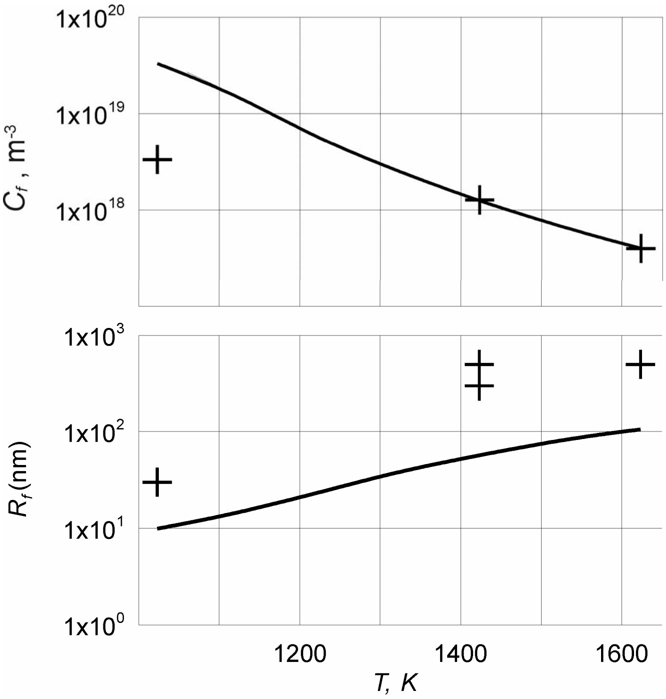

Fig. 1. Dependence of the volume concentrations C_f and radii R_f of intergranular bubbles from temperature under conditions of the test [11]

2.3. Tests of Zimmermann

In experiments [13] the fission gas behavior and swelling of UO_2 fuel were investigated at temperatures between 1000 and 2000 K under steady-state irradiation conditions. Two types of the UO_2 micro-specimens were irradiated: unrestrained samples of outer diameter 5.1 and inner diameter 2.2 mm (annular pellets) and height 1 mm, with mean grain diameter of 10 μm; restrained samples (compressive stress from 2 to 50 MPa) of diameter 3 mm and height 5.7 mm, mean grain diameter 7 μm. Specimens of the first type were subjected to irradiation at fission rates from $3.1\cdot10^{19}$ to $1.4\cdot10^{20}$ fissions/m^{3}s to burn-ups from 0.4 to 12.6 % of U atoms, with mean fuel temperatures from 1250 to 2000 K. The second-type specimens were irradiated at fission rates from $4.5\cdot10^{13}$ to $6.3\cdot10^{13}$ fissions/(cm^{3}s) to burn-ups from 2.0 to 9.8 % of U atoms; with mean fuel temperatures from 1450 to 1920 K. Temperature gradients in both types of specimens were negligible.

Post-test examination of samples subjected to high irradiation doses at temperatures above 1500 K revealed presence of large (more than 10 nm in size) intragranular bubbles. Unfortunately there is rather scarce information in [13] about the way of loading of the type 2 specimens. It is not clear whether the compression was of hydrostatic or single-axial type, and was there any mechanical interaction of fuel with molybdenum cladding. So it was impossible to determine the fuel internal stress state and, consequently, the corresponding hydrostatic pressure, which is one of the MFPR code input parameters. For this reason calculations have been carried out only for the first type (unrestrained) specimens.

The calculation results for Xe fractional release along with the experimental data are presented in Fig. 2 for temperatures from 1250 to 2000 K, the markers representing the experimental data.

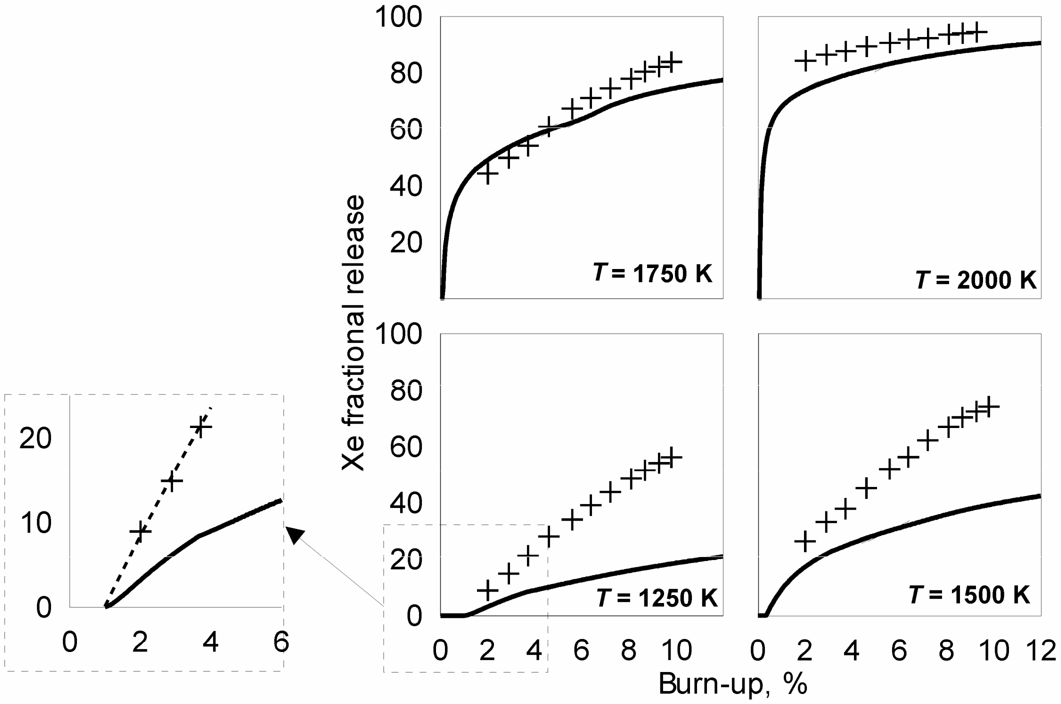

Fig. 2. MFPR simulations (curves) of Xe fractional release in the Zimmermann test, markers representing the experiment. The inset shows the data in the finer scale

As seen, the model predicts the FP release commencement in agreement with the experiment (at least at temperature at which the data can be extracted more or less reliably). Comparing other predictions with experimental data one concludes that the agreement is satisfactory at intermediate and high temperatures whereas the model essentially underestimates the release at low temperatures. Note also that uncertainties due to variation of the fission rate within the experimental errors were found to be inessential at low and high temperatures whereas at intermediate temperatures they attained ~10 %.

However, observations in the Zimmermann tests at low temperature 1250 K are also in qualitative contradiction with other observations, e. g. in the Halden Boiling Water Reactor (HBWR) tests. Indeed, in accordance with the Halden empirical dependence [14] of the critical burn-up B^* (in GWd/t) at which the gas release commences on the temperature T (in K) at the pellet centre:

$$B^*(T) = 5.68 \cdot 10^{-3} e^{\frac{9800}{T-273}}, \qquad (22)$$

the release cannot be observed up to 15 % of burn-up at $T = 1250$ K. Taking into account that the smallest release that can be detected by the in-pile measuring system in those test was 1 % for the pellet stack, considerable local release ~20 % (in the pellet centre) was needed to obtain 1 % integral release [12]. This result well corresponds to the model predictions at 1250 K, see Fig. 2.

Conclusions

The model of intergranular transports described in paper on p. 17 has been further developed. The modifications involved more realistic modelling of the shape, size and concentration of the grain-edge bubbles, critical revision of the applicability of the underlying mean field approach, and improvement of the model for the irradiation induced re-solution of gas atoms from the bubbles. In particular, the concentration of the grain-edge bubbles gas was considered as depending on temperature, whereas unjustified complex shape of the grain edge bubbles has been replaced by spherical one corresponding to the target model accuracy. In the modified model the corner bubbles are not distinguished from edge ones. In addition, the correlation was modified between concentration of the grain-face bubbles and temperature.

Implementation of the advanced model in the MFPR code and numerical treatment of various available data on gas release from irradiated fuel and grain face microstructure shows a satisfactory agreement of the code predictions with experimental results. In particular, the modified code allows description of the Kashibe and Une test in satisfactory agreement with the measurements of the bubbles sizes and grain-face coverage. Also a satisfactory agreement has been demonstrated of the model predictions with the measured bubble concentrations in the Pati test and Xe fractional releases in the Zimmermann test.

References

1. *Une K., Kashibe S.*// J. Nucl. Sci. Technol. 1990. Vol. 27. P. 1002.
2. *Kashibe S., Une K.*// Ibid. 1991. Vol. 28. P. 1090.
3. *White R.J., Tucke M.O.*// J. Nucl. Mater. 1983. Vol. 118. P. 1.
4. *Beere W., Reynolds G.L.*// Ibid. 1973. Vol. 47. P. 51.
5. *Dollins C.C., Nichols F.A.* // Ibid. 1976. Vol. 91. P. 143.
6. *Heames T.J., Williams D.A., Bixler N.E., Grimley A.J., Wheatley C.J., Johns N.A., Domogala P., Dickson L.W., Alexande C.A., Osborn-Lee I., Zawadzki S., Rest J., Mason A., Lee R.Y.* VICTORIA: A Mechanistic Model of Radionuclide Behaviour in the Reactor Coolant System under Severe Accident Conditions. NUREG/CR-5545. 1992.
7. *Veshchunov M.S., Ozrin V.D., Shestak V.E., Tarasov V.I., Dubourg R., Nicaise G.* Development of the mechanistic code MFPR for modelling fission-product release from irradiated UO_2 fuel // Nuclear Engineering and Design. 2006. Vol. 236. P. 179–200.
8. *Berdyshev A.V., Veshchunov M.S.* Modelling of grain face diffusion transport and swelling in UO_2 fuel (Preprint / Nuclear Safety Institute (IBRAE) RAS, no IBRAE-2002-14). Moscow: NSI (IBRAE) RAS, 2002.
9. *Nelson R.S.* // J. Nucl. Mater. 1969. Vol. 31. P. 153.
10. *Rest J., Zawadzki S.A.*. FASTGRASS, A Mechanistic Model for the Prediction of Xe, I, Cs, Te, Ba and Sr release from Nuclear Fuel under Normal and Severe-Accident Conditions. NUREG/CR-5840 TI92 040783. 1994.
11. *Pati S.R., Dapt M.J., O'Boyle D.R.* // J. Nucl. Mater. 1974. Vol. 50. P. 227.
12. *Bagger C., Mogensen M., Walker C.T.* // Ibid. 1994. Vol. 211. P 11.
13. *Zimmermann H.* // Ibid. 1978. Vol. 75. P. 154.
14. *Vitanza C., Kolstad E., Graziani U.* ANS Topical Mtg. on Light Water Reactor Fuel Performance. Portland, Oregon, USA, 1979.

Model for Intragranular Bubble Diffusivity in Irradiated UO_2 Fuel

M.S. Veshchunov, V.E. Shestak

Introduction

The motion of a bubble through a solid essentially requires the transfer of atoms from the leading surface to the trailing surface. Three routes are available to the atoms: they can diffuse around the surface of the bubble (surface mechanism), or through the solid near the bubble (volume mechanism), or via the vapour phase within the bubble (gas phase mechanism). The bubble mobility is described by the bubble diffusion coefficient which depends on the bubble radius R_b. This dependence is different for the various diffusion mechanisms [1, 2]. The bubble mobility in UO_2 is largest for the surface diffusion mechanism (at least for bubbles with $R_b \leq 10\,\mu m$) and is inversely proportional to R_b^{-4}, whereas a slower dependence on the bubble radius ($\propto R_b^{-3}$) is typical for the two other mechanisms.

The effect of the internal gas pressure in restricting bubble movement can be very considerable. In the work on helium-filled cavities in nickel [3] it was shown that the gas pressure in small cavities with radius < 2.5 nm reduced their mobility to such an extent that it was effectively zero.

For the gas bubbles in UO_2 Baker's data [4] show that small intragranular fission gas bubbles (average diameter ~2 nm), formed during the irradiation were virtually immobile on subsequent annealing at temperatures < 1500 °C. With the growth of a bubble radius from 2 to ~10 nm, the bubble diffusivity increases, in contradiction with the standard theoretical predictions.

In order to explain Baker's observations, Mikhlin [5] proposed that a factor which can dramatically affect the surface diffusion mechanism is the presence of a dense gas within the bubble. At the bubble surface a U adatom may not be able to jump into a neighbouring atomic site because such a jump is prevented by adatom interaction with gas atoms [5]. As a result, the net rate of surface diffusion is reduced.

However, in this approach the two other mechanisms (volume and gas phase) of bubble migration become rate controlling steps for small nanometre bubbles and thus do not allow strong reduction of the total diffusivity (in contradiction with Baker's observations). Therefore, additional reasons for reduction of the total bubble diffusivity should be searched.

Such reasons can be apparently associated with faceting of small bubbles observed in the same tests [4]. Indeed, the small intragranular bubbles in uranium dioxide irradiated at $T < 1800\,°C$ were faceted and this was assumed by Baker as a major cause of their immobility. Moreover, noticeable bubble movement has been observed only at annealing temperatures > 1700 °C for bubbles of diameter 5–20 nm. At these temperatures the bubbles were spherical.

Earlier Willertz and Shewmon [6] found that faceted helium bubbles in gold diffuse a factor 10^{-4}–10^{-5} slower than theoretically possible from the unrestrained diffusion of surface atoms. On this base, Willertz and Shewmon [6] and Beere [7] have assumed that for faceted bubbles, bubble migration may be limited by the rate at which new steps are nucleated on the facets. It is also known that relocation of steps rather than their nucleation on a crystallographic surface might be a rate controlling process of the surface migration [8]. In both cases the surface kinetics controlled by the rate at which deposition and solution of atoms occur at the two-phase interface [8] becomes the rate determining step of faceted bubble migration.

In the current paper the influence of the interface kinetics on the bubble diffusivity mechanisms will be further studied. A special attention will be paid to the effect of the gas pressure in restricting small bubbles movement. This will allow explanation of further suppression (in comparison with Mikhlin's mechanism) of the diffusivity of small intragranular bubbles.

In addition, an improved consideration of bubble mobility under irradiation conditions will be presented in the next Section. It is important to note that the formulas for the bubble diffusivities were derived by Shewmon [1] and Nichols [2] for equilibrium conditions. Under irradiation conditions so-called a-thermal effects dependent on fission rate might be important. For instance, the effective uranium self-diffusion coefficient may considerably increase under irradiation in UO_2 crystals [9]. Naturally this can result in the enhancement of the bubble diffusivity. Most pronouncedly this effect can be demonstrated for the bubble volume diffusion mechanism which is directly associated with uranium self-diffusion in the crystal bulk.

1. Bubble diffusivity by volume diffusion mechanism under irradiation conditions

In order to calculate bubble mobility under irradiation conditions, the standard procedure for calculation of bubble mobility in thermally equilibrium crystals (e.g., [10]) should be generalized by additional consideration of non-equilibrium concentration of point defects (vacancies and interstitials).

The stresses induced on the bubble surface by an external force $\vec{F}$ exerted on the bubble in the isotropic crystal take the form in the spherical system of coordinates (r, θ, φ) [10]:

$$\sigma_{rr}(\theta) = -\frac{3F}{4\pi R_b^2}\cos\theta, \qquad \sigma_{r\theta}(\theta) = \sigma_{r\varphi}(\theta) = 0 \qquad (r = R_b), \tag{1}$$

where θ is the angle between the vectors $\vec{n}$ and $\vec{F}$, $\vec{n}$ is the normal to the bubble surface vector, R_b is the bubble radius. These stresses induce a force completely compensating the external force:

$$\vec{F}' = \int \sigma_{rr} \cos\theta \, dS \times \frac{\vec{F}}{F} = -\vec{F}.$$

Under conditions of thermodynamic equilibrium on the bubble surface, the chemical potentials of point defects (vacancies and interstitials) obey the boundary conditions on this surface:

$$\mu_v(R_b, \theta) = \mu_{v0} + \omega\sigma_{nn} = \mu_{v0} + \omega\sigma_{rr}(R_b, \theta), \tag{2}$$

$$\mu_i(R_b, \theta) = \mu_{i0} - \omega\sigma_{rr}(R_b, \theta), \tag{3}$$

where σ_{nn} are the normal stresses at the bubble surface, ω is the atomic volume of uranium atoms (in the approximation $\omega \approx |\omega_v| \approx |\omega_i|$, see Appendix A), μ_{v0} and μ_{i0} are the equilibrium chemical potentials (normally zero) of vacancies and interstitials, respectively, in the absence of stresses.

Far from the bubble the chemical potentials are determined by the irradiation induced values:

$$\mu_{v,i}(\infty) = \bar{\mu}_{v,i}. \tag{4}$$

In the steady-state approximation the chemical potentials obey the Laplace-type equations:

$$\Delta\mu_{v,i}(\vec{r}) = 0. \tag{5}$$

Solution of Eq. (5) with the boundary conditions Eqs. (1)–(4) has the form

$$\mu_v\left(\vec{r}\right)=\bar{\mu}_v-\left(\bar{\mu}_v-\mu_{v0}\right)\frac{R_b}{r}-\frac{3\omega}{4\pi}\frac{\vec{F}\cdot\vec{r}}{r^3}, \tag{6}$$

$$\mu_i\left(\vec{r}\right)=\bar{\mu}_i-\left(\bar{\mu}_i-\mu_{i0}\right)\frac{R_b}{r}+\frac{3\omega}{4\pi}\frac{\vec{F}\cdot\vec{r}}{r^3}. \tag{7}$$

The point defect fluxes are determined by the chemical potential gradients, in accordance with relationships:

$$\vec{I}_v=-M_v\vec{\nabla}\mu_v=-\frac{D_vc_v}{\omega kT}\vec{\nabla}\mu_v, \tag{8}$$

$$\vec{I}_i=-M_i\vec{\nabla}\mu_i=-\frac{D_ic_i}{\omega kT}\vec{\nabla}\mu_i, \tag{9}$$

where $M_{v,i}$ are the kinetic coefficients connected with the diffusivities $D_{v,i}$ of vacancies and interstitials by the relationship $D_{v,i}=M_{v,i}\omega kT/c_{v,i}$.

Substitution of Eqs. (6) and (7) in Eqs. (8) and (9) yields:

$$\vec{I}_v=-\frac{D_vc_v}{\omega kT}\left[\frac{3}{4\pi}\left(-\frac{\vec{F}\omega}{r^3}+\frac{\left(\vec{F}\cdot\vec{r}\right)\vec{r}\omega}{r^5}\right)+\left(\bar{\mu}_v-\mu_{v0}\right)\frac{R_b\vec{r}}{r^3}\right], \tag{10}$$

$$\vec{I}_i=-\frac{D_ic_i}{\omega kT}\left[\frac{3}{4\pi}\left(\frac{\vec{F}\omega}{r^3}-\frac{\left(\vec{F}\cdot\vec{r}\right)\vec{r}\omega}{r^5}\right)+\bar{\mu}_i\frac{R_b\vec{r}}{r^3}\right]. \tag{11}$$

Correspondingly, the induced atomic flux is equal to

$$\vec{I}_a=-\vec{I}_v+\vec{I}_i=\frac{\left(D_vc_v+D_ic_i\right)}{kT}\left[\frac{3}{4\pi}\left(-\frac{\vec{F}}{r^3}+\frac{\left(\vec{F}\cdot\vec{r}\right)\vec{r}}{r^5}\right)\right]-\left[D_v\left(\bar{c}_v-c_v^{(eq)}\right)-D_i\bar{c}_i\right]\frac{R_b\vec{r}}{\omega r^3}. \tag{12}$$

Migration velocity of a segment of the bubble surface $\vec{v}\,'\left(R_b,\theta\right)$ can be represented as the sum of the term $\vec{v}$ corresponding to the bubble relocation velocity (as a whole) and of the term $\dot{R}_b\vec{n}$ corresponding to the variation of the bubble radius [10]:

$$\vec{v}\,'\left(R_b,\theta\right)=\vec{v}+\dot{R}_b\vec{n}. \tag{13}$$

This velocity obeys the geometrical condition

$$\vec{v}\,'\left(R_b,\theta\right)\cdot\vec{n}\left(R_b,\theta\right)=\omega\vec{I}_a\left(R_b,\theta\right)\cdot\vec{n}\left(R_b,\theta\right). \tag{14}$$

Substituting Eq. (12) in (14) and comparing with Eq. (13), one obtains

$$\dot{R}_b=-\left[D_v\left(\bar{c}_v-c_{v0}\right)-D_i\bar{c}_i\right]\frac{1}{R_b}, \tag{15}$$

$$\vec{v}=\frac{3\omega}{2\pi}\frac{\left(D_vc_v+D_ic_i\right)}{kT}\frac{\vec{F}}{R_b^3}=\frac{3\omega}{2\pi}\frac{\tilde{D}_U}{kT}\frac{\vec{F}}{R_b^3}, \tag{16}$$

where $\tilde{D}_U=D_vc_v+D_ic_i$ is the effective self-diffusion coefficient of uranium atoms (see Appendix A).

It is straightforward to show that in the more general approach, $\left|\omega_{v,i}\right| \neq \omega$, with the corrected boundary conditions Eqs. (2) and (3) (as explained in Appendix A), the effective self-diffusion coefficient introduced in Eq. (16) takes the form $\tilde{D}_U = \gamma_v D_v c_v + \gamma_i D_i c_i$, in correspondence with Eq. (A.9).

Therefore, for the bubble mobility that obeys the relationship $\vec{v} = u_b \vec{F}$, one obtains

$$u_b = \frac{3\omega}{2\pi kT} \frac{\tilde{D}_U}{R_b^3}. \qquad (17)$$

In accordance with the Einstein equation $D_b = kTu_b$, the bubble diffusivity is proportional to its mobility and thus can be deduced from Eq. (17) as

$$D_b^{(vol)} = \frac{3\omega}{2\pi} \frac{\tilde{D}_U}{R_b^3}. \qquad (18)$$

Under irradiation conditions the effective self-diffusion coefficient consists of thermal (Arrhenius type) and a-thermal (fission rate dependent) parts [9]:

$$\tilde{D}_U = D_U^{(0)} \exp\left(-E_U / T\right) + AF, \qquad (19)$$

where $D_U^{(0)} = 2 \cdot 10^{-4}$ m^2/s, $E_U = 64200$ K, $A \approx 1.2 \cdot 10^{-39}$ m^5 and F is the fission rate.

Correspondingly, for irradiated crystal Eq. (19) should be substituted in Eq. (18). This determines the enhanced bubble diffusivity by volume diffusion mechanism under irradiation conditions.

2. Influence of the interface kinetics on bubble diffusivity

As explained in Introduction, faceting had pronounced effect in restricting bubble motion in UO_2 crystals.

Qualitatively the observations of faceted bubbles can be explained as suppression by adsorbed gas atoms of so-called «roughening» transition (from smooth (faceted) to rough surface) on UO_2 crystal faces, when gas adsorption coverage is close to 1. The smaller is the bubble, the higher is the gas pressure in the bubble and the closer is gas adsorption to complete coverage; therefore, the transition for small bubbles might be strongly suppressed (i.e., shifted to higher temperatures), in agreement with the above presented Baker's observations [4] that only small bubbles (~2 nm) had faceted surface (and probably for this reason were immobile, as explained below).

As explained in Introduction, the rate of movement of a bubble with a smooth (faceted) surface may be determined by the rate at which solution and deposition of uranium atoms occur at the two-phase interface. This rate of solution/deposition per unit area can be presented in the general form:

$$W = K_n \left(\mu_s - \mu_{eq}\right)^n, \qquad (20)$$

where K_n is the kinetic («reaction») constant, μ_s and μ_{eq} are the interface and equilibrium chemical potentials of uranium atoms, respectively. It is customary to take n equal to 1 or 2 [8], however, as proposed in [1], also a larger positive number n can be used to approximate the case in which the cavity are crystallographic and the rate of solution/ deposition is determined by the rate of nucleation or growth of atomic steps in the cavity surface.

Under such conditions the bubble diffusivity becomes proportional to the reaction constant K_n and obeys a more slow dependence from bubble radius R_b, as shown in [1]:

$$D_b \propto K_n R_b^{n-3}. \qquad (21)$$

This slow dependence from R_b results in a noticeable suppression of the mobility for small bubbles (in comparison with the bulk diffusion mechanism which provides $D_b \propto R_b^{-3}$). However, an additional effect can be apparently connected with suppression of K_n for small bubbles with R_b ~1 nm.

Indeed, in such small bubbles the gas pressure is extremely high, $p = 2\gamma/R_b \sim 1$ GPa, and for this reason, the surface coverage θ of gas atoms adsorbed on the internal bubble surface should be very high, e. g., following the Langmuire adsorption law, $\theta = \dfrac{k_{ad}p}{1+k_{ad}p} \to 1$.

However, this simplest formulation of the adsorption law is valid only for the ideal gas (and at low coverage). For small bubbles with high pressure a new expression for the adsorption isotherm should be derived.

2.1. Non-linear Langmuire adsorption law

In small bubbles with $R_b \le 5$ nm the gas state obeys the van der Waals law, $p\left(V_b - N_b B\right) = N_b kT$, where N_b is the number of gas atoms, V_b is the bubble volume and $B \approx 8.5 \cdot 10^{-29}$ m^3/atom is the van-der-Waals constant for Xe gas.

In this case the chemical potential of gas atoms takes the form: $\mu_g = \mu_g^{(0)} + kT\ln p + Bp$, whereas the chemical potential of adsorbed gas atoms is $\mu_{ad} = \mu_{ad}^{(0)} + kT\ln\left(\theta/(1-\theta)\right)$, where $0 \le \theta \le 1$ is the surface coverage of adsorbed monolayer. This simple expression for μ_{ad} is valid in both limits of $\theta \to 0$ and $\theta \to 1$ (possibly with different values of $\mu_{ad}^{(0)}(T)$), when the two-dimensional lattice gas of adatoms (in the case $\theta \to 0$) or of their vacancies (in the case $\theta \to 1$) can be considered as ideal. In the current consideration the second case, $\theta \to 1$, is of interest.

In the thermodynamic equilibrium between gas and adsorbed atoms $\mu_{ad} = \mu_g$, therefore, in this case the dependence of the surface coverage on pressure becomes steep and non-linear:

$$\theta = \frac{k_{ad}p\exp\left(Bp/kT\right)}{1+k_{ad}p\exp\left(Bp/kT\right)}, \qquad (22)$$

where $k_{ad} = \exp\left[\left(\mu_g^{(0)} - \tilde{\mu}_{ad}^{(0)}\right)/kT\right]$ is the unknown adsorption constant.

It is clear that under high-coverage condition, $\theta \to 1$, solution/deposition of uranium atoms on the surface will be blocked by adsorbed gas atoms, resulting in a strong suppression of the kinetic constant K_n. In the microscopic consideration of adsorption/desorption processes it is conventionally assumed that K_n is proportional to the surface area unoccupied with gas atoms, $K_n = k_\theta^{(n)}\left(1-\theta\right)$, where $k_\theta^{(n)}$ is the second unknown constant of the model, therefore, in the case of the above-derived non-linear Langmuire adsorption law for small bubbles (with high gas pressure $p = 2\gamma/R_b$), Eq. (22), one obtains

$$K_n \approx \frac{k_\theta^{(n)}}{1+k_{ad}\left(2\gamma/R_b\right)\exp\left(2\gamma B/R_b kT\right)} \approx \left(k_\theta^{(n)}/2\gamma k_{ad}\right)R_b\exp\left(-2\gamma B/R_b kT\right), \qquad (23)$$

where γ is the surface tension. Therefore, the bubble diffusivity, Eq. (21), can be strongly suppressed for small intragranular bubbles with $R_b \approx 1$ nm owing to extremely small value of the exponent, $\exp\left(-2\gamma B/R_b kT\right)$, which attains $\approx 10^{-4}$ at $T \approx 1273$ K.

2.2. Bubble diffusivity by volume diffusion mechanism

In order to adequately implement this effect of the bubble mobility suppression, one should self-consistently consider the problem of the bulk self-diffusion in the matrix along with the two-phase interface kinetics at the bubble surface. For the first order kinetics ($n = 1$ in Eq. (20)), the calculations presented in the Appendix B yield for the bubble diffusivity:

$$D_b^{(\mathrm{vol})} = \frac{3\omega}{4\pi R_b^3} \frac{K_1 \omega R_b \cdot 2\tilde{D}_U}{K_1 \omega R_b + \left(2\tilde{D}_U / kT\right)}. \qquad (24)$$

Generalization to the higher order kinetics, $n > 1$, results in

$$D_b^{(\mathrm{vol})} = \frac{3\omega}{4\pi R_b^3} \frac{K_n \omega R_b^n \cdot 2\tilde{D}_U}{K_n \omega R_b^n + \left(2\tilde{D}_U / kT\right)}, \qquad (25)$$

which is correctly reduced to the known relationships in the two limiting cases:

$$D_b^{(\mathrm{vol})} \to \frac{3\tilde{D}_U \omega}{2\pi R_b^3},$$

when $K_n \omega R_b^n >> \tilde{D}_U / 2kT$ (the volume diffusion mechanism), and

$$D_b^{(\mathrm{vol})} \to \frac{3K_n \omega^2}{4\pi R_b^{3-n}} kT,$$

when $K_n \omega R_b^n << \tilde{D}_U / 2kT$ (the interface kinetics mechanism).

Substituting Eq. (23) in Eq. (25), one finally obtains:

$$D_b^{(\mathrm{vol})} = \frac{3\omega}{4\pi R_b^3} \frac{\left(\omega k_\theta^{(n)} / 2\gamma k_{\mathrm{ad}}\right) \exp\left(-2\gamma B / R_b kT\right) R_b^{n+1} \cdot 2\tilde{D}_U}{\left(\omega k_\theta^{(n)} / 2\gamma k_{\mathrm{ad}}\right) \exp\left(-2\gamma B / R_b kT\right) R_b^{n+1} + \left(2\tilde{D}_U / kT\right)}. \qquad (26)$$

Therefore, for small bubbles the two-phase interface kinetics becomes the rate limiting step in the bubble diffusivity:

$$D_b^{(\mathrm{vol})} \to \frac{3\omega^2 kT}{4\pi R_b^{2-n}} \left(k_\theta^{(n)} / 2\gamma k_{\mathrm{ad}}\right) \exp\left(-2\gamma B / R_b kT\right), \qquad (27)$$

which tends to 0 when $R_b \to 0$.

2.3. Bubble diffusivity by vaporization/condensation mechanism

Vaporization/condensation of UO$_2$ in the gas phase provides the interface kinetic limitation to the gas-phase mechanism of bubble diffusivity. This contribution can be represented in the form [11]

$$D_b^{(\mathrm{vap})} = \frac{3\Omega^2}{4\pi s^2 k N_b} P_{\mathrm{UO}_2(g)} \sqrt{\frac{\pi R}{8mT}}, \qquad (28)$$

where N_b is the number of gas atoms in a bubble, k is the Boltzmann constant, R is the universal gas constant, $s = 3.0 \cdot 10^{-10}$ m and πs^2 is the effective cross-section for elastic collisions between Xe atoms and UO$_2$ molecules, the mass m is defined by $m = m_1 m_2 / \left(m_1 + m_2\right)$, where m_1 and m_2 are the molar masses of Xe and UO$_2$ $P_{\mathrm{UO}_2(g)}$ is the equilibrium partial pressure of UO$_2$ gas given by

$$P_{\mathrm{UO}_2(g)} = P_0 \exp(-\Delta H_{\mathrm{vap}} / T), \qquad (29)$$

where $\Delta H_{\mathrm{vap}} \approx 71.682 \cdot 10^3$ K is the heat of vaporization. For small nanometre bubbles N_b is proportional to the bubble volume, therefore, $D_b^{(\mathrm{vap})} \propto R_b^{-3}$.

In a small bubble with high pressure the evaporation/condensation of U atoms will take place from the surface areas unoccupied with gaseous adatoms, therefore, Eq. (28) should be multiplied by the factor $\left(1 - \theta\right)$. In the case of the non-linear Langmuire adsorption law, Eq. (22), for small bubbles (with high gas pressure $p = 2\gamma / R_b$) one obtains

$$D_b^{(\mathrm{vap})} \approx \frac{3\Omega^2}{4\pi s^2 k N_b} P_{\mathrm{UO}_2(g)} \sqrt{\frac{\pi R}{8mT}} \frac{1}{1 + \left(2\gamma k_{\mathrm{ad}} / R_b\right) \exp\left(2\gamma B / R_b kT\right)}, \qquad (30)$$

which tends to 0 when $R_b \to 0$ as:

$$D_b^{(\mathrm{vap})} \approx \frac{3\Omega^2}{4\pi s^2 k N_b}\sqrt{\frac{\pi R}{8mT}}P_{\mathrm{UO}_2(g)}\frac{R_b}{2\gamma k_{\mathrm{ad}}}\exp\left(-2\gamma B/R_b kT\right). \tag{30a}$$

2.4. Bubble diffusivity by surface diffusion mechanism

As mentioned in Introduction, in accordance with Mikhlin's model [5] a U adatom may not be able to jump into a neighbouring atomic site at the bubble surface because such a jump is prevented by adatom interaction with gas atoms. Under assumption that a U adatom would not diffuse unless a certain volume $V_0 \approx 1.5 \cdot 10^{-27}\,\mathrm{m}^3$ surrounding the adatom (so called adatom interaction zone) was free of gas atoms, the net rate of surface diffusion is reduced by a factor $\left(1 - V_0/V_b\right)^{N_b}$:

$$D_b^{(surf)} = D_s\frac{3\omega^{4/3}}{4\pi R_b^4}\left(1-\frac{V_0}{V_b}\right)^{N_b} \approx D_s\frac{3\omega^{4/3}}{4\pi R_b^4}\exp\left(-\frac{V_0 P_b}{kT + BP_b}\right), \tag{31}$$

where $P_b = 2\gamma/R_b$ is the bubble pressure, $V_b = 4\pi R_b^3/3$ is the bubble volume, B is van-der-Waals constant, D_s is the surface self-diffusion coefficient, evaluated in [12] as $D_s = 50 \cdot \exp\left(-450000/RT\right)$ m^2/s, with 1200 °C < T < 1800 °C and R in J mol^{-1}·K^{-1}.

This approach was criticised in [13], since there is no intrinsic reason why a gas atom in an adatom interaction zone should prevent the adatom from moving, but it has been shown to give results which compare quite favourably with experiments.

An alternative justification for the surface diffusion reduction can be found taking into consideration that atomic jumps into a neighbouring atomic site at the bubble surface can be prevented by occupation of this site by an adsorbed gas atom. Consideration of this mechanism can be carried out by application of the Langmuire adsorption law to gas atoms on the bubble surface, similarly to consideration in the previous sections.

Indeed, in this case the U adatom jump frequency $\gamma_g(r)$ on the equilibrium gas bubble surface is less than its jump frequency γ_0 on the free surface, $\gamma_g(r) = \gamma_0 w(r)$, where $w(r)$ is the probability that there is a free surface site in the neighbourhood non-occupied with gas atoms, i. e., $w(r) = (1-\theta)$. Eventually this results in renormalization of the bubble diffusivity by the same factor $(1-\theta)$, which can be calculated using the non-linear Langmuire adsorption law for non-ideal gases, Eq. (22):

$$D_b^{(\mathrm{surf})} = D_s\frac{3\omega^{4/3}}{4\pi R_b^4}\frac{1}{1+\left(2\gamma k_{ad}/R_b\right)\exp\left(2\gamma B/R_b kT\right)}, \tag{32}$$

which tends to 0 when $R_b \to 0$ as:

$$D_b^{(\mathrm{surf})} \approx D_s\frac{3\omega^{4/3}}{8\pi\gamma k_{\mathrm{ad}} R_b^3}\exp\left(-2\gamma B/R_b kT\right). \tag{32a}$$

3. Model implementation in the MFPR code and validation

New formulations for the bubble volume diffusivity, Eq. (26), and for the vaporization/condensation mechanism, Eq. (30), have been implemented in the MFPR code [14] in the form

$$D_b^{(\mathrm{vol})} = \frac{2\tilde{D}_U \omega}{V_b}\left(1 + \frac{2\tilde{D}_U}{kT\omega}\frac{1}{k_\theta^{(n)} R_b^n}\frac{2\gamma k_{\mathrm{ad}}}{R_b}\exp\left(2\gamma B / R_b kT\right)\right)^{-1}, \tag{33}$$

$$D_b^{(\mathrm{vap})} \approx \frac{3\Omega^2}{4\pi s^2 k N_b} P_{\mathrm{UO}_2(g)} \sqrt{\frac{\pi R}{8mT}} \frac{1}{1 + \left(2\gamma k_{\mathrm{ad}} / R_b\right)\exp\left(2\gamma B / R_b kT\right)}, \tag{34}$$

where V_b is the bubble volume, N_b is the number of gas atoms in the bubble, $\tilde{D}_U$ is the effective self-diffusion coefficient of uranium atoms, Eq. (19); constants $k_\theta^{(n)}$ and k_{ad} are the model parameters, determined in calculations presented below as $10^{45}\,(\mathrm{N{\cdot}m^3{\cdot}s})^{-1}$ and $10^{-4}\,\mathrm{m^2/N}$, respectively, by fitting calculations to the available data on small bubbles diffusivity.

Comparison of the standard volume diffusivity of bubbles $D_b^{(\mathrm{vol})} = 2D_U\omega/V_b$, which includes only the thermal part of the uranium self-diffusion coefficient $D_U = D_U^{(0)}\exp\left(-E_U / T\right)$ and thus is valid only for non-irradiation conditions, with the modified one expressed by Eqs. (33) and (19), is presented in Fig. 1. One can see that for bubbles with $R_b > 2$ nm the modified value of the bubble volume diffusivity calculated under irradiation conditions (with the typical fission rate ~ $10^{19}\,\mathrm{m^{-3}s^{-1}}$) practically does not depend on temperature at $T \leq 1400$ K and noticeably exceeds the standard value (especially at low temperatures). At higher temperatures $T \geq 1600$ K the thermal part of the uranium self-diffusion coefficient exceeds the a-thermal part and the modified volume diffusivity practically coincides with the standard one. Consideration of the interface kinetic limitation in the new model provides considerable suppression of the volume diffusivity for small bubbles with $R_b \leq 2$ nm.

Similarly, modification of the vaporization/condensation model taking into account suppression by gas atoms adsorbed on the bubble surface, Eq. (34), diminishes the bubble diffusivity by this mechanism for small bubbles, Fig. 2.

The surface diffusion mechanism was considered in two formulations: the standard Mikhlin's model, Eq. (31) and the modified model, Eq. (32), as presented in Fig. 3.

Superposition of the diffusion mechanisms allows calculation of the total bubble diffusivity, Fig. 4. In the case of the standard Mikhlin's formulation for the surface diffusion mechanism, Fig. 4a, results are in a reasonable agreement with Baker's [4] and Cornell's [15] data, however, are inconsistent with Gulden's data [16], as shown in Fig. 5. In the case of the modified formulation Eq. (32), Fig. 4b, coincidence is not so good with Baker's and Cornell's data, however, the calculation results are in much better qualitative and quantitative agreement with Gulden's measurements (and are still in the range of discrepancy between the three data sets), Fig. 5.

It is important to note from Figs. 1–3 that at temperatures below 1200 K under irradiation conditions with typical fission rates (~$10^{19}\,\mathrm{m^{-3}s^{-1}}$) the irradiation-enhanced volume diffusivity becomes higher than the bubble diffusivity by the surface mechanism and thus determines the diffusivity of intragranular bubbles. This is important conclusion for analysis of bubbles coalescence and $\mathrm{UO_2}$ fuel swelling under normal operation conditions, especially at the fuel pellets periphery where low temperature conditions are sustained.

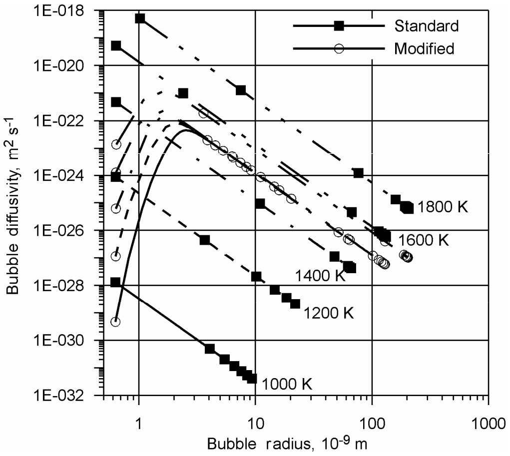

Fig. 1. Volume bubble diffusivity under irradiation conditions as a function of bubble radius at different temperatures calculated by different models: the standard formulation and the modified model for the irradiation-enhanced bubble diffusivity with consideration of the interface kinetic limitation

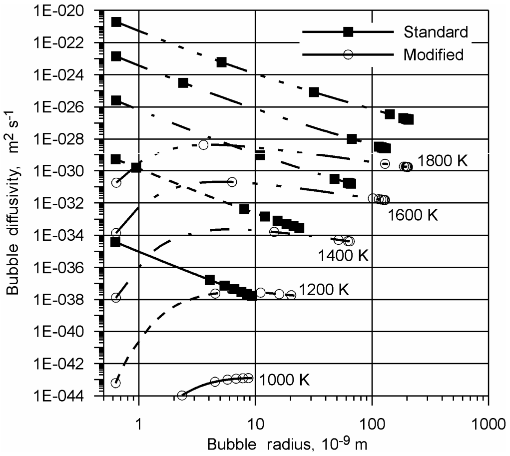

Fig. 2. Vaporization/condensation bubble diffusivity as a function of bubble radius at different temperatures calculated with and without consideration of gas adsorption

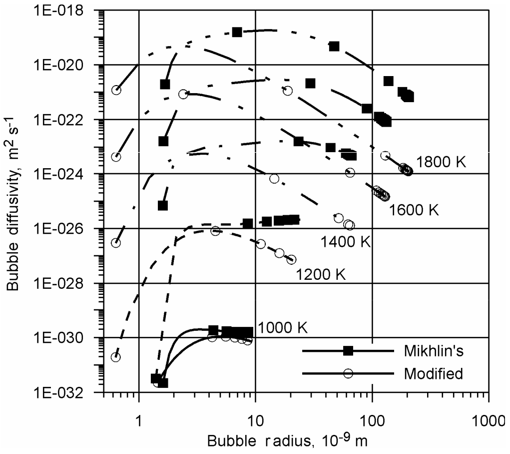

Fig. 3. Surface bubble diffusivity under irradiation conditions as a function of bubble radius at different temperatures calculated by different models: the standard Mikhlin's formulation, Eq. (31), and the modified model, Eq. (32)

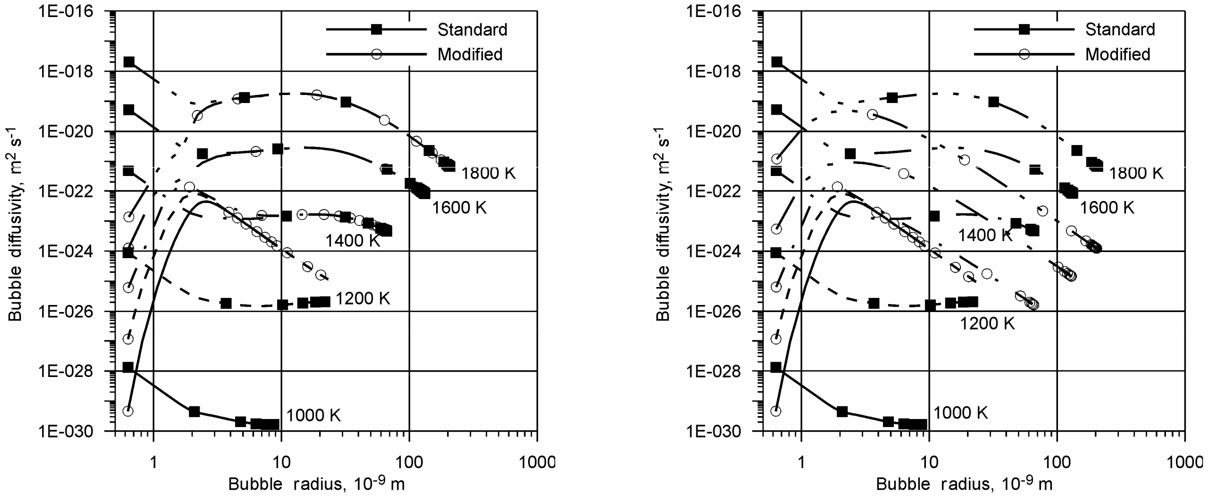

a)

b)

Fig. 4. Total bubble diffusivity as a function of bubble radius at different temperatures calculated with and without consideration of the interface kinetics: a) — using Mikhlin's formulation for the surface diffusion mechanism; b) — using modified formulation, Eq. (32).

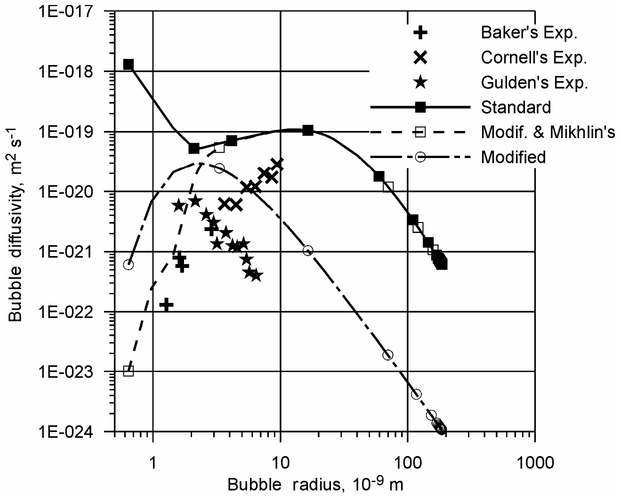

Fig. 5. Total bubble diffusivity as a function of bubble radius at 1773 K experimentally measured and calculated without (solid line) and with consideration of the interface kinetics; for the latter case two options for the surface diffusion mechanism are presented: Mikhlin's formulation, Eq. (31) (dashed line) and modified formulation, Eq. (32) (dashed-dotted line).

Conclusions

The advanced model for intragranular bubble diffusivity in irradiated UO_2 fuel was developed. Three various mechanisms (surface, volume and gas-phase) for the gas-filled bubble diffusivity were considered.

It was shown that the bubble mobility by the volume diffusion mechanism can be strongly enhanced under irradiation conditions, in comparison with the standard consideration valid for equilibrium conditions. For instance, at relatively low temperatures ≤ 1200 K and typical fission rates ($\sim 10^{19}\,m^{-3}s^{-1}$) the volume diffusion mechanism becomes the largest one and thus determines mobility of intragranular bubbles.

The influence of the interface kinetics on bubble diffusivity by volume diffusion, evaporation/condensation and surface diffusion mechanisms was additionally studied. A special attention was paid to the effect of the internal gas pressure in restricting small bubbles movement. For this case a new expression for the non-linear Langmuire adsorption law for gas atoms was derived. This allowed explanation of further suppression (in comparison with Mikhlin's model for the bubble migration mechanism by surface diffusion) of the diffusivity of small intragranular bubbles.

The standard Mikhlin's model was critically analysed and modified, using the non-linear Langmuire adsorption law.

The improved models for various mechanisms of the bubble diffusivity were implemented in the MFPR code and validated against Baker's, Cornell's and Gulden's measurements of small nanometre bubbles mobility. New unknown model parameters characterising the interface kinetic processes were determined by fitting the MFPR calculations to the experimental data.

Acknowledgments

The original publication of this article in the Journal of Nuclear Materials [17] is greatly acknowledged.

Appendix A

Let us consider behaviour of atoms and point defects in crystal under hydrostatic stress field $\sigma_{ii}(\vec{r}) = -P(\vec{r})$. In the case of constant field, $P = P_0 = \text{const}$, the equilibrium chemical potentials of point defects can be calculated as

$$\mu_{v,i} = \mu_{v,i0} - \omega_{v,i}P_0, \qquad (A.1)$$

where $\omega_{v,i} = \pm\gamma_{v,i}\omega$ is the increase of the crystal volume when one defect is introduced in the crystal bulk by relocation of an atom to (from) the crystal surface; $\gamma_{v,i} = |\omega_{v,i}|/\omega$ normally ≤ 1. Indeed, in this case to attain the equilibrium state the reversible work connected with the crystal volume increase under the external stress, $-\omega_{v,i}P_0$, has to be compensated by the chemical potential of the newly created point defect, $\mu_{v,i}$.

It is worthwhile to note that a similar consideration of the equilibrium boundary conditions on the bubble surface will modify the usual Eqs. (2) and (3) (obtained under simplified assumption $\gamma_v \approx \gamma_i \approx 1$) by substitution of $|\omega_{v,i}|$ instead of ω in the r.h.s. of Eqs. (2) and (3), respectively (or, equivalently, by multiplication of ω by $\gamma_{v,i}$).

In the case of spatially non-homogeneous field with a constant gradient $\vec{\nabla}P = \text{const}$, $\sigma_{ii}(\vec{r}) = -P(\vec{r}) = -P_0 + \vec{r}\cdot\vec{\nabla}P$, under steady state conditions the chemical potentials of point defects obey the Laplace-type equation:

$$\Delta\mu_{v,i} = 0, \qquad (A.2)$$

which has the solution, generalizing Eq. (A.1):

$$\mu_{v,i} = \mu_{v,i0} - \omega_{v,i}P(r). \qquad (A.3)$$

Therefore, the point defects diffusion fluxes are calculated as

$$\vec{I}_{v,i} = -M_{v,i}\vec{\nabla}\mu_{v,i} = M_{v,i}\omega_{v,i}\vec{\nabla}P =$$
$$= \pm M_{v,i}|\omega_{v,i}|\vec{\nabla}P = \pm\frac{D_{v,i}c_{v,i}\gamma_{v,i}}{kT}\vec{\nabla}P, \qquad (A.4)$$

where $D_{v,i} = M_{v,i}\omega_a kT/c_{v,i}$ is the diffusivity of vacancies (interstitials).

Assuming that the pressure gradient is small, the Gibbs potential of the crystal $\Phi(P,T) = F(P,T) + PV$ can be decomposed:

$$\Phi(P,T) \approx \Phi(P_0,T) + (P - P_0)V,$$

taking into consideration that

$$d\Phi = -SdT + VdP.$$

In this case for the atomic chemical potential one obtains:

$$\mu_a = \frac{\partial\Phi(P,T)}{\partial N} \approx \frac{\partial\Phi(P_0,T)}{\partial N} + (P-P_0)\frac{\partial V}{\partial N} = \mu_{a0} + (P-P_0)\omega, \quad (A.5)$$

thus the atomic flux is calculated as:

$$\vec{I}_a = -M_a\vec{\nabla}\mu_a = -M_a\omega\vec{\nabla}P, \quad (A.6)$$

or, in accordance with the Einstein equation for the self-diffusion, $M_a = D_a/\omega kT$:

$$\vec{I}_a = -\frac{D_a}{kT}\vec{\nabla}P. \quad (A.7)$$

On the other hand,

$$\vec{I}_a = -\vec{I}_v + \vec{I}_i, \quad (A.8)$$

therefore, substituting Eqs. (A.4) and (A.7) in (A.8), one obtains:

$$D_a = \gamma_v D_v c_v + \gamma_i D_i c_i. \quad (A.9)$$

In the approximation $\gamma_v \approx \gamma_i \approx 1$ one obtains:

$$D_a \approx D_v c_v + D_i c_i. \quad (A.10)$$

Appendix B

In this Appendix self-consistent consideration of the bulk self-diffusion in the crystal matrix and the two-phase interface kinetics at the bubble surface is presented. For simplicity, only one type of defects is considered (generalization to two types is straightforward following consideration in Section 1).

The vacancy chemical potential $\mu_v(\vec{r})$ in the matrix obeys the Laplace-type equation:

$$\Delta\mu_v = 0. \quad (B.1)$$

Under conditions of thermodynamic equilibrium on the bubble surface, the chemical potential obeys the boundary conditions on this surface:

$$\mu_v^{(eq)} = \mu_{v0} + \gamma_v\omega\sigma_{nn}, \quad (B.2)$$

where σ_{nn} are the normal stresses at the bubble surface ($\vec{n} = \vec{R}_b/R_b$ is the normal vector), ω is the atomic volume of uranium atoms, μ_{v0} is the equilibrium vacancy concentration in the absence of stresses, γ_v is the vacancy dilation factor (see Appendix A).

The stresses induced on the bubble surface by an external force $\vec{F}$ exerted on the bubble in the isotropic crystal take the form [10]

$$\sigma_{rr} = -\frac{3F}{4\pi R_b^2}\cos\theta, \quad \sigma_{r\theta} = 0,$$

$$\sigma_{r\varphi} = 0, \quad (r = R_b), \quad (B.3)$$

where θ is the angle between the vectors $\vec{n} = \vec{R}_b/R_b$ and $\vec{F}$.

Solution of Eq. (B.1) with the equilibrium boundary conditions Eq. (B.2) and Eq. (B.3) has the form

$$\mu_v^{(eq)}(\vec{r}) = \mu_{v0} - \frac{3\gamma_v\omega}{4\pi}\frac{\vec{F}\cdot\vec{r}}{r^3}, \quad (r = R_b). \quad (B.4)$$

In the absence of the thermodynamic equilibrium at the bubble surface when the interface kinetics becomes essential, the boundary conditions on the bubble surface can be searched in the form

$$\mu_v^{(s)}(\vec{r}) = \mu_{v0} - \alpha\frac{3\gamma_v\omega}{4\pi}\frac{\vec{F}\cdot\vec{r}}{r^3}, \quad (r = R_b), \quad (B.5)$$

where α is an unknown parameter.

In this (non-equilibrium) case the diffusion flux of uranium atoms to the bubble surface is

$$\vec{I}_{dif} = \frac{\gamma_v D_v c_v}{\omega kT}\vec{\nabla}\mu_v = -\alpha\frac{3D_u}{4\pi kT}\left(\frac{\vec{F}}{R_b^3} - \frac{3(\vec{F}\cdot\vec{R}_b)\vec{R}_b}{R_b^5}\right), \quad (B.6)$$

whereas the interface kinetic flux is

$$\vec{I}_{\mathrm{int}} = K_1\left(\mu_v^{(s)} - \mu_v^{(eq)}\right) = \\ = K_1\left(1-\alpha\right)\frac{3\omega}{4\pi}\frac{\left(\vec{F}\cdot\vec{R}_b\right)}{R_b^3}. \qquad \text{(B.7)}$$

Equating the normal components of the two fluxes $\vec{I}_{\mathrm{dif}}\cdot\vec{n} = \vec{I}_{\mathrm{int}}\cdot\vec{n}$, one obtains

$$\alpha = \frac{K_1\omega R_b}{K_1\omega R_b + 2\left(D_u/kT\right)}. \qquad \text{(B.8)}$$

The bubble velocity, which obeys the relationship

$$\vec{v}\cdot\vec{n} = \omega\vec{I}\cdot\vec{n}, \qquad \text{(B.9)}$$

can be calculated from Eq. (B.9) after substitution of Eq. (B.8) in Eq. (B.6):

$$\vec{v} = \frac{3\vec{F}\omega}{4\pi R_b^3}\frac{K_1\omega R_b\cdot\left(2D_u/kT\right)}{K_1\omega R_b + \left(2D_u/kT\right)}. \qquad \text{(B.10)}$$

Therefore, for the bubble mobility that obeys the relationship $\vec{v} = u_b\vec{F}$, one obtains

$$u_b = \frac{3\omega}{4\pi R_b^3}\frac{K_1\omega R_b\cdot\left(2D_u/kT\right)}{K_1\omega R_b + \left(2D_u/kT\right)}. \qquad \text{(B.11)}$$

Finally, for the bubble diffusivity which obeys the Einstein's relationship $D_b = kTu_b$, one obtains

$$D_b^{(\mathrm{vol})} = \frac{3\omega}{4\pi R_b^3}\frac{K_1\omega R_b\cdot 2D_u}{K_1\omega R_b + \left(2D_u/kT\right)}. \qquad \text{(B.12)}$$

References

1. *Shewmon P.G.* // Trans. AIME. 1964. Vol. 230. P. 1134.
2. *Nichols F.A.* // J. Am. Ceram. Soc. 1968. Vol. 51. P. 468.
3. *Marochov N., Perryman L.J. , Goodhew P.J.*// J. Nucl. Mater. 1987. Vol. 149. P. 296.
4. *Baker C.* // Ibid. 1977. Vol. 71. P. 117.
5. *Mikhlin E.Ya.* // Ibid. 1979. Vol. 87. P. 405.
6. *Willertz L.E., Shewmon P.G.* // Metall. Trans. 1970. Vol. 1A. P. 2217.
7. *Beere W.* // J. Nucl. Mater. 1972. Vol. 45. P. 91.
8. *Burton W., Cabrera N., Frank F.*// Phil. Trans. 1951. Vol. A243. P. 299–358.
9. *Matzke Hj.* // Adv. Ceram. 1986. Vol. 17. P. 1.
10. *Geguzin Ya.E., Krivoglaz M.A.* The Movement of Microscopic Inclusions in Solid State. Moscow: Metallurgiya, 1971 (in Russian).
11. *Heames T.J., Williams D.A., Bixler N.E., Grimley A.J., Wheatley C.J., Johns N.A., Domogala P., Dickson L.W., Alexande C.A., Osborn-Lee I., Zawadzki S., Rest J., Mason A., Lee R.Y.* VICTORIA: A Mechanistic Model of Radionuclide Behaviour in the Reactor Coolant System under Severe Accident Conditions. NUREG/CR-5545. 1992.
12. *Maiya P.S.* // J. Nucl. Mater. 1971. Vol. 40. P. 57.
13. *Perryman L.J., Goodhew P.J.* // Acta Metall. 1988. Vol. 36. P. 685–2692.
14. *Veshchunov M.S., Ozrin V.D., Shestak V.E., Tarasov V.I., Dubourg R., Nicaise G.* // Nucl. Eng. Des. 2006. Vol. 236. P. 179.
15. *Cornell R.M., Bannister G.H.* // Proc. Brit. Ceram. Soc. 1967. Vol. 7. P. 855.
16. *Gulden M.E.* // J. Nucl. Mater. 1967. Vol. 23. P. 30.
17. *Veshchunov M.S., Shestak V.E.* Advanced Model for Grain Bubble Diffusivity in Irradiated UO_2 Fuel // J. Nucl. Mater. (*Accepted for publication*).

Model for Evolution of Intragranular Bubbles and Crystal Defects in UO_2 under Irradiation Condition

M.S. Veshchunov, V.E. Shestak

Introduction

One of the main deficiencies of the existing codes is connected with oversimplified consideration of microscopic defects in the UO_2 crystal structure, which can strongly influence fission products transport out of grains and release from fuel pellets. Hence, the basic postulation of these codes is based on consideration of equilibrium state of intragranular gas bubbles formed from the solid solution of gas atoms in UO_2 matrix under irradiation conditions. Such an approach radically simplifies the theory, since in this case the defect structure of the crystal (including point defects, such as vacancies and interstitials, and extended defects, such as dislocations) is practically excluded from consideration. However, this consideration is well grounded only in the initial stage of steady-state irradiation, when density of generated dislocations is relatively low. At high burn-ups the dislocation density significantly increases [1] and influences the intragranular bubbles evolution. Namely, considerable suppression of the intragranular bubbles generation leading to stabilization of their concentration in the late stage of irradiation accompanied with a noticeable increase of the mean bubble size, was observed in the high burn-up UO_2 fuel [2], in remarkable contradiction with the standard codes predictions.

Furthermore, under transient and/or annealing conditions the approximation of equilibrium bubbles is not anymore valid, and interactions of bubbles with point defects and dislocations become essential. Indeed, during bubbles growth and coalescence extended defects such as dislocation loops uniformly distributed in the grain bulk, may act as the main sources of vacancies (necessary for the bubble equilibration) and afford the equilibrium concentration of the point defects in the crystal bulk. This explains dislocation creep and enhanced bubble growth by dislocation sweeping observed under annealing conditions.

In this situation a new mechanism for gas release due to dislocation creep emerges (paper on p. 87). This mechanism considers sweeping of bubbles and delivery them to the grain boundaries by climbing dislocation segments in the course of vacancy generation (necessary for equilibration of growing bubbles) under annealing conditions. Extensive validation of the MFPR dislocation creep model showed that experimental results on gas release during post-irradiation annealing [3, 4] could be adequately simulated in the whole temperature range of the tests with an appropriate choice of the initial dislocation density. Therefore, the new model for the dislocation evolution under steady irradiation conditions should provide appropriate initial conditions for the post-irradiation annealing and transient regimes.

According to the present model prediction, generation of dislocation loops occurs mainly during the initial period of irradiation, concurrently with the fuel densification process, and therefore, may be significantly influenced by the kinetics of pore sintering. For this reason, comparative analysis of existing models for pore evolution under irradiation conditions, the most adequate model and its further development will be presented (paper on p. 58). Consequently, in the MFPR code both processes of dislocation loops generation and pore shrinkage are considered simultaneously and self-consistently with the point defects and gas bubbles evolution.

According to the present model, dislocations are generated under irradiation in the form of di-interstitials and continuously grow up by absorption/evaporation of point defect in two types, dislocation loops and dislocation network. Taking into account that the introduction of this type of extended defects will complicate the system of equations in MFPR, a simple approach is developed by considering bi-modal distribution of loops, their evolution and transformation into dislocation network.

After implementation of the new model in the MFPR code, additional parameters characterising the crystal defect structure naturally arise. However, being physically grounded, these new microscopic parameters can be fixed from the analysis of available experimental data, and then used without any artificial tuning in further calculations. Results of the defect model validation against the tests [1, 2] (in which variation of the intra-granular dislocation density were directly measured with burn-up) are presented.

The new model with the determined microscopic parameters is applied to analysis of high burn-up fuel in a wide temperature range and allows formulation of a simple threshold criteria for fuel restructuring, in a good agreement with recent observations.

1. Evolution of point defects (vacancies and interstitials)

The system of the MFPR equations for evolution of point defects in irradiated UO_2 fuel should be modified by self-consistent consideration of pore shrinkage and dislocation loop generation. Evolution of the vacancy and interstitial distribution is described in the mean field approximation [5] in terms of the dimensionless concentrations, c_v and c_i (number of vacancies and interstitials per uranium atom), by the following equations:

$$\dot{c}_v = -(k_v^2 + k_{v,g.b.}^2) D_v c_v - \alpha D_i c_i c_v + (1-\xi) K + K_e + K_b + K_p , \tag{1.1}$$

$$\dot{c}_i = -(k_i^2 + k_{i,g.b.}^2) D_i c_i - \alpha D_i c_i c_i + K - K_d , \tag{1.2}$$

where D_v and D_i are the vacancy and interstitial diffusion coefficients, respectively; α is the recombination constant given by $\alpha = 4\pi r_c/\Omega$, $r_c = 0.1 \div 0.5$ nm; k_v^2 and k_i^2 are the total sink strengths of vacancies and interstitials into the extended defects (gas bubbles, pores, vacancy loops and dislocations), respectively; $k_{v,g.b.}^2$ and $k_{i,g.b.}^2$ are the grain boundary sink strengths for vacancies and interstitials, respectively; K is the Frenkel pair production rate (d.p.a. s^{-1}) which can be estimated (for the PWR normal operation conditions) by $K = F z_s \Omega$, where F is the fission rate and the parameter $z_s = (1 \div 5) \cdot 10^5$ characterises the damage formation in the fission track volume; ξK is the rate at which vacancies are removed from solution to form vacancy loops, ξ is the adjustable parameter, $0 < \xi < 1$ [6, 7]; K_e is the rate of the vacancy thermal production; K_p is the rate of the irradiation re-solution (knockout) of vacancies from pores; K_b is the rate of the irradiation induced re-solution of vacancies from gas bubbles; K_d is the rate of the interstitial absorption due to the interstitial loop generation.

The grain boundary sink strength for vacancies and interstitials can be estimated from the relationship [5]

$$k_{g.b.}^2(i,v) = \frac{k_{i,v} R_g \coth\left(k_{i,v} R_g\right) - 1}{R_g^2 \left[\dfrac{1}{3} + \dfrac{1}{k_{i,v}^2 R_g^2} - \dfrac{\coth\left(k_{i,v} R_g\right)}{k_{i,v} R_g} \right]} . \tag{1.3}$$

In accordance with [5–7], the total sink strength of vacancies and interstitials are equal to

$$k_{i,v}^2 = 4\pi R_b C_b + 4\pi \bar{R}_p C_p + Z_{i,v} \left(\rho_d + 2\pi R_l C_l + 2\pi \bar{R}_{vl} C_{vl} \right) . \tag{1.4}$$

The rate of the vacancy thermal production has the form:

$$K_e = D_v \left[4\pi R_b C_b c_v^{(bs)} + 4\pi \bar{R}_p C_p c_v^{(ps)} + Z_v \left(\rho_d + 2\pi R_l C_l + 2\pi \bar{R}_{vl} C_{vl} \right) c_v^{(eq)} \right], \qquad (1.5)$$

where $c_v^{(eq)}$ is the thermal equilibrium vacancy concentration; $c_v^{(bs)}$ and $c_v^{(ps)}$ are the boundary concentrations of vacancies on the bubble and pore surfaces; ρ_d is the dislocation network density; C_b and R_b are the gas bubbles concentration and mean bubble radius, respectively; C_p and $\bar{R}_p$ are the pore concentration and mean radius, respectively; C_{vl} and $\bar{R}_{vl}$ are the vacancy loops concentration and mean radius, respectively; C_l and R_l are the interstitial loops concentration and mean radius, respectively.

The vacancy production rate from pores due to knockout by fission fragments passing through pores were described in [8] in the form

$$K_p = 4\pi \bar{R}_p^2 C_p 2\Omega F \lambda \eta, \qquad (1.6)$$

where the number of vacancies knocked out of a pore per collision $\eta = 100$ and the length of the fission fragment path $\lambda = 10^{-6}$ m, in accordance with estimations of [7].

The vacancy production rate from bubbles due to knockout by fission fragments passing through bubbles, which was introduced in [9] as the thermal annealing of bubbles (to equilibrium volume) in molten zone of fission tracks, can be represented in the form

$$K_b = 4\pi R_b C_b \left[D_v \left(c_v - c_v^{(eq)} \right) - D_i c_i \right] - \frac{d(C_b V_b)}{dt}, \qquad (1.7)$$

i. e., as a difference between the rate balance of point defects sinking into bubbles and the real rate of bubbles volume growth. In this case the bubbles are considered as equilibrium (owing to the thermal annealing in fission tracks) and their growth is determined by absorption of gas atoms (as the rate controlling step). In accordance with the “thermal spike” model [10], molten zones appear in the fission tracks during some time interval $\tau^* \approx 10^{-11}$ s, which is long enough for relaxation of small nanometre bubbles to the equilibrium (“capillary”) state in the melt, as explained in [9].

The rate of the interstitial absorption due to the interstitial loop generation in the bi-modal approximation for loops (see below Eq. (2.6)) is equal to

$$K_d = \pi R_l^2 B \frac{dC_l}{dt}, \qquad (1.8)$$

where B is the Burgers vector length.

The dislocation sink strength for interstitials is larger than that for vacancies due to the higher elastic interaction between dislocations and interstitials [5]:

$$Z_i = Z_v \left(1 + 2\varepsilon \right), \; 0 < 2\varepsilon \ll 1. \qquad (1.9)$$

The thermal equilibrium vacancy concentration, $c_v^{(eq)}$, and interstitial concentration, $c_i^{(eq)}$, are approximated by the Arrhenius correlation:

$$c_{v,i}^{(eq)} = \exp\left(-E_{v,i}^{(eq)} / kT \right), \qquad (1.10)$$

with the activation energies $E_v^{(eq)} = 2.2$ eV and $E_i^{(eq)} = 6.0$ eV [11].

The interstitial diffusivity may be given by expressions

$$D_i = \frac{2}{3} x_i^2 a^2 \nu_i \exp(-E_i^{(m)} / kT), \qquad (1.11)$$

where $\nu_i = 5 \cdot 10^{12}\,\mathrm{s}^{-1}$ is the jump frequency, $E_i^{(m)} = 0.6$ eV is the migration activation energy, $x_i^2 = 10^{-2} \div 1$ is deviation from stoichiometry factor [12]; or

$$D_i = \left(\frac{a}{2} \right)^2 \nu_i \exp(-28000 / RT), \qquad (1.12)$$

where $\nu_i = 10^{13}\,\mathrm{s}^{-1}$ is the interstitial jump frequency, $a = 5.5 \cdot 10^{-10}$ m is the lattice parameter and $R = 8.314$ [11].

The uranium self-diffusion coefficient D_U at low temperatures (below 1000 °C) under steady irradiation conditions is completely athermal and depends only on the fission rate F [11]. At high temperatures (up to 1500 °C), D_U slowly increases with temperature up to its thermal value. So the uranium self-diffusion coefficient may be evaluated as the sum of two (athermal and thermal) terms:

$$D_U = AF + D_U^{(0)} \exp\left(-\frac{E_U}{kT}\right), \quad (1.13)$$

with $A \approx 1.2 \cdot 10^{-39}\,\mathrm{m}^5$, $D_U^{(0)} = 2 \cdot 10^{-4}\,\mathrm{m}^2/\mathrm{s}$ and $E_U/k = 64200\,\mathrm{K}$ [11].

The athermal diffusivity can be reasonably evaluated within so-called "thermal rods" mechanism [13] which describes enhanced migration of U atoms in molten zones of fission tracks during a short period of the thermal spike. Within this mechanism one should also take into consideration that existing point defects recombine in molten zones of the fission tracks, thus, all interstitials in the melted volume vanish ($c_i << c_v$) and do not participate in the enhanced mass transport. Therefore, rapid relocation of U atoms in molten tracks results in spatial redistribution (transport) of vacancies in the crystal owing to this event and in corresponding enhancement of the effective vacancy diffusivity.

Indeed, the uranium self-diffusion coefficient D_U can be generally represented as superposition of the vacancy and interstitial migration mechanisms:

$$D_U \approx D_v c_v + D_i c_i, \quad (1.14)$$

which become comparable in steady state under low temperature irradiation conditions, as follows from Eqs. (1.1) and (1.2) (see, e. g., [9]):

$$D_i c_i \approx D_v c_v \left(k_v^2/k_i^2\right) \approx D_v c_v, \quad (1.15)$$

and, therefore,

$$D_U \approx 2D_v c_v \approx 2D_i c_i. \quad (1.16)$$

Therefore, the effective vacancy diffusivity D_v can be calculated from Eqs. (1.13) and (1.16) using steady-state solution of Eqs. (1.1) and (1.2) for c_v and c_i with D_i defined in Eq. (1.11) or Eq. (1.12).

At high temperatures ($T \geq 1500$ °C) the thermal effects dominate over the radiation ones and the steady state vacancy concentration is determined by its thermal equilibrium value, $c_v \approx c_v^{(eq)}$, whereas

$$D_U \approx D_v c_v >> D_i c_i \quad (1.17)$$

instead of Eq. (1.16) (see, e.g., [9]).

2. Evolution of extended defects (bubbles, pores and dislocations)

The boundary concentrations of vacancies on the bubble and pore surfaces, $c_v^{(bs)}$ and $c_v^{(ps)}$, are given by

$$c_v^{(bs)} = c_v^{(eq)} \exp\left(-\Omega \delta P_b / kT\right),$$
$$c_v^{(ps)} = c_v^{(eq)} \exp\left(-\Omega \delta P_p / kT\right). \quad (2.1)$$

The difference between the actual and equilibrium bubble (pore) gas pressures, $\delta P_{b,p}$, is defined as

$$\delta P_x = P_x - P_h - \frac{2\gamma}{R_x},$$
$$P_x = \frac{N_x kT}{\left(V_x - B_{Xe} N_x\right)},$$
$$x = b,\ p, \quad (2.2)$$

where P_h is the external hydrostatic pressure, γ is the effective surface tension for UO_2, $P_{b,p}$ is the gas pressure in a bubble or pore given by the van der Waals equation, $N_{b,p}$ is the number of gas atoms in a bubble or pore, $V_{b,p}$ is the bubble or pore volume, and B_{Xe} is the van der Waals constant for xenon.

In the case of steady state irradiation conditions, the bubble volume, V_b, can be calculated using the equilibrium equation, $\delta P_b = 0$, and the corresponding boundary condition takes the form $c_v^{(bs)} = c_v^{(eq)}$.

It was shown [9] that the factor F_n entering transport equations for the intragranular gas-bubble system (paper on p. 7) and determining the probability that two gas atoms that have come together actually stick and form a bubble, is proportional to the probability that a vacancy is located in a certain position (collision of two atoms), and therefore is equal to the vacancy concentration c_v. Correspondingly, in the MFPR code the nucleation factor is calculated in a self-consistence manner:

$$F_n = c_v. \qquad (2.3)$$

Evolution of pores is described in paper on p. 58. Following [7], the main equation has the form

$$\frac{dV_p}{dt} = 4\pi R_p \left(D_v \left(c_v - c_v^{(ps)} \right) - D_i c_i \right) - 4\pi R_p^2 2\Omega F \lambda \eta , \qquad (2.4)$$

where

$$c_v^{(ps)} \approx c_v^{(eq)} \exp\left(\frac{\Omega}{kT} \left(\frac{2\gamma}{R_p} + P_h \right) \right).$$

The vacancy loops concentration is found from the equation [7]:

$$\frac{d}{dt} C_{vl} = -\frac{2\pi \bar{R}_{vl}}{\Omega_{vl}} \left[Z_i D_i c_i - Z_v D_v \left(c_v - c_v^{(eq)} \right) \right] C_{vl} + \frac{\xi K}{\Omega_{vl}} , \qquad (2.5)$$

where the vacancy loop volume is $\Omega_{vl} \equiv \pi \bar{R}_{vl}^2 B$.

The nucleation rate of (interstitial type) dislocation loops is determined by formation (and following growth) of di-interstitial clusters (see, for example, [14]). In the bi-modal approximation for the dislocation loop size distribution:

$$\frac{dC_l}{dt} = \frac{\alpha_l D_i c_i^2}{\Omega} , \qquad (2.6)$$

where α_l is the dislocation loop nucleation constant,

$D_i \alpha_l = 4\pi r_{ii} (D_i + D_i)/\Omega = 8\pi r_{ii} D_i/\Omega$.

Under an assumption $r_{ii} \approx r_{iv} \approx a$, where a is the lattice parameter and

$D_i \alpha = 4\pi r_{iv} (D_i + D_v)/\Omega \approx 4\pi r_{iv} D_i/\Omega$ is the vacancy-interstitial recombination constant (see Eqs. (1.1) and (1.2)), one can estimate $\alpha_l \approx 2\alpha$. Ionic charge effects (discussed, for example, in [12]) can violate the assumption $r_{ii} \approx r_{iv} \approx a$ and therefore, change the values of the constants α_l and α .

It is usually assumed [15] that dislocation loops are generated during the initial stage of irradiation until

$$D_i c_i - D_v \left(c_v - c_v^{eq} \right) > 0 . \qquad (2.7)$$

Calculations of the loop size distribution [14] confirm that the loop population achieves a steady state condition during some initial nucleation period.

This stipulation can be simply justified, if one notices that the dislocation bias to interstitials (due to elastic interactions of dislocations with point defects) takes place for finite loops, but not for small interstitial clusters. This implies that when $D_i c_i - D_v \left(c_v - c_v^{eq} \right)$ becomes negative, the small clusters will not be stable and thus will disappear, whereas already formed loops may proceed to grow owing to non-zero bias factor ε, in accordance with the presented below Eq. (2.8).

This conclusion is also in a fair agreement with direct observations [16, 17]. In these tests the UO$_2$ specimens were irradiated in a neutron flux of $1.4 \cdot 10^{18}$ slow neutrons · m^{-2}, which induced the fission rate ≈ $1.2 \cdot 10^{20}$ m^{-3}s^{-1} in the specimens. At low doses dislocation loops, formed from platelets of interstitial atoms, were produced. These became resolvable in the electron microscope as a 2.5 nm diameter black spots at a dose of $4 \cdot 10^{21}$ m^{-3}, and grew in area proportional to the total dose. After a dose of 10^{24} m^{-3}, these dislocation loops had grown sufficiently to coalesce with neighbouring loops to form a dislocation network. With further increase in dose the network coarsened after a dose $2.2 \cdot 10^{25}$ m^{-3}, when dislocation density attained $2 \cdot 10^{13}$ m^{-2}.

The mean dislocation loop radius growth rate obeys the following equations [15]:

$$\begin{cases} \dfrac{dR_l}{dt} = \dfrac{2\pi}{B\ln\left(8R_lR_d^{-1}\right)}\left[\left(1+2\varepsilon\right)D_ic_i - D_v\left(c_v - c_v^*\right)\right], & \text{if } R_l < R_s = \left(\dfrac{3}{4\pi C_l}\right)^{\frac{1}{3}}; \\ \dfrac{dR_l}{dt} = \dfrac{2\pi}{B\ln\left(\pi\rho_d R_d^2\right)^{-1/2}}\left[\left(1+2\varepsilon\right)D_ic_i - D_v\left(c_v - c_v^*\right)\right], & \text{if } R_l \ge R_s, \end{cases} \tag{2.8}$$

where R_s characterises the mean distance between dislocations, R_d is the dislocation core radius estimated as $R_d \cong 3B$, B is the Burgers vector, $c_v^* = c_v^{eq}\exp\left(-\left(\gamma_f + E_l\right)\Omega/BkT\right)$ is the boundary vacancy concentration at dislocation loop, γ_f denotes UO$_2$ fuel stacking fault energy, Ω is atomic volume, E_l is dislocation loop elastic energy, which is determined as

$$\begin{cases} E_l = \dfrac{E_{\mathrm{UO_2}}B}{2\left(1-\nu_{\mathrm{UO_2}}^2\right)4\pi}\dfrac{1}{\left(1+\dfrac{R_l}{B}\right)}\ln\left(1+\dfrac{R_l}{B}\right), & \text{if } R_l < R_s = \left(\dfrac{3}{4\pi C_l}\right)^{\frac{1}{3}}; \\ E_l = 0, & \text{if } R_l \ge R_s, \end{cases} \tag{2.9}$$

since at $R_l \ge R_s$ the dislocation loops are approximated as straight dislocations (see Eq. (2.10) below), e. g., $R_l \to \infty$.

UO$_2$ fuel Poisson's ratio and Young's modulus in Eq. (2.9) can be determined using the MATPRO data base [18]:

$$E_{\mathrm{UO_2}} = 2.334\cdot10^{11}\left[1-2.752\left(\frac{s}{1+s}\right)\right]\left(1-1.0915\cdot10^{-4}T\right)\exp\left(-\beta x\right);$$
$$\nu_{\mathrm{UO_2}} = 0.316,$$

where T is the fuel temperature, s is the fuel swelling; x is the magnitude of deviation from stoichiometry in UO$_{2\pm x}$ fuel; β is 1.34 for hyperstoichiometric fuel or 1.75 for hypostoichiometric fuel.

However, in experimental observations [1, 16] only perfect dislocations with the $b = \frac{1}{2}[110]$ Burgers vector (i. e., without dissociation into partial dislocations and formation of stacking faults, typical for the fcc-lattice metals) was evidenced. For this reason, only perfect dislocations without stacking fault energy term (i. e., $\gamma_f = 0$) will be considered in further calculations:

$$c_v^* = c_v^{eq}\exp\left(-\frac{E_l\Omega}{BkT}\right).$$

The dislocation sink strength for vacancies is evaluated as [15]

$$Z_v = \begin{cases} 2\pi\left[\dfrac{1}{\ln\left(\pi\rho_d R_d^2\right)^{-1/2}} + \dfrac{2\pi R_l C_l}{\rho_d \ln\left(8R_l R_d^{-1}\right)}\right], \quad \rho_d(t) = \rho_d(0), \\ \qquad\qquad\qquad\qquad\qquad\qquad \text{if } R_l < R_s = \left(\dfrac{3}{4\pi C_l}\right)^{\frac{1}{3}}; \\ 2\pi\dfrac{1}{\ln\left(\pi\rho_d R_d^2\right)^{-1/2}}, \quad \rho_d(t) = \rho_d(0) + 2\pi R_l C_l, \quad \text{if } R_l \geq R_s, \end{cases} \tag{2.10}$$

where $\rho_d(0)$ is the initial network dislocation density. In this approach it is assumed that when dislocation loops are large compared to the sphere of influence, i. e., $R_l \geq R_s$, the dislocation loops may be best approximated as straight dislocations of the length equal to their circumferences by using the relationship that the corresponding dislocation line density is $2\pi R_l C_l$. In this approximation the growth rates of dislocation loops are given by Eq. (2.8) corresponding to the case $R_l \geq R_s$.

The model based on the above presented system of Eqs. (1.1)–(1.17) and Eqs. (2.1)–(2.10) was implemented in the MFPR code.

3. Validation of the new MFPR code version

3.1. Experimental data

The new dislocation model was validated against experimental data of [1, 2]. In these experiments the detailed characteristics of intragranular bubbles and dislocations in UO$_2$ fuel pellets in a wide range of burn-ups 6 – 83 GWd/t under steady irradiation conditions were examined. The maximum irradiation temperatures of the specimens were roughly estimated as 650 – 750 °C within the accuracy limits ±50 °C.

From the measured values of the bubbles concentration, mean bubbles diameter and dislocation density, one can evaluate the sink strengths of the dislocation and intragranular bubble subsystems in these tests. In accordance with this evaluation, the total sink strength attains the maximum value $\sim 10^{16}\,\mathrm{m}^{-2}$ at burn-up approximately 23 GWd/t and remains practically invariable at higher burn-ups up to 83 GWd/t. Measured average bubble diameter increases approximately from the value of 2 nm at burn-up ~20 GWd/t to ~6 nm at burn-ups higher than 80 GWd/t. The bubbles concentration increases up to $10^{24}\,\mathrm{m}^{-3}$ at burn-up 20 GWd/t, and then slowly decreases within one order of magnitude (approximately to $\sim 10^{23}\,\mathrm{m}^{-3}$) at burn-ups > 80 GWd/t.

It should be noted that usually the codes (e. g., [19, 20] using a constant (default) value for the bubble nucleation factor, F_n) predict a monotonous growth of the bubbles concentration under steady irradiation conditions, in contradiction with recent observations of [1, 2]. Coupling of the nucleation factor with the vacancy concentration, Eq. (2.3), allows a more adequate consideration of the irradiation effects on intragranular bubbles evolution in high-burnup fuel. Indeed, a typical behaviour of the vacancy concentration under steady irradiation conditions calculated by the MFPR code with the implemented defect model is rather non-monotonous as shown in Fig. 1. A strong decrease of the vacancy concentration in a late stage of irradiation results in a strong suppression of the nucleation factor, Eq. (2.3), and eventually stabilises the bubbles concentration, as demonstrated in the following Section 3.2.

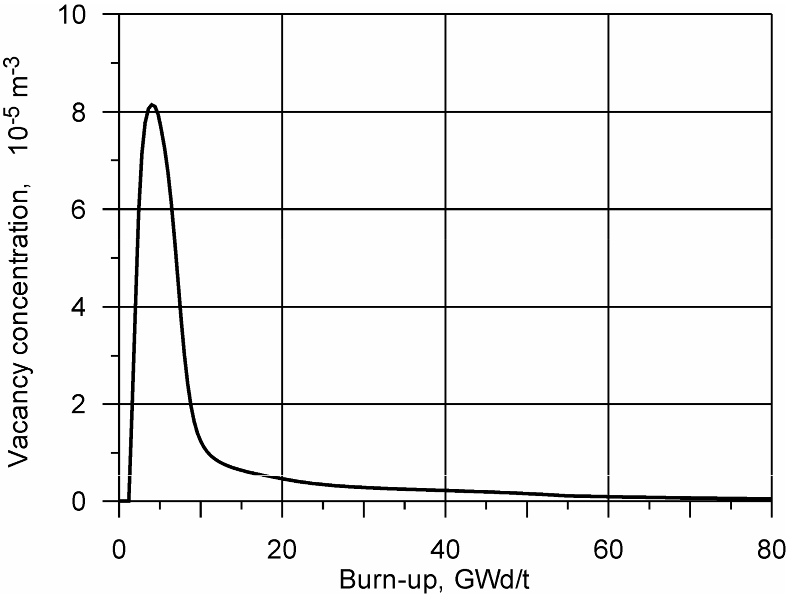

Fig. 1. Vacancy concentration as a function of burn-up under irradiation temperature 1073 K and fission rate 10^{19} $m^{-3}s^{-1}$

3.2. Calculation results

Calculations with the MFPR code were performed for the UO_2 fuel with the initial grain diameter 9 nm, porosity 5 % and mean pore radius $\overline{R}_p = 1$ μm. Irradiation at temperature 1073 K with the fission rate $F = 10^{19}\,\mathrm{m^{-3}s^{-1}}$ and burn-up up to 100 MWd/kg was simulated. The initial dislocation density and mean vacancy loop radius are chosen as $\rho_0 = 10^{10}\,\mathrm{m^{-2}}$ and $\overline{R}_{vl} = 1$ nm, respectively.

The re-solution constant b_0 of gas atoms from bubbles was varied in calculations from $2\cdot10^{-23}\,\mathrm{m^3}$ to $0.5\cdot10^{-23}\,\mathrm{m^3}$ following quantitative evaluation of this parameter in [9]. The parameter of the vacancy loop formation ξ was varied from 10^{-8} to 10^{-2}; the damage formation in fission tracks factor z_s was varied from $1\cdot10^5$ to $4\cdot10^5$.

The other parameters correspond to the following MFPR base set values: the interstitial bias factor $2\varepsilon = 3\,\%$; the vacancy-interstitial recombination radius $r_c \approx 0.5$ nm.

The best fit to the experimental data is attained at $\xi \approx 10^{-3}$, $b_0 \approx 0.5\cdot10^{-23}\,\mathrm{m^3}$ and $z_s \approx 2\cdot10^5$ [21]. The final calculation results with the fixed set of parameters are presented in Fig. 2.

Results of validation of the defect model against various steady-irradiation experiments show that the main microscopic parameters can essentially differ from the corresponding values typical for metals, despite the basic physical mechanisms of the defect structure evolution being similar in different materials. Therefore, a similar formalism of the defect model (either for point defects [5, 6], or for dislocations [14, 15]), originally developed for irradiated metals, with a new set of the microscopic parameters allows a mechanistic description of the defect system evolution in the ceramic material. In particular, basing on the results for the dislocation density evolution, the model can be applied to mechanistic prediction of the threshold temperature for the fuel restructuring observed in the rim-zone of high burn-up UO_2 fuel, as demonstrated in the following Section 4.

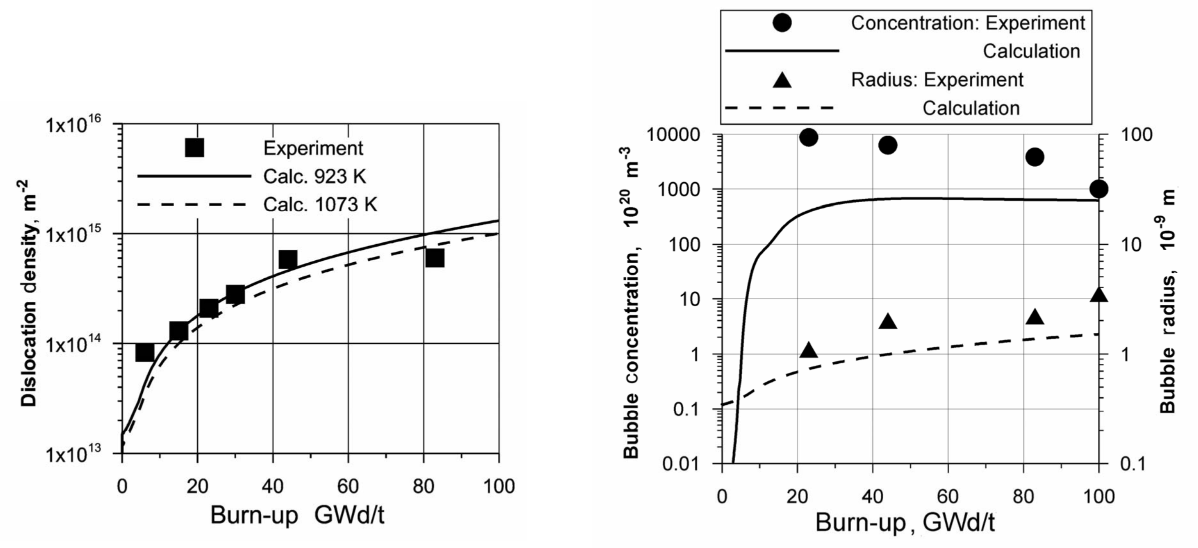

Fig. 2. Results of calculations of dislocations density, intragranular bubbles concentration and mean bubble radius as a function of burn-up (damage formation factor $z_s = 2\cdot10^5$; bubble re-solution constant $b_0 = 0.5\cdot10^{-23}$ m^3; vacancy loop formation factor $\xi = 10^{-3}$) in comparison with experimental data [1, 2]

4. Model predictions for fuel restructuring at high burn-ups

As observed in [1] at ≈ 900 K, tangled dislocation networks with low-angle grain boundaries were formed by accumulation of dislocations in the 44 GWd/t fuel, when dislocation density attained $\approx 6\cdot10^{14}$ m^{-2}. For the higher burn-up fuel of 83 GWd/t, dislocations further accumulated and ultimately evolved into sub-divided grains with high-angle boundaries. The sub-divided grains with high-angle boundaries were postulated in [1] as the nucleus for the recrystallization of fuel.

This result well correlates with other observations of the burnup threshold between 55 and 82 GWd/t [22].

In accordance with the general theory of cell structure formation [23], dislocation structures tend to develop with increasing dislocation density and to form dislocation clusters in which neighbouring dislocations mutually screen their stress field. The cell structure terminates the structural evolution, when dislocation density attains a certain ultimate value. One can expect that dependence of this ultimate value on temperature would be rather weak, owing to its physical nature (i.e., stress screening).

From analysis of the above presented test observations [1], the transition from low-angle to large-angle cells occurs in the range of dislocation density from $\approx 6\cdot10^{14}$ to $\approx 10^{15}$ m^{-2} , Fig. 2. Application of these ultimate criteria to higher temperatures is presented in Fig. 3, where dislocation density evolution with burn-up was calculated by the MFPR dislocation model with microscopic parameters fixed from the analysis of the test [1] in the previous Section 3.2.

From these calculations it is seen that the temperature threshold at which no restructuring occurs, at least up to 100 GWd/t, is at 1300–1400 K, in a good agreement with recent observations (see [22]).

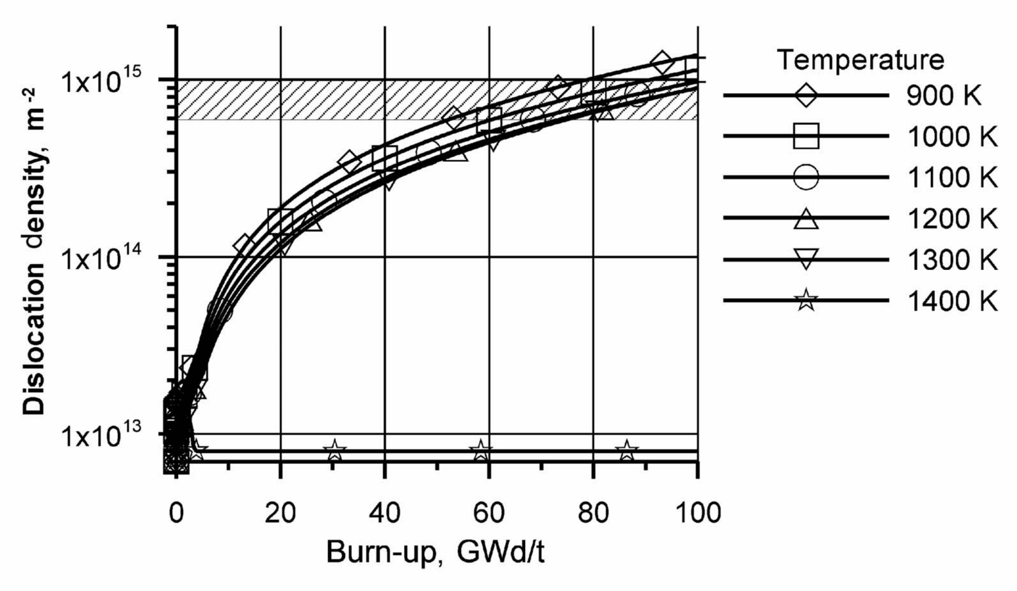

Fig. 3. Dislocations density as a function of burn-up, calculated in steady state irradiation conditions at different temperatures

Conclusions

The model for dislocations generation and evolution under irradiation conditions was developed and implemented in the MFPR code. Being combined with the MFPR set of microscopic equations for evolution of point defects and their interactions with gas bubbles, a completely self-consistent consideration of the whole system of point and extended defects in irradiated fuel, including point defects: vacancies, interstitials and gas atoms, as well as extended defects: bubbles, dislocations, vacancy loops and pores, was attained.

The MFPR code was validated against steady irradiation experiments, in which the dislocation density and the bubble concentration and mean size were directly measured with burn-up. MFPR allows a satisfactory prediction of the considerable suppression of the intragranular bubble concentration growth accompanied with the noticeable increase of the mean bubble size in the late stage of irradiation, observed in the recent tests with the high burn-up fuel [2]. Results for the dislocation density evolution obtained in these calculations are also in an adequate agreement with the high burn-up fuel measurements [1].

Sensitivity study of the new code version against the MFPR basic and new parameters allows refinement of these parameters. Being physically grounded, these microscopic parameters were fixed to attain the best fit to the experimental data [1, 2], and now can be used without any artificial tuning in further calculations.

For instance, the MFPR is successfully applied to prediction of the threshold temperature for the fuel restructuring observed in the rim-zone of high burn-up UO_2 fuel in recent tests [22].

References

1. *Nogita K., Une K.* // Nucl. Instrum. Meth. Phys. Res. 1994. Vol. B91. P. 301.
2. *Kashibe S., Une K., Nogita K.* // J. Nucl. Mater. 1993. Vol. 206. P. 22.
3. *Une K., Kashibe S.*// J. Nucl. Science and Technology. 1990. Vol. 27(11). P. 1002–1016.
4. *Zacharie I., Lansiart S., Combette P., Trotabas M., Coster M., Groos M.* // J. Nucl. Mater. 1998. Vol. 255. P. 85–91.
5. *Brailsford A.D., Bullough R.* // Philos. Trans. Royal. Soc. 1981. Vol. A 302. P. 87.
6. *Bullough R., Eyree B.L., Krishan K.* // Proc. R. Soc. Lond. 1975. Vol. A. 346. P. 81.
7. *Dollins C.C., Nichols F.A.* // J. Nucl. Mater. 1978. Vol. 78. P. 326.
8. *Stehle H., Assmann H.* // Ibid. 1974. Vol. 52. P. 303.
9. *Veshchunov M.S.* // Ibid. 2000. Vol. 227. P. 67–81.
10. *Seitz F.* // Disc. Faraday Soc. 1949. Vol. 5. P. 271.
11. *Matzke H.* // Adv. Ceram. 1986. Vol. 17. P. 1.
12. *Rest J., Hofman G.L.* // J. Nucl. Mater. 2000. Vol. 277. P. 231.
13. *Dienst W.* et al. // Ibid. 1972. Vol. 42. P. 285.
14. *Hayns M.R.* // Ibid. 1975. Vol. 56. P. 67.
15. *Yoo M.H.* // Ibid. 1977. Vol. 68. P. 193.
16. *Whapham A.D., Sheldon B.E.* Electron Microscope Observation of the Fission-Gas Bubble Distribution in UO_2.. AERE-R-4970. 1965.
17. *Whapham A.D.* // Nuclear Applications. 1966. Vol. 2. P. 123.
18. SCDAP/RELAP5 MOD2 CODE. Manual. Vol. 4: MATPRO — A Library of Material Properties for LightWater Reactor Accident Analysis. NUREG/GR-5273, EGG-255. Vol. 4. 1990.
19. *Heames T.J., Williams D.A., Bixler N.E., Grimley A.J., Wheatley C.J., Johns N.A., Domogala P., Dickson L.W., Alexande C.A., Osborn-Lee I., Zawadzki S., Rest J., Mason A., Lee R.Y.* VICTORIA: A Mechanistic Model of Radionuclide Behaviour in the Reactor Coolant System under Severe Accident Conditions. NUREG/CR-5545. 1992.
20. *Rest J., Zawadzki S.A.* FASTGRASS, A Mechanistic Model for the Prediction of Xe, I, Cs, Te, Ba and Sr release from Nuclear Fuel under Normal and Severe-Accident Conditions. NUREG/CR-5840 TI92 040783. 1994.
21. *Shestak V.E., Tarasov V.I., Veshchunov M.S.* Modelling of Defect Structure Evolution in Irradiated UO_2 Fuel in Framework of the MFPR Code. (Preprint / Nuclear Safety Institute (IBRAE) RAS, no IBRAE-2004-02). Moscow: NSI (IBRAE) RAS, 2004.
22. *Kinoshita M., Sonoda T., Kitajima S., Sasahara A., Kameyama T., Matsumura T.* High Burnup RIM Project: (III) Properties of Rim-Structured Fuel // Proc. of the 2004 Intern. Meeting on LWR Fuel Performance (Sep. 19–22 2004, Orlando, Florida). 2004.
23. *Hansen N., Kuhlmann-Wilsdorf D.* // Mater. Sci. Eng. 1986. Vol. 81. P 141.

Model for Evolution of As-Fabricated Pores in UO$_2$ Fuel under Irradiation Conditions

V.D. Ozrin, V.I. Tarasov

Introduction

The changes of fuel volume under irradiation regime are of primarily importance for design and modelling of the fuel rods, identification of their life-limiting properties and tailoring of dimensional stable fuel. In this connection, study of behavior of as-fabricated pores seems to be an actual problem as the fuel densification due to pore sintering counterbalances the effects due to intragranular bubble growth resulting in the net fuel swelling. These effects are closely related to evolution of point (vacancies and interstitials) and extended (dislocation loops and dislocation network) defects. Indeed, in accordance with the direct experimental observations in [1, 2] the dislocation loops are generated (in form of di-interstitials) mainly during the initial period of irradiation. This process is concurrent with the fuel densification and therefore may be significantly influenced by the kinetics of pore sintering. For this reason, the model of pore behavior is an inherent constituent of general model of evolution of defects in the fuel matrix.

One of the first models for pore sintering was developed by MacEwen and Hastings [3] in the framework of simple vacancy-dislocation approach. Later the model has been developed by Brailsford and Boullough [4] considering the vacancy loop nucleation from displacement cascades and by Dollins and Nichols [5] suggested the knockout mechanism of vacancies from pores in fission tracks. The most comprehensive approach self-consistently considering evolution of the intragranular defects was suggested the framework of MFPR [6] project developed during the last decade by NSI (IBRAE) RAS and IRSN (France).

In early MFPR models, the fuel densification model was considered in connection with calculation of the dislocation loop density under irradiation conditions, e.g., see general paper [6]. It was based on the assumption of vacancy knockout from pores and considered decrease of the pore mean size and no gas trapping up to complete disappearance of pores. However, in reality pores never disappear completely since a rather wide size distribution exists, on the one hand, and pores are a sink for gas atoms in the UO$_2$ matrix, on the other hand. Moreover, in recent paper [7] a detailed experimental results on the gas location after reactor operations were given notably based on careful and original micro-analytical exams (SEM, EPMA, SIMS). In particular, it was shown that in the central hot zone of the fuel pellet near 5 % is trapped in fission gas porosities whereas 8 % is trapped in as fabricated porosities, not removed by irradiation. This amount is very significant and must be taken into account in transient or accident conditions.

For this reason, an advanced model of pore evolution has been developed and implemented into the version 1.4.3 of MFPR code. The underlying ideas and analytical justification of this model are described in detail in this paper. To clarify the consideration, many intragranular processes simulated by general MFPR model are omitted so that the only objects under consideration are pores, vacancies, interstitials and vacancy loops. In the next section a mathematical formulation is given for simultaneous self-consistent consideration of dislocation loops generation and pore shrinkage along with the point defects. Section 1 presents the analytical consideration in the framework of pore uni-modal approach revealing the main features of the model. In the next section, the model is generalized taking into account peculiarities of the pore distribution function followed from the available experimental data. Discussion finalizes the paper.

1. Model

As mentioned in Introduction, in this work a simplified model is analyzed, in which the grain boundary effects are neglected while the self-consistent consideration of evolution of intragranular objects is restricted by point defects, vacancy loops and pores. The initial pore size distribution is described by concentrations C_p which depend on initial pore radius. In this approach C_p values are considered as fixed while the pore radii are time dependent. With these concentrations, which are considered as initial data, the fuel swelling s_p due to pores is calculated in the framework of discrete representation as

$$s_p\left(t\right)=\frac{4\pi}{3}\sum_p C_p R_p^3\left(t\right), \tag{1}$$

where R_p is the pore radius depending on time t. In the limiting case the sum in Eq. (1) transforms into integral:

$$s_p\left(t\right)=\frac{4\pi}{3}\int p_c^0\left(R_0\right)R_p^3\left(t;R_0\right)dR_0\,, \tag{2}$$

where p_c^0 is initial the density distribution function.

This approach will be applied in this and the next sections. In Section 3, an alternative representation will be also considered, which assumes time dependence of the concentrations. In this case Eq. (2) is written as

$$s_p\left(t\right)=\frac{4\pi}{3}\int p_c\left(t;R_p\right)R_p^3 dR_p \tag{3}$$

with the time dependent density distribution function p_c .

Under above assumptions, the general mathematical model [6] (described also in paper on p. 47) is reduced the system of four coupled ordinary differential equations of the first order with respect to time for vacancy, interstitial and vacancy loop concentrations, C_v, C_i and C_{vl} as well as for pore volume V_p:

$$\begin{aligned}
\dot{c}_v &= -4\pi D_v\sum_p C_p R_p\left(c_v-c_v^{ps}\right)-2\pi R_{vl}C_{vl}D_v\left(c_v-c_v^{eq}\right)-\alpha D_i c_v c_i+\\
&\quad+\left(1-\zeta_e\right)K+8\pi\lambda\eta\Omega G C_p R_p^2,\\
\dot{c}_i &= -4\pi D_i\sum_p C_p R_p c_i-\frac{2}{BR_{vl}}Z_i c_{vl}c_i-\alpha D_i c_v c_i+K,\\
\dot{C}_{vl} &= \frac{2}{BR_l}\left(Z_v D_v\left(c_v-c_v^{eq}\right)-Z_i D_i\left(c_i-c_i^{eq}\right)\right)C_{vl}+\frac{\zeta_e K}{\pi B R_{vl}^2},\\
\dot{V}_p &= 4\pi R_p\left(D_v\left(c_v-c_v^{ps}\right)-D_i c_i\right)-8\pi\lambda\eta\Omega G R_p^2,
\end{aligned} \tag{4}$$

where c_x are the dimensionless concentrations of object type x that relate to the number concentration, C_x, as:

$$c_{v,i}=\Omega C_{v,i}\,, \tag{5}$$

where $\Omega = 4.09\cdot10^{-29}\,\mathrm{m}^3$ is the molecular volume for UO_2. The corresponding boundary and initial conditions are written as

$$\begin{gathered}
c_v\big|_{t=0}=c_v^{eq},\quad c_i\big|_{t=0}=c_i^{eq},\quad C_{vl}\big|_{t=0}=0,\\
\frac{4\pi}{3}\sum_p C_p R_p^3\left(0\right)=s_p\left(0\right).
\end{gathered} \tag{6}$$

In the above equations the dependencies of physical parameters on external factors are given in accordance with Ref. [7]: $\zeta_l = 2\cdot10^{-4}$ is the fraction of vacancies that directly form vacancy clusters, $\eta = 100$ is the dimensionless parameter, and $\lambda = 1\ \mu\mathrm{m}$. The atomic displacement rate K is estimated for the PWR normal operation conditions as

$$K = z_s\Omega G\,, \tag{7}$$

where G is the fission rate and $z_s = 2\cdot10^5$ is the damage formation in the fission track volume. The recombination constant α is estimated as $\alpha = 4\pi r_c/\Omega$, where $r_c \approx 0.5$ nm. The vacancy loop radius R_l and the length B of the Burger's vector are assumed to be equal to 1 nm and $\Omega^{-1/3} \approx 0.345\,\text{nm}$, respectively. The dimensionless sink strength factors Z_i and Z_v are defined as

$$Z_v = -\frac{4\pi}{\ln\left(\pi\rho_d R_d^2\right)},$$
$$Z_i = \left(1+\varepsilon\right), \tag{8}$$

where the parameter $\varepsilon = 0.03$ is introduced to take into account the slight preference of the sink strength of interstitials over that for vacancies due to their higher elastic interaction with dislocations [4], R_d is the dislocation core radius estimated as $\cong B$, ρ_d is the mean dislocation length per unit volume, which is assumed in the following analysis to be equal to MFPR initial density of $10^{10}\,\text{m}^{-2}$; with this assumption one evaluates Z_v and Z_i as 0.833 and 0.858, respectively.

The vacancy boundary concentration is found as

$$c_v^{ps} \approx c_v^{eq} \exp\left[\frac{\Omega}{kT}\left(\frac{2\gamma}{R_p} + P_h\right)\right], \tag{9}$$

while T is the temperature, γ is the surface tension, P_h is external pressure. The thermal equilibrium concentrations are approximated by Arrhenius correlation

$$c_{v,i}^{eq} = \exp\left(-E_{v,i}^{eq} / kT\right), \tag{10}$$

where $E_v^{eq} = 2.2\,\text{eV}$ and $E_i^{eq} = 6.0\,\text{eV}$ [8] are the activation energies. The other model parameters including the point defects diffusivities are specified in paper on p. 47.

2. Uni-modal pore distribution

It is reasonable to start examination of the model peculiarities with analytical consideration of the uni-modal pore distribution. In this case the pores are considered of the same size and the sum $\sum_p C_p R_p$ in Eq. (4) is replaced by $C_p R_p$.

2.1. Variable Change

First, it is convenient to introduce new dimensionless variables:

$$\begin{gathered} s_i(t) = c_i(t), \\ s_v(t) = c_v(t) - c_v^{eq}, \\ s_l = \pi B R_{vl}^2 C_{vl}, \end{gathered} \tag{11}$$

$$\rho = s_p^{1/3} = \left(C_p V_p\right)^{1/2} = \left(\frac{4\pi}{3} C_p\right)^{1/3} R_p = \frac{R_p}{\rho_p}, \tag{12}$$

where

$$\rho_p \equiv \left(\frac{3}{4\pi C_p}\right)^{1/3} \tag{13}$$

characterizes the pore separation. Then, neglecting the difference between c_v^{ps} and c_v^{eq} (which is valid considering large pores with R_p >> 1 nm) the system Eqs. (4, 6) is rewritten in the form

$$\begin{aligned}
\frac{ds_v}{dt} &= -\left(\omega_{vp}\rho + \omega_{vl}s_l\right)s_v - \omega_a\left(s_v s_i + c_v^{eq} s_i\right) + \left(1-\zeta_l\right)\omega_f + \omega_{KO}\rho^2,\\
\frac{ds_i}{dt} &= -\left(\omega_{ip}\rho + \omega_{il}s_l\right)s_i - \omega_a\left(s_v s_i + c_v^{eq} s_i\right) + \omega_f,\\
\frac{ds_l}{dt} &= \left(\omega_{vl}s_v - \omega_{il}s_i\right)s_l + \zeta_l\omega_f,\\
\frac{d\rho}{dt} &= \frac{\omega_{vp}s_v - \omega_{ip}s_i}{3\rho} - \frac{\omega_{KO}}{3};
\end{aligned} \tag{14}$$

$$s_v\big|_{t=0} = 0, \quad s_i\big|_{t=0} = 0, \quad s_l\big|_{t=0} = 0, \quad \rho\big|_{t=0} = s_0^{1/3}. \tag{15}$$

In these equations the characteristic frequencies were introduced:

$$\begin{gathered}
\omega_{vp} = \frac{3D_v}{\rho_p^2}, \qquad \omega_{ip} = \frac{3D_i}{\rho_p^2}, \qquad \omega_{vl} = \frac{2Z_v D_v}{BR_l}, \qquad \omega_{il} = \frac{2Z_i D_i}{BR_l},\\
\omega_a = \alpha\left(D_v + D_i\right), \quad \omega_f = z_s\Omega G, \quad \omega_{KO} = 6\lambda\eta\Omega G/\rho_p.
\end{gathered} \tag{16}$$

Typical values (at $T = 1250$ K and $G = 10^{19}$ $m^{-2}s^{-1}$) of these parameters are given in Table 1.

Table 1. Typical values of kinetic coefficients ω_x

x	vp	ip	vl	il	a	f	KO
ω_x (s^{-1})	$2.8\cdot10^{-5}$	$1.9\cdot10^{4}$	$3.3\cdot10^{2}$	$2.3\cdot10^{11}$	$7.2\cdot10^{12}$	$8.2\cdot10^{-5}$	$0.9\cdot10^{-7}$

Pore concentration at initial swelling of 5 % and $R_p = 1$ µm is equal to $1.2\cdot10^{16}$ m^{-3} so that $\rho_p = 3.9\cdot10^{-6}$ m.

2.2. Balance

The system Eq. (14) satisfies the balance condition:

$$\frac{ds_p}{dt} + \frac{ds_l}{dt} + \frac{ds_v}{dt} - \frac{ds_i}{dt} = 0, \tag{17}$$

from which it follows taking into account initial conditions Eq. (15) that

$$\Delta s_p \equiv s_p(0) - s_p(t) = s_p(0) - \rho^3(t) = s_l(t) + s_v(t) - s_i(t). \tag{18}$$

2.3. Exact solution for vacancy-interstitial subsystem

In absence of pores and vacancy loops Eq. (14) reduces to a system:

$$\begin{aligned}
\dot{s}_v &= -\omega_a\left(s_v s_i + c_v^{eq} s_i\right) + \omega_f,\\
\dot{s}_i &= -\omega_a\left(s_v s_i + c_v^{eq} s_i\right) + \omega_f.
\end{aligned} \tag{19}$$

Solution is written as

$$
\begin{aligned}
s_v(t) &= \frac{\omega}{\omega_a}\tanh\left(\omega\left(t+\delta t\right)\right)+\frac{c_v^{eq}}{2},\\
s_i(t) &= \frac{\omega}{\omega_a}\tanh\left(\omega\left(t+\delta t\right)\right)-\frac{c_v^{eq}}{2},
\end{aligned}
\tag{20}
$$

where

$$
\omega=\sqrt{\omega_a^2\left(\frac{c_v}{2}\right)^2+\omega_a\omega_f}\approx 2.5\cdot 10^4\ \text{s}^{-1},
$$

$$
\omega\delta t=\frac{1}{2}\ln\frac{2\omega+\omega_a c_v^{eq}}{2\omega-\omega_a c_v^{eq}}\approx\frac{\omega_a}{2\omega}c_v^{eq}\approx 0.2. \tag{21}
$$

It is seen that the characteristic time for vacancy-interstitial system is $\sim\omega^{-1}\sim 10^{-4}$ s, which is several orders of magnitude less that the characteristic time of evolution of other intragranular objects.

2.4. Quasi-stationary approach for vacancy-interstitial sub-system

As follows from the above consideration, the stationary conditions are quickly attained for vacancy and interstitial concentrations. This allows essential simplification of further consideration. Setting equal zero the derivatives in the first and second equations in Eq. (14) one gets a system of algebraic equations:

$$
\begin{aligned}
&\omega_v s_v+\omega_a\left(s_v s_i+c_v^{eq}s_i\right)-\omega_f+\omega_{lKO}=0,\\
&\omega_i s_i+\omega_a\left(s_v s_i+c_v^{eq}s_i\right)-\omega_f=0,
\end{aligned}
\tag{22}
$$

where

$$
\begin{aligned}
\omega_v &\equiv \omega_{vp}\rho+\omega_{vl}s_l,\\
\omega_i &\equiv \omega_{ip}\rho+\omega_{il}s_l,\\
\omega_{lKO} &\equiv \zeta_l\omega_f-\omega_{KO}\rho^2.
\end{aligned}
\tag{23}
$$

One of the variables (e.g., s_i) can be excluded subtracting the second equation from the first one:

$$
s_i=\frac{\omega_v s_v+\omega_{lKO}}{\omega_i}. \tag{24}
$$

With this substitution the system (22) reduces to algebraic equation of the second order:

$$
f_2 s_v^2+f_1 s_v+f_0=0\,, \tag{25}
$$

where

$$
\begin{aligned}
f_0 &= \omega_i\left(\omega_{lKO}-\omega_f\right)+\omega_a\omega_{lKO}c_v^{eq},\\
f_1 &= \omega_v\omega_i+\omega_a\left(\omega_v c_v^{eq}+\omega_{lKO}\right),\\
f_2 &= \omega_a\omega_v.
\end{aligned}
\tag{26}
$$

It is evident that the coefficients f_1 and f_2 are positive while f_0 is negative. Therefore, Eq. (25) has the only physically meaningful solution:

$$
s_v=\frac{-f_1+\sqrt{f_1^2-4f_0f_2}}{2f_2}. \tag{27}
$$

To estimate the sought-for concentrations taking into account the typical ω values one concludes that

$$
\begin{aligned}
\omega_v &\approx \omega_{vl}s_l,\\
\omega_i &\approx \omega_{il}s_l
\end{aligned}
\tag{28}
$$

provided $s_l >> 10^{-8}$. Next, with the more strict condition $s_l >> 0.001$ one derives neglecting the equilibrium concentrations that $f_0\approx-\omega_{il}\omega_f s_l$, $f_1\approx\omega_{vl}\omega_{il}s_l^2$, $f_2\approx\omega_a\omega_{vl}s_l$ and therefore $\left|f_0 f_2\right|<<f_1^2$. This allows to find explicit formulas:

$$
s_v\approx-\frac{f_0}{f_1}=\frac{\omega_f}{\omega_{vl}s_l},\qquad s_i\approx\frac{\omega_f}{\omega_{il}s_l}. \tag{29}
$$

Using these formulas one estimates the typical values for s_v and s_i as $4\cdot 10^{-6}$ and $6\cdot 10^{-15}$, respectively. These estimates indicate that neither vacancies nor interstitials notably contribute to the fuel swelling, which is generally of a few percent.

2.5. Vacancy loop and pore sub-system

2.5.1. Equations for s_l and ρ

The remaining equations describe time dependence of vacancy loop concentrations and pore radius:

$$\frac{ds_l}{dt} = \left(\omega_{vl} s_v - \omega_{il} s_i\right) s_l + \zeta_l \omega_f, \qquad\qquad \frac{d\rho}{dt} = \frac{\omega_{vp} s_v - \omega_{ip} s_i}{3\rho} - \frac{\omega_{KO}}{3} \tag{30}$$

in which vacancy and interstitial concentrations depend explicitly on s_l and ρ, see Eqs. (24, 27), the initial conditions being written as

$$s_l\big|_{t=0} = 0, \quad \rho\big|_{t=0} = s_p^{1/3}(0). \tag{31}$$

2.5.2. Stationary regime

At stationary regime for pores and vacancy loops it follows from the equation for pore radius that

$$\omega_{vp} s_v - \omega_{ip} s_i = 0 \tag{32}$$

as ρ approaches zero. However, it can be shown that the approximate equality Eq. (32) is valid under stationary conditions only for vacancies and interstitials because of the two terms tend to compensate each other. Indeed, taking into account the above estimates one derives that

$$\begin{aligned} \omega_{vp} s_v - \omega_{ip} s_i &= \left(\omega_{vp} - \omega_{ip}\frac{\omega_v}{\omega_i}\right) s_v - \omega_{ip}\frac{\omega_{lKO}}{\omega_i} = \frac{Z_v \varepsilon \omega_{il} \omega_{vp}}{Z_{i_i} \omega_i} s_l s_v - \frac{\omega_{ip}\omega_{lKO}}{\omega_i} \approx \\ &\approx \frac{Z_v \varepsilon \omega_{il} \omega_{vp} \omega_f}{Z_{i_i} \omega_i \omega_{vl}} - \frac{\omega_{ip}\omega_{lKO}}{\omega_i}. \end{aligned} \tag{33}$$

Taking into account that $|\omega_{lKO}| < \zeta_l \omega_f$ one estimates ratio of the second term to the first one in the *rhs* of this equation as $\zeta_l/\varepsilon \sim 10^{-2} << 1$. With this conclusion one estimates the ratio of the two terms in the *rhs* of equation for *ρ* of system Eq. (27) as

$$\frac{\omega_{vp} s_v - \omega_{ip} s_i}{\omega_{KO}\rho} \approx \frac{\varepsilon \omega_{vp} \omega_f}{\omega_{KO} \omega_{vl} s_l \rho} = \frac{\varepsilon B R_l z_s}{4\lambda\eta Z_v \rho_p s_l \rho} << 1, \tag{34}$$

provided that $\rho s_l >> 10^{-5}$[1]. It is seen that this ratio depends neither on temperature nor fission rate.

This is illustrated in Fig. 1 where the strictly calculated ratio Eq. (34) is plotted for wide range of external conditions.

---

[1] Note that similar conclusions are generally not valid for the third equation (for s_l) in the system Eq. (14).

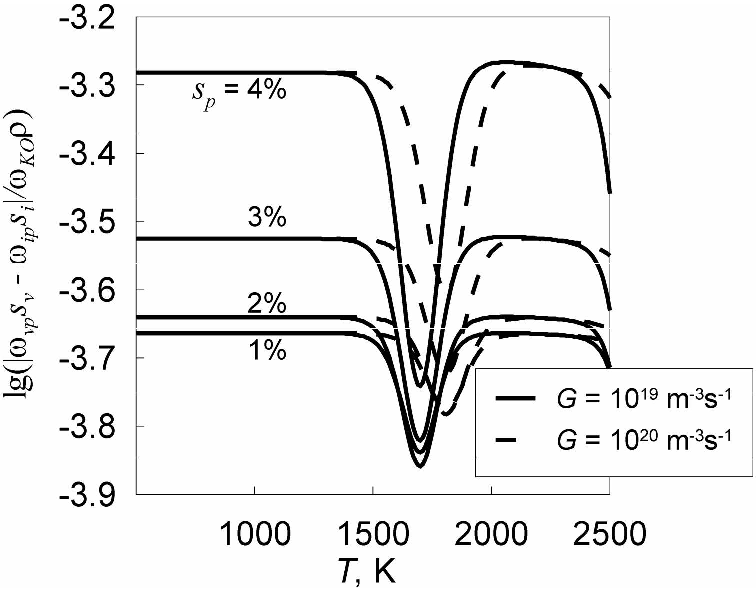

Fig. 1. Ratio of the first to the second term in the rhs of equation for ρ, see Eq. (27), as function of the temperature and for different fission rates and pore swelling

2.5.3. Approximate solution

The above results allow deducing the approximate solution for time dependence of pore radius. Indeed, dropping the term $\left(\omega_{vp}s_v - \omega_{ip}s_i\right)/3\rho$ in Eq. (30) results in

$$\rho(t) = \rho(0) - \int_0^t \omega_{KO}(t)\,dt = \rho(0) - \frac{6\lambda\eta\Omega}{\rho_p}\int_0^t G(t)\,dt = \rho(0) - \frac{6\lambda\eta b(t)}{\rho_p}, \qquad (35)$$

where *b* is the burn-up (measured in number of fissions per one U atom):

$$b(t) = \Omega\int_0^t G(t)\,dt. \qquad (36)$$

Turning back to the original variables, Eq. (35) is re-written in form

$$R_p(t) = R_p(0) - 6\lambda\eta b(t). \qquad (37)$$

In particular, if the fission rate is constant then the pore radius linearly depends on time:

$$R_p(t) = R_p(0) - 6\lambda\eta\Omega G t. \qquad (38)$$

In accordance with the above conclusions vacancies and interstitials do not contribute to the fuel porosity, therefore the vacancy loop swelling can be easily deduced from the balance condition, Eq. (18):

$$s_l(t) \approx \frac{4\pi}{3}C_p\left(R_p^3(0) - R_p^3(t)\right) = 6s_p(0)\lambda\eta b(t)\begin{pmatrix}1 - 6\lambda\eta b(t) + \\ +12\left(\lambda\eta b(t)\right)^2\end{pmatrix}. \qquad (39)$$

Note that expressions Eq. (35) — (39) seem to be universal ones depending only on the burn-up; in particular there is no dependence on the temperature. Also note, that the above conclusions are valid provided the pore radius is not too small. However the validity range overlaps all reasonable values of the pore swelling. These peculiarities are illustrated by Fig. 2 in which the strict solution of Eq. (30) is plotted for steady irradiation conditions at $T = 1250$ K, $G = 10^{19}$ m^{-3}s^{-1} and different values of initial pore swelling.

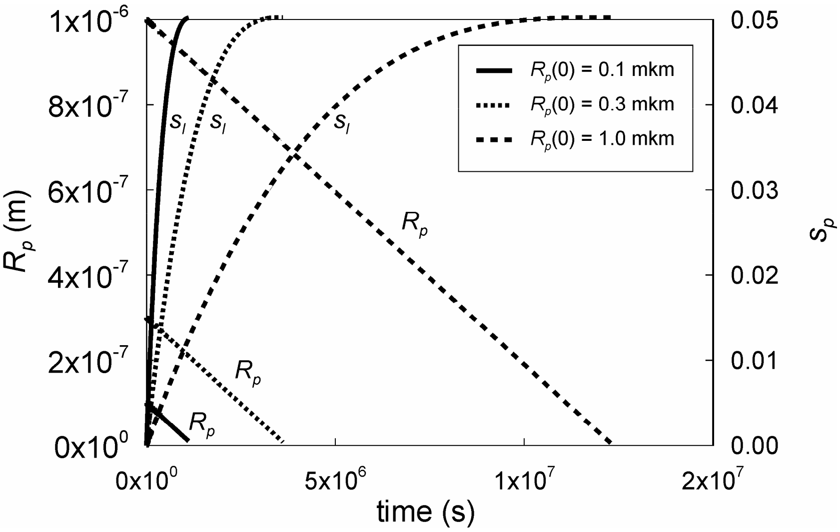

Fig. 2. Time dependence of pore radius (left y-axis) and vacancy loop swelling (right y-axis) calculated with constant fission rate $G = 10^{19}$ m^{-3}s^{-1} and initial pore swelling 0.05 and for three values, 0.1, 0.3 and 1 μm, of initial pore radius

3. Pore size distribution

3.1. Experimental data on pore size distribution

The typical porosity in the fresh fuel sample is shown in Fig. 3 borrowed from Ref. [10]. It is seen that the pores are almost uniformly distributed over the sample occupying both grain interior and intergranular spaces so it is straightforward to conclude that the vast majority of pores are located in grains interior.

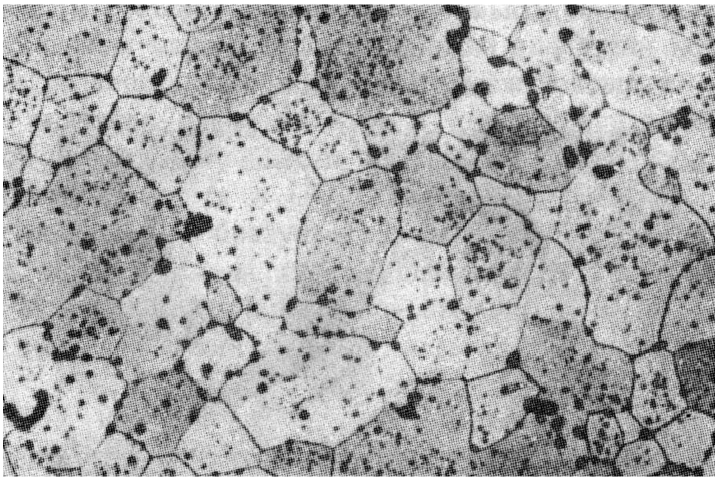

Fig. 3. Pore distribution in the fuel sample [10]

The measurements of the relative pore volume distribution (swelling distribution due to pores) p_s were performed in [11]. However, these data relate to the overall pore distribution without distinguishing the intra- and intergranular pores. Fig. 4 presents the distribution p_s for the fresh and irradiated (23 GWd/t) fuel over the pore size classes c defined as

$$c = 10\lg\left(d_p / d_0\right), \qquad (40)$$

where d_p is the pore diameter and $d_0 = 0.56$ μm. In this figure the distribution for the fresh fuel is represented by two curves corresponding to upper and lower limits of experimentally measured porosity (which is due to uncertainty in measured initial density: 10.35±0.15 g cm^{-3}).

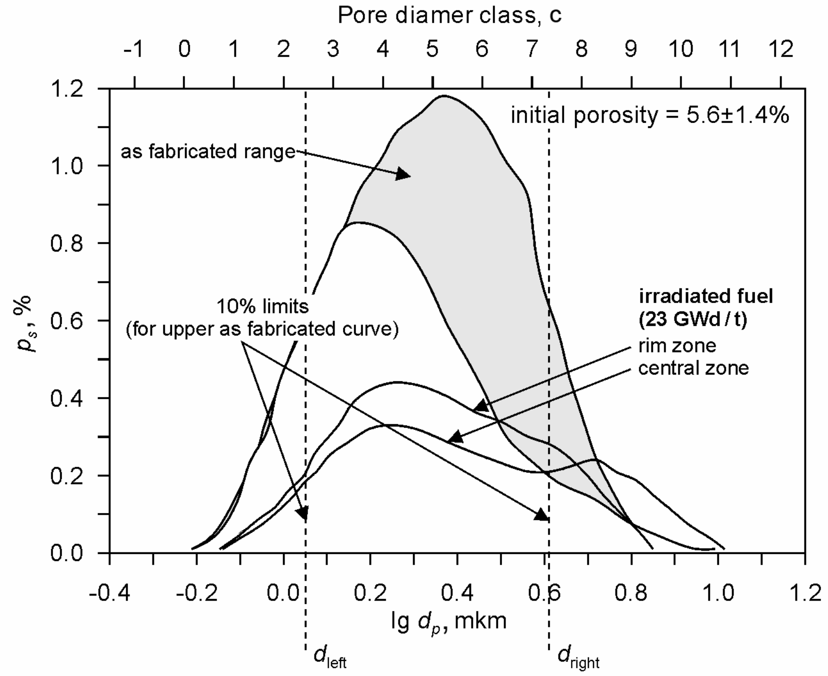

Fig. 4. Pore volume concentration per pore size class [11]. The shaded area represents the uncertainty of distribution for the fresh fuel

As seen, swelling distribution is concentrated within a short interval of pore size class. This is indicated in Fig. 4 by two vertical dashed lines representing 10 % left and right limits for the upper curve (corresponding to the upper porosity limit for the fresh fuel), $d_{\text{left}} \approx 1.1$ μm and $d_{\text{right}} \approx 4.1$ μm: 10 % of the total swelling is due to pores with $d_p < d_{\text{left}}$ and, similarly, 10 % is due to pores with $d_p > d_{\text{right}}$. For other curves the limits slightly differ from the cited values. Note that one expects lesser reliability for experimental results for both the left and right tails of the distributions due to lack of statistics and resolution of the experimental method. In particular, only pores with diameters larger than about 0.5 μm were considered in the pore volume analysis [11].

Table 2 presents the total area below each curve (i.e., the total swelling) as well the effective mean pore radius $\overline{R}_p \equiv d_0 10^{<\lg d_p / d_0>} / 2$.

Table 2. Total swelling and mean pore radius for the distributions of [11]

Location	Total swelling, %	$\overline{R}_p$, μm
Fresh fuel (lower limit)	4.3	0.61
Fresh fuel (upper limit)	7.0	0.65
Irradiation 23 GWd/t, central zone	2.3	0.69
Irradiation 23 GWd/t, rim zone	2.6	0.69

As seen, the fuel densification due to irradiation is almost the same over the pellet corresponding to the decrease of the total pore volume by a factor of 2-3. It is also worth noting that the mean pore diameter before (especially for the upper limit) and after irradiation is almost the same within the uncertainty interval for the average pore size for the fresh fuel.

If p_c is the distribution of the pore concentrations, so that $p_c(R_p)dR_p$ is the concentration of pores with the radius from R_p to $R_p + dR_p$, then the above introduced distribution $p_s(R_p)$ is derived as

$$p_s\left(R_p\right) = \frac{4\pi R_p^4}{3\ln 10} p_c\left(R_p\right). \qquad (41)$$

Using this equation and the above data on p_s one evaluates the pore concentration distribution, which is plotted in Fig. 5. The shaded area represents the range that is definitely beyond the experimental observation.

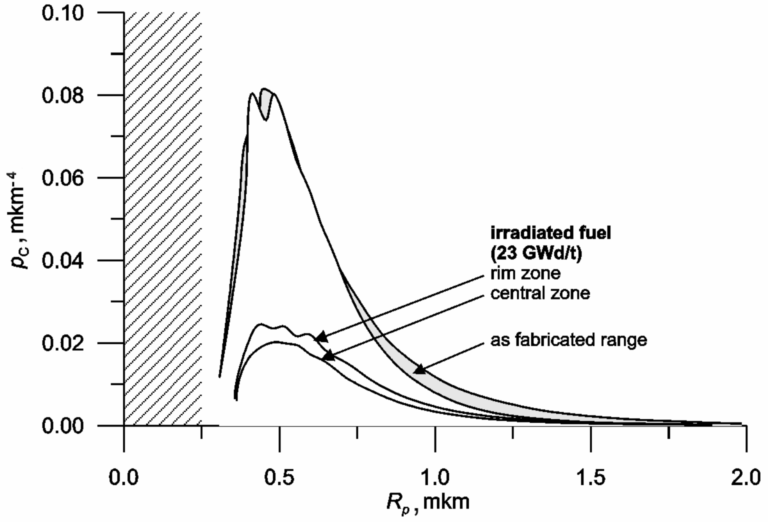

Fig. 5. Pore concentration distribution

As seen, the curves have the sharp maximum and long tails. However, as discussed above, 90 % of the total porosity corresponds to inequality $R_p > d_{\text{left}}/2 \approx 0.5\ \mu\text{m}$, the distributions being monotonic within that range. The peculiarities of pore size distribution are summarized in Table 3 where the contributions are given of different pores sizes to the total number of pores (per one grain with radius 5 μm) and swelling.

Table 3. Pore size distribution of swelling (nominator, %) and number of pores per one grain (denominator) for Assmann experiment

	Pore radius range, μm			
Location	0-0.5	0.5-1.0	1-2	2-4
Fresh fuel (lower limit)	0.4/11.5	2.3/17.6	1.4/1.8	0.3/0.1
Fresh fuel (upper limit)	0.4/12.2	2.5/18.7	3.2/3.6	0.4/0.1
Irradiated (23 GWd/t), central zone	0.1/2.4	0.8/5.8	0.8/0.9	0.6/0.1
Irradiated (23 GWd/t), rim zone	0.1/3.0	1.0/7.2	1.1/1.3	0.4/0.1

In accordance with the above conclusions, it is seen from the table, that the first interval contributes significantly the total number of pores but insignificantly to the total swelling. Indeed, 25-40 % of all the pores have radii less than 0.5 μm, however in this range the data are unreliable. In any case this range contributes negligibly to the swelling (less than several per cent of its value). Considering only pores with $R_p > 0.5\ \mu\text{m}$ one concludes that the range 0.5–1.0 μm represents 85–90 % of the large pores. Therefore, the overwhelming majority of pores are much less than the typical fuel grains. On the other hand, one finds in average one pore with $R_p \sim R_{gr}$ per a dozen grains.

3.2. Models for pore distribution

Turning back to Fig. 5, it worth noting that all the curves are similar to each other. This is explicitly illustrated by Fig. 6, in which the distributions are plotted in the logarithmic scale. It is seen that within the interval $R_{\rm left} \approx 0.5 < R_p < R_{\rm right} \approx 2$ μm (which dominantly contributes to the swelling) the $\lg p_c$ almost linearly depend on R_p implying the exponential decay of the distribution p_c with the size.

Moreover, the curves for irradiated fuel and for the fresh fuel (upper limit) are almost parallel[2]. This is in complete agreement with theoretical consideration of pore size evolution presented in the next section according to which the distribution function is translated with time leftward along the R-axis. As for the region $R_p < R_{\rm left}$, the abrupt dip of the curve seems to be related to low experimental resolution.

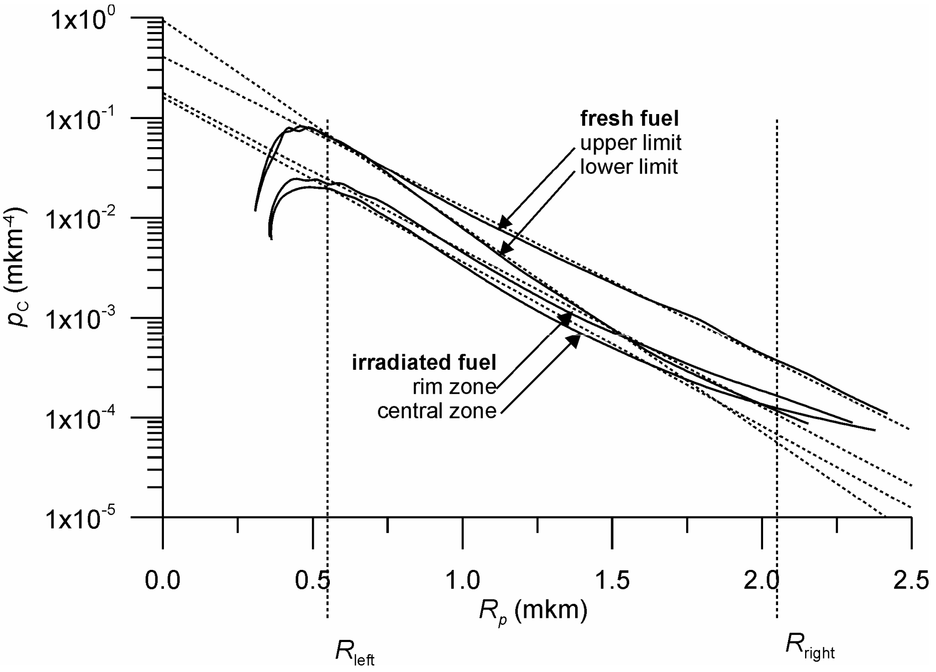

Fig. 6. Pore concentration distribution (logarithmic scale)

The simplest model taking into account the peculiarities of experimental distributions can be formulated in form

$$p_c(R_p) = \begin{cases} 0, & R_p < R_{\rm cutoff}, \\ \dfrac{c_0}{R_0} e^{-R_p/R_0}, & R_p \ge R_{\rm cutoff}, \end{cases} \qquad (42)$$

where c_0 and R_0 are the fitting parameters and $R_{\rm cutoff}$ is the arbitrary cut-off radius that can be chosen from 0 to $R_{\rm left}$ in accordance with the above mentioned uncertainty of experimental data for small pores. However, note that although the variation of $R_{\rm cutoff}$ within the cited range results in essential uncertainty in pore concentration, the contribution to the total fuel swelling is less than 10 % (cf. Table 3).

Distribution Eq. (42) is normalized to the total concentration of the pores:

$$C_p = \int p_c(R)dR = c_0 e^{-x}, \qquad (43)$$

where $x = R_{\rm cutoff} / R_0$. Mean pore radius $<R_p>$, volume $<V_p>$ and fuel swelling s_p can be calculated as

---

[2] As for the curve representing the lower bound for the fresh fuel, it seems to be out of general tendency and will be excluded from further consideration.

$$
\begin{gathered}
< R_p >= R_0\left(1+x\right), \\
< V_p >= 8\pi R_0^3\left(1+x+\frac{1}{2}x^2+\frac{1}{6}x^3\right), \\
s_p =< V_p > C_p = 8\pi R_0^3 c_0 e^{-x}\left(1+x+\frac{1}{2}x^2+\frac{1}{6}x^3\right).
\end{gathered}
\tag{44}
$$

Fitting parameters, c_0 and R_0, of Eq. (42) can be found identifying the calculated C_p and $<R_p>$ with the corresponding data followed from experiment. Table 4 presents the parameters calculated by approximation the experimental curves for p_c within the interval $0.5 < R_p < 2$ μm. Two limiting cases are considered: $R_{\text{cutoff}} = 0$ and $R_{\text{cutoff}} = 0.5$ μm. The calculated mean values of pore radius ($<R_p>$) and the fuel swelling ($<s_p>$) are also given in the table.

Table 4. The mean values of pore radius calculated with distribution p_c for Assmann experiment

Fuel sample	c_0 (μm^{-3})	R_0 (μm)	$R_{\text{cutoff}} = 0$		$R_{\text{cutoff}} = 0.5$ μm	
			$<R_p>$ (μm)	s_p (%)	$<R_p>$ (μm)	s_p (%)
Fresh (upper limit)	0.118	0.29	0.29	7.3	0.79	6.6
Irradiated, central zone	0.042	0.26	0.26	2.0	0.76	1.7
Irradiated, rim zone	0.049	0.28	0.28	2.6	0.78	2.3

It is seen that experimental mean radii are between predictions of the limiting cases (cf. with Table 2). For different specimen locations and irradiations, the mean radii are rather close to each other, in agreement with the above conclusion. As expected, in accordance with Eq. (44), $<R_p>$ is essentially greater for the choice $R_{\text{cutoff}} = 0.5$ μm than for $R_{\text{cutoff}} = 0$. Nevertheless, both the models predict the fuel swelling in reasonable agreement with the underlying experimental data presented in Table 2.

3.3. Evolution of pore distribution

As has been shown in Section 2.5.3 the approximate solution for the pore radius can be written in the closed form as

$$R_p(t) = R_p(0) - vt, \tag{45}$$

with the effective velocity v defined as

$$v = L\bar{g}\left(t\right), \tag{46}$$

where

$$L \equiv 2\lambda\eta \tag{47}$$

is the length factor and $\bar{g}(t)$ is the average burn-up rate per one UO$_2$ molecule:

$$\bar{g}\left(t\right) \equiv \frac{\Omega}{t}\int_0^t G(\tau)d\tau. \tag{48}$$

Applying Eq. (45) to an individual pore one concludes that the change of the pore radius is determined only by the total number of fissions per unit volume and do not depend on the initial pore size. In particularly, this means that the evolution of the pore size distribution is the parallel translation along the time axis as schematically illustrated in Fig. 7 by example of above introduced model with two limiting values of parameter R_{cutoff}.

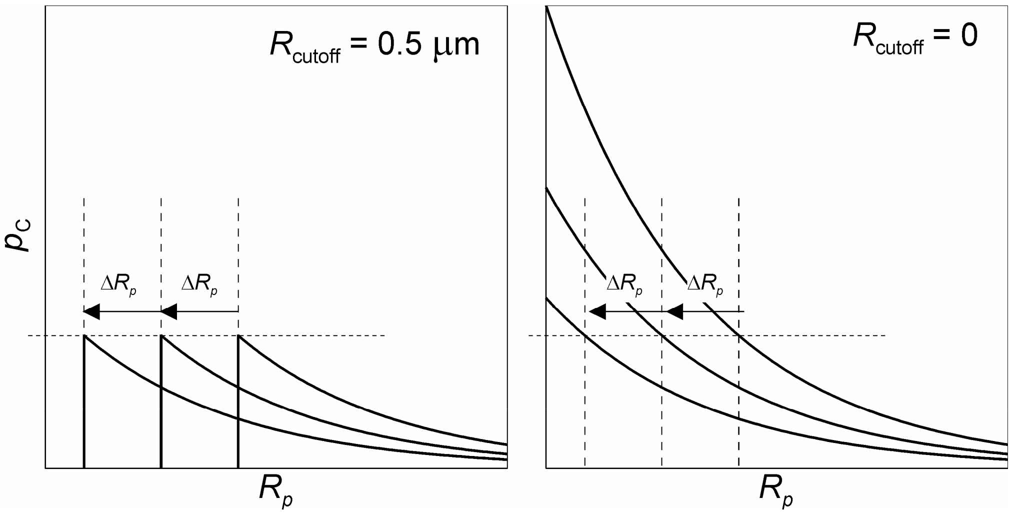

Fig. 7. Time dependence of pore distribution by example of model Eq. (42)

This result is in a perfect agreement with experimental data demonstrating the translation shifts of the distributions along ordinate axis, cf. Fig. 6.

It can be easily shown that the time-dependent distribution of pore concentration can be written as

$$p_c(R,t)=\frac{c_0}{R_0}\exp\left(-vt\right)\begin{cases}0, & R<R_{\text{cutoff}}(t),\\ \exp\left(-R/R_0\right), & R\geq R_{\text{cutoff}}(t),\end{cases} \tag{49}$$

where

$$R_{\text{cutoff}}(t)=\max\left(0,R_{\text{cutoff}}-vt\right). \tag{50}$$

The time dependence of the total pore concentration is written as

$$C_p(t)=\int_0^\infty p_c(R,t)dR=c_0\mathrm{e}^{-\max(vt,R_{\text{cutoff}})/R_0}=C_p\left(0\right)\begin{cases}1, & vt<R_{\text{cutoff}},\\ \mathrm{e}^{-\left(vt-R_{\text{cutoff}}\right)/R_0}, & vt\geq R_{\text{cutoff}}.\end{cases} \tag{51}$$

Equations (43) and (44) are also valid for time-dependent distribution with the substitution:

$$x(t)=\frac{\max\left(0,R_{\text{cutoff}}-vt\right)}{R_0}. \tag{52}$$

In particular, the fuel swelling is calculated as

$$s_p=8\pi R_0^3c_0\mathrm{e}^{-\max\left(vt,R_{\text{cutoff}}\right)/R_0}\left(1+x+\frac{1}{2}x^2+\frac{1}{6}x^3\right). \tag{53}$$

In the case of the $R_{\min}=0$ these equations reduce to

$$\begin{aligned}&C_p\left(t\right)=C_p\left(0\right)\mathrm{e}^{-vt}=c_0\mathrm{e}^{-vt},\\ &R_p\left(t\right)=R_0,\\ &s_p\left(t\right)=8\pi R_0^3c_0\mathrm{e}^{-vt}.\end{aligned} \tag{54}$$

Note that Eqs. (45) — (47) can be used to tune the length factor $L = \lambda\eta$ fitting the experimentally observed densification. From data of Table 3 one estimates that $L \approx 10.7\ \mu\text{m}$. In particular, under conditions of Assmann's test Eq. (50) applied to R_{cutoff} is written as

$$R_{\text{cutoff}}(t) = \max\left(0,\ 0.5 - 0.0118b\right), \qquad (54)$$

the burn-up b and radii being expressed in GWd/t and μm, respectively. This equation demonstrates that R_{cutoff} and therefore all other mean values are time-dependent, provided burn-up is less than the critical value:

$$b_{\text{crit}} \approx 42\ \text{GWd/t}. \qquad (55)$$

After that the mean radius holds constant whereas the total concentration and swelling decay exponentially.

The calculated dependencies of the pore mean radius and fuel swelling due to pores are plotted in Fig. 8. As seen, there are some differences in initial coverage and swelling between the two limiting choices of the cut-off radius that quickly approaches zero with time demonstrating contiguity of both the models in description of the integral pore properties. This demonstrates that both the models are close to each other so the choice can be made basing on conditions of numerical convenience.

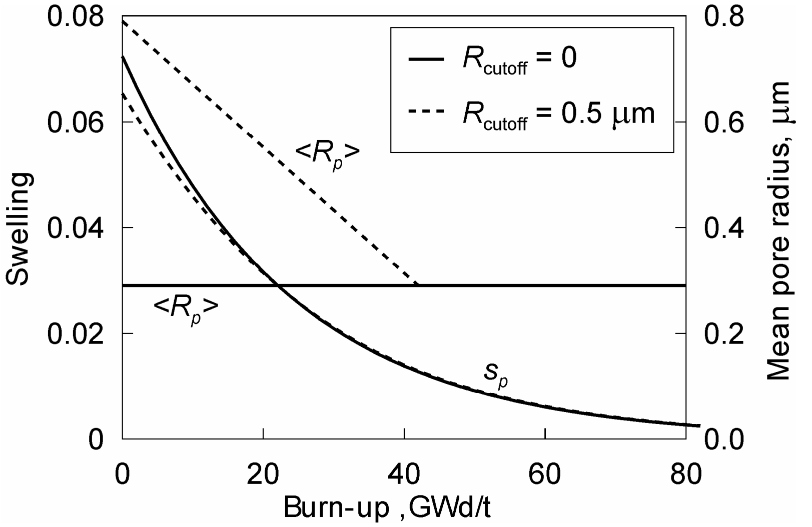

Fig. 8. Time dependence of the mean pore radius and fuel swelling due to pores calculated with two limiting values of the cut-off radius

Conclusions

Analytical examination has been performed of the MFPR model of evolution of as-fabricated pores under irradiation conditions taking into consideration pore size distribution. It was shown that the quasi-stationary treatment of vacancy-interstitial sub-system is valid under a wide range of conditions. This allows radical simplifying the numerical realization of the model. Moreover, the approximate solution has been derived in the closed form of the equation for the pore radius, which further increases the efficiency of numerical scheme. Available experimental data on pore size distribution indicate that it can be approximated by distribution of exponential type. In the lack of the data the ambiguity still remains describing the distribution of smallest pores resulting in essential uncertainty in simulation of the pore concentration in that range. Fortunately, small pores make only minor contribution to the total fuel swelling that can be reliably estimated in the framework of the suggested model.

References

1. *Whapham A.D., Sheldon B.E.* Electron Microscope Observations of the Fission-Gas Bubble Distribution in UO_2. United Kingdom Atomic Energy Authority, Harwell (England). Technical Report AERE-R-4970. 1965.
2. *Whapham A.D., Sheldon B.E.* // Nucl. Appl. 1966. Vol. 2. P. 123.
3. *MacEwen S.R., Hastings I.J.* // Phil. Mag. 1975. Vol. 31. P. 35.
4. *Brailsford A.D., Bullough R.* // Philos. Trans. Royal. Soc. 1981. Vol. A 302. P. 7.
5. *Dollins C.C., Nichols F.A.* // J. Nucl. Mater. 1978. Vol. 78. P. 326.
6. *Veshchunov M.S.* et. al. Development of the mechanistic code MFPR for modelling fission-product release from irradiated UO_2 fuel // Nucl. Engineering and Design. 2006. Vol. 236. P. 79–200.
7. *Noirot J.* et al. Fission gas inventory in PWR high burn up fuel: experimental characterization and modeling // 2004 Intern. Meeting on LWR Fuel Performance (Orlando, Florida, USA; September 19–22, 2004). 2004.
8. *Matzke H.* // Adv. Ceram. 1986. Vol. 17. P. 1.
9. *Shestak V.E., Tarasov V.I., Veshchunov M.S.* Modeling of defect structure evolution in irradiated UO_2 fuel in framework of MFPR code. (Preprint / Nuclear Safety Institute (IBRAE) RAS, no IBRAE-2002-02). Moscow: NSI (IBRAE) RAS, 2002.
10. *Degaltzev Yu.G., Ponomarev-Stepnoj N.N., Kuznetzov V.F.* Behaviour of high-temperature nuclear fuel under irradiation. Moscow: Energoatomizdat, 1987. (in Russian).
11. *Assmann H., Manzel R.* // J. Nucl. Mater. 1977. Vol. 68. P. 60–364.

Model for Grain-Face Bubbles Coalescence in Irradiated UO$_2$ Fuel

M.S. Veshchunov

Introduction

Kinetics of intergranular bubbles development is the key determination of the fission products release from irradiated UO$_2$ fuel and fuel pellets swelling. For this reason, many experimental investigations of bubbles growth and coalescence have been carried out, that allowed better understanding of these phenomena. However, there is still no general agreement what mechanisms are responsible for observed coalescence of intergranular bubbles during their growth under various conditions (steady irradiation, annealing or transient).

Zacharie et al., on the base of their tests [1] performed with pre-irradiated UO$_2$ fuel under high temperature annealing conditions, assumed that during heat treatment grain-face bubbles became mobile, migrated at random on grain surface and coalesced. Their model was later improved by Berdyshev and the author [2] (see also [3]) using the general theory of Krivoglaz [4] for bubbles coalescence by random migration on two-dimensional surfaces. However, in both models [1] and [2] the effective bubble mobility evaluated by fitting model calculations to measurements [1] turned to be several orders of magnitude higher in comparison with available data.

In a recent paper [5] White analysed an extensive set of experimental data on intergranular porosity development in various tests and proposed a new mechanism for intergranular bubbles coalescence based on consideration of the (immobile) nearest neighbours growth and overlapping in a random two-dimensional distribution of bubbles. This mechanism allowed a reasonable prediction of the critical grain-face coverage of ≈ 19 % at which the onset of bubble coalescence occurs, however, further progression of bubbles coalescence by the proposed mechanism was strongly overestimated.

The mechanism considered by White will be critically analysed and improved in the current paper, and then compared with the other coalescence mechanism proposed by Zacharie et al. [1]. It will be shown that depending on test conditions, each of these mechanisms can determine kinetics of intergranular bubbles coalescence during their growth and migration.

On the base of analysis of available experimental data, a new general model self-consistently considering both mechanisms will be finally formulated.

1. Coalescence by growth of randomly distributed bubbles

1.1. Model formulation

As proposed by White [5], the onset of the intergranular bubbles coalescence may be understood on the basis of a simple argument adapted to the two-dimensional case from the work of Chandrasekhar [6] who calculated the distribution of nearest neighbours in a random three-dimensional array of particles. For calculation of further bubbles progression, a more general kinetic model for the bubbles coalescence in the three-dimensional case with consideration of a real bubble size distribution function evolution developed by Mansur et al.

[7, 8], was adapted to the two-dimensional case in the mean-field approximation (with a mono-modal bubble size distribution function) [5].

Following this approach, it is assumed that fission gas atoms diffuse to the grain boundaries and are rapidly absorbed into the bubble nuclei randomly distributed over the surface. In the mean field approximation for the face bubbles with the mean circular projection radius $R(t)$ and the area $A = \pi R^2$, each bubble will be surrounded by a circle with the radius $2R$, in which no other bubble centres can reside. Any bubble centre located in this exclusion zone would find its perimeter within the perimeter of the parent bubble and coalescence would occur. Any further growth of the mean projected area of bubbles by an amount $dA = 2\pi R dR$, effectively increases the area of the exclusion zone by $4dA$ and opens the possibility that $4NdA$ bubbles may be swept out by the parent bubble.

In that event the bubble perimeters will interact and coalescence occurs. Considering each bubble in turn, the total rate of loss of bubbles by coalescence following an increase in area is given by

$$dN = -2N^2 dA$$

or

$$\frac{dN}{dt} = -2N^2 \frac{dA}{dt}, \qquad (1)$$

where the factor of 4 is reduced to 2 to avoid counting each interaction twice.

The obtained in [5] Eq. (1) correctly describes a smooth growth of a bubble (by diffusion sinking of gas atoms) up to the moment of its coalescence with a neighbour, however, it does not take into consideration an abrupt jump of its size owing to coalescence. After averaging over distribution of bubbles, such jumps will disappear, however, effectively will enhance the mean bubble size growth rate.

In the mean field approximation such averaging procedure can be performed in the following way. At first, in the lack of the bubbles diffusion growth, one can notice that variation of the total occupied grain boundary area (coverage) due to bubbles coalescence (by any mechanism) is zero, $d\left(N\bar{A}\right)/dt = 0$, where $\bar{A}$ is the bubbles averaged projection area. This reflects the mass conservation law for gas atoms (obeying the ideal gas state equation, if $R \geq 5\,\text{nm}$) in equilibrium bubbles in the course of their coalescence (see Section 2.1). Therefore, the coverage can increase only owing to bubbles diffusion growth.

Indeed, in the case of non-zero bubbles diffusion growth, the mass conservation law takes the form

$$\frac{d\left(N\bar{A}\right)}{dt} = N\frac{\partial \bar{A}}{\partial t}, \qquad (2)$$

where

$$\frac{d\left(N\bar{A}\right)}{dt} = N\frac{d\bar{A}}{dt} + \bar{A}\frac{dN}{dt}. \qquad (3)$$

Here $\partial\bar{A}/\partial t$ denotes variation of the bubbles mean projection area owing solely to bubbles diffusion growth (considered in derivation of Eq. (1)), whereas $d\bar{A}/dt$ denotes total variation of the bubble mean area owing to bubbles growth and coalescence. In this new notation Eq. (1) takes the form

$$\frac{dN}{dt} = -2N^2\frac{\partial \bar{A}}{\partial t}. \qquad (4)$$

Substituting Eqs. (2) and (4) in Eq. (3), one obtains

$$\frac{d\bar{A}}{dt} = \left(1 + 2N\bar{A}\right)\frac{\partial \bar{A}}{\partial t}. \qquad (5)$$

Superposition of Eqs. (4) and (5) yields

$$\frac{dN}{d\bar{A}} = -\frac{2N^2}{1 + 2N\bar{A}}. \qquad (6)$$

This consideration is not valid at high coverage $S = N\bar{A}$, when probability of multiple coalescence among three and more bubbles becomes non-negligible leading to formation of interconnected bubbles chains. It is conventionally assumed that the onset of gas release through bubble interconnection commences after attainment of the saturation value $S^* \approx 0.5$. After this the total amount of gas atoms in the bubbles is not anymore conserved, so, Eq. (2) is not anymore valid. In this stage the bubbles coalescence obeys the saturation coverage condition:

$$N\bar{A} = 0.5 \qquad (7)$$

or

$$\frac{d\left(N\bar{A}\right)}{dt} = N\frac{d\bar{A}}{dt} + \bar{A}\frac{dN}{dt} = 0, \quad (7')$$

instead of Eq. (6), since the diffusion flux $J_{\text{dif}}\left(t\right)$ flux from the grain bulk to the grain boundaries is completely transferred into open porosity via interconnected face bubbles (see Section 3).

1.2. Model solution

An explicit solution of Eq. (6) can be searched in the following way. Substitution of Eq. (5) into Eq. (2) yields

$$\frac{d\left(N\bar{A}\right)}{dt} = \frac{N}{1+2N\bar{A}}\frac{d\bar{A}}{dt}$$

or

$$\frac{d\left(N\bar{A}\right)}{d\bar{A}} = \frac{N}{1+2N\bar{A}} = \frac{1}{\bar{A}}\frac{N\bar{A}}{1+2N\bar{A}},$$

or

$$\frac{d\left(N\bar{A}\right)}{d\left(\ln\bar{A}\right)} = \frac{N\bar{A}}{1+2N\bar{A}}. \quad (8)$$

Solution of Eq. (8) has the form

$$N\bar{A} = N_0\bar{A}_0 + \frac{1}{2}\ln\frac{N_0}{N} \quad (9)$$

or

$$N = N_0\exp\left(-2\left(N\bar{A} - N_0\bar{A}_0\right)\right). \quad (10)$$

This implies that variation of N_0/N is much slower than predicted by Eq. (1). Indeed, analysis of Eq. (10) shows that in the case $N_0\bar{A}_0 \to 0$, N_0/N varies from 1 (when $N\bar{A} = N_0\bar{A}_0$) to $e^2 \approx 7.4$ (when formally $N\bar{A} \to 1$); the saturation value $N\bar{A} = 0.5$ is attained at $N_0/N = e \approx 2.7$, whereas Eq. (1) erroneously predicts variation of N_0/N within several orders of magnitude, as shown in Fig. 6 of [5].

Therefore, coalescence by the proposed mechanism is not strong and provides only ≈ 3-fold reduction of the bubbles surface concentration N before attainment of the saturation coverage. In this situation, an enhanced face bubbles coalescence observed under normal irradiation conditions [9] and characterised by 1–2 orders of magnitude reduction of *N*, may be explained by another mechanism considered in Section 2.

On the other hand, as above explained, after attainment of the saturation coverage ≈ 0.5, Eq. (9) is not anymore valid. During the saturation stage the variation of N becomes significantly steeper, as seen from Eq. (7):

$$N = 0.5\bar{A}^{-1}. \quad (11)$$

This case will be considered in Section 3.

2. Bubbles coalescence by random migration

2.1. Model formulation

In order to explain the observed kinetics of grain-face swelling under annealing conditions, Zacharie et al. [1] assumed that during heat treatment face bubbles became mobile and migrated at random on grain surface, and then coalesced. The theory of coalescence of bubbles in a two-dimensional array based on the analysis of the bubble size distribution function evolution was developed by Krivoglaz [4]. Apparently lacking these theoretical results, the authors [1] attempted their own approach to the same problem. Despite that their new calculations were rather cumbersome, Zacharie et al. managed to reproduce the main kinetic dependencies of bubble concentration and size on time in a qualitative agreement with the general theory [4]. As a result, an explicit equation for intergranular swelling as a function of treatment time and temperature was derived in their work. This equation provided a good description of the measured swelling values after fitting of the main model parameter (bubble diffusivity).

In the subsequent paper of Berdyshev and the author [2] the general theory [4] for the bubbles coalescence kinetics was adapted to the two-dimensional case in the mean-field approximation (with a mono-modal bubble size distribution function), and the main analytical results of [1] were deduced in a more straightforward and simple way (see also [3]). This allowed elimination of some inconsistencies in the approach of [1] and improvement of the model predictions.

However, in both models [1] and [2] the effective bubble diffusivity evaluated by fitting of the model predictions to the experimental data [1] turned to be several orders of magnitude higher in comparison with the conventional data for the bubble diffusivity.

Indeed, the diffusion coefficient D_b determined by the surface diffusion mechanism (apparently the most rapid and thus rate determining for UO$_2$) of spherical intragranular bubble migration was evaluated by Shewmon [10] as $D_b = 3D_s\Omega^{4/3}/2\pi R_b^4$, where D_s is the surface self-diffusion coefficient, R_b is the bubble radius, $\Omega \approx 4.1\cdot 10^{-29}\,\mathrm{m}^3$ is the atomic volume. For lenticular grain face bubbles with the semi-dihedral angle $\theta \approx 50°$ and the projection radius $\rho_b = R_b \sin\theta$ the bubble diffusivity depends on the migration direction. In the case of migration in the direction of the grain boundary relocation (perpendicular to the grain boundary), the bubble diffusivity was recently calculated by the author as

$$D_b = \left(3D_s\Omega^{4/3}/2\pi\rho_b^4\right)\cdot \sin^4\theta \big/ \left(1-\cos^3\theta\right) \approx$$
$$\approx 3D_s\Omega^{4/3}/4\pi\rho_b^4$$

[11]. A similar calculation for bubble migration along the surface of the grain boundary yields

$$D_b = \frac{3D_s\Omega^{4/3}}{2\pi\rho_b^4}\sin\theta \approx 0.77\cdot\frac{3D_s\Omega^{4/3}}{2\pi\rho_b^4}. \quad (12)$$

The data for the surface diffusion coefficient obtained by mass transfer methods give the following relationship for the surface diffusion coefficient of uranium atoms [12]:

$$D_s\left[m^2/s\right] = 50\cdot\exp\left(-450000/RT\right), \quad (13)$$

with $1473 < T < 2073$ K and R in J·mol^{-1}·K^{-1}.

Despite the values of D_s from Eq. (13) have been estimated by Matzke [13] to be within an experimental scatter band of 2 orders of magnitude for the temperature range examined, they provided a very low mobility (by several orders of magnitude) of face bubbles in comparison with the mobility necessary for correct description of Zacharie's observations [1] by the proposed random migration mechanism (see [3]).

On the other hand, results of the tracer studies of Marlowe and Kazanoff [14] corrected by Olander [15] were confirmed by Zhou and Olander [16] giving much higher values for the surface diffusion coefficient D_s (e. g., 5 orders of magnitude higher than predicted by Eq. (13) at 1988 K) with a pre-exponential coefficient of $D_0 \sim 5\cdot 10^2$ m^2/s and an activation energy of 300 ± 60 kJ/mol. The latter value is in a rather good agreement with the value of 310 kJ/mol obtained by Zacharie et al. [1] for the activation energy of random migration of grain face bubbles. This value of the activation energy was also used in fitting calculations [2, 3] with the pre-exponential coefficient of $D_0 \sim 10^2$ m^2/s, however, with a somewhat slower dependence of the bubble diffusivity from the bubble projection radius, $\propto \rho_b^{-3.4}$, which is avoided in the current model formulation, Eq. (12).

For this reason, it is attempted to use for the surface diffusion coefficient D_s the following Arrhenius correlation, based on the evaluation [16] and consistent with the activation energy measurements in [1]

$$D_s\left[m^2/s\right] = D_0\cdot\exp\left(-\frac{Q}{RT}\right) = 5\cdot 10^2\exp\left(-\frac{310000}{RT}\right) = 5\cdot 10^2\exp\left(-\frac{37286.5}{T}\right). \quad (14)$$

Nevertheless, one should keep in mind that the surface diffusivity from Eq. (14) is extremely high, e. g., at 1988 K $D_s \approx 3.6\cdot 10^{-6}$ m^2/s is comparable with the gaseous Xe self-diffusivity; therefore, rather exotic mechanisms have to be engaged to ground this option [15, 16]. Furthermore, mobility of small bubbles (with radius up to 10 nm) in UO$_2$

directly measured in various tests [17–19] is suitably described by the surface diffusion mechanism with the standard surface diffusivity from Eq. (13) [20], being therefore in remarkable contradiction with Eq. (14).

In the mean field approximation (considering only the mean bubble size) variation of the surface concentration of face bubbles N due to coalescence obeys the rate equation [2, 3]

$$\frac{dN}{dt} = -\omega_{cls} N^2 . \qquad (15)$$

The coalescence frequency of bubbles randomly moving on a surface can be represented by the formula derived in [4]

$$\omega_{cls} = \frac{8\pi D_b}{\ln\left(D_b \tau_0 / 2\rho_b^2\right)} \approx 8\pi\alpha D_b , \qquad (16)$$

which is valid with the logarithmic accuracy under condition $\left|\ln S\right| >> 1$, where $S = AN = \rho_b^2 / R_c^2$ is the surface coverage, $R_c \approx \left(\pi N\right)^{-1/2}$ is the radius of the bubble sinking zone, τ_0 is the characteristic time of the two-fold increase of the mean bubble projection radius ρ_b, evaluated as $\tau_0 \approx R_c^2 / D_b$. Being a weak (logarithmic) function of its argument, the parameter $\alpha \approx \left|\ln S\right|^{-1}$ slowly varies from 0.15 to 0.4 at low coverage (from 0.001 to 0.1) and will be approximated by a constant value ≈ 0.2.

At first, the simplest case with invariable grain face coverage is considered:

$$N\overline{A} = N\pi\rho_b^2 = \text{const} = N_0\pi\rho_0^2 = N_0\overline{A}_0 , \qquad (17)$$

where N_0 and ρ_0 are the initial concentration and mean projection radius of bubbles at the moment t_0, respectively. For instance, this case is realised in the lack of the diffusion flux from the grain bulk to the grain boundaries.

A more realistic realisation of Eq. (17) appears after attainment of the saturation coverage $S^* \approx 0.5$, when the diffusion flux is completely compensated by the release flux into open porosity; however, in this case the condition $\left|\ln S\right| \approx \alpha^{-1} >> 1$ of applicability of Eq. (16) is not valid. This implies, in particular, that formal extension of the model to consideration of high-temperature annealing tests (in which the saturation coverage is sustained) is not completely reliable. Nevertheless, it will attempted below (in Section 2.2), in order to consider this situation approximately.

The system of Eqs. (12) and (15)–(17) results in the equation

$$\frac{dN}{N^4} = -\frac{12\alpha D_s \Omega^{4/3} \sin\theta}{N_0^2 \rho_0^4} dt \approx -\frac{9\alpha D_s \Omega^{4/3}}{N_0^2 \rho_0^4} dt , \qquad (18)$$

which has the solution:

$$\frac{N_0^3}{N^3} = 1 + \frac{27\alpha D_s \Omega^{4/3} N_0}{\rho_0^4}\left(t - t_0\right). \qquad (19)$$

This solution (valid under simplifying condition, Eq. (17)) corresponds to the considerations in the previous papers [1–3].

In a more general case, when the saturation coverage is not attained, Eq. (17) should be substituted by the mass balance equation:

$$\frac{d\left(N \cdot N_g\right)}{dt} = 2J_{\text{dif}} , \qquad (20)$$

where $J_{dif}\left(t\right)$ is the diffusion flux to a grain boundary from each of two neighbouring grains, N_g is the mean number of gas atoms in a face bubble. In neglect of the external pressure in comparison with the internal bubble pressure $P_b = 2\gamma \sin\theta / \rho_b$, it obeys the ideal gas state law (if ρ_b approximately ≥ 5 nm):

$$N_g = \frac{P_b V_b}{kT} = \frac{8\pi\gamma\rho_b^2}{3kT}\varphi\left(\theta\right), \qquad (21)$$

where

$$\varphi\left(\theta\right) = \left(1 - 1.5 \cdot \cos\theta + 0.5 \cdot \cos^3\theta\right)\sin^{-2}\theta \approx 0.29$$

for lenticular bubbles, $\gamma \approx 1$ J/m^2 is the surface tension [21].

Therefore, integrating Eq. (20) one obtains

$$N\rho_b^2 = N_0\rho_0^2 + f\left(t\right), \qquad (22)$$

where $f\left(t\right) = \frac{3kT}{4\pi\gamma\varphi\left(\theta\right)} \int_{t_0}^{t} J_{\text{dif}}\left(t\right) dt ,$

or, in accordance with Eq. (2):

$$N\frac{\partial \bar{A}}{\partial t}=\frac{3kT}{4\gamma\varphi(\theta)}J_{\mathrm{dif}}(t). \qquad (23)$$

After substitution of Eq. (22) in Eq. (15) one obtains the equation

$$\frac{dN}{N^4}=-\frac{9\alpha D_s\Omega^{4/3}}{N_0^2\rho_0^4}\left(1+\frac{f(t)}{N_0\rho_0^2}\right)^{-2}dt, \qquad (24)$$

which has the solution:

$$\frac{N_0^3}{N^3}=1+\frac{27\alpha D_s N_0\Omega^{4/3}}{\rho_0^4}\int_{t_0}^{t}\left(1+\frac{f(t)}{N_0\rho_0^2}\right)^{-2}dt. \qquad (25)$$

2.2. Analysis of experiments

Microscopic behaviour of intergranular bubbles under steady irradiation conditions was observed by Kashibe and Une [9]. The specimens were taken from UO_2 pellets irradiated in commercial BWR (burn-up: 6–28 GWd/t) at a point between the fuel rim and middle. Grain face bubble concentration and fractional coverage were examined by scanning electron microscope fractography. In addition, radii of face bubbles were also evaluated. The irradiation temperature at the location of the specimens may be evaluated as ~ 1500 K from their maximum linear heat generation rates (between 300 and 370 W/cm). The grain sizes of the fuel and irradiation rate were approximately equal to 9 μm and $1.8\cdot10^{19}$ m^{-3}s^{-1}, respectively. During irradiation the concentration of the intergranular bubbles at first increased owing to bubbles nucleation from $\sim 1.6\cdot10^{13}$ m^{-2} (at burn-up ~16 GWd/t) to $\sim 4\cdot10^{13}$ m^{-2} (at burn-up ~ 23 GWd/t) and then dropped to $\sim 1.6\cdot10^{12}$ m^{-2} (at burn-up ~ 28 GWd/t). The mean bubble projection radius increased from ~ 20 nm at 23 GWd/t to ~ 110 nm at 28 GWd/t, and fractional coverage correspondingly increased from ~ 5 % to ~ 10 %. Therefore, one can conclude that the bubbles coalescence prevailed over generation of new bubbles on grain faces in the late stage of irradiation (from 23 to 28 GWd/t). This is in a qualitative agreement with the assumption of White [5] that, once coalescence of face bubbles occurs, the geometric size of the initial population would tend to absorb any newly nucleated bubbles giving the effect that the nucleation was a one-off process.

In order to simulate the bubbles coalescence during irradiation period between 23 and 28 GWd/t, the following parameters of Eq. (22) are chosen in accordance with the above presented experimental data:

$$t_0\approx 6\cdot10^7\text{ s},\ t_f\approx 7\cdot10^7\text{ s and } f(t_f)\approx N_0\rho_0^2,$$

$$\text{since } N(t_f)\rho_b^2(t_f)\approx 2N_0\rho_0^2.$$

Owing to monotonic growth of the function $f(t)$, one can evaluate for this case:

$$\frac{\Delta t}{4}<\int_{t_0}^{t_f}\left(1+\frac{f(t)}{N_0\rho_0^2}\right)^{-2}dt<\Delta t, \qquad (26)$$

where $\Delta t=t_f-t_0$. Therefore, from Eq. (25) one obtains

$$1+\frac{27\alpha D_s\Omega^{4/3}N_0}{4\rho_0^4}\Delta t<\frac{N_0^3}{N^3}<1+\frac{27\alpha D_s\Omega^{4/3}N_0}{\rho_0^4}\Delta t \qquad (27)$$

or

$$\left(1+\frac{27\alpha D_s\Omega^{4/3}N_0}{4\rho_0^4}\Delta t\right)^{1/3}<\frac{N_0}{N}<\left(1+\frac{27\alpha D_s\Omega^{4/3}N_0}{\rho_0^4}\Delta t\right)^{1/3}. \qquad (28)$$

For the test conditions ($T\approx 1500$ K, $N_0\approx 4\cdot10^{13}$ m^{-2}), Eqs. (28) and (14) yields $60<N_0/N<10^2$, or $4\cdot10^{11}$ m^{-2} $<N<$ $6\cdot10^{11}$ m^{-2}, in a reasonable agreement with the measured value $N\approx 1.6\cdot10^{12}$ m^{-2}. Some underestimation of the final concentration might be connected with unaccounted new bubbles generation during the considered period, and/or with the above discussed uncertainty of the used correlation for the surface diffusivity, Eq. (14), as well as uncertainty in evaluation of the parameter α in Eq. (16).

Therefore, one can conclude that the coalescence mechanism might be effective in the steady irradiation tests [9], in which face bubbles were relatively small, $\rho_0 \leq 0.1$ μm.

However, under high-temperature annealing conditions when the mean bubble radius rapidly increases during heat-up stage and exceeds 0.1 μm, the bubbles mobility ($\propto \rho_b^{-4}$) decreases making this coalescence mechanism less effective.

Indeed, for the annealing tests [1] (described in more detail in the next Section 3) the model for bubbles coalescence by their random migration apparently underpredicts the coalescence rates measured at temperatures 1683–1988 K, even if the same correlation, Eq. (14), which provides a reasonable agreement with the steady irradiation tests, is used.

At high temperature 1988 K in the period from the initial moment $t_0 = 3 \cdot 10^2$ s to the final moment $t_f = 3.6 \cdot 10^4$ s the mean projected bubble radius ρ_b increased from ~ 0.3 μm to ~ 0.7 μm and the surface concentration of bubbles N decreased from ~ $1.7 \cdot 10^{12}$ m^{-2} to ~ $0.34 \cdot 10^{12}$ m^{-2}, the coverage being fairly constant ≈ 0.49–0.55 and rather close to the theoretical value of the saturation coverage 0.5. Application of Eq. (19) to the annealing test conditions results in a notable underestimation of the bubble coalescence, $N_0/N \approx 1.46$ and $\rho_b/\rho_0 \approx 1.21$, in comparison with the experimentally measured values ≈ 5 and 2.3, respectively.

The agreement with the measurements can be somewhat improved by formal extension of the parameter $\alpha \approx |\ln S|^{-1}$ (which should be <<1) from 0.2 (corresponding to low coverages) to 1. The best fit to experimental data can be obtained, however, only by multiplication of the surface diffusivity, Eq. (14), by an additional factor of 50, Fig. 1. This apparently brings the surface diffusivity value out of the physically grounded limits (see remarks presented after Eq. (14)).

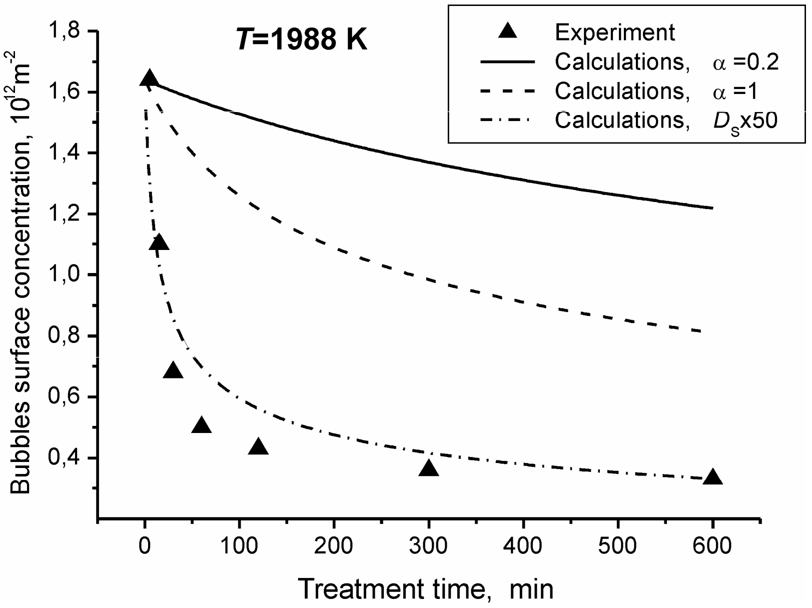

Fig. 1. Variation of the bubbles surface concentration with the treatment time at the annealing temperature 1988 K in the tests [1]. Comparison of measurements with calculations using the random migration mechanism for bubbles coalescence with two values of the model parameter α = 0.2 and 1, and with the surface diffusivity increased by a factor of 50

The model underestimation is also strong at lower temperatures, e.g., during annealing at 1818 K from $t_0 = 1.8\cdot10^3$ s to $t_f = 3.6\cdot10^4$ s (at almost constant coverage 0.48–0.56) the calculated values are $N_0/N \approx 1.2$ and $\rho_b/\rho_0 \approx 1.1$, whereas the experimentally measured values were ≈ 2.6 and 1.6, respectively. Similarly to the case of 1988 K, the best fit is attained only by multiplication of the surface diffusivity by a factor of 30, Fig. 2.

It is clear that application of a more widely used correlation for the surface diffusion coefficient, Eq. (13), instead of Eq. (14) will completely suppress the bubbles coalescence rate.

Therefore, the other coalescence mechanism by growth of randomly distributed bubbles (presented in Section 1) will be reconsidered for annealing conditions as a complementary approach. As mentioned in Section 1, being rather weak at low coverage, this mechanism becomes much more effective after attainment of the saturation coverage that is typical for the annealing conditions.

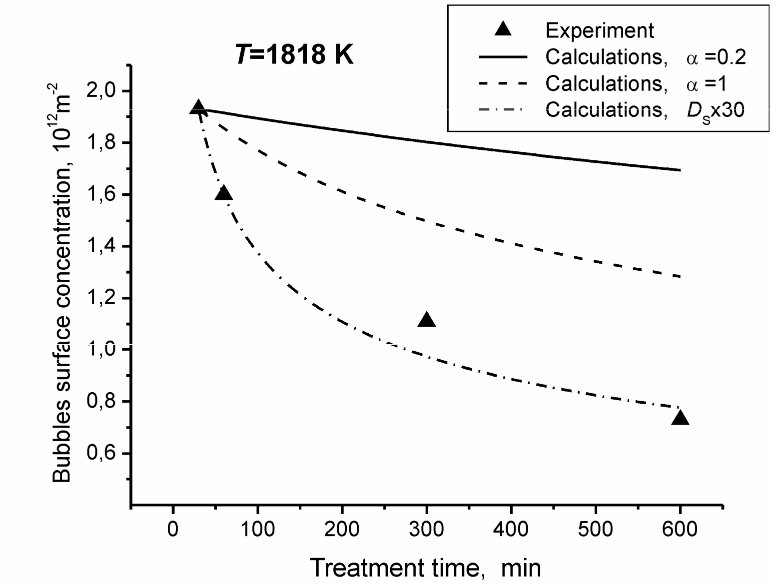

Fig. 2. Variation of the bubbles surface concentration with the treatment time at the annealing temperature 1818 K in the tests [1]. Comparison of measurements with calculations using the random migration mechanism for bubbles coalescence with two values of the model parameter α = 0.2 and 1, and with the surface diffusivity increased by a factor of 30

3. Bubbles coalescence at the saturation coverage

3.1. Model formulation

As above mentioned, consideration of the grain-face bubbles coalescence mechanism presented in Section 1 is valid until coverage attains the saturation value ≈ 0.5, i.e., $N\bar{A} \le 0.5$. In accordance with the percolation mechanism [22], after attainment of the saturation coverage manifested by face bubbles interkinkage and formation of channels (or bubble chains) on grain faces interconnected with open porosity (at grain edges), gas release (venting) from face bubbles through the channels commences.

Owing to gas venting (with the flux denoted as $J_{\mathrm{out}}(t)$), the chains collapse and disintegrate in a smaller amount of bubbles diminishing the mean surface concentration of bubbles with a rate denoted as $\partial N/\partial t$, thus reducing the grain face coverage (proportional to total amount of gas atoms in bubbles) below the saturation value.

Since face bubbles continue to grow owing to the diffusion flux from the grain bulk $2J_{\text{dif}}(t)$, the saturation coverage and bubbles interlinkage quickly reinstate and the processes of gas venting and bubble chains collapse repeat, and so on, keeping the mean coverage close to the saturation value, while the mean bubble size $\bar{A}(t)$ continuously increases (however, with a decreased rate).

In this case, instead of Eq. (2), which is not anymore valid because of gas venting, the mass balance equation in the mean field approximation takes the form

$$\frac{d(N\bar{A})}{dt} = N\frac{\partial\bar{A}}{\partial t} + \bar{A}\frac{\partial N}{\partial t}, \qquad (29)$$

and, instead of Eq. (23):

$$\begin{aligned} &N\frac{\partial\bar{A}}{\partial t} + \bar{A}\frac{\partial N}{\partial t} = \\ &= \frac{3kT}{8\gamma\varphi(\theta)}\left(2J_{\text{dif}} - J_{\text{out}}\right), \end{aligned} \qquad (29')$$

where, as before, $\partial\bar{A}/\partial t$ denotes the bubbles diffusion growth rate and $\partial N/\partial t$ denotes variation of the bubbles surface concentration owing to chains collapse (as above described).

In the simplest approach one can assume that the venting flux $J_{\text{out}}(t)$ is completely balanced by the rate of bubbles vanishing in the process of chains collapse, i. e., $J_{\text{out}} = -\left(3kT/8\gamma\varphi(\theta)\right)^{-1}\bar{A}\partial N/\partial t$. In this case, as results from Eq. (29), the diffusion growth of the bubble mean size is not violated and obeys Eq. (23) as before. However, as will be shown below, in this case the model significantly overestimates the bubbles coalescence rate.

More generally one should assume that only some part $\beta \le 1$ of the release flux corresponds to bubble vanishing, i. e., $\beta J_{\text{out}} = -\left(3kT/8\gamma\varphi(\theta)\right)^{-1}\bar{A}\partial N/\partial t$, whereas the other part $(1-\beta)$ of the flux reduces the size of non-vanished bubbles in the chains. In this case the diffusion growth rate of the bubble mean size $\bar{A}$ is also violated, i. e., $\left(3kT/8\gamma\varphi(\theta)\right)^{-1} N\partial\bar{A}/\partial t = 2J_{\text{dif}} - (1-\beta)J_{\text{out}}$, as can be deduced from Eq. (29').

On the other hand, in this stage bubbles coalescence additionally obeys the saturation coverage condition:

$$N\bar{A} = 0.5 \qquad (30)$$

or

$$\frac{d(N\bar{A})}{dt} = N\frac{d\bar{A}}{dt} + \bar{A}\frac{dN}{dt} = 0. \qquad (30')$$

Under condition of the invariable coverage, Eq. (30'), corresponding to conservation of the total amount of gas atoms in grain face bubbles (see Section 2.1), the diffusion flux $2J_{\text{dif}}(t)$ to the grain boundaries is completely transferred into open porosity via interconnected face bubbles and thus is compensated by the release flux $J_{\text{out}}(t)$, i. e., $2J_{\text{dif}}(t) = J_{\text{out}}(t)$. Therefore, the mass balance equation, Eq. (29), can be represented in the form:

$$\begin{aligned} &\frac{d(N\bar{A})}{dt} = N\frac{\partial\bar{A}}{\partial t} - \\ &- \beta\frac{3kT}{4\gamma\varphi(\theta)}J_{\text{dif}}(t) = 0, \end{aligned} \qquad (31)$$

instead of Eq. (23). The model parameter β effectively describes in the mean-field approximation a rather complicated process of gas venting and for this reason cannot be determined mechanistically in the current approach. Therefore, it will be determined below by fitting the model calculations to the experimental data.

The coalescence rate equation, Eq. (4), based on consideration of the couple coalescence with the nearest neighbours, at saturation coverage should be supplemented with an additional term describing the bubbles coalescence rate owing to channels formation and collapse, denoted above as $\partial N/\partial t$:

$$\frac{dN}{dt} = -2N^2\frac{\partial\bar{A}}{\partial t} + \frac{\partial N}{\partial t}. \qquad (32)$$

The system of equations, Eqs. (29)–(32), completely determines the evolution of face bubbles during coalescence at the critical coverage. Indeed, superposition of Eqs. (29), (30') and (32) yields

$$\frac{d\bar{A}}{dt} = \left(1 + 2N\bar{A}\right)\frac{\partial \bar{A}}{\partial t} = 2\frac{\partial \bar{A}}{\partial t}, \qquad (33)$$

and taking into account from Eqs. (30) and (30’) that

$$\frac{dN}{dt} = -2N^2\frac{d\bar{A}}{dt}, \qquad (34)$$

one obtains a relationship

$$\frac{dN}{dt} = -4N^2\frac{\partial \bar{A}}{\partial t}. \qquad (35)$$

Substitution of Eq. (31) in Eq. (35) finally results in a new coalescence rate equation:

$$\frac{dN}{N} = -\frac{3\beta kT}{\gamma\varphi(\theta)} J_{\mathrm{dif}}(t)\,dt, \qquad (36)$$

which has the solution

$$\ln\left(\frac{N}{N_0}\right) = -\frac{3\beta kT}{\gamma\varphi(\theta)} \int_{t_0}^{t} J_{\mathrm{dif}}(t)\,dt = -\frac{3\beta kT}{\gamma\varphi(\theta)} F(t), \qquad (37)$$

where $F(t) = \int_{t_0}^{t} J_{\mathrm{dif}}(t)\,dt$

or

$$\frac{N}{N_0} = \exp\left(-4\pi\beta f(t)\right) = \frac{\bar{A}_0}{\bar{A}}, \qquad (38)$$

where

$$f(t) = \frac{3kT}{4\pi\gamma\varphi(\theta)} F(t) = \frac{3kT}{4\pi\gamma\varphi(\theta)} \int_{t_0}^{t} J_{\mathrm{dif}}(t)\,dt.$$

Therefore, the concentration variation is characterised by a rather strong (exponential) dependence on gas release and thus can be significant under heat-up conditions of high-temperature annealing or transient tests.

3.2. Analysis of experiments

Detailed experimental study of the bubble growth and coalescence kinetics under annealing conditions was carried out in [1]. In these tests the intergranular swelling for similar base-irradiated samples, was measured at various annealing times along with observations of the grain face microstructure evolution. Unstressed samples of uranium dioxide taken from the pressurised water reactor fuel after two normal operating cycles, i. e., with burn-up of ~ 25 GWd/t, were subjected to thermal treatment in a laboratory furnace at temperatures between 1403 and 1988 K for duration between 5 min and 10 h. During irradiation stage fuel core temperature did not exceed 1373 K. The variation of the quantity of fission gas released over time was measured at each temperature. The samples were also subjected to a series of isothermal swelling measurements. Their comparison provides information on the intergranular, intragranular, open and closed porosity.

It is straightforward to evaluate from the test data that the saturation coverage ≈ 0.5 was attained very quickly, at least after $3\cdot10^2$ s at 1988 K, and then kept fairly constant. As indicated in Section 2.2, at high temperature 1988 K in the period from the initial moment $t_0 = 3\cdot10^2$ s to the final moment $t_f = 3.6\cdot10^4$ s the mean bubble projection radius ρ_b increased from ~ 0.32 μm to ~ 0.7 μm and the surface concentration of bubbles N reduced from ~ $1.7\cdot10^{12}$ m^{-2} to ~ $0.34\cdot10^{12}$ m^{-2}. During this period gas release, which is proportional to $F(t)$ (defined in Eq. (37)), varied from ≈ 10 to ≈ 30 % and thus made up ≈ 20 %. Taking into account that the fuel burnup was estimated in [1] as 25 GWd/t equivalent to the total fission gas atoms generation $\approx 1.6\cdot10^{26}$ m^{-3}, and the mean grain diameter as 9.3 μm, one can evaluate that $F(t)$ attained $\approx 0.5\cdot10^{20}$ m^{-2} in this test. Substituting these values in Eq. (38) and using the maximum value of the model parameter $\beta = 1$, one can find that at $t_f = 3.6\cdot10^4$ s reduction of the bubbles concentration is overestimated by one order of magnitude ($N_0/N \approx 36$ instead of ≈ 5). To avoid this strong overestimation, one should choose a smaller value of $\beta \approx 0.46$, see Fig. 3.

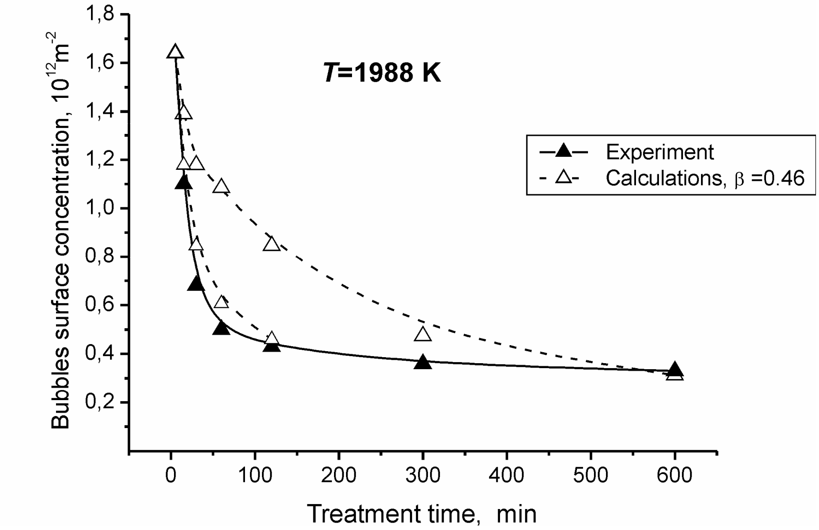

Fig. 3. Variation of the bubbles surface concentration with the treatment time at the annealing temperature 1988 K in the tests [1]. Comparison of calculations using the coalescence mechanism by growth of randomly distributed bubbles with the model parameter $\beta = 0.46$ against two sets of experimental data for gas release during coalescence at the critical coverage

At lower temperatures the agreement is also reasonable, for instance, at 1818 K in the interval from $t_0 = 3{\cdot}10^3$ s (when the coverage attained the saturation value) to $t_f = 3.6{\cdot}10^4$ s gas release was ≈ 6 %, therefore, $F(t)$ attained $\approx 0.15{\cdot}10^{20}$ m^{-2} in this test. In this case Eq. (38) with the same parameter $\beta = 0.46$ predicts decrease of the concentration $N_0/N \approx 1.6$ and increase of the mean bubble projection radius $\rho_b/\rho_0 \approx 1.3$, whereas the measured values were ≈ 2.6 and 1.6, respectively, Fig. 4.

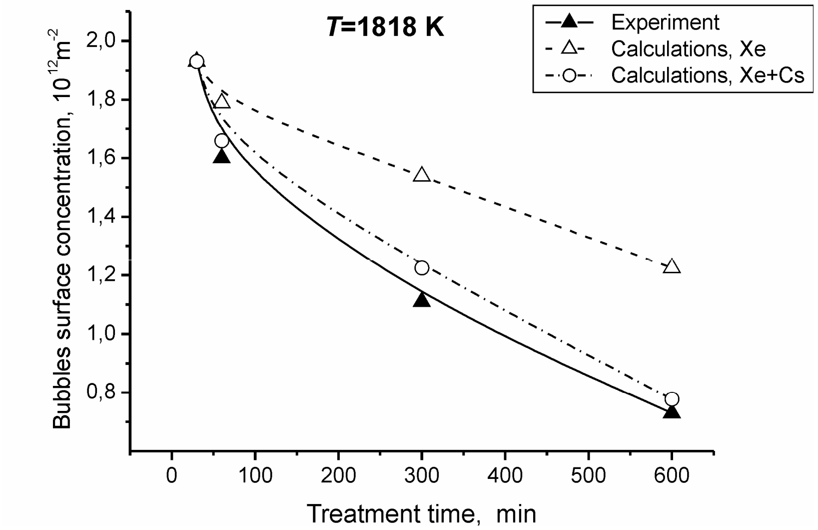

Fig. 4. Variation of the bubbles surface concentration with the treatment time at the annealing temperature 1818 K in the tests [1]. Comparison of measurements with calculations using the coalescence mechanism by growth of randomly distributed bubbles ($\beta = 0.46$) with and without consideration of Cs release during coalescence at the critical coverage

Further improvement of the model predictions can be obtained by additional consideration of evaporation of chemically active elements (mainly Cs) into bubbles at grain faces that can notably enhance the source term $J_{\text{out}}(t) = 2J_{\text{dif}}(t)$ at annealing temperatures (by adding the evaporation flux $J_{\text{evap}}(t)$, i. e., $2J_{\text{dif}}(t) \rightarrow 2J_{\text{dif}}(t) + J_{\text{evap}}(t)$) and thus increase $F(t)$ in Eqs. (37) and (38), resulting in the enhancement of the bubbles coalescence rate. This is illustrated in Fig. 4 by the second (dashed) calculated curve, where it is assumed $J_{\text{evap}}(t) \approx J_{\text{out}}(t)$, since normally in the annealing tests the Cs release is comparable with the gas release.

This model improvement (along with the final fitting of the parameter β) can be realised by adequate calculation of Cs release after implementation of the model in the MFPR code [3] designed for mechanistic calculation of fission products (FP) release with self-consistent consideration of FP chemical interactions and fuel microstructure evolution (see Section 4).

At temperature 1903 K a similar release ≈ 5–6 % occurred during a shorter annealing period from $3 \cdot 10^2$ s to $1.8 \cdot 10^4$ s. During this period variation of concentration predicted by the model with and without consideration of evaporation flux shows the same tendency as at 1818 K, see Fig. 5.

At the lowest test temperature 1683 K the concentration was measured only at two moments and the saturation coverage was not attained in the first measurement point ($S \leq 0.4$); for this reason, calculation of this test was not attempted.

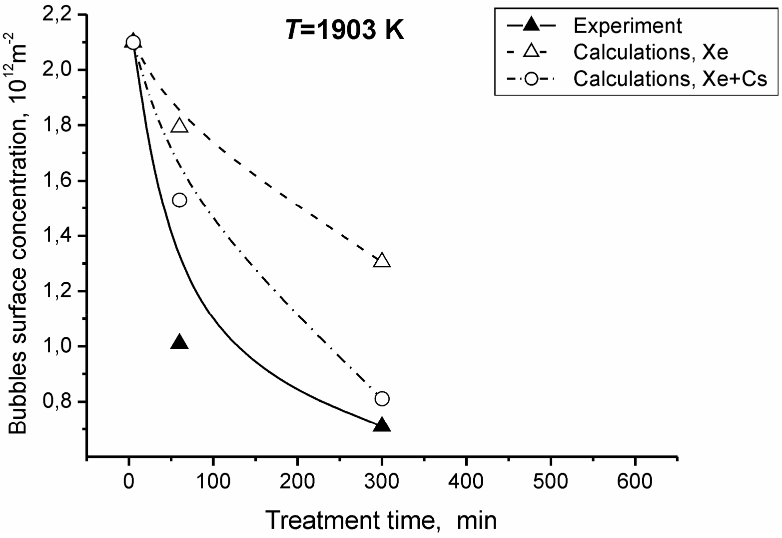

Fig. 5. Variation of the bubbles surface concentration with the treatment time at the annealing temperature 1903 K in the tests [1]. Comparison of measurements with calculations using the coalescence mechanism by growth of randomly distributed bubbles (β = 0.46) with and without consideration of Cs release during coalescence at the critical coverage

4. General formulation of the coalescence model

In the general case one should consider superposition of the two coalescence mechanisms by random bubbles migration and by bubbles growth. In this case probability of a bubble coalescence with its neighbours during time interval dt is the sum of probabilities of two independent events described by Eqs. (4) and (15), respectively. Therefore, the bubbles coalescence rate at low coverage in the mean field approximation takes the form

$$\frac{dN}{dt} = -2N^2 \frac{\partial \bar{A}}{\partial t} - \omega_{cls} N^2 . \qquad (39)$$

Substitution of Eqs. (23) and (24) in Eq. (39) yields

$$\frac{dN}{dt} = -N \frac{3kT}{2\gamma\varphi(\theta)} J_{\text{dif}}(t) - $$
$$-N^4 \frac{9\pi^2 \alpha D_s \Omega^{4/3}}{N_0^2 \bar{A}_0^2} \left(1 + \frac{\pi f(t)}{N_0 \bar{A}_0} \right)^{-2} ,$$
$$\text{if } N\bar{A} < 0.5 . \qquad (40)$$

At the saturation coverage Eq. (39) should be supplemented with the additional term describing the bubbles coalescence rate owing to channels formation and collapse from Eq. (32):

$$\frac{dN}{dt} = -2N^2 \frac{\partial \bar{A}}{\partial t} - \omega_{cls} N^2 + \frac{\partial N}{\partial t} . \qquad (41)$$

In this cases superposition of Eqs. (41), (29) and (30') yields, instead of Eq. (35):

$$\frac{dN}{dt} = -4N^2 \frac{\partial \bar{A}}{\partial t} - \omega_{cls} N^2 , \qquad (42)$$

which after substitution of Eqs. (30) and (31) takes the form

$$\frac{dN}{dt} = -N\beta \frac{3kT}{\gamma\varphi(\theta)} J_{\text{dif}}(t) - $$
$$-36\pi^2 \alpha D_s \Omega^{4/3} N^4 ,$$
$$\text{if } N\bar{A} = 0.5 . \qquad (43)$$

The source term $J_{\text{dif}}(t)$ should include also evaporation flux of chemically active elements (first of all Cs) from grain boundaries into bubbles, as explained in Section 3.2.

The model in the form of Eqs. (40) and (43), will be implemented in the MFPR code developed for mechanistic modelling of fission product release from irradiated UO_2 fuel [3]. This will allow self-consistent calculation of bubbles growth and coalescence in the course of fission products generation and release in various regimes (including transients) and, in particular, a more adequate comparison of the model predictions with the above described measurements. This work is foreseen in the nearest future.

Conclusions

Two different mechanisms of grain-face bubbles coalescence in irradiated UO_2 fuel proposed by Zacharie et al. [1] and White [5] are critically analysed and further developed. The first mechanism is based on consideration of random migration of bubbles over grain faces [1], whereas the second mechanism is based on consideration of growth and impingement of randomly distributed (immobile) face bubbles [5].

The coalescence of face bubbles due to their random migration is reconsidered on the base of the general kinetic theory [4]. This allows elimination of some inconsistencies in the modelling approach of [1] and improvement of the model predictions, especially in the case of continuous bubbles growth owing to absorption of gas atoms. The extension of the model to this case allows modelling of bubbles coalescence under irradiation conditions. In particular, it is shown that the migration mechanism can be effective for steady state irradiation conditions studied in the tests [9], however, is apparently insufficient for description of high-temperature annealing tests [1].

On the other hand, the improved mechanism of coalescence by growth and impingement of randomly distributed bubbles predicts rather weak decrease of face bubbles concentration under steady state irradiation conditions, however, becomes effective for simulation of high-temperature annealing tests with noticeable gas release. After attainment of the critical coverage, formation of channels on grain faces (interconnected with open porosity at grain edges) and their collapse owing to gas venting from face bubbles through the channels efficiently increase the bubble coalescence rate. In this case the bubble concentration variation is characterised by a rather strong (exponential) dependence on gas release and thus becomes significant under heat-up conditions of annealing or transient tests.

As a result, the general coalescence model which includes superposition of both mechanisms is formulated and proposed for implementation in the MFPR code [3], designed for mechanistic description of fission products release and fuel microstructure evolution; this will allow adequate modelling of grain face bubbles coalescence and fuel swelling under various operation conditions of nuclear reactors (steady irradiation, transient and post-irradiation annealing).

Acknowledgments

The original publication of this article in the Journal of Nuclear Materials [23] is greatly acknowledged.

References

1. *Zacharie I., Lansiart S., Combette P., Trotabas M., Coster M., Groos M.* // J. Nucl. Mater. 1998. Vol. 255. P. 85–91, 92–104.
2. *Berdyshev A.V., Veshchunov M. S.* Modelling of Grain Face Diffusion Transport and Swelling in UO_2 Fuel. (Preprint / Nuclear Safety Institute (IBRAE) RAS, no IBRAE-2002-14). Moscow: NSI (IBRAE) RAS, 2002.
3. *Veshchunov M.S., Ozrin V.D., Shestak V.E., Tarasov V.I., Dubourg R., Nicaise G.* // Nucl. Eng. Des. 2006. Vol. 236. P. 179–200.
4. *Geguzin Ya.E., Krivoglaz M.A.* Migration of Macroscopic Precipitates in Solid Materials. Moscow: Metallurgiya, 1971 (in Russian).
5. *White R.J.* // J. Nucl. Mater. 2004. Vol. 325. P. 61–77.
6. *Chandrasekhar S.* // Rev. Mod. Phys. 1943. Vol. 15. P. 1.
7. *Mansur L.K.* // Nuclear Technology. 1978. Vol. 40. P. 5–34.
8. *Mansur L.K., Okamoto P.R., Taylor A., Chey-Yu Li* // Int. Conf. Defects and Defect Clusters in BCC Metals and Their Alloys (August 14–16, 1973) / Ed. R.J. Arsenault // Nucl. Metall. 1973. 18.
9. *Kashibe S., Une K.* // J. Nucl. Sci. Technol. 1991. Vol. 28. P. 1090.
10. *Shewmon P.G.* // Trans. AIME. 1964. Vol. 230. P. 1134.
11. *Veshchunov M.S.* // J. Nucl. Mater. 2005. Vol. 346. P. 208–219.
12. *Maiya P.S.* // Ibid. 1971. Vol. 40. P. 57.
13. *Matzke Hj.* // Surfaces and Interfaces of Ceramic Materials / Eds.: L.C. Dufour, J. Novotny. Dordrecht: luwer Academic, 1989. P. 241.
14. *Marlowe M.O., Kazanoff A.I.* // J. Nucl. Mater. 1968. Vol. 25. P. 328.
15. *Olander D.R.* // Ibid. 1981. Vol. 96. P. 243.
16. *Zhou S.Y., Olander D.R.* // Surf. Sci. 1984. Vol. 136. P. 82.
17. *Baker C.* // J. Nucl. Mater. 1977. Vol. 71. P. 17.
18. *Cornell R.M., Bannister G.H.* // Proc. Brit. Ceram. Soc. 1967. Vol. 7. P. 855.
19. *Gulden M.E.* // J. Nucl. Mater. 1967. Vol. 23. P. 30.
20. *Mikhlin E.Ya.* // Ibid. 1979. Vol. 87. P. 405.
21. *White R.J., Tucker M.O.* // Ibid. 1983. Vol. 118. P. 1.
22. *Heame, T.J., Williams D.A., Bixler N.E., Grimley A.J., Wheatley C.J., Johns N.A., Domogala P., Dickson L.W., Alexande C.A., Osborn-Lee I., Zawadzki S., Rest J., Mason A., Lee R.Y.* VICTORIA: A Mechanistic Model of Radionuclide Behaviour in the Reactor Coolant System under Severe Accident Conditions. NUREG/CR-5545. 1992.
23. *Veshchunov M.S.* Modelling of grain face bubbles coalescence in irradiated UO_2 fuel // J. Nucl. Mater. 2007. Vol. 374. P. 44–53.

Modelling of Fission Gas Release from Irradiated UO_2 Fuel under High-Temperature Annealing Conditions

M.S. Veshchunov, V.E. Shestak

Introduction

As shown in the authors papers [1–3], in the absence of irradiation in the annealing stage, the subsystem of point defects (vacancies and interstitials) rather quickly attains its equilibrium state ($c_{v,I} = c_{v,i}^{eq}$), if point defect sources (growing dislocation loops) are uniformly distributed in the bulk of the grain. For instance, the relaxation time for point defects at the annealing temperature 1500 °C can be estimated as $\tau_{eq} \approx \left(D_v k_v^2\right)^{-1} \approx 10^{-3}–10^{-1}$ s, where $D_v \approx 10^{-10}–10^{-9}$ cm^2/s, is the thermal value of the vacancy diffusion coefficient and $k_v^2 \approx 10^{11}–10^{12}$ cm^{-2}, is the total sink strength for the point defects. A more slow process of the bubble growth occurs owing to the gas atom and point defect diffusion transport to bubbles. Since $D_g c_g << D_u$, where $D_u \approx 10^{-16} – 10^{-15}$ cm^2/s is the thermal value of the uranium self-diffusion coefficient, D_g and c_g are gas atom diffusivity and concentration, respectively, the gas transport determines the bubble growth rate during the initial period of the annealing stage. Despite a relative slowness of this process (in comparison with thermalisation of point defects), sinking of gas atoms into bubbles may occur during a few minutes at high temperatures. Hence, under annealing conditions at 1500 °C, the characteristic time τ_s of diffusion sinking of gas atoms into bubbles is estimated as $\tau_s \sim (D_g k_v^2)^{-1} \approx 10^2$ s; after this time practically all gas atoms are captured by bubbles, and gas transport to grain boundaries and the subsequent release can be provided only by bubbles.

At high temperatures $T > 1800$ °C thermal resolution of gas atoms from bubbles can prevent gas atoms from complete sinking into bubbles leading to an additional diffusion flux of remaining gas atoms from grain interior to boundaries (see papers of this Collection on pp. 17 and 25).

Microstructure observations of irradiated fuel in the annealing tests confirm that gas release is accompanied with a rapid growth of the intragranular bubbles (up to hundreds nm at high annealing temperatures) and a noticeable decrease (by several orders of magnitude) of the bubble number density [4–6]. This process of the bubble number decrease is usually associated with the Brownian motion of the bubbles leading to their coalescence into larger ones in the grain bulk and transport to the grain boundaries. However, evaluation of the experimental data by the MFPR code shows that a rather low mobility of small bubbles at $T \leq 1800$ °C measured in [7] does not allow a correct description of the bubble system evolution (see Section 2). An additional assumptions on the bubble diffusivity increase up to values determined by the surface diffusion (i.e., by several orders of magnitude) during annealing (e.g., recommended in [6]), slightly improve the description of bubbles size growth at high temperatures ($T \geq 1700$ °C), however, overestimates their growth (and gas release) at lower temperatures.

A complementary mechanism of bubble growth under annealing conditions associated with the thermal coalescence of bubbles (i.e., Ostwald ripening) considered in various papers [8–10, 1], turns out to be also too weak to explain these observations, as demonstrated in the authors' paper [2].

For this reason, a more realistic approach to this problem is further attempted (see Section 1.1.1). In accordance with [11], the migration of bubbles assumed to be caused by mass transport both on the bubble surface and through the matrix around the bubble. This mechanism provides an increase of the bubble diffusion coefficient leading to the bubble radius increase for large bubbles $r \geq 10$ nm due to activation of the surface diffusion mechanism, in a reasonable agreement with direct observations of bubble mobility [12, 13], and for this reason, under annealing conditions turns to be effective mainly at high temperatures $T \geq 1700$ °C (see Section 2). However, this mechanism is still insufficient to simulate gas release measured in the annealing tests.

As above mentioned, during bubbles growth and coalescence extended defects such as dislocation loops uniformly distributed in the grain bulk, may serve as the main source for vacancies (necessary for the bubble equilibration) and afford the equilibrium concentration of the point defects in the crystal bulk. This explains the observed dislocation creep and enhanced bubble growth by dislocation sweeping under annealing conditions [14].

In this situation an additional mechanism for gas release due to dislocation creep emerges (see Section 1.3). This new mechanism considers sweeping of bubbles and delivery them to the grain boundaries by climbing dislocation segments in the course of vacancy generation (necessary for equilibration of growing bubbles).

However, after some time a strong pinning of dislocations by swept bubbles can saturate this source of point defects, and grain boundaries apparently become the dominant source of vacancies during the subsequent period of the annealing tests. In this situation a vacancy flux directed from grain surface to its interior arises that induces bubble biased migration along the vacancy gradient in the opposite direction, as proposed recently by Evans [15]. Strictly speaking, a mechanism of bubble migration to the grain boundaries along the vacancy gradient was initially analysed and described in [16] and [17]. Later Evans proposed to apply this mechanism to the description of the enhanced gas release at annealing. However, in his paper [15] he did not present any quantitative calculations, but restricted himself by a qualitative consideration of the phenomenon.

In order to handle this problem quantitatively, a simple analytical model was developed in the authors' paper [2]. Under simplifying assumption of equilibrium state for growing bubbles and neglecting bulk sources of point defects (i. e. dislocations), the model allowed not only to explain a continuous increase of gas release during the annealing stage, but also to relate it quantitatively to the kinetics of bubble coalescence and swelling, in agreement with measurements (see Section 1.1). As shown below in Section 2, a similar model implemented in the MFPR code can really improve code predictions, if the above mentioned mechanism of Mikhlin for enhanced bubble diffusivity (leading to enhanced bubble coalescence) [11] is additionally taken into consideration. However, adequate consideration of dislocation sources acting in the initial period of annealing stage (as above explained) significantly suppresses gas release predicted by this simplified model. As a result, this dislocation mechanism provides so called "burst release" observed in the initial stage of annealing, whereas vacancy mechanism (considered by Evans) combined with the advanced model for bubble diffusivity (proposed by Mikhlin) provides more gradual release in a late period of annealing stage.

1. Main models and mechanisms

1.1. Bubble migration in the vacancy gradient

As above mentioned, a mechanism of bubble migration to the grain boundaries along the vacancy gradient was initially analysed and described in [16] and [17]. Later Evans [15] proposed to apply a similar mechanism to the description of the enhanced gas release at annealing. In order to handle this problem quantitatively, a simple analytical model was developed in the authors papers [2, 3] which is briefly presented in the current section.

In order to simplify modelling, a homogeneous space distribution in the grain of equal-size and equilibrium bubbles is considered. As above explained, after some initial period of the annealing stage (i.e., after saturation of the dislocation sources due to their pinning by bubbles, see Section 1.3.1), grain boundaries become the main source of vacancies and for this reason, vacancy flux from boundaries to grain interior appears. In accordance with the theoretical predictions [16] and [17], bubble flux in the opposite direction arises. Since (as above explained) gas atoms sinking into the bubbles is a relatively quick process which occurs during the initial 10^2–10^3 s of the annealing stage, in a late stage of annealing bubble coalescence determines vacancy deficit in the grain bulk and corresponding vacancy flux from the boundaries. For this reason, the described model [2] self-consistently accounts for both processes of gas release and bubble coalescence (swelling) observed in the annealing tests.

In accordance with [16], the bubble velocity $\vec{v}$ in the gradient of vacancy concentration c is determined by the relationship

$$\vec{v} = 2D_v \vec{\nabla} c_v, \tag{1}$$

where D_v and c_v are the uranium vacancy diffusion coefficient and bulk concentration (number of vacancies per U atom) in the UO_2 matrix, respectively.

Correspondingly, gas atom flux $\vec{J}_g$ to the grain boundary via bubble migration, takes the form

$$\vec{J}_g = \rho_b \vec{v} N_b, \tag{2}$$

where $\rho_b(t)$ is the bubble number density and $N_b(t)$ is the number of gas atoms in a bubble, both being spatially homogeneous in accordance with the above accepted model simplification.

As above explained, practically all gas atoms were captured by bubbles within a relatively short initial period of the annealing stage, and for this reason, the total gas content N_g in the spherical grain with the radius R_g takes the form

$$N_g \approx \rho_b N_b (4\pi/3) R_g^3, \tag{3}$$

and its variation with time is determined by the gas flux, Eq. (2) at the grain surface:

$$-\frac{dN_g}{dt} = J_g(R_g) 4\pi R_g^2. \tag{4}$$

After substitution of Eqs. (1–3) in Eq. (4), one gets

$$-\frac{dN_g}{dt} = \frac{6 N_g D_v \nabla c_v (R_g)}{R_g}. \tag{5}$$

On the other hand, the diffusion vacancy flux at the grain boundary $D_v \nabla c_v (R_g)$ determines time variation of the total volume of intragranular bubbles due to their coalescence and subsequent equilibration

$$\frac{d(4\pi R_b^3 \rho_b)}{3dt} = \frac{3 D_v \nabla c_v (R_g)}{R_g}. \tag{6}$$

For large enough bubbles (with radius $R_b \geq 5$ nm that is attained rather quickly in the initial stage of annealing) obeying the ideal gas law, the equilibrium condition takes the form

$$\frac{4\pi R_b^3}{3} \frac{2\gamma}{R_b} = kTN_b. \tag{7}$$

Substitution of Eqs. (6) and (7) in Eq. (5) finally yields

$$-\frac{dN_g}{dt} = \frac{kT}{\gamma} \frac{3N_g}{4\pi R_g^3} \frac{d}{dt}(N_g R_b). \tag{8}$$

The analytical solution of Eq. (8) has the form

$$A N_g R_b = \ln(B/N_g), \tag{9}$$

where $A = \frac{kT}{\gamma} \frac{3}{4\pi R_g^3}$ and B is the integration constant.

Solution of Eq. (9) shows that gas release $\left(N_0 - N_g\right)/N_0$ smoothly increases along with the bubble radius R_b growth and approaches to 100 % when $R_b >> 100$ nm. Comparison of the numerical solution with measurements of Baker and Kileen [5] at 1600 °C demonstrated that the model is able to correctly describe the whole annealing stage, if the correct time evolution of the bubbles radius is used in calculations, Fig. 1.

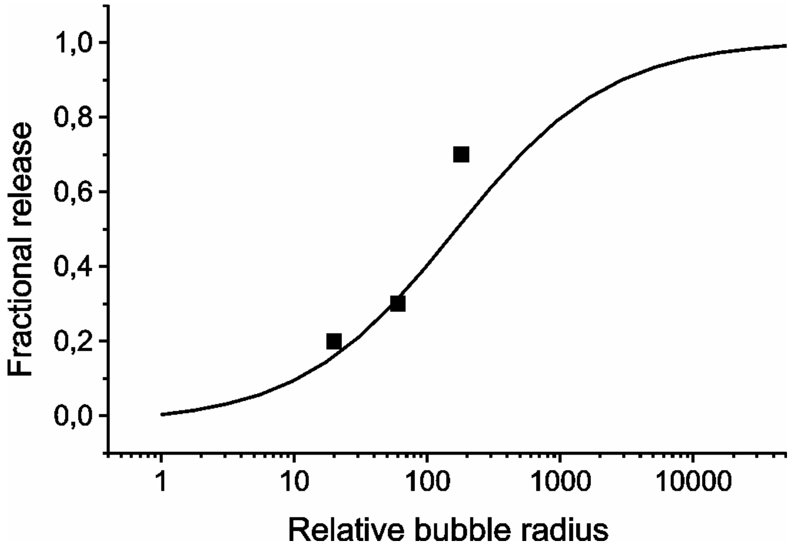

Fig. 1. Model prediction of gas release dependence on the relative mean bubble radius (R_b/R_0) during annealing stage, in comparison with experimental observations [5] at 1600 °C at a variety of moments (50 s, 1.4 h, 24 h)

Therefore, adequate description of bubble coalescence under annealing conditions becomes an important prerequisite for correct prediction of gas release. For this reason, in order to provide an adequate description of bubble coalescence due to their Brownian motion, an advanced approach to the bubble diffusivity proposed in the Mikhlin's paper [11] was implemented in the MFPR code.

1.1.1. Mikhlin's model for bubble diffusivity

In accordance with [11], the migration of bubbles is assumed to be caused by mass transport both on the bubble surface and through the matrix around the bubble, and the bubble diffusion coefficient is given by

$$D_b = D_b^{(\mathrm{vol})} + D_b^{(\mathrm{surf})},$$

$$D_b^{(\mathrm{vol})} = \frac{3}{4\pi} D_U \left(\frac{\Omega^{1/3}}{R_b} \right)^3,$$

$$D_b^{(\mathrm{surf})} = \frac{3}{2\pi} D_0^{(s)} \left(\frac{\Omega^{1/3}}{R_b} \right)^4 \left(1 - \frac{3q}{4\pi R_b^3} \right)^{N_b}, \quad (10)$$

where N_b is the number of gas atoms in the bubble, q is the bubble suppression parameter or the adatom interaction zone. For a realistic estimation of q, a knowledge of the effective potentials using theoretical or computer simulation techniques should be obtained. However, in the papers [18] and [19] a good agreement between calculations and various experimental data was obtained with $q = 5\times10^{-28}$ m^3. A similar value was used in [20] for description of gas bubble mobilities in UO$_2$. The same value hence is used in the current paper. Parameter $D_0^{(s)}$ for the surface diffusion coefficient directly from [11] (accurately fitted to the available experimental data) is used for the surface diffusion part in the MFPR bubble diffusivity model: $D_0^{(s)}\left[m^2/s\right] = 50 \cdot \exp\left(-450000/RT\right)$, with $1473 < T < 2073$ K and R in J·mol^{-1}·K^{-1}.

The model provides an increase of the bubble diffusion coefficient along with the bubble radius increase for bubbles $R_b \geq 10$ nm due to activation of the surface diffusion mechanism, in a reasonable agreement with direct observations of bubble mobility in [12] and [13]. This can enhance gas release under annealing in the temperature interval between 1630 and 1715°C (see Section 2), as observed in the experiment.

Further improvement of the bubble diffusivity model is considered in paper of this Collection on p. 34.

1.2. Vacancy field model

In order to take into account more adequately the above described mechanism of bubble biased migration, the numerical diffusion model of vacancy field evolution in the grain bulk during annealing of irradiated fuel is developed. This model simulates time and spatial variation of bulk vacancy concentration in the presence of extended vacancy sources (grain surface and climbing dislocations) and sinks (growing and equilibrating inter-granular bubbles). As a result, the new model self-consistently describes such kinetic processes as bubble volume relaxation and bubbles biased migration in the vacancy gradient.

Evolution of the vacancy distribution in a spherical grain is described in terms of the dimensionless concentration, c_v (number of vacancies per uranium atom), by diffusion equation

$$\frac{\partial c_v}{\partial t} = \frac{1}{r^2}\frac{\partial}{\partial r}\left(r^2 D_v \frac{\partial c_v}{\partial r}\right) - 4\pi D_v R_b C_b \left(c_v - c_v^{bs}\right) + \rho_d v_d b\,, \qquad (11)$$

where D_v is the vacancy diffusion coefficient, c_v^{bs} is the boundary concentration of vacancies near the bubble surface, C_b and R_b are bubble concentration and radius, respectively; ρ_d and v_d are dislocations density and creep velocity, respectively; $b = 2(3\Omega/4\pi)^{1/3}$ is the Burgers vector length (equal to the lattice parameter in neglect of dislocations with multiple Burgers vectors), Ω being the vacancy volume in the UO$_2$ matrix. Eq. (11) is solved with the following boundary and initial conditions:

$$\left.\frac{\partial c_v}{\partial r}\right|_{r=0} = 0, \quad c_v\big|_{r=R_{gr}} = c_v^{eq}, \quad c_v\big|_{t=0} = c_v^{eq}, \qquad (12)$$

where c_v^{eq} is the thermal equilibrium concentration approximated by Arrhenius correlation $c_v^{eq} = \exp\left(-E_v^{eq}/kT\right)$ with the activation energy of $E_v^{eq} = 2.2\,\mathrm{eV}$ [21]. Note that the equilibrium concentration relates the vacancy diffusivity to the equilibrium uranium self-diffusion coefficient, D_U^{eq}, by a relationship $D_U^{eq} = c_v^{eq} D_v$. Taking into account the MFPR approximation for the uranium self-diffusion coefficient $D_U^{eq} = D_0 \exp(-E_U/T)$, where $D_0 = 2{\cdot}10^{-4}\,\mathrm{m^2/s}$ and $E_S/k = 64200\,\mathrm{K}$ (see also [21]), one gets correlation for the vacancy diffusivity:

$$D_v = D_0 \exp(-E_v/\mathrm{T}),$$

$$E_v/k = \left(E_U - E_v^{eq}\right)/k \approx 38670\,\mathrm{K}.$$

The second term in the right hand side of Eq. (11) describes a mechanism of vacancy sinking into bubbles that is closely connected with the bubble relaxation. The boundary concentration of vacancies at the bubble surface is given by

$$c_v^{bs} = c_v^{eq} \exp\left(-\Omega\delta p/kT\right). \qquad (13)$$

It depends on the difference between the actual and equilibrium bubble gas pressures, δp, and determines the rate of the bubble volume relaxation:

$$\frac{dV_b}{dt} = 4\pi D_v R_b \left(c_v - c_v^{bs}\right). \qquad (14)$$

In Eq. (13) the pressure difference is defined as

$$\delta p = p - p_h - \frac{2\gamma \sin\theta}{R_b}, \quad p = \frac{N_b kT}{\left(V_b - B_{\mathrm{Xe}} N_b\right)},$$

where p_h is the external hydrostatic pressure, γ is the effective surface tension for UO$_2$, B_{Xe} is the van der Waals constant for Xe, p is the gas pressure in a bubble given by the van der Waals equation of state, V_b is the bubble volume, and N_b is the number of gas atoms in a bubble.

1.2.1. Thermal re-solution of gas atoms from bubbles

The kinetic equation for the number N_b of gas atoms in a bubble with the radius R_b under annealing conditions with the account for the thermal re-solution of gas atoms from a bubble in the van der Waals approximation, takes the form

$$\frac{dN_b}{dt} = 4\pi D_g c_g R_b \left(1 - \frac{c_g^{eq}}{c_g}\right), \qquad (15)$$

where

$$c_g^{eq} = PK_S\varphi(P,T) \tag{16}$$

and

$$\varphi(P,T) = \exp(B_{Xe}P/kT) \tag{17}$$

is the function accounting for the gas phase non-ideality (typical for small bubbles with $R_b \le 5\,\text{nm}$) in the van der Waals approximation, see [1, 2].

The temperature dependence of K_s is supposed to be of Arrhenius type:

$$K_S(T) = K_S(T_0)\exp\left(\frac{E_S}{kT_0} - \frac{E_S}{kT}\right), \tag{18}$$

where $K_S(T_0)$ is the solubility at a fixed temperature T_0, and E_S is the activation energy of the solid solution. Numerical values of these two parameters were estimated in [2] on the basis of available experimental data as $K_S(T_0) \approx 2\cdot10^7$ J^{-1} and $E_S = 3$ eV.

In the framework of the implemented vacancy model, the vacancy concentration sharply decreases during annealing in the central regions of the grain. This results in a strong overpressurisation of bubbles so that the thermal re-solution effect grows to be significant at high temperatures. In particular it suppresses complete sinking of gas atoms into the bubbles and thus leads to an additional flux of gas atoms out of the grain (see paper of this Collection on p. 142). For these reasons, calculations with the vacancy field model implemented in the MFPR code are always performed simultaneously with the activated thermal re-solution model.

1.2.2. Intragranular bubbles and gas atoms transport in the vacancy field model

The MFPR transport equation for the gas-in-bubbles concentration is modified in the new vacancy field approach by adding the term considering bubble biased migration with velocity v_b^{vac}. In accordance with consideration in Section 1.1, the bubble velocity in the gradient of vacancy concentration c_v is determined by

$$v_b^{\text{vac}}(r) = 2D_v\frac{\partial c_v}{\partial r}, \tag{19}$$

where D_v is the vacancy diffusion coefficient.

An additional flux of gas atoms in the same vacancy field gradient (similar to the flux of bubbles) is considered, in order to avoid underestimation of gas atom flux out of the grain which is assumed in many experimental works (e.g., [5, 6, 22]) to be the main source of the observed long-term release “tail” at a late stage of annealing. Atom velocity v_g^{vac} in the gradient of vacancy concentration is determined in accordance with [23] by

$$v_g^{\text{vac}}(r) = D_v\frac{\partial c_v}{\partial r}. \tag{20}$$

However, validation of the MFPR code with the implemented model for the individual gas atoms transport in the vacancy gradient, Eq. (20), did not show any essential contribution of this mechanism to gas release. Namely, an increase in fractional release in calculations for tests [24] and [22] due to this transport does not exceed 1 % .

1.3. Dislocation creep

The third term in the r.h.s. of Eq. (11) describes the dislocation source of vacancies. During the bubble growth under annealing conditions, dislocation loops and grain boundaries serve as sources for vacancies (necessary for the bubble growth) and afford the equilibrium concentration of point defects in the crystal bulk. However, in the initial stage of the annealing tests (until dislocations are not pinned by attached bubbles), the role of the grain boundary as a source of vacancies is negligible as compared to that of a system of dislocations. Indeed, this is seen from the ratio of total source strength values for grain boundaries $k_{gb.}$ and dislocations k_d, which is estimated as [25]

$$k_{gb}^2/k_d^2 \approx 3/(R_{gr}k_d), \tag{21}$$

where the source strength of dislocation system is evaluated as $k_d^2 \approx 2\pi\rho_d$. Since the usual grain size is $R_{gr} \sim 10^{-5}$ m and density of dislocation lines in irradiated fuel is $\rho_d \sim 3\cdot 10^{14}\,\mathrm{m}^{-2}$, one gets $k_{gb}^2 / k_d^2 \sim 10^{-2}$.

Ejection of vacancies from a dislocation line to the fuel matrix causes the effect of dislocation creep. This may explain the observed dislocation creep and enhanced bubble growth by dislocation sweeping under annealing conditions [14]. Being swept by climbing dislocations, bubbles are transported to the grain boundaries by dislocations leading to an additional gas release.

A simple model for dislocation creep was proposed by R. Galimov (Nuclear Safety Institute (IBRAE) RAS) and implemented in the MFPR code [3]. In this model edge dislocations are considered in the mean field approximation, i.e., they are uniformly distributed in the bulk of the grain with the mean density of dislocation lines ρ_d and random orientations of their directions and Burgers vectors. Under these assumptions, the number of bubbles swept by climbing dislocations in the unit volume and unit time are evaluated as

$$F_{b\to d} = 2\left(R_{\text{core}} + 2R_b\right)\rho_d v_d Y_b, \qquad (22)$$

where $Y_b = N_b\rho_b$ is the volume density of gas atoms in the bubbles, whereas variation of the dislocation density ρ_d is calculated in neglect of new dislocation loops generation under annealing conditions:

$$\frac{\partial \rho_d}{\partial t} = -\frac{3}{2d_{gr}}\rho_d v_d. \qquad (23)$$

Therefore, an additional contribution to the gas flux reaching grain boundaries provided by climbing dislocations is evaluated as

$$F_{d\to f}^{\text{creep}} = \frac{3\rho_d v_d}{2d_{gr}} \int_{t_0}^{t} dt\left(F_{b\to d}/\rho_d\right). \qquad (24)$$

For a crystal with a non-equilibrium concentration of bulk vacancies, c_v, the dislocation velocity v_d is determined by the flux of vacancies ejecting by dislocations to the grain bulk:

$$v_d = \frac{2\pi D_v\left(c_v^{eq} - c_v\right)}{b\ln\left(L/R_d\right)}, \qquad (25)$$

where $L = (\pi\rho_d)^{-1/2}$ characterises a mean distance between dislocations, R_d is the dislocation core radius estimated as $R_d \cong 3a$, and b is the Burgers vector length (equal to the lattice parameter a in neglect of dislocations with multiple Burgers vectors).

Being implemented in the MFPR code, the model predicts a noticeable increase of gas release (see Section 2), however, calculations demonstrate that a complete coverage of dislocations by swept bubbles is attained rather quickly during some initial interval of annealing. In this situation dislocation creep can be significantly suppressed by the pinning effect of attached bubbles, and grain boundaries become the main source of vacancies in the grain. In this stage the bubble biased migration in the vacancy gradient considered in Section 1.1, becomes the dominating mechanism of gas release. Therefore, the switch of the gas release mechanism from the dislocation creep to the bubble biased migration in the vacancy gradient is governed by dislocation pinning by attached bubbles.

1.4. Dislocation pinning by attached bubbles

Being swept by dislocations, bubbles can retard dislocation movement. If $c_b^{(d)}$ bubbles with radius R_b are attached to the unit length of a dislocation and each bubble exerts the force F_b on the dislocation, then the total retarding force acting on the unit length of the dislocation is calculated as $F_d = c_b^{(d)}F_b$. Consideration of the external force F_d acting on the dislocation, converts Eq. (25) for the dislocation velocity to the following form [26]:

$$v_d = -\frac{2\pi D_u}{b\ln\left(L/R_d\right)}\left(\frac{b^2F_d}{kT} - \frac{\delta c}{c_v^{eq}}\right), \qquad (26)$$

where $D_u = D_v c_v^{eq}$ is the uranium atom self-diffusion coefficient.

On the other hand, if bubbles are swept along with the moving dislocation, then

$$v_b = v_d, \qquad (27)$$

where the bubble velocity v_b is determined by the intragranular bubble mobility D_b/kT and the force F_b exerting by the dislocation on the bubble:

$$v_b = \frac{D_b}{kT} F_b, \qquad (28)$$

and the bubble diffusion coefficient D_b is defined by Eq. (10).

Superposition of Eqs. (26)–(28) allows calculation of the resulting force F_b and dislocation velocity v_d:

$$v_d = \frac{\left(B/b^2\right)\left(\delta c/c_v^{eq}\right)}{\left(Bc_b^{(d)}/D_b\right)+1}, \qquad (29)$$

where

$$B = \frac{2\pi D_u b}{\ln\left(L/R_d\right)}. \qquad (30)$$

These results are valid until the force F_b does not exceed the maximum force F_m that a bubble can exert on a dislocation, $F_m \propto Gb^2$ (estimated, for example, in [16]), where $G \approx 100\,\text{kJ/cm}^3$ is the dislocation linear tension,

$$F_b = \frac{kT}{D_b} \cdot \frac{\left(B/b^2\right)\left(\delta c/c_v^{eq}\right)}{\left(Bc_b^{(d)}/D_b\right)+1} \le F_m. \quad (31)$$

In the opposite case the bubble will be detached from the dislocation.

Numerical evaluation of Eq. (29) shows that due to a small value of $D_u \approx 10^{-15}\,\text{cm}^2/\text{s}$ at $T \le 1600\,°\text{C}$, the denominator of Eq. (29) remains ~ 1 even after a complete coverage of dislocation by bubbles with $R_b \sim 10\,\text{nm}$ (for which diffusivity D_b at 1500 °C is $\approx 10^{-16}\,\text{cm}^2/\text{s}$ [11]). The complete coverage occurs when condition

$$c_b^{(d)} 2R_b = 1 \qquad (32)$$

becomes valid. This means that the pinning effect is not very strong up to this moment and dislocations can further move with a somewhat reduced velocity.

However, after this moment a rapid coalescence of bubbles attached to dislocations commences leading to the strong pinning of dislocations after some relatively short time interval. It is assumed in the model that after complete coverage of dislocations by bubbles, Eq. (32) remains valid independently of the bubble radius. This leads to a steep increase of the bubble radius R_b and decrease of the bubble concentration $c_b^{(d)}$ in the course of further absorption of bubbles by moving dislocations. For large bubbles with $R_b \sim 10\,\text{nm}$ the ideal gas law is valid and thus for the number of gas atoms $Y_b^{(d)}$ in the bubbles attached to dislocations one can readily derive

$$Y_b^{(d)} = c_b^{(d)} \frac{4}{3}\pi R_b^3 \frac{2\gamma}{R_b kT}. \qquad (33)$$

Being combined with Eq. (32), this results in

$$R_b(t) = Y_b^{(d)}(t)\frac{3kT}{4\pi\gamma}. \qquad (34)$$

Substituting this relationship into Eq. (29), one obtains a steep increase of the denominator of Eq. (29) in the course of gas atoms absorption:

$$Bc_b^{(d)}/D_b \propto R_b^3 \propto Y_b^3, \qquad (35)$$

since large bubbles migrate via surface diffusion mechanism an thus obey $D_b \propto R_b^{-4}$ (see Eq. (10)).

This means, for example, that after rapid growth of bubble radius within one order of magnitude the dislocation velocity will practically turn to zero, i.e., dislocations will be pinned by attached bubbles. This allows to use Eq. (32) as the simplest criterion for dislocation pinning. More accurate results can be attained using Eq. (29) for the velocity of dislocations retarded by attached bubbles.

2. Simulations of annealing tests

2.1. Validation procedure

Testing of the MFPR code was conducted by comparison of the code predictions with experimental data on fission product release during post-irradiation annealing [22, 24].

In order to have a reference point, at first calculations with the base set of the MFPR parameters and models (i.e., vacancy field and dislocation creep are not taken into account) have been done. Then calculations using dislocation model with instantaneous vacancies transport from moving dislocations to equilibrating bubbles (i.e., vacancy model is turned off) were performed. Besides, calculations with dislocation model switched off (i.e., under an assumption that grain boundaries are the main source of vacancies, cf. [15]) were done. After this, the vacancy field and dislocation creep mechanisms were taken into account simultaneously in calculations. Pinning of dislocations was considered in the simplest approach when coverage of a dislocation by attached bubbles attained 100 % (see Section 1.3.1).

Since calculations with the MFPR base set strongly underestimated release at high temperatures (≥1630 °C), additional calculations with surface diffusion mechanism for intragranular bubbles (i.e., increased by several order of magnitude) were performed. As demonstrated in Section 1.1, an increase of intragranular bubbles size due to their coalescence in the annealing stage can significantly enhance gas release due to their biased migration in the vacancy field. Calculations with the increased intragranular bubbles diffusivity afforded by the mechanism of surface diffusion, confirmed this prediction and improved calculation results at high temperatures. However, such a procedure is not physically grounded and significantly exaggerates mobility of small bubbles (with $R_b < 10\,\mathrm{nm}$), in a remarkable contradiction with observations [12, 13] (see also [11]).

For this reason, a more realistic approach to the bubble diffusivity in accordance with the Mikhlin's model (see Section 1.1.1) was implemented in MFPR and used for calculations. The advanced model provides an increase of the bubble diffusion coefficient for large bubbles in comparison with the base diffusivity; this tends to explain a noticeable increase of gas release in the temperature interval between 1630 and 1715 °C, where bubbles become sufficiently large (several tens nm) due to coalescence under annealing conditions, as observed by scanning electron microscope in the experiments [22] and [24].

Validation of individual models of the code shows that in addition, the grain growth mechanism strongly affects the FP release at high temperatures, even if grain growth is not substantial (< 5 %). So, it appears reasonable to validate the full model (including vacancy field model, dislocation creep model and Mikhlin's mechanism for bubble diffusivity) simultaneously with activated grain growth for different values of the grain boundary velocity. The grain growth model of the MFPR code is presented in paper of this Collection on p. 109.

The vacancy diffusion coefficient is not measured directly in experiments but might be evaluated from measured data for the uranium atom self-diffusion coefficient and calculated equilibrium vacancy concentration data (as explained in Section 1.2). For this reason, the accuracy of the obtained in such a way vacancy diffusion coefficient is not high and is estimated within one order of magnitude. Hence in the present validation procedure this coefficient was additionally amplified within one order of magnitude, in order to avoid possible underestimation of the Evan's mechanism for bubbles migration in the vacancy field.

Initial dislocation density in the dislocation creep model was evaluated from available experimental data as described below in Section 2.2.

Validation procedure is described in detail in [3]. Here the main results of calculations for the two tests [24] and [22] are presented.

2.2. Calculation results

In the experiments [24] unstressed samples of uranium oxide taken from pressurised water reactor fuel after two normal operating cycles, i.e., with burn-up of 25 GWd/t, were subjected to thermal treatment in a laboratory furnace at temperatures between 1403 and 1988 K for duration between 5 min and 10 h. The variation of the quantity of fission gas released over time was determined at each temperature. During irradiation stage fuel core temperature did not exceed 1100 °C.

Superposition of the above described mechanisms and models, allows an adequate description of the annealing tests, Fig. 2. It should be noted that dislocation density of as-irradiated fuel in the pellet peripheral region was measured in [27]. It increased with burn-up in the range of 6–44 GWd/t from $\approx 8\cdot10^{13}$ to $6\cdot10^{14}\,\mathrm{m}^{-2}$. However, only part of the observed dislocations is mobile in an irradiated crystal, since they are effectively pinned by extended defects such as arrays of dislocations, etc. Indeed, in direct observations of Whapham [28] dislocation loops had grown sufficiently to coalesce with neighbouring loops to form a dislocation network when dislocation density attained $\sim 2\cdot10^{13}\,\mathrm{m}^{-2}$. Due to such structures formation, only a part of dislocations can be considered as mobile and capable for climbing and sweeping the intragranular gas bubbles.

The critical value of the mobile dislocations density is evaluated as

$$\rho_d^{crt} = \rho_d^0 + 2\pi R_d^{crt} C_d,$$

$$R_d^{crt} = \left(\frac{3}{4\pi C_d}\right)^{\frac{1}{3}}, \qquad (36)$$

where ρ_d^0 is the initial dislocation density in the fresh fuel, C_d is the dislocation loops concentration (see paper of this Collection on p. 47). For this reason, the values of density close to the critical value $\rho_d^{crt} \approx 8\cdot10^{13}\,\mathrm{m}^{-2}$, evaluated from Eq. (36), were used in calculations. The best fit was attained with the dislocation density $\rho_d = 0.5\cdot\rho_d^{crt} \approx 4\cdot10^{13}\,\mathrm{m}^{-2}$, as presented in Fig. 2.

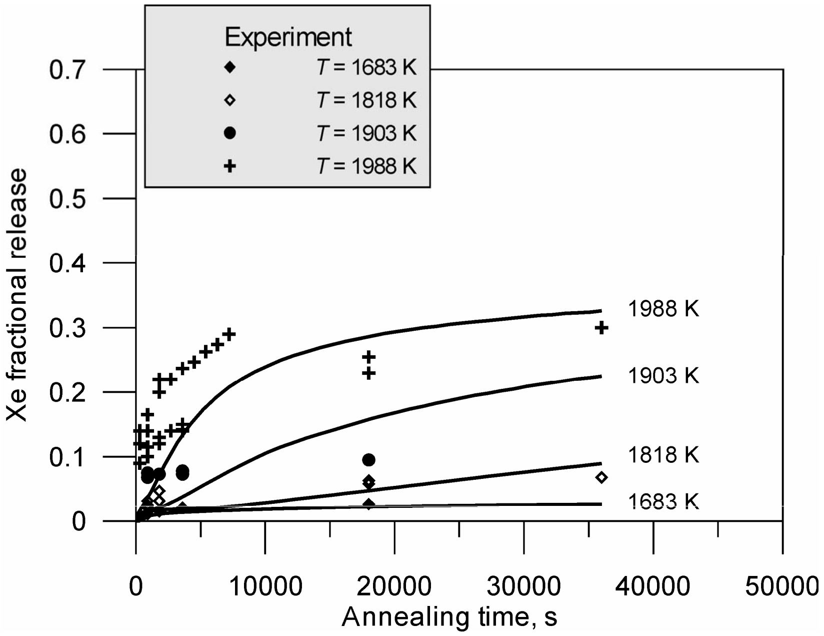

Fig. 2. Experimental data [24] (points) and MFPR calculation results (lines) for Xe release as a function of annealing time at different temperatures

In order to check the validity of the model predictions, additional calculations of spatially averaged intragranular bubble size and density evolution during annealing were carried out. Results of these calculations are presented in Fig. 3. From this figure it is seen that the significant increase of gas release at 1988 K correlates with the noticeable increase of intragranular bubbles size due to their coalescence with enhanced diffusion coefficient at this temperature, this in a reasonable agreement with semi-quantitative predictions in Section 1.1. On the other hand, a noticeable increase of the intragranular bubbles size at 1988 K in comparison with that at lower temperatures, was reported by experimentalists [24]. Direct measurements of bubble size and density during annealing were performed in the tests [22].

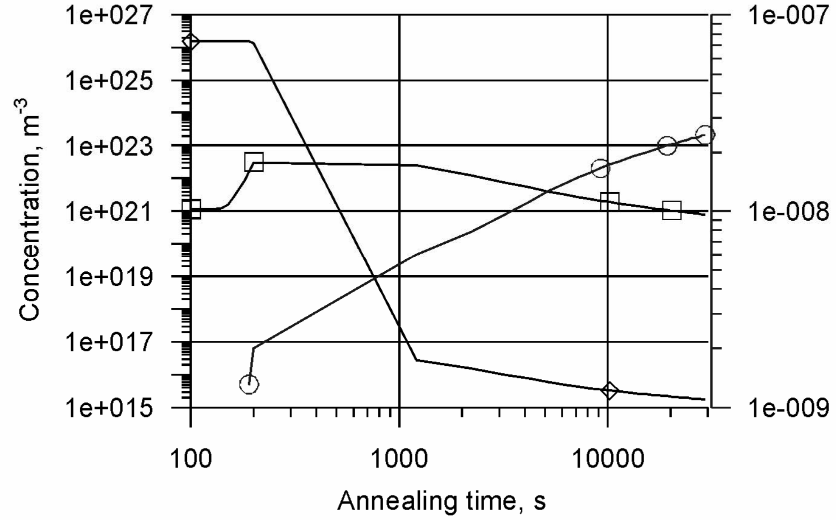

Fig. 3. Gas atom and bubble concentrations and bubble radius as functions of annealing time at T = 1988 K

In the experiments [22] samples of uranium oxide taken from pressurised water reactor fuel after 1 to 4 normal operating cycles, i.e., with burn-up of 6 to 28 GWd/t, were subjected to thermal treatment in a laboratory furnace at temperatures between 1773 and 2073 K for duration up to 5 h. Release rate of Kr^{85} was measured continuously. Experimental data for Kr^{85} release as a function of annealing time at temperature 2073 K for different burn-ups are compared with the calculation results in Fig. 4.

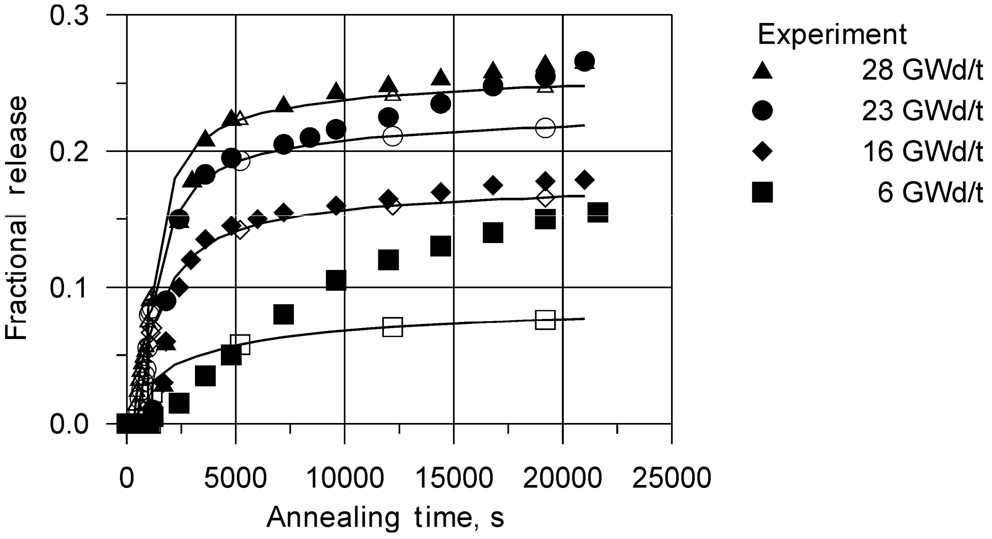

Fig. 4. Experimental data [22] (points) and MFPR calculation results (lines) for Kr release as a function of annealing time at temperature 2073 K for different burn-ups

A good agreement with the measured bubbles concentration is also attained in these calculations. In the end of annealing stage the measured mean bubble diameter was ≈ 55 nm [22] whereas calculated diameter is equal to 62 nm, Fig. 5.

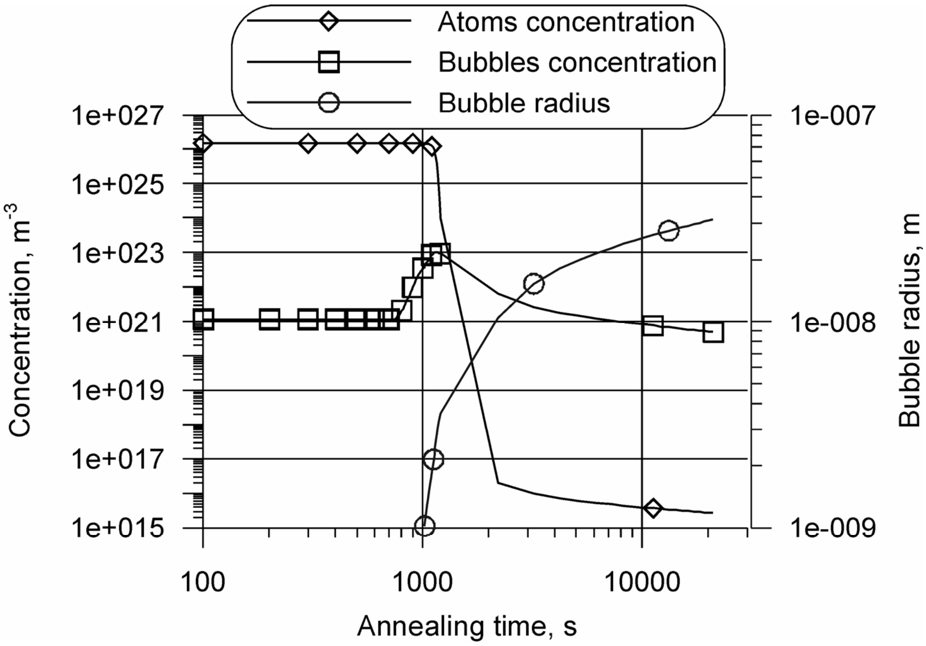

Fig. 5. Gas atom and bubble concentrations and bubble radius as functions of annealing time at temperature 2073 K and burn-up 25 GWd/t

2.3. Discussion

Validation of the MFPR code with the newly implemented models against post-irradiation annealing experiments shows that dislocation transport mechanism provides a steep increase of gas release (i.e., burst release) in the beginning of the annealing stage, however, underestimates the total gas release in late stage of annealing. On the other hand, the Evans mechanism of bubbles biased transport in vacancy gradient [15] also strongly underestimates gas release at high temperature annealing. Increasing by one order of magnitude of vacancy diffusivity provides substantial improvement of release calculation results, however, the mean bubble size remains noticeably smaller in comparison with experimental data. Moreover, inclusion of dislocation sources with a realistic density in consideration of the vacancy field significantly suppresses the Evans mechanism of gas release, since the vacancy flux from grain boundaries noticeably diminishes in this case.

Considerable improvement in the predictions of these two models can be attained by increase of diffusion coefficients for large bubbles. This procedure of bubble diffusion coefficient enhancement can be grounded within the advanced model [11] for different mechanisms (volume or surface) of bubble diffusivity depending on bubble size. Nevertheless, application of this bubble diffusion model is still insufficient to explain high release observed in the tests.

Only self-consistent operation of the four mechanisms: vacancy model (bubbles biased migration in vacancy gradient) with account for the bubble thermal re-solution mechanism, dislocation creep model, advanced bubble diffusivity model and grain growth model, allows a reasonable agreement with experimental data at all annealing test temperatures. In this case dislocation transport mechanism provides a short-termed burst release observed in the initial time interval of the annealing tests. After this time interval when dislocations become effectively pinned by attached bubbles, the competitive vacancy mechanism and, at high temperatures (≥ 1700 °C), grain growth mechanism become important, affording the observed smooth increase of gas release in the late stage of annealing at high temperatures.

Conclusions

The numerical diffusion model of vacancy field evolution in the grain bulk during annealing of irradiated fuel was developed and implemented in the MFPR code. The model simulates time and spatial variation of bulk vacancy concentration in the presence of extended vacancy sources (grain surface and climbing dislocations) and sinks (growing and equilibrating inter-granular bubbles). As a result, the new model self-consistently describes such processes as bubble volume relaxation, migration of bubbles due to dislocations creep and bubbles biased migration in the vacancy gradient.

Validation of the numerical diffusion model of vacancy field evolution implemented in the MFPR code against high temperature annealing experiments has demonstrated that discrepancy between the code predictions and experimental values for xenon fractional release and intragranular bubble size evolution has essentially decreased in comparison with the basic set of models calculations.

The new modelling results confirm the important role of crystal point defects (vacancies) and extended defects (dislocations) in the phenomenon of fission gas release during post-irradiation annealing. Only simultaneous and self-consistent consideration of these defects evolution and their interactions with fission gas bubbles, allows reasonable agreement of code calculations with experimental data.

References

1. *Veshchunov M.S.* On the theory of fission gas bubble evolution in irradiated UO_2 fuel // J. Nucl. Mater. 2000. 277. Vol. P. 67–81.
2. *Veshchunov M.S., Berdyshev A.V., Tarasov V.I.* Development of Fission Gas Bubble Models for UO_2 Fuel in Framework of MFPR Code. (Preprint / Nuclear Safety Institute (IBRAE) RAS, no IBRAE-2000-08). Moscow: NSI (IBRAE) RAS, 2000.
3. *Ozrin V.D., Shestak V.E., Tarasov V.I., Veshchunov M.S.* Modelling of fission gas release during high-temperature annealing of irradiated UO_2 fuel. (Preprint / Nuclear Safety Institute (IBRAE) RAS, no IBRAE-2002-19). Moscow: NSI (IBRAE) RAS, 2002.
4. *Turnbull J.A., Cornell R.M.* // J. Nucl. Mater. 1970. Vol. 36. P. 161.
5. *Baker C., Kileen C.* Fission gas release during post irradiation annealing of UO_2 // Materials for nuclear reactor core applications. London: BNES, 1987. Paper 24. P. 183.
6. *Kashibe S., Une K., Nogita K.* // J. Nucl. Mater. 1993. Vol. 206. P. 22.
7. *Gulden M.E.* // Ibid. 1967. Vol. 23. P. 30.
8. *MacInnes D.A., Brearley I.R.* // Ibid. 1982. Vol. 107. P. 123.
9. *Brearley I.R., MacInnes D.A.* // Ibid. 1983. Vol. 118. P. 68.
10. *Elton P.T.* et al. // Ibid. 1985. Vol. 135. P. 63.
11. *Mikhlin E.Ya.* // Ibid. 1979. Vol. 87. P. 405.
12. *Cornell R.M., Bannister G.H.* // Proc. Brit. Ceram. Soc. 1967. Vol. 7. P. 855.
13. *Baker C.J.* // Nucl. Mater. 1977. Vol. 71. P. 117.
14. *Whapham A.D., Sheldon B.E.* Electron Microscope Observation of the Fission-Gas Bubble Distribution in UO_2. AERE-R-4970. 1965.
15. *Evans J.H.* // J. Nucl. Mater. 1997. Vol. 246. P. 121.
16. *Geguzin Ya.E., Krivoglaz M.A.* Migration of Macroscopic Precipitates in Solid Materials. Moscow, 1971. (in Russian).
17. *Nichols F.A.* // Acta Met. 1972. Vol. 20. P. 207.
18. *Chkuaseli V.F., Matzke Hj.* // J. Nucl. Mater. 1993. Vol. 201. P. 92.
19. *Chkuaseli V.F., Matzke Hj.* // Ibid. 1995. Vol. 223. P. 61.
20. *Perryman L.J., Goodhew P.J.* // Acta Metall. 1988. Vol. 36. P. 2685–2692.

21. *Matzke Hj.* // Adv. Ceram. 1986. Vol. 17. P. 1.
22. *Une K., Kashibe S.* // J. Nucl. Science and Technology. 1990. Vol. 27(11). P. 1002–1016.
23. *Bakai A.S., Turkin A.A.* // J. Nucl. Mater. 1988. Vol. 152. P. 331.
24. *Zacharie I., Lansiart S., Combette P., Trotabas M., Coster M., Groos M.* // Ibid. 1998. Vol. 255. P. 85–91.
25. *Brailsford A.D., Bullough R.* // Philosophical Transactions of the Royal Society. 1981. Vol. A302. P. 87.
26. Kosevich A.M. Dislocations in the Theory of Elasticity. Kiev: Naukova Dumka, 1978. (in Russian).
27. *Nogita K., Une K.* // Nucl. Instrument and Methods in Phys. Res. 1994. Vol. B91. P. 301.
28. *Whapham A.D., Sheldon B.E.* // Nucl. Appl. 1966. Vol. 2. P. 123.

Model for Evolution of Intragranular Gas Bubbles and Fission Gas Release in UO$_2$ Fuel under Transient Irradiation Conditions

M.S. Veshchunov, V.E. Shestak

Introduction

General analysis of the intragranular bubbles behaviour demonstrates that re-solution of gas atoms from bubbles is often treated in an over-simplified manner, and for this reason, additional studies of the irradiation effects on intragranular bubbles should be carried out [1].

Development of a new model for a self-consistent consideration of the irradiation induced re-solution of gas atoms from bubbles and its implementation in the MFPR code, are presented in the current paper. This allows a significant improvement in predictions for microscopic observations of intragranular bubbles evolution and, as a result, for gas release in various transient tests.

1. Advanced model for gas atoms re-solution from bubbles

According to the Nelson's model [2] for intragranular bubbles, the re-solution rate is independent of the bubble size only for very small bubbles ($R_b \le 1{-}1.5$ nm). For larger spherical bubbles only a fraction of gas atoms within a critical distance from the bubble surface $\lambda \approx 1{-}1.5$ nm may escape, therefore, the resolution rate becomes inversely proportional to the bubble radius:

$$J_{\mathrm{res}} = bN_b, \qquad (1)$$

where

$$b \approx b_0 \frac{\lambda}{\lambda + R_b} \qquad (2)$$

is the resolution probability, and N_b is the number of atoms in a bubble. On the other hand, it was pointed out in [2] that for larger bubbles the ejection of a gas atom into surrounding matrix does not automatically result in its resolution. In accordance with available studies of the thermal desorption of inert gas from solids, it was presumed in [2] that those gas atoms knocked to within the first two or three atomic distances (i.e., $\delta \sim 1$ nm) from the bubble would tend to return back to the bubble.

In order to take this tendency into quantitative consideration, one can assume that the influx of the ejected atoms back to the bubble proceeds by diffusion within the re-solution layer δ. Such a consideration generalises the standard treatment of the thermal re-solution of gas atoms from bubbles, and is similar to the consideration [3] of the re-solution process from grain boundaries. The built-up concentration barrier c_δ of the re-solution layer determines the diffusion flux from the grain with the mean bulk concentration c_g of gas atoms in the matrix:

$$J_{\mathrm{dif}} = 4\pi D\left(c_g - c_\delta\right)\left(R_b + \delta\right), \qquad (3)$$

and the net flux of atoms deposited on the bubble:

$$J_\delta = 4\pi D c_\delta R_b \frac{\left(R_b + \delta\right)}{\delta}, \qquad (4)$$

which counterbalances the re-solution flux J_{res} back into the grain in accordance with the flux matches:

$$J_\delta = J_{\mathrm{dif}} + J_{\mathrm{res}}. \qquad (5)$$

Superposition of Eqs. (1–5) yields an equation for c_δ:

$$J_\delta = 4\pi D c_\delta R_b \frac{(R_b+\delta)}{\delta} - bN_b = 4\pi D\left(c_g - c_\delta\right)\left(R_b+\delta\right). \qquad (6)$$

Substitution of the solution of Eq. (6) in the equation for the growth rate of the bubble

$$\frac{dN_b}{dt} = J_{\text{dif}} \qquad (7)$$

yields

$$\frac{dN_b}{dt} = 4\pi D c_g R_b - bN_b \frac{\delta}{R_b+\delta}, \qquad (8)$$

thus, leading to an additional re-normalisation of the re-solution probability b in the standard equation for the bubble growth rate (obtained disregarding the re-solution barrier c_δ).

Therefore, the self-consistent consideration of the gas atom re-solution from and influx back to bubbles allows application of the standard equation for the bubble growth rate:

$$\frac{dN_b}{dt} = 4\pi D c_g R_b - b' N_b, \qquad (9)$$

however, with the following expression for the re-solution probability

$$b' \approx b_0 \frac{\lambda}{R_b+\lambda} \cdot \frac{\delta}{R_b+\delta}. \qquad (10)$$

In the limiting case of a very large value of the re-solution layer thickness δ comparable with the inter-bubble distance, Eq. (10) transforms back into the Nelson's expression for b, Eq. (2). However, in accordance with the above mentioned Nelson's notification, this value is small and comparable with the value of λ, i.e., $\delta \sim \lambda \sim$ 1–1.5 nm, and for this reason, Eq. (10) will be further used in the simplified form:

$$b' \approx b_0 \left(\frac{\lambda}{R_b+\lambda}\right)^2. \qquad (11)$$

On the other hand, strictly speaking Eq. (2) was derived in [2] for small bubbles with $R_b \le 5$ nm, i. e., for the van der Waals bubbles with the gas density being effectively independent of bubble size. For larger bubbles the dependence of b on R_b may be slower, and Eq. (11) may be rewritten in a more general form:

$$b' \approx b_0 \left(\frac{\lambda}{R_b+\lambda}\right)^\alpha, \qquad (12)$$

with $1 \le \alpha \le 2$. In order to analyse the effect of superposition of the two power laws in the effective dependence of b' on R_b in Eq. (12), two limiting values $\alpha = 1$ and 2 corresponding to Eqs. (2) and (11), respectively, will be used in the following consideration.

2. Qualitative consideration

In order to analyse the bubble growth qualitatively, it is sufficient to consider the behaviour of a sole growing bubble during a time interval between two subsequent collisions with other bubbles [1]. Owing to a relatively low Brownian mobility of bubbles at $T \le 1800°$ C [4], the time between two subsequent collisions of a bubble (in the absence of temperature gradients in the grain) is really very large. In this case the analysis of the growing bubbles behaviour can be performed on the basis of Eq. (9) along with the kinetic equation for the number of vacancies x in a bubble, in terms of the nodal line Poincaré formalism, Fig. 1 (compare with [1]).

In the case of applicability of the ideal gas law (that is strictly valid for large bubbles with $R_b > 5$ nm) the first nodal line $dx/dt = 0$ is described by the "capillarity" equation $N \propto x^{2/3}$. The second nodal line $dN/dt = 0$ is represented by an equation $N \propto x^{1/3}$ for small bubbles with $R_b \le \lambda \sim 1$ nm, and by an equation $N \propto x^{2/3}$ for larger bubbles, if Eq. (3.2) is valid. In both these cases an intersection of the two nodal lines determines a unique critical point I of the stable node type, i.e., particles (gas atoms (N) and vacancies (x)) move toward the node from all quadrants in the neighbourhood, Fig. 1. The critical point apparently determines the radius of the stable bubbles and explains the validity of the "bimodal" bubble size distribution, observed in the steady state tests. When a bubble deviates from this stable state, diffusion fluxes of the gas atoms and point defects arise which return the bubble back to the initial state. An account of the Brownian mobility of bubbles (increasing with temperature) may enlarge the mean size of bubbles, but will not change the situation qualitatively, since the system is still characterised by the unique stable critical point.

However, the situation can change when Eq. (11) is used instead of Eq. (2). In this case the nodal line $dN/dt = 0$ is described by a relationship $N \propto x$ for large bubbles $R_b >> \lambda$, and a new critical point of the saddle type appears at the intersection of the two nodal lines, Fig. 2. In the case of a sufficiently high bubble mobility (i.e., at high temperatures), bubbles can surmount the "distance" between the two critical points due to their collisions and coalescence, and thus "infiltrate" through the saddle point into the large-bubble area where they grow further unrestrictedly.

Therefore, under conditions of transient tests with temperature increase, self-consistent consideration of the gas atom re-solution from and influx back to bubbles allows prediction of the onset and growth of very large intragranular bubbles. This qualitatively corresponds to the observations in the transient tests [5], and will be analysed quantitatively by application of the enhanced dependence of re-solution probability b on bubble radius R_b derived in Eq. (11), in the following Section 3.1.

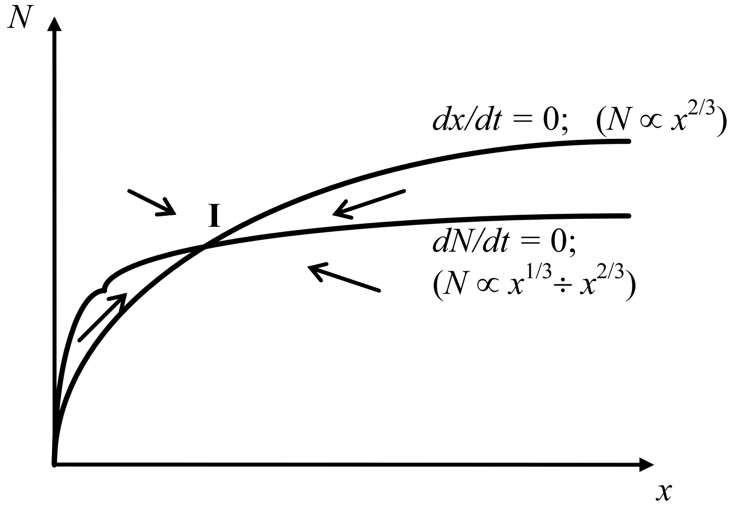

Fig. 1. Schematic diagram of nodal lines in the case of a slow dependence of b on R_b, i.e., $\alpha = 0 \div 1$. Velocity vectors and the critical point I (stable node) are indicated

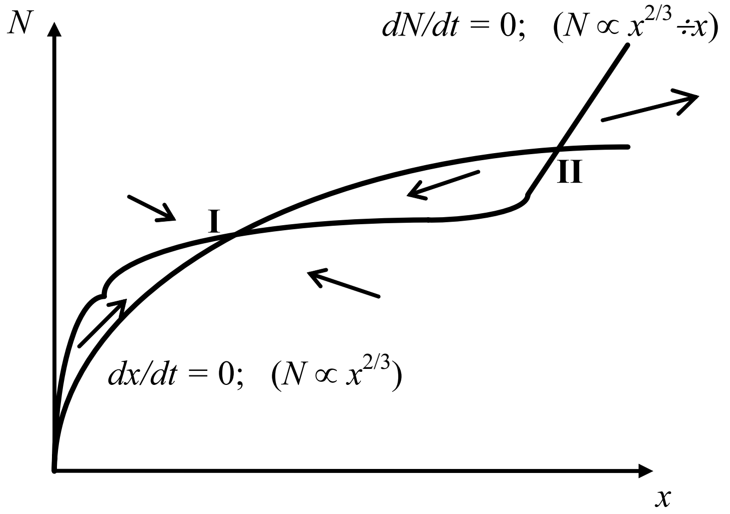

Fig. 2. Schematic diagram of nodal lines in the case of a rapid dependence of b on R_b, i.e., $\alpha = 1 \div 2$. Two critical points I (stable node) and II (saddle) are indicated

2. Model validation

2.1. ITU tests

Transmission electron microscopy (TEM) has been used in an extensive study [5] of the microstructure of base-irradiated and transient-tested samples of LWR nuclear fuels. The steady state base irradiation of 3 % enriched UO_2 fuel was performed at a maximum linear power of 260 W/cm (corresponding to the fission rate $\approx 1.3 \cdot 10^{13}$ fissions/(s·cm^3)) to an average burn-up of 4.5 %. The transient-tested samples came from pellets of the base-irradiated fuel which had been further subjected in reactor to power increases up to a maximum of 420 W/cm (fission rate $\approx 2.1 \cdot 10^{13}$ fissions/(s·cm^3)) with hold time up to 60 h ($= 2.2 \cdot 10^5$ s).

Under steady-state irradiation conditions most of the fission gas produced was retained in solution in the fuel matrix or precipitated into small fission bubbles with a narrow size distribution and an average diameter of 8 nm. The bubble spatial distribution was homogeneous, with an average density of $(1.2–1.9) \cdot 10^{22}$ m^{-3}.

The effect of the transient test was to increase the fuel center temperature from 1200° C by about 300° C, causing significant changes to fuel microstructure. The major microstructural change in the fuel center resulting from the transient was the formation of a new population of large fission bubbles with a broad bubble size distribution (30 to 500 nm in diameter) and an average bubble density of $7 \cdot 10^{18}$ m^{-3}. The temperature rise at the fuel periphery, on the other hand, was small and the microstructure remained essentially similar to that of the base-irradiated fuel, with similar density and distribution of small fission bubbles.

Results of the standard MFPR version calculations of the transient tests [5] show that the increase of temperature from 1200 to 1500° C and fission rate from $1.3 \cdot 10^{13}$ to $2.1 \cdot 10^{13}$ fissions/(s·cm^3) leads to an insignificant increase of the mean bubble diameter and the bubble distribution function width, as well as conservation of the bimodal character of this distribution (in accordance with qualitative predictions in Section 2), also at longer times after transient, Fig. 3. An agreement with observations might be improved only by a significant increase of the bubble mobility by several orders of magnitude.

Implementation in the MFPR code of the advanced model for gas re-solution from bubbles, Eq. (11) coupled with the Mikhlin's bubble diffusivity model [6] (which is described and modified in paper of this Collection on p. 34), allows qualitative and quantitative improvement of the code predictions. Owing to the onset of the new critical point at the intersection of the two nodal lines in the phase portrait of the system, Fig. 2, and higher bubbles diffusivities at elevated temperatures (provided by the Mikhlin's model), the formation of the "trimodal" bubble distribution function (i.e., single atoms and two populations of bubbles) with an extended interval of bubble sizes is predicted. Moreover, distribution function widens continuously with time after transient and becomes very similar to the observations [5], Fig. 4.

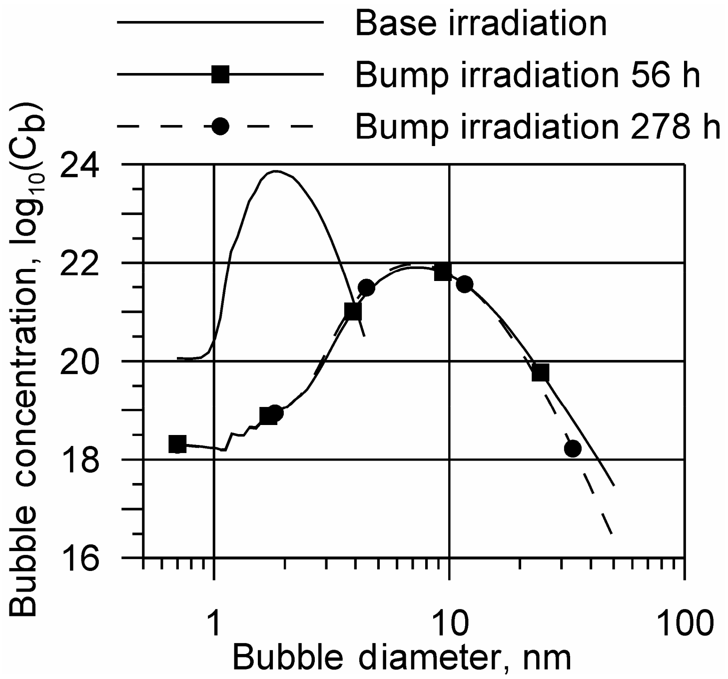

Fig. 3. Size distribution function for intragranular bubbles calculated by MFPR with standard model for gas re-solution from bubbles.

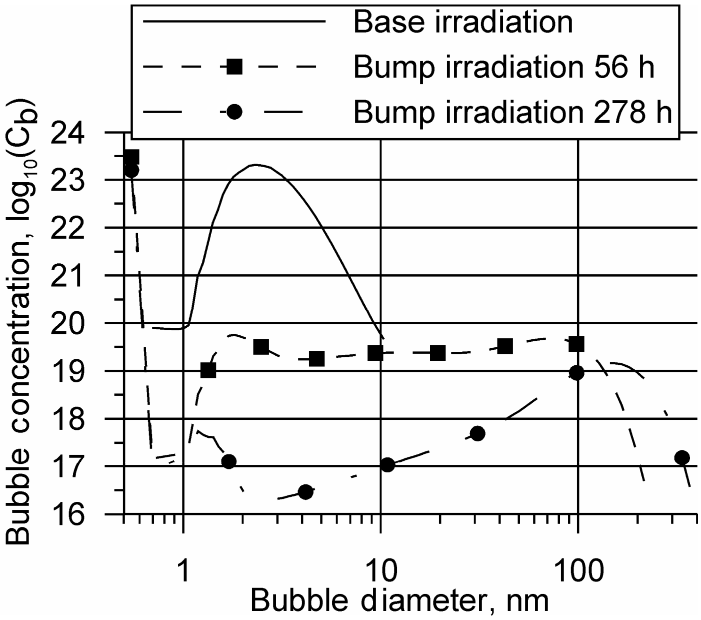

Fig. 4. Size distribution function for intragranular bubbles calculated by MFPR with advanced model for gas re-solution from bubbles

2.2. Risø tests

Transient tests [7] have been carried out in the Risø Project to explore fuel performance at increasing burn-up levels to ~45 MWd/t and beyond, especially for power increases (transients) late in life.

The tests were performed with the fuel of PWR design, pellet diameter 9 mm, pellet density 93.7 % TD and grain diameter 6 μm. The ANF fuel had been irradiated in the Biblis-A reactor (Germany) to burn-up of 4.3-4.4 % FIMA (pin average). The highest linear power seen by this fuel was 26.7 kW/m. The fuels did not release more than 0.3 % of their fission gas inventory during the base irradiation. According to the calculations [7], the temperature of the cladding surface determined by film boiling was 613 K in case of PWR fuel and 563 K in the case of the BWR fuel, whereas fuel centerline temperature ranged from ~1773 K at linear heat rating 30 kW/m to ~2273 K at linear heat rating 40 kW/m.

Bump irradiation was carried out in the DR3 reactor. The approach to the terminal power was made either in two large jumps or in multiple steps of 2 or 5 kW/m. In all of the instrumented tests, the fuel center temperature and the fission gas pressure in the plenum were simultaneously measured. Post-test examinations of the specimens allow authors of [7] to plot fractional gas releases and grain growth as functions of terminal local fuel temperature.

Fig. 5 shows measured and calculated release curves for three representative sections of transient-tested ANF fuel with hold times 4, 40 and 62 h. Calculation results plotted in these figures were obtained with the same set of models and model parameters as in the previous calculations in Section 3.1, and are in a reasonable agreement with experimental results (taking into account uncertainties in fuel temperature evaluation in the tests).

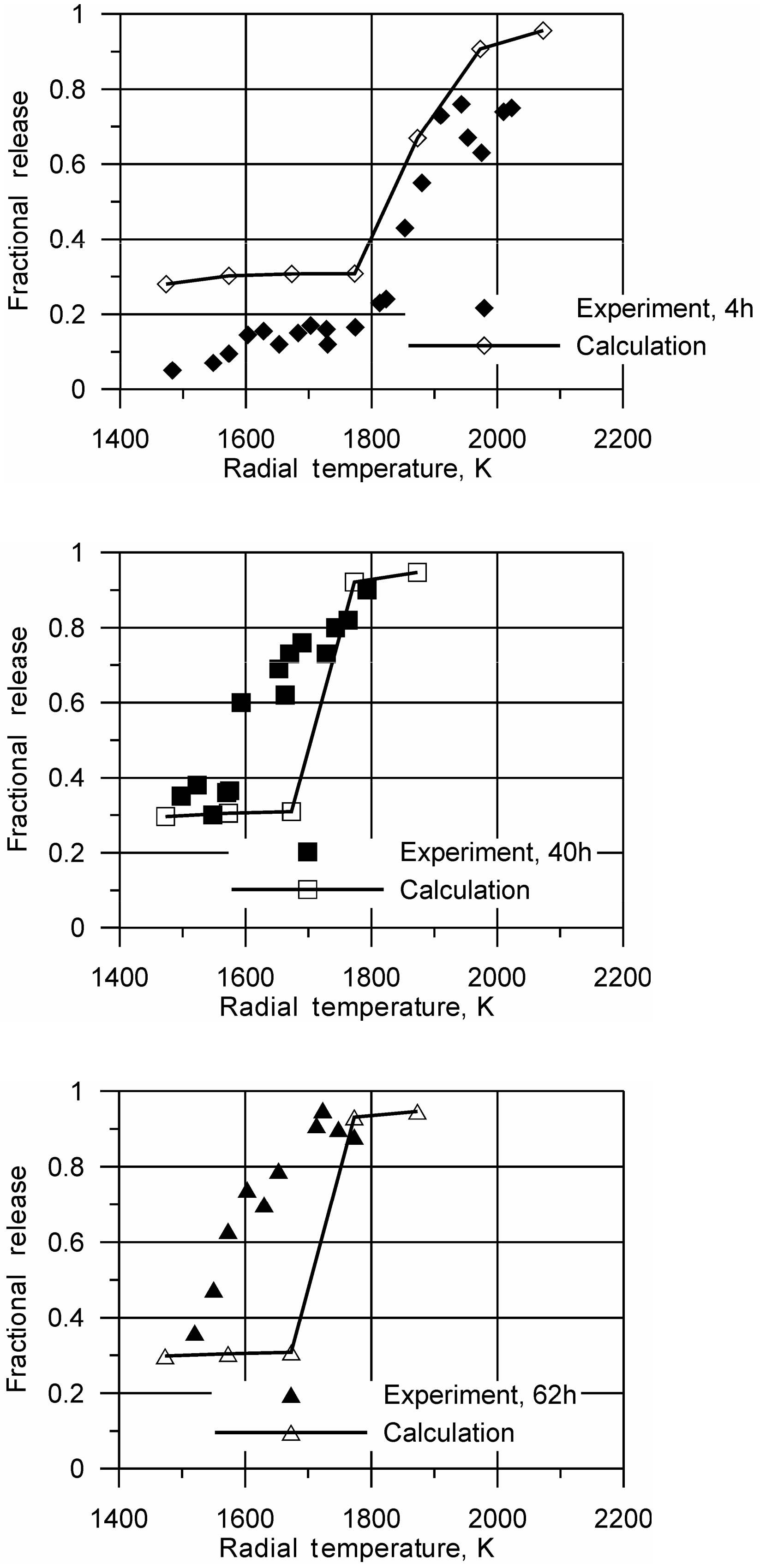

Fig. 5. Fraction of Xe released from the UO_2 as a function of the terminal local fuel temperature

Comparison of the local grain size measured in [7] and calculated by the MFPR code with the advanced grain growth model (presented in paper of this Collection on p. 109) is shown in Fig. 6. It is seen from these calculations that the grain growth kinetics under transient conditions is also reasonably simulated by the MFPR code[1].

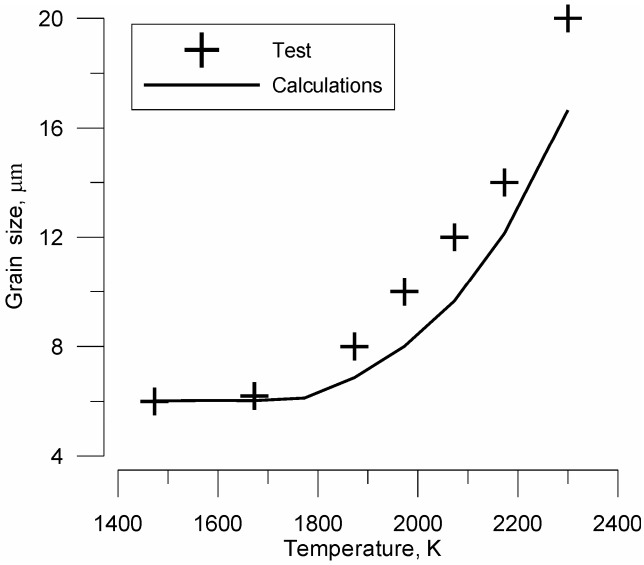

Fig. 6. UO_2 grain size measured in [7] and calculated by MFPR as a function of the terminal local fuel temperature

Conclusions

A new model for self-consistent consideration of the irradiation induced re-solution of gas atoms from bubbles is developed and implemented in the MFPR code. The model modifies the standard Nelson's model [2] by additional consideration of the influx of the ejected atoms back to the bubble by diffusion within the re-solution layer which becomes essential for intragranular bubbles with $R_b \geq 5$ nm. As a result, the new model allows prediction of the onset and growth of very large intragranular bubbles under conditions of transient tests with temperature increase, in qualitative and quantitative agreement with the ITU test observations [5].

Being applied to the transient conditions of the Risø tests [7], the model allows reasonable prediction by the MFPR code of fractional gas releases (measured by post-test examinations of the specimens) as a function of the terminal local fuel temperature. Being combined with the advanced grain growth model (paper of this Collection on p. 109), the code also allows reasonable predictions of the grain sizes measured in various radial positions of fuel pellets.

References

1. *Veshchunov M.S.* // J. Nucl. Mater. 2000. Vol. 277. P. 67.
2. *Nelson R.S.* // Idid. 1969. Vol. 31. P. 153.
3. *Turnbull J.A.* // Ibid. 1974. Vol. 50. P. 62.
4. *Baker C.* // Ibid. 1977. Vol. 71. P. 117.
5. *Ray I.L.F., Thiele H., Matzke Hj.* // Ibid. 1992. Vol. 188. P. 90.
6. *Mikhlin E.Ya.* // Ibid. 1979. Vol. 87. P. 405.
7. *Bagger C., Mogensen M., Walker C.T.* // Ibid. 1994. Vol. 211. P. 11.

---

[1] The authors thanks Mr. D. Antropov for these calculations.

Model for Grain Growth Kinetics in UO_2 fuel

M.S. Veshchunov, D.S. Antropov

Introduction

Grain growth is the process by which the mean grain size of aggregates of crystals increases. The driving force for this process results from the decrease in free energy which accompanies reduction in total grain boundary area. Second-phase inclusions act as pinning agents to grain boundaries since the attachment of an inclusion reduces the total boundary energy by an amount equal to the specific surface energy times the area occupied by the inclusions. If the inclusions are relatively immobile, a boundary pinned at an inclusion (with the pinning force F_b) can only move by breaking free. This occurs when the driving force ΔG for the boundary migration exceeds the pinning force $n_b F_b$ exerted by n_b bubbles (per unit boundary square) on the boundary. In the case of mobile second-phase inclusions (e.g., gas bubbles or pores), they migrate along with the boundaries, in some circumstances giving a boundary migration rate controlled by the movement of the second-phase particles.

Speight and Greenwood [1] proposed a grain growth theory that includes the sweeping of entrapped microbubbles by the front of an advancing grain boundary. The basic postulate of their theory is that small bubbles, because they exert a minimal drag force on an advancing grain surface, are swept along with the moving boundary, whereas large bubbles, because of their higher drag, can detach from the advancing surface.

This theory was applied in the VICTORIA code [2] to modelling grain growth and grain boundary sweeping. Various types of grain boundary pores and bubbles (i.e., grain face, edge and corner) which exert different drag forces owing their different shapes and sizes were additionally considered in the code following Rest [3]. In this approach the drag force exerted by an attached bubble moving along with the boundary is calculated as the pinning force F_m, evaluated for immobile inclusions. For this reason, the grain boundary velocity is determined in [2] by the resulting force $\Delta G - n_b F_m$ acting on the boundary and the grain boundary mobility u_{gb}:

$$v_{gb} = u_{gb}\left(\Delta G - F_b n_m\right).$$

Naturally, such an approach is valid only for estimation of the pinning effect on the boundary exerted by immobile inclusions. In the general case the resulting drag force can be significantly lower and essentially dependent on the inclusions mobility. For this reason, the drag force should be calculated self-consistently with the grain boundary velocity as proposed by Nichols [4].

However, Nichols analysed a simplified problem of a single boundary movement representing an average behaviour of an aggregate of crystals, without consideration of a real size distribution of grains and their coalescence. Such a consideration can be done in the framework of Hillert's mean-field approach [5] and was performed in the authors' papers [6, 7]. Besides, an additional consideration of various types of grain boundary pores and bubbles (i.e., grain face, edge and corner) which exert different drag forces owing to their different shapes and sizes, was carried out and eventually resulted in

$$\bar{v}_{gb} = \frac{d\bar{R}_{gr}}{dt} = v_{gb}^{(0)}\left(1 + \frac{81 v_{gb}^{(0)}\bar{R}_{gr}}{8\xi\gamma_{gb}}\cdot\left(n_f b_f^{-1} + n_e b_e^{-1} + n_c b_c^{-1}\right)\right)^{-1}, \qquad \text{(I.1)}$$

where $v_{gb}^{(0)} = u_{gb} \cdot \Delta G$ is the grain boundary velocity without bubbles, $\bar{R}_{gr}$ is the mean grain radius, n_i and b_i are concentrations and mobilities of face (*f*), edge (*e*) and corner (*c*) bubbles, respectively.

Another deficiency of Nichols' analysis [4] is associated with consideration of a retarding effect using the standard mechanisms of bubble mobility derived by Shewmon [8] for intragranular bubbles. However, besides a more complicated (so called "lenticular") shape of grain face bubbles, the migration mechanism of these bubbles might be essentially different from that of the intragranular bubbles, owing to their specific location on and interaction with a grain boundary. A new mechanism of the lenticular grain-face bubble migration which controls the bubble mobility and determines the drag force exerted on the grain boundary, proposed in the authors' paper [7] will be presented in Section 1.

In Section 2 the new mechanism of the intergranular face bubble migration is applied to consideration of the peripheral bubbles in the mean field approximation following the original publication of the authors [9].

In Section 3 of the current paper further improvement of the grain growth model controlled simultaneously by intergranular pores and bubbles migration, is presented. For this purpose, pore coalescence during grain growth (considered in the authors' papers [10]) and pores shrinkage, caused by vacancies knockout from pores under irradiation and by vacancies thermal evaporation, are self-consistently considered in the improved model.

Implementation of the advanced grain growth model in the MFPR code and its validation against various tests are presented in Sections 4 and 5.

1. Grain growth kinetics controlled by grain-face bubble migration

In accordance with [4, 8], the mobility of a spherical intragranular bubble with radius R_b is determined by various migration mechanisms:

$$b \propto R_b^{-n}, \qquad (1.1)$$

where $n = 3$ for the mechanisms of lattice diffusion and gas phase transport, and $n = 4$ for the surface diffusion mechanism.

It was usually assumed that the same migration mechanisms can be also applied to the grain face bubbles with some renormalisation of the proportionality coefficient in Eq. (1.1), owing to a more complicated lenticular form of these bubbles (see below Section 2.3). However, a more profound difference from free intragranular bubbles arises on grain faces, which can significantly reduce the intergranular bubble mobility and thus migration velocity of the grain boundary. This new rate determining mechanism proposed in [7] of bubble migration will be presented in this Section.

1.1. Phenomenological consideration

Before presenting a more detailed "microscopic" consideration of the grain boundary migration with attached bubbles, a phenomenological approach to calculation of the retarding force exerted by bubbles on the moving boundary will be presented.

The driving force for the boundary migration can be derived from the pressure gradient across the boundary arising from its curvature given by expression $\Delta G = \xi \gamma_{gb} / R_{gr}$. This pressure gradient between the two adjacent grains provides different boundary conditions also for gas bubbles in these grains; in particular, an additional external hydrostatic pressure $p_{\exp} = \Delta G$ is applied to the spherical segment of the lenticular bubble surface in the shrinking grain.

In order to clarify the nature of the drag force exerted on the grain boundary by an attached bubble, at first a simplified limiting case of a complete equilibrium of the lenticular bubble with both grains (shrinking and growing) separated by the boundary under steady-state conditions, will be considered, Fig. 1. In this limiting case:

$$\Delta p_2 \equiv p_b - 2\gamma_s / R_2 = 0, \qquad (1.2)$$

$$\Delta p_1 \equiv p_b - 2\gamma_s / R_1 - \Delta G = 0, \qquad (1.3)$$

where p_b is the internal bubble pressure, R_1 and R_2 are the curvature radii of the two surface segments of the bubble.

One can see from Eqs. (1.2) and (1.3) that the curvature radii of the two bubble surfaces are different, this induces different contact angles θ_1 and θ_2 with the grain boundary:

$$R_1 \cdot \sin\theta_1 = R_2 \cdot \sin\theta_2 = \rho_b, \qquad (1.4)$$

where ρ_b is the projected radius of the bubble in the plain of the boundary.

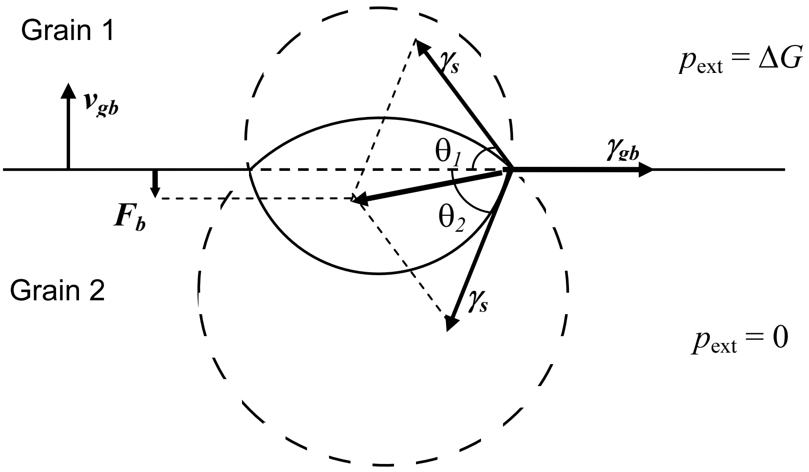

Fig. 1. Determination of the drag force exerted by attached lenticular bubble on moving grain boundary

Assuming a balance between the surface tension forces in the plane of the grain boundary under steady-state conditions:

$$\gamma_{gb} = \gamma_s \left(\cos\theta_1 + \cos\theta_2\right), \qquad (1.5)$$

one can calculate a net force exerting by the bubble on the grain boundary in the normal to the grain boundary direction (see Fig. 1):

$$2\pi\rho\gamma_s \left(\sin\theta_2 - \sin\theta_1\right) - F_b. \qquad (1.6)$$

Substituting Eqs. (1.2)–(1.5) in Eq. (1.6), one gets

$$F_b = \Delta G \cdot \pi\rho_b^2, \qquad (1.7)$$

and therefore, the driving force for the grain boundary migration is reduced proportionally to the reduction of the grain boundary area owing to its coverage with bubbles:

$$\Delta G' = \Delta G - F_b n_b = \Delta G\left(1 - n_b \cdot \pi\rho_b^2\right). \qquad (1.8)$$

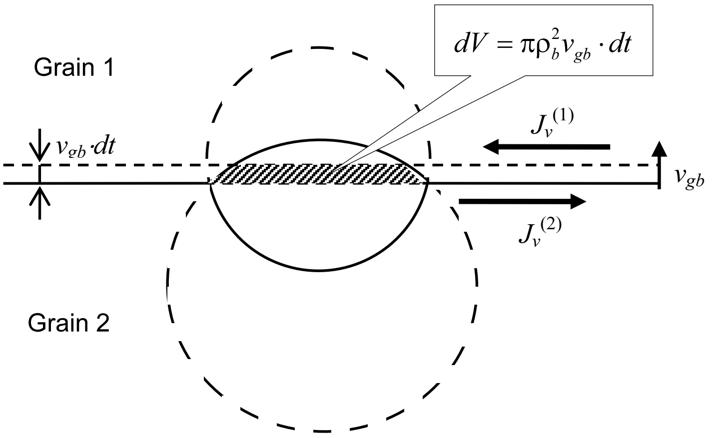

Fig. 2. Determination of vacancy fluxes along the grain boundary in two adjacent grains providing relocation of a lenticular bubble coherently with the grain boundary

The above presented consideration of the bubble equilibrium with the two grains can be justified only in the case when the rate determining process of bubble mobility is infinitely fast in comparison with the grain boundary migration. In a more general case of a finite bubble mobility, a complete equilibrium between the bubble and the two grains is not attained, hence Eqs. (1.2) and (1.3) are not anymore valid. It is straightforward to show that in order to uphold a coherent migration of the grain boundary and the attached bubble in this case, the values Δp_1 and Δp_2 become non-zero and obey the relationship

$$\begin{aligned}\Delta p_1 = p_b - \frac{2\gamma}{R_1} - \Delta G = \\ = -\Delta p_2 = \frac{2\gamma_s}{R_2} - p_b = \varepsilon > 0.\end{aligned} \tag{1.9}$$

Indeed, during a time interval dt the grain boundary moves over a distance $v_{gb} \cdot dt.$ If the bubble is “frozen” at its position, the volume of the upper part of the bubble will be decreased by a value $dV = \pi\rho_b^2 v_{gb} \cdot dt$, whereas the volume of the lower part will be increased by the same value dV, see Fig. 2. In order to sustain the bubble migration with the grain boundary velocity v_{gb}, vacancy fluxes along the upper and lower surfaces of the grain boundary, $J_v^{(1)}$ and $J_v^{(2)}$, should compensate these volume variations:

$$\begin{aligned}J_v^{(1)} 2\pi\rho_b \Omega dt = -J_v^{(2)} 2\pi\rho_b \Omega dt = \\ = dV = \pi\rho_b^2 v_{gb} \cdot dt,\end{aligned} \tag{1.10}$$

where Ω is the vacancy volume. It is assumed that each of the vacancy fluxes ($J_v^{(1)}$ or $J_v^{(2)}$) occurs in a thin surface layer with a thickness $w \approx 0.5$ nm of the corresponding grain (grain 1 or grain 2), characterised by a relatively high self-diffusion coefficient D_{gb}.

These fluxes will be farther calculated in the following Section 1.2, nevertheless, from the physical point of view (confirmed by calculations presented below) it is clear that the values of $J_v^{(1)}$ and $J_v^{(2)}$ are determined by the pressure differences Δp_1 and Δp_2, respectively, which should obey condition $\Delta p_1 = -\Delta p_2$, Eq. (1.9), in order to sustain relationship $J_v^{(1)} = -J_v^{(2)}$, Eq. (1.10).

Eqs. (1.4)–(1.6) are still valid for the considered case of a non-equilibrium bubble with the steady-state lenticular shape, and along with Eq. (1.9) determine the retarding force:

$$\begin{aligned}F_b = 2\pi\rho\gamma_s \left(\sin\theta_2 - \sin\theta_1\right) = \\ = \pi\rho_b \left(\Delta G + 2\varepsilon\right).\end{aligned} \tag{1.11}$$

Substitution Eq. (1.11) in Eq. (1.9) results in

$$v_{gb} = u_{gb}\left[\Delta G\left(1 - n_b \cdot \pi\rho_b^2\right) - 2\varepsilon n_b \cdot \pi\rho_b^2\right]. \tag{1.12}$$

Superposition of Eqs. (1.12) and Eq. (1.10) with explicitly calculated fluxes $J_v^{(1)}$ and $J_v^{(2)}$ as a function of ε will finally determine the migration of the grain boundary with attached bubbles.

The same result, Eq. (1.12), derived in the present Subsection in phenomenological approach (i.e., by consideration of mechanical forces, acting on the boundary and bubbles), can be obtained in a more accurate microscopic approach based on self-consistent calculation of vacancy fluxes across and along the grain boundary, which will be presented in the following Subsection 1.2.

1.2. Microscopic consideration

In accordance with Cole, Feltham and Gilliam [11], migration of a grain boundary of a growing grain takes place in steps of one interatomic spacing a as atoms transfer from the neighbouring grain across the boundary under the pressure difference ΔG across the boundary:

$$v_{gb}^{(0)} = \frac{2\upsilon a\Omega}{kT}\Delta G \exp\left(-\frac{Q}{kT}\right) \equiv u_{gb}\Delta G, \quad (1.13)$$

where v is the atomic oscillation frequency on the grain boundary, Q is the activation energy for self-diffusion in the grain boundary, Ω is the atomic volume. The grain boundary mobility $u_{gb} = \frac{2\upsilon a\Omega}{kT}\exp\left(-\frac{Q}{kT}\right)$ can be also evaluated following Burke and Turnbull [12] as

$$u_{gb} = \frac{D_{gb}\Omega}{2wkT}, \quad (1.14)$$

where $2w \approx 1$ nm is the thickness of the grain boundary, D_{gb} is the self-diffusion coefficient in the grain boundary.

The above described process of atomic jumps can be equivalently considered as translations of vacancies from the growing grain to the adjacent one with the same rate as translations of atoms in the opposite direction. The corresponding flux of vacancies $\tilde{J}_v^{(0)}$ in the normal to the grain boundary direction is uniform over the grain boundary surface (with the total area S) and thus determines the grain boundary relocation during the time interval dt, in accordance with the following relationship: $\tilde{J}_v^{(0)}\Omega S \cdot dt = S \cdot dx$. Therefore, the grain boundary migration velocity $v_{gb}^{(0)} = dx/dt$ can be represented in the form $v_{gb}^{(0)} = \tilde{J}_v^{(0)}\Omega$, and thus

$$\tilde{J}_v^{(0)} = u_{gb}\Delta G/\Omega. \quad (1.15)$$

In the presence of attached bubbles with the surface coverage n$_b$ and mean projected radius ρ_b, the vacancy flux takes place across the reduced surface of the grain boundary $S\left(1 - n_b\pi\rho_b^2\right)$. In the limiting case (corresponding to an infinite bubble mobility, or $\varepsilon \to 0$), when the lenticular bubble attains equilibrium with both grains separated by the boundary, the vacancy flux is still uniform over the reduced grain boundary surface, and thus, Eq. (1.15) can be used in the balance equation:

$$v_{gb}^{(0)} S = \tilde{J}_v^{(0)}\Omega S\left(1 - n_b\pi\rho_b^2\right). \quad (1.16)$$

Therefore, in this case the grain boundary velocity is calculated as

$$v_{gb}^{(0)} = u_{gb}\Delta G\left(1 - n_b \cdot \pi\rho_b^2\right), \quad (1.17)$$

in agreement with Eq. (1.8).

In a more general case of a limited bubble mobility when a complete equilibrium between the bubble and the grains is not attained and $\varepsilon > 0$, a spatial variation of the vacancy chemical potential over the grain boundary faces takes place. On the one hand, this chemical potential variation induces the vacancy fluxes to (from) the bubble along the upper (lower) surface of the grain boundary, $J_v^{(1)}$ and $J_v^{(2)}$, introduced in Eq. (1.10). On the other hand, the pressure drop across the boundary becomes also non-uniform over the grain face area. In order to calculate the total vacancy flux across the boundary in this case, one should self-consistently consider the vacancy transport along and across the grain boundary, on the base of calculation of the spatial variation of the vacancy chemical potential.

As shown by Speight and Beere [13], variation of the surface chemical potential $\mu\left(r\right) = \sigma_{nn}\left(r\right)\Omega$ in a grain reflects exactly the steady state distribution of normal stresses over the grain boundary area unoccupied by bubbles. In the currently considered problem with a moving grain boundary under pressure difference across the boundary, such a conclusion should be generalised and independently applied to each of the two adjacent grains, $\mu_{1,2}(r) = \sigma_{nn}^{(1,2)}(r)\Omega$. The integral of these stresses over the area (with the mean radius $R_c \approx \left(\pi n_b\right)^{-1/2}$) associated with one bubble must equal the total load applied to each face of the grain boundary. Hence, following [13], one obtains

$$\Omega^{-1}\int_{\rho_b}^{R_c} \mu_{1,2}(r) 2\pi r dr = \sigma_{1,2}\pi R_c^2 - \left(\frac{2\gamma_s}{R_{1,2}} - p_b\right)\pi\rho_b^2, \tag{1.18}$$

where the first term on the r.h.s. arises from the normal stresses $\sigma_{1,2}$ at each of two surfaces of the grain boundary in the absence of attached bubbles. In the presently considered case these stresses uphold the pressure gradient ΔG across the grain boundary, i.e.,

$$\sigma_2 = \sigma_1 + \Delta G. \tag{1.19}$$

The second term on the r.h.s. of Eq. (1.18) expresses the force which the bubble surface tension exerts on the boundary. This term can be calculated as the integral of the normal stress on the lenticular bubble surface:

$$\mu_{1,2}\left(R_{1,2},\theta\right) = \sigma_{nn}^{(1,2)}\left(\theta\right)\Omega = \left(\frac{2\gamma_s}{R_{1,2}} - p_b\right)\Omega$$

over the corresponding surface segment of the bubble:

$$\int \sigma_{nn}^{(1,2)}\left(R_{(1,2)}\right) dS_{1,2} = \left(\frac{2\gamma_s}{R_{1,2}} - p_b\right)\pi\rho_b^2.$$

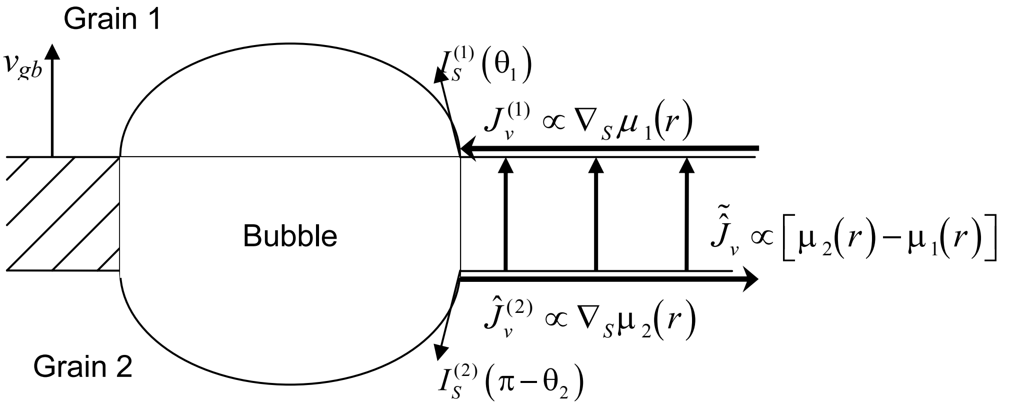

Fig. 3. Schematic representation of vacancy fluxes along and across the grain boundary

As illustrated in Fig. 3, the chemical potential gradients along the grain face surfaces, $\nabla_s\mu_1$ and $\nabla_s\mu_2$, determine the vacancy surface fluxes $J_v^{(1)}$ and $J_v^{(2)}$, introduced in Eq. (1.10), whereas the chemical potential drop across the grain boundary $\partial\mu(r) = \mu_2(r) - \mu_1(r)$ determines the vacancy flux across the grain boundary:

$$\tilde{J}_v(r) = u_{gb}\delta\mu(r)/\Omega^2. \tag{1.20}$$

Integrating this flux over the grain boundary area unoccupied by bubbles and using Eq. (1.18) one can calculate the grain boundary velocity:

$$v_{gb}=\frac{u_{gb}}{\Omega\pi R_c^2}\int_{\rho_b}^{R_c}\left(\mu_2(r)-\mu_1(r)\right)2\pi r dr=u_{gb}n_b\left[(\sigma_2-\sigma_1)\pi R_c^2-\left(\frac{2\gamma_s}{R_2}-\frac{2\gamma_s}{R_1}\right)\pi\rho_b^2\right]. \qquad (1.21)$$

The second term on the r.h.s. of Eq. (1.21) is calculated from Eq. (1.9):

$$\frac{2\gamma_s}{R_2}-\frac{2\gamma_s}{R_1}=2\varepsilon+\Delta G. \qquad (1.22)$$

Substitution of Eqs. (1.19) and (1.22) in Eq. (1.21) results in

$$v_{gb}=u_{gb}\left[\Delta G\left(1-n_b\cdot\pi\rho_b^2\right)-2\varepsilon n_b\cdot\pi\rho_b^2\right], \qquad (1.23)$$

which exactly coincides with Eq. (1.12).

An additional relationship between v_{gb} and ε can be obtained from the balance equation, Eq. (1.10), if the surface vacancy fluxes $J_v^{(1)}$ and $J_v^{(2)}$ are properly ascertained. These fluxes obey the continuity equations on each face of the grain boundary, which in the system of coordinates moving along with the grain boundary take the form

$$\vec{\nabla}_S\cdot\vec{J}_v^{(1,2)}\pm\tilde{J}_v(r)\mp v_{gb}\Omega^{-1}=0 \qquad (1.24)$$

or

$$\frac{D_{gb}w\Omega}{kT}\nabla_s^2\mu_{1,2}\pm\frac{u_{gb}\left(\mu_2-\mu_1\right)}{\Omega}\mp v_{gb}=0, \qquad (1.25)$$

with the boundary conditions

$$\left(\frac{d\mu_{1,2}}{dr}\right)_{r=R_c}=0 \quad \text{and} \quad \mu_{1,2}\left(\rho_b\right)=\left(\frac{2\gamma_s}{R_{1,2}}-p_b\right)\Omega. \qquad (1.26)$$

It is straightforward to see that integration of Eq. (1.25) over the surface non-occupied with the bubbles, directly results in the first part of Eq. (1.21), if Eq. (1.10) is valid.

Solution of Eqs. (1.25) and (1.26) determines the vacancy fluxes at the bubble surface [7]:

$$J_v^{(1)}=-J_v^{(2)}=\frac{D_{gb}w\Omega}{2kT}\left(\Delta G+2\varepsilon-\frac{v_{gb}}{u_{gb}}\right)\chi\frac{K_1\left(\chi\rho_b\right)I_1\left(\chi R_c\right)-I_1\left(\chi\rho_b\right)K_1\left(\chi R_c\right)}{I_0\left(\chi\rho_b\right)K_1\left(\chi R_c\right)+K_0\left(\chi\rho_b\right)I_1\left(\chi R_c\right)}, \qquad (1.27)$$

where $\chi=\sqrt{2u_{gb}kT/D_{gb}w\Omega}$, and $I_{0,1}(x)$ and $K_{0,1}(x)$ represent the first and the second modified Bessel functions of the zeroth and first kind, respectively.

Substitution of Eq. (1.27) in Eq. (1.10) results in the additional relationship for the grain boundary velocity:

$$v_{gb}=\left(\Delta G+2\varepsilon\right)\pi\rho_b^2\left[\frac{D_{gb}w\Omega\chi\varphi\left(\chi\rho_b,\chi R_c\right)}{\pi kT\rho_b^3}\left(1+\frac{D_{gb}w\Omega\chi\varphi\left(\chi\rho_b,\chi R_c\right)}{kT\rho_b u_{gb}}\right)^{-1}\right], \qquad (1.28)$$

where $\varphi\left(\chi\rho_b,\chi R_c\right)=\frac{K_1\left(\chi\rho_b\right)I_1\left(\chi R_c\right)-I_1\left(\chi\rho_b\right)K_1\left(\chi R_c\right)}{I_0\left(\chi\rho_b\right)K_1\left(\chi R_c\right)+K_0\left(\chi\rho_b\right)I_1\left(\chi R_c\right)}$.

In the meaningful limit $R_c >> w$, $\rho_b \geq w$, one has with a very good accuracy $\varphi\left(\chi\rho_b, \chi R_c\right) \approx 1$, until $\rho_b < R_c$:

$$v_{gb} = \left(\Delta G + 2\varepsilon\right)\pi\rho_b^2 \left[\frac{D_{gb} w\Omega\chi}{\pi k T \rho_b^3}\left(1 + \frac{D_{gb} w\Omega\chi}{kT\rho_b u_{gb}}\right)^{-1}\right] = F_b b_f . \tag{1.29}$$

Superposition of Eqs. (1.23) and (1.29) allows exclusion of the parameter ε and final calculation of the grain boundary velocity:

$$v_{gb} = \frac{u_{gb}\, b_f / n_b}{u_{gb} + b_f / n_b}\Delta G , \tag{1.30}$$

where the bubble mobility is presented by the expression in brackets of Eq. (1.29):

$$b_f = \frac{D_{gb} w\Omega\chi}{\pi k T \rho_b^3}\left(1 + \frac{D_{gb} w\Omega\chi}{kT\rho_b u_{gb}}\right)^{-1} . \tag{1.31}$$

A further simplification of Eq. (1.31) can be attained using evaluation of the grain boundary mobility u_{gb} in Eq. (1.14) resulting in $\chi \approx w^{-1}$. In this case the bubble mobility can be approximated as

$$b_f = \frac{D_{gb}\Omega}{\pi k T \rho_b^3}\left(1 + \frac{2w}{\rho_b}\right)^{-1} \approx \frac{D_{gb}\Omega}{\pi k T \rho_b^3} . \tag{1.32}$$

2. Retarding effect of peripheral bubbles on grain growth in irradiated fuel

In the current section the new mechanism of the peripheral intergranular bubble migration associated with vacancy fluxes along grain boundary is considered following the original publication of the authors [9].

The shape of UO_2 grains is considered as truncated octahedron or tetrakaidecahedron (TDK) [14]. The TDK has 14 faces, six of which are square and eight hexagonal, 36 edges and 24 corners. When packed together an array of TDKs can fill all available space in a solid and thus represents an appropriate basic building block. The meeting point of each grain face is shared by two grains, each grain edge by three grains and each grain corner by four grains. Face bubbles are uniformly distributed over these faces with the surface concentration $n_f = 1/\pi R_c^2$ and bubbles of the two other types (N_e edge and N_c corner bubbles, associated with one grain face) are located on the periphery of the faces, Fig. 4.

Tucker has further rationalized the TDK structure by assuming that the grain is composed of fourteen circular faces with radius *e* [15]. The grain edge porosity is represented in this model by a tube (or "toroid") threading around the circumference of the grain face. The volume of toroid is equal to the volume of edge porosity V_Σ associated with one. Toroid is formed by rotation of arc GH (IH) around the vertical axis passing through the center of grain face [15], as shown in Fig. 5.

In the process of the grain boundary migration, toroid changes its form similarly to grain face bubbles and one should distinguish between upper and lower surfaces of toroid. Each of these surfaces is determined by their own radius of curvature $b_{1,2}$ and contacted angle $\theta_{1,2}$, which obey to so-called «lacing equation»:

$$\frac{b_1 \sin\left(\theta_1 + \phi - \pi/2\right)}{\sin(\pi - \phi)} = \frac{b_2 \sin\left(\theta_2 + \phi - \pi/2\right)}{\sin(\pi - \phi)} (= m) , \tag{2.1}$$

that is analogous to the relationship (1.4) for the face bubbles.

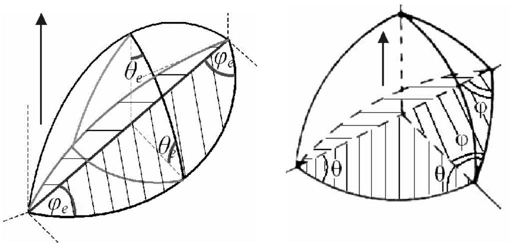

Fig. 4. Peripheral grain boundary bubbles (edge and corner)

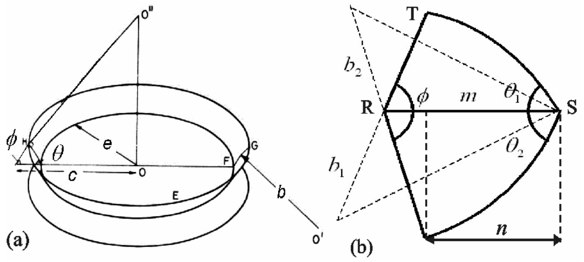

Fig. 5. Toroid (a) and its cross-section (b)

2.1. Continuity equation for vacancy fluxes on grain face

The vacancy flux to the periphery of the grain face will be calculated within the mean field approximation. In this approach vacancy sinks into the face bubbles are represented as a sink uniformly distributed over the grain face with the strength:

$$S = \frac{J_{1,2}^{\text{face}}(r = \rho_b) \cdot 2\pi\rho_b\Omega}{\pi R_c^{\ 2}}. \tag{2.2}$$

From the condition of coherent relocation of the grain boundary-bubble complex, Eq. (1.10), the distributed sink strength, Eq. (2.2) of face bubbles occupying the grain face with the surface concentration $n_f = 1 / \pi R_c^2$ tares the form

$$S = \mp \rho_b^2 v_{gb} / R_c^2. \tag{2.3}$$

The continuity equations at each face of the grain boundary in the system of coordinates moving along with the grain boundary, takes the form

$$-\vec{\nabla}_S J_{1,2} \pm u_{gb}\left(\mu_2 - \mu_1\right)/\Omega \mp v_{gb} \mp S = 0 \tag{2.4}$$

with the boundary conditions at the grain face periphery [15]:

$$\mu_{1,2}\left(r = e\right) = \left(K_{1,2}\gamma_s - p_{\text{tor}}\right)\Omega, \tag{2.5}$$

where $K_{1,2}$ is the toroid surface curvature and p_{tor} is the gas pressure in the toroid. The first term in Eq. (2.4) is the vacancy flux along the upper (lower) face of the grain boundary:

$$J_{1,2} = -\frac{D_{gb}w}{kT\Omega}\nabla_S\mu_{1,2}, \tag{2.6}$$

and the second term is the vacancy flux across the grain boundary.

Superposition of equations (2.4) forms the system of Laplace and Helmholtz type equations for $\mu_2 + \mu_1$ and $\mu_2 - \mu_1$ which has solution (see Appendix A):

$$\mu_{1,2}(r) = -\frac{\Delta G}{2} \mp \left(\left(\Delta G + 2\varepsilon_{\text{tor}}\right)\Omega - \left(v_{gb} + S\right)\frac{\Omega}{u_{gb}} \right) \frac{I_0\left(\chi r\right)}{2I_0\left(\chi e\right)} \mp \left(v_{gb} + S\right)\frac{\Omega}{2u_{gb}}, \tag{2.7}$$

where $\varepsilon_{\text{tor}} = K_2\gamma_S - p_{\text{tor}}$.

Correspondingly, the total vacancy flux to (from) the grain boundary periphery with perimeter 2π*e*, along the upper (lower) surface of the grain boundary is

$$J_{1,2} = \mp\left(\left(\Delta G + 2\varepsilon_{\text{tor}}\right) - \frac{v_{gb}+S}{u_{gb}}\right)\frac{\pi e D_{gb} w \chi}{kT}\,\frac{I_1(\chi e)}{I_0(\chi e)}. \tag{2.8}$$

Self-consistency of the above presented mean-field approximation is shown in Appendix B.

2.2. Coherent migration of edge and corner bubbles

The calculated vacancy flux to the periphery should be distributed between two kinds of the peripheral bubbles. Such a distribution can be described by two weighing factors η_e, η_c, so that the vacancy flux to (from) each kind of the bubbles is equal to

$$I_{1,2}^{(e,c)} = \eta_{e,c} J_{1,2} / N_{e,c}\,. \tag{2.9}$$

These factors can be found from condition of the equal velocities of the two kinds of the bubbles:

$$v_e = v_c = v_{gb}\,. \tag{2.10}$$

Indeed, displacement of the grain boundary with the attached peripheral bubbles is associated with relocation of the bubbles cross-sections, dashed in Fig. 4. Areas of these cross-sections are S_e and S_c. Therefore, a part of the bubble volume swept by the moving grain boundary $dV_{e,c} = S_{e,c} v_{gb}$ should be compensated by the vacancy fluxes $I_{1,2}^{(e,c)}$ over the grain boundary faces, which provide bubbles migration with the grain boundary velocity v_{gb} (compare with a similar consideration for the face bubbles in Eq. (1.10)):

$$v_{gb} S_{e,c} = I_{1,2}^{(e,c)} \Omega\,. \tag{2.11}$$

Comparing Eqs. (2.10) and (2.12) one can evaluate

$$\eta_{e,c} = \frac{S_{e,c} N_{e,c}}{S_c N_c + S_e N_e}\,. \tag{2.12}$$

2.3. Forces exerted on peripheral bubbles and toroid

Similarly to consideration of face bubbles in Section 1.2, the integral of the normal stress over the unoccupied area associated with one «toroidal bubble» must equal the total load applied to each face of the grain boundary. Hence, one obtains

$$\begin{aligned} \Omega^{-1} \int_{S_{face}} \mu_{1,2}(r) 2\pi r dr &= \\ = \sigma_{1,2} \pi e^2 - \left(K_{1,2}\gamma_s - p_{tor}\right) S_{tor} &, \end{aligned} \tag{2.13}$$

where the first term on the r.h.s. arises from the normal stresses $\sigma_{1,2}$ at each of two surfaces of the grain boundary in the absence of the attached toroidal bubble. In the presently considered case of the moving boundary these stresses uphold the pressure gradient Δ*G* across the grain boundary, i.e.,

$$\sigma_2 = \sigma_1 + \Delta G\,. \tag{2.14}$$

The second term on the r.h.s. of Eq. (2.13) expresses the force which the toroid surface tension exerts on the boundary. This term can be calculated, for example, analogously to the l.h.s. of Eq. (2.13) as the integral of the normal stress on the toroidal bubble $\mu_{1,2}\left(R_{1,2},\theta\right) = \sigma_{nn}^{(1,2)}(\theta)\Omega = \left(K_{1,2}\gamma_s - p_{tor}\right)\Omega$ over the corresponding segment of the toroidal bubble:

$$\begin{aligned} F_{1,2} = \int \sigma_{nn}^{(1,2)} \cos\theta \cdot dS_{1,2} &= \\ = \left(K_{1,2}\gamma_s - p_{\text{tor}}\right) S_{\text{tor}} &, \end{aligned}$$

where S_{tor} is the toroid projection area. In order to sustain a coherent migration of the grain boundary and the attached toroid, the vacancy fluxes $J_v^{(1)}$ and $J_v^{(2)}$, which are determined by the pressure differences Δp_1 and Δp_2, respectively, should obey the relationship $J_v^{(1)} = -J_v^{(2)}$, which results in the condition $\Delta p_1 = -\Delta p_2$:

$$\begin{aligned} p_{\text{tor}} - \Delta G - K_1\gamma_S &+ \\ + p_{\text{tor}} - K_2\gamma_S &= 0 \end{aligned}\,. \tag{2.15}$$

Therefore, the force acting on the toroid F_{tor} is equal to:

$$F_{tor} = F_2 - F_1 = \left(K_2\gamma_S - K_e\gamma_S\right)S_{tor} = \left(\Delta G + 2\varepsilon_{tor}\right)S_{tor}, \tag{2.16}$$

After substitution of Eqs. (2.8) and (2.9) in Eq. (2.15) and taking into account Eq. (2.16) one obtains:

$$v_{gb} = \frac{D_{gb}\Omega}{kTS_{tor}}\left[\frac{S_e N_e}{\pi e \eta_e} + 2w\left(1 + \frac{\rho_b^2}{R_c^2}\right)\right]^{-1} F_{tor}. \tag{2.17}$$

Similarly one obtains the force acting on the edge and corner bubbles:

$$F_{e,c} = \left(\Delta G + 2\varepsilon_{e,c}\right)\cdot S_{e,c}, \tag{2.18}$$

where $\varepsilon_{e,c} = \varepsilon_{e,c}\left(R_{e,c1}, R_{e,c2}, p_{e,c}\right)$ from the corresponding conditions for coherent migration of the boundary and the attached bubbles.

2.4. Grain boundary retarding effect

The grain boundary velocity depends on the net force acting on the boundary:

$$v_{gb} = \frac{dR_{gr}}{dt} = u_{gb}\left(\Delta G - F_f n_f - F_e n_e - F_c n_c\right), \tag{2.19}$$

where n_i is the surface concentration of the *i*-th bubbles.

Each grain face with the surface area πe^2 has one toroid bubble, so, one should assign to the toroid bubbles the surface concentration $1/\pi e^2$. The force acting on the toroid must be equal to the sum of forces acting on the edge and corner bubbles:

$$F_{\text{tor}} = \left(F_e n_e + F_c n_c\right)\pi e^2. \tag{2.20}$$

In this case the grain boundary retarding effect associated with the toroid coincides with one associated with the peripheral bubbles. Therefore, the grain boundary velocity can be represented in the form

$$v_{gb} = u_{gb}\left(\Delta G - F_f n_f - F_{\text{tor}}/\pi e^2\right). \tag{2.21}$$

Superposition of Eqs. (1.29), (2.17), (2.20) and (2.21) results in the relationship for the boundary velocity:

$$v_{gb} = u_{gb}\Delta G\left[1 + u_{gb}\left(\frac{D_{gb}\Omega}{kT\pi\rho_b^3}\right)^{-1} n_f + u_{gb}\left(\frac{S_e N_e}{\pi e \eta_e} + 2w\left(1 + \frac{\rho_b^2}{c^2}\right)\right)\cdot\left(\frac{D_{gb}\Omega}{kT}\right)^{-1}\frac{S_{\text{tor}}}{S_{\text{face}}}\right]^{-1}. \tag{2.22}$$

For a more realistic description of grain growth with consideration of size distribution and coalescence of grains one can obtain for the mean grain velocity a new relationship instead of Eq. (2.22), taking into account the relationship $\Delta G = \xi\gamma_{gb}/R_{gr}$ and assumption about different diffusion coefficient along ($D_{gb}^{(l)}$) and across ($D_{gb}^{(p)}$) the grain boundary (see Section 4 below):

$$\bar{v}_{gb} = \bar{v}_{gb}^{(0)}\left[1 + \frac{81 v_{gb}^{(0)}\bar{R}_{gr} n_f kT}{8\xi\gamma_{gb}\Omega\sqrt{D_{gb}^{(p)}D_{gb}^{(l)}}}\left(n_f\pi\rho_b^3 + \frac{S_{\text{tor}}}{S_{\text{face}}}\left(\frac{S_e N_e}{\pi e \eta_e} + 2w + 2w\rho_b^2/c^2\right)\right)\right]^{-1}, \tag{2.23}$$

where $S_{\text{tor}} \approx 2\pi e^2\sqrt{\Delta V/V_0}$ from geometrical consideration.

3. Combined retarding effect of pores and bubbles on grain growth in irradiated fuel

The grain growth model presented in Section 2 was in [10] further developed and applied to the analysis of the normal grain growth kinetics controlled by pore migration during fresh UO_2 thermal treatment (sintering). Additional consideration of fuel densification (i.e., porosity reduction) allows explanation of complicated grain growth kinetics characterised by non-integer growth exponents observed in recent tests [16].

Under irradiation conditions pores additionally shrink owing to vacancy knockout mechanism suggested by Dollins and Nichols [17]. Self-consistent consideration of both pore shrinkage mechanisms will be presented in the current Section.

Furthermore, the retarding effect on the moving grain boundaries from both types of intergranular porosity, i.e., pores and gas-filled bubbles, should be simultaneously considered in the general case of porous fuel under irradiation conditions.

3.1. Effect of pores on normal grain growth kinetics

Grain growth in the final stage of UO_2 fuel sintering is the result of interactions between grain boundaries and residual porosity. Pores on the grain boundaries give rise to drag effect which impedes boundary motion. In the majority of experimental studies grain growth was approximated by a more slow kinetic equation:

$$\bar{R}_{gr}^{n}(t) - \bar{R}_{gr}^{n}(0) = K't$$

with the growth exponent $n = 3$ or 4. Recently it was revealed that in many cases the grain growth kinetics must be described by non-integer exponents, somewhat different from 3 or 4 [16].

For explanation of the normal grain growth kinetics, a series of models has been proposed, most of them based on consideration of Kingery and François [18]. They assumed that, as grains are removed in the growth process, pores migrating with the boundaries are brought together, and pore growth occurs together with grain growth, see [10]. After, say, twofold increase of the mean grain size, an amount of grains N_{gr} decreases by one order of magnitude ($N_{gr} \propto \bar{R}_{gr}^{-3}$), and practically all pores are located at grain corners, so amount of pores N_p becomes proportional to the amount of grains, $N_p \propto N_{gr}$.

Shrinkage of an isolated pore owing to vacancies evaporation during thermal annealing can be calculated by application of the Speight and Beere's approach [13] (for the grain face cavities) to the case of the corner pore, which is located at intersection of 6 grain faces (4 hexagonal and 2 square):

$$\frac{\partial V_p}{\partial t} \approx -\frac{3.67\pi\Omega D_{gb} w}{\beta kT}\frac{2\gamma_s}{R_p}, \quad (3.1)$$

where D_{gb} is the grain boundary self-diffusion coefficient of uranium atoms, $\beta = \ln\left(R_c / R_p\right) - 0.25\left(1 - R_c^2 / R_p^2\right)\left(3 - R_c^2 / R_p^2\right)$ is the dimensionless factor, $\left(\pi R_c^2\right)^{-1} = n_p$ determines the radius of the pore sinking zone R_c, which can be estimated taking into account that 24 corners are distributed over the grain surface with the area of $\approx 4\pi R_{gr}^2$, i.e.,

$$n_p \approx 6/\pi R_{gr}^2 \quad \text{and} \quad R_c \approx R_{gr}\big/\sqrt{6}, \quad (3.2)$$

where n_p is the surface concentration of corner pores on the boundary.

Therefore, decrease of an isolated pore radius can be evaluated from Eqs. (3.1)–(3.2) as

$$\frac{\partial R_p}{\partial t} \approx -\frac{5.5\Omega D_{gb} w}{\beta kT}\frac{\gamma_s}{R_p} \equiv -\frac{\alpha}{R_p}, \quad (3.3)$$

where

$$\alpha = \frac{5.5\Omega D_{gb} w\gamma_s}{\beta kT}. \quad (3.4)$$

Neglecting pores shrinkage, one can obtain (following Kingery and François [18]) that variation of total porosity in the course of pores coalescence is zero, $d\left(N_p\bar{V}_p\right)/dt = 0$. However, taking pores shrinkage into consideration, one will obtain that in this case

$$\frac{d\left(N_p\bar{V}_p\right)}{dt} = N_p\frac{\partial\bar{V}_p}{\partial t}, \qquad (3.5)$$

where

$$\frac{d\left(N_p\bar{V}_p\right)}{dt} = N_p\frac{d\bar{V}_p}{dt} + \bar{V}_p\frac{dN_p}{dt} \qquad (3.6)$$

and

$$N_p \propto N_{gr} \propto \bar{R}_{gr}^{-3}. \qquad (3.7)$$

Here $\partial\bar{V}_p/\partial t$ denotes variation of the pore mean volume owing solely to pores shrinkage, Eq. (3.1), whereas $d\bar{V}_p/dt$ denotes total variation of the pore mean volume owing to pores simultaneous shrinkage and coalescence [10].

Substituting Eqs. (3.1), (3.6) and (3.7) in Eq. (3.5), one obtains

$$\frac{d\bar{R}_p}{dt} - \frac{\bar{R}_p}{\bar{R}_{gr}}\frac{d\bar{R}_{gr}}{dt} = -\frac{\alpha}{3\bar{R}_p^3}. \qquad (3.8)$$

In the case when the corner pore mobility controls grain boundary movement, the relationship for the mean grain radius growth controlled by pore mobility, similar to Eq. (I.2), takes the form

$$\frac{d\bar{R}_{gr}}{dt} \approx \frac{8}{81}\frac{\gamma_{gb}\xi}{\bar{R}_{gr}}\frac{b_p}{n_p} \approx 0.1\frac{\gamma_{gb}\xi}{\bar{R}_{gr}}\frac{b_p\pi\bar{R}_{gr}^2}{6}, \qquad (3.9)$$

where Eq. (3.2) was used for n_p, and $b_p \approx \frac{3D_s\Omega^{4/3}}{2\pi kTR_p^4}$, if the surface diffusion mechanism controls the pore migration kinetics. Substituting this value in Eq. (3.9), finally one obtains

$$\frac{d\bar{R}_{gr}}{dt} = \varphi\frac{\bar{R}_{gr}}{\bar{R}_p^4}, \qquad (3.10)$$

where $\varphi \approx \frac{\gamma_{gb}\xi}{40}\frac{D_s w\Omega}{kT}$.

The system of Eqs. (3.8) and (3.10) has the solution

$$\bar{R}_p \propto \bar{R}_{gr}^{(1-\alpha/3\varphi)}, \qquad (3.11)$$

and

$$\bar{R}_{gr}^{4(1-\alpha/3\varphi)}(t) - \bar{R}_{gr}^{4(1-\alpha/3\varphi)}(0) = Kt. \qquad (3.12)$$

The total porosity reduction can be calculated as $V_{\text{pores}} = N_p\bar{V}_p \propto N_p\bar{R}_p^3 \propto \left(\frac{\bar{R}_p}{\bar{R}_{gr}}\right)^3$ and after substitution of Eq. (3.11)

$$V_{\text{pores}} = N_p\bar{V}_p \propto \bar{R}_{gr}^{-\alpha/\varphi} = \bar{R}_{gr}^{-a}, \qquad (3.13)$$

where $a = \alpha/\varphi$.

Substituting Eqs. (3.4) and (3.12) in Eq. (3.13), one can evaluate

$$a = \alpha/\varphi \approx \frac{220}{\xi\beta}\frac{D_{gb}}{D_s}, \qquad (3.14)$$

where $\xi \approx 1$–2, parameter β depends on the fuel porosity (see designations after Eq. (3.1)) and for the fuel density 96–98 % varies in the range 0.2–0.3. Numerical estimations of Eq. (3.14) were presented in [10].

3.2. Irradiation conditions

Under irradiation conditions an additional mechanism of the irradiation-induced vacancy knockout should be taken in consideration, which results in the following rate equation (instead of Eq. (3.8)):

$$\frac{d\bar{R}_p}{dt} = \frac{\bar{R}_p}{\bar{R}_{gr}}\frac{d\bar{R}_{gr}}{dt} - \frac{\alpha}{3\bar{R}_p^3} - 2\lambda\eta\Omega F, \qquad (3.15)$$

where the new term corresponds to the vacancy knockout model suggested by Dollins and Nichols [17]:

$$\frac{\partial \bar{V}_p}{\partial t} = -8\pi\lambda\eta\Omega F\bar{R}_p^2, \tag{3.16}$$

where F is a fission rate, $\eta = 100$ is the number of vacancies knocked out of a pore per collision and $\lambda = 10^{-6}$ m is the length of the fission fragment path.

In Hillert's mean field approximation for grains coalescence, Eq. (I.1), the mean grain boundary velocity supplemented with the new type of inclusions (pores) takes the form

$$\bar{v}_{gb} = \frac{d\bar{R}_{gr}}{dt} = v_{gb}^{(0)}\left(1 + \frac{81 v_{gb}^{(0)}\bar{D}_{gr}}{16\xi\gamma_{gb}}\left(n_f b_f^{-1} + n_e b_e^{-1} + n_c b_c^{-1} + n_p b_p^{-1}\right)\right)^{-1}, \tag{3.17}$$

where, for the prototypic case of large pores with $R_p \geq 1$ μm the surface diffusion mechanism controls the pore migration kinetics:

$$b_p \approx \frac{3D_s\Omega^{4/3}}{2\pi kTR_p^4}. \tag{3.18}$$

Finally, taking into consideration the new term, the modified Eq. (2.23) takes the form

$$\bar{v}_{gb} = \bar{v}_{gb}^{(0)}\left[1 + \frac{81 v_{gb}^{(0)}\bar{R}_{gr}}{8\xi\gamma_{gb}}\left(n_f b_f^{-1} + \frac{S_{tor}}{S_{face}}\left(\frac{D_{gb}\Omega}{kT}\right)^{-1}\left(\frac{S_e N_e}{\pi e\eta_e} + 2w\left(1 + \frac{\rho_b^2}{R_c^2}\right)\right) + n_p b_p^{-1}\right)\right]^{-1}, \tag{3.19}$$

which in combination with Eq. (3.15) determines the grain growth kinetics controlled by pore and bubble migration in irradiated fuel.

4. Model implementation

New model was implemented in the integral code MFPR, which is developed for analysis of fission products release from irradiated UO_2 fuel [19, 20]. The code simulates evolution of concentration and size of intergranular bubbles, and thus the newly implemented model allows self-consistent calculation of the grain boundary retarding effect by the attached bubbles.

The normal grain growth kinetics in non-irradiated and non-porous fuel is represented in the MFPR code in the standard parabolic form:

$$v_{gb}^{(0)} = v_0\left(\bar{R}_0/\bar{R}_{gr}\right)\cdot\exp\left(-E_{gb}/T\right), \tag{4.1}$$

with activation energy $E_{gb} = 44\,200$ K recommended by Speight and Greenwood [1]. Correspondingly, the diffusivity across the grain boundary evaluated from Eq. (1.14) following Burke and Turnbull [12] is $D_{gb}^{(p)} \approx 4\cdot10^{-6}\cdot\exp(-44200/T)$ m^2/s, whereas the diffusivity along the grain boundary measured by Alcock et al. [21] is $D_{gb}^{(l)} \approx 4\cdot10^{-6}\cdot\exp(-35\,250/T)$ m^2/s. This contradiction can be explained by an assumption that the diffusivity along the grain boundary differs from the diffusivity across the grain boundary [7].

Under this assumption Eq. (1.32) takes the form

$u_b = D_{gb}^{(l)} w\Omega\chi / \pi kT\rho_b^3$, where

$\chi = \sqrt{2u_{gb}kT / D_{gb}^{(l)} w\Omega}$ and

$u_{gb} \approx D_{gb}^{(p)}\Omega / 2wkT$, i.e.,

$$\chi = w^{-1}\sqrt{D_{gb}^{(p)} / D_{gb}^{(l)}}.$$

Therefore, instead of Eq. (1.32) one gets a modified expression for the bubble mobility:

$$u_b \approx \frac{\Omega}{\pi kT\rho_b^3}\sqrt{D_{gb}^{(p)} D_{gb}^{(l)}}. \tag{4.2}$$

5. Model validation

5.1. Turnbull's tests

Validation of the new code version was performed against Turnbull's tests [22], where high-temperature grain growth in irradiated UO_2 fuel was measured. In these experiments the effect of grain size on the swelling and gas release properties of uranium dioxide was studied. Small cylindrical specimens 10 mm long and 3 mm diameter were prepared from 2 % enriched uranium dioxide of near theoretical density. The fuel samples were irradiated at $T = 1750$ °C for period of 2, 4 and 6 months in UKAEA reactor DIDO in a flux of $\approx 2.4 \cdot 10^{17}$ thermal neutrons/($m^2 \cdot s$). During irradiation the temperature was maintained by electrical heating; fission heating produced a temperature gradient within the specimens ≈ 100 °C from center to surface. There were three types of samples with the initial grain diameter $d_{gr} = 7$ μm (specimens A and B) and 40 μm (specimen C), the latter being produced by preliminary annealing of specimens A during 72 hours at $T = 1700$ °C in hydrogen. Specimens B and C were pre-irradiated to 0.02 % burn-up at 80 °C. So, the following identification of the specimens is used:

- specimen A, 7 μm starting grain size;
- specimen B, 7 μm starting grain size, pre-irradiated to 0.02 % burn-up at 80 °C;
- specimen C, 40 μm starting grain size, pre-irradiated to 0.02 % burn-up at 80 °C.

Examination of large-grained specimen C showed the unchanged average grain size, whereas specimens A and B exhibited identical grain growth characteristics with the grain size increasing from 7 μm to 18 μm after 6 months irradiation.

The density of the samples was close to theoretical one, for this reason, parameters of Eq. (4.1) were fitted to reproduce the out-of-pile annealing behaviour of specimen C (i. e., growing from 7 to 40 μm during 72 hours at $T = 1700$ °C): $2\overline{R}_0 = 7$ μm, $v_0 = 1.4$ m/s. The surface concentration of grain face bubbles was estimated as $\approx 4 \cdot 10^{10}$ m^{-2} from the post-test fracture surface image presented in [22].

In order to reveal retarding effect of grain face and peripheral bubbles, experimental results for grain growth kinetics and swelling are compared in Fig. 6 with theoretical curves calculated with several versions of the MFPR code:

- Initial code version, where the standard (surface diffusion) mechanism is applied to the intergranular bubble migration (Fig. 6a) [6];
- Intermediate version, where the new (grain boundary diffusion) mechanism is applied to the grain-face bubbles migration and the standard (surface diffusion) mechanism is applied to the peripheral bubbles (Fig. 6b) (Section 1 of the current paper);
- Final version, where the new mechanism is applied to migration of all intergranular bubbles (Fig. 6c) (Section 2 of the current paper).

In the standard approach using bubble mobility u_s determined by the bubble surface diffusion mechanism, Eq. (1.1) calculations strongly overpredict the measured grain growth kinetics for all three specimens, Fig. 6a.

The new model predicts a rather good agreement for the samples B and C and slightly overpredicts the growth of the sample A. From comparison of curves in Figs. (6b) and (6c) it is seen, that contribution of the peripheral bubbles to the grain boundary retarding effect is essential under the Turnbull's test conditions.

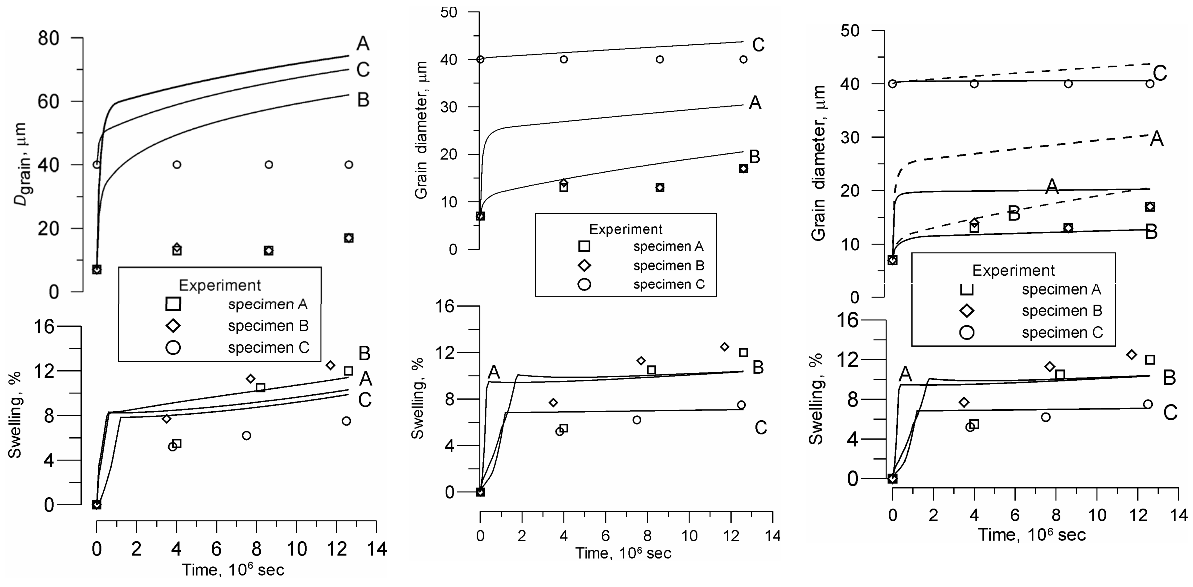

(a) Standard migration mechanism

(b) Grain boundary diffusion mechanism applied to grain face bubbles

(c) Grain boundary diffusion mechanism applied to all grain boundary bubbles (solid lines) in comparison with case (b) (dashed lines)

Fig. 6. MFPR simulation of grain size in Turnbull's test [22]

5.2. Tests of Bourgeois et al.

In the tests [16] already discussed in Section 3.1, the normal grain growth kinetics of fresh UO_2 pellets with the relative density ρ (in % with respect to the theoretical density) annealed in dry hydrogen was studied. Grain sizes and changes in density were measured for two batches, T0 and T12, contained respectively 0 and 12 Wt% U_3O_8. Initial grain sizes T0 and T12 were 8.8 and 10.4 µm and initial pore size can be obtained from expression for intergranular porosity:

$$\rho = \frac{V_{gr}}{V_{gr} + 6V_{\text{pore}}}. \qquad (5.1)$$

In order to reveal influence of pores on normal grain growth kinetics, at first calculations with the standard model neglecting retarding effect of pores were performed, Eq. (4.1.), Fig. 7.

Results of calculations with the implemented new model are presented in Fig. 8. Owing to a large uncertainty in determination of the diffusion coefficients and the coefficient β (from Eq. (3.1)), these parameters were slightly adjusted in order to provide the best agreement between theoretical simulations and experimental points. In these simulations the grain boundary diffusion coefficient D_{gb} was chosen as $4.2\cdot10^{-6}\cdot\exp(-35250/T)$ m^2/s, β was estimated as 0.15 and the surface diffusion coefficient D_s as $56\cdot\exp(-48945/T)$ m^2/s, in a rather close agreement with estimations presented in [24]. Results of calculation with the improved code version show a reasonable agreement for the samples T12 and some underestimation of grain growth for the samples T0.

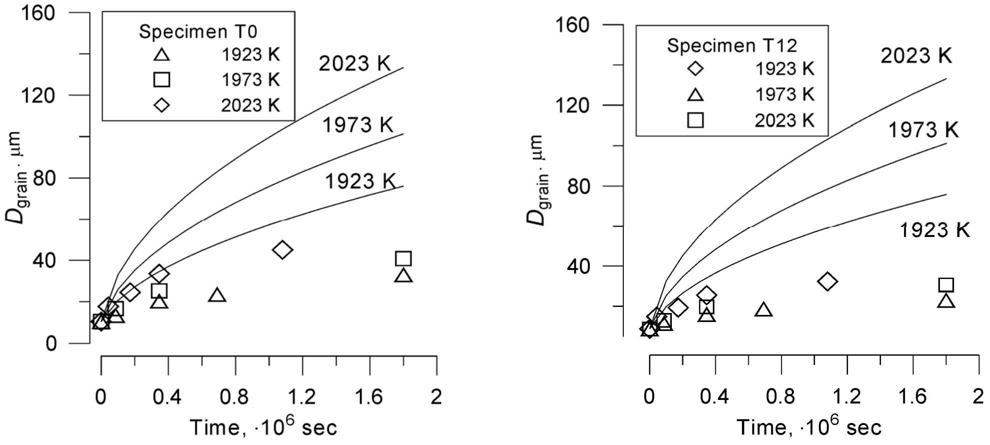

Fig. 7. MFPR simulations of Bourgeois' tests [16].
Standard model for normal grain growth neglecting retarding effect of pores

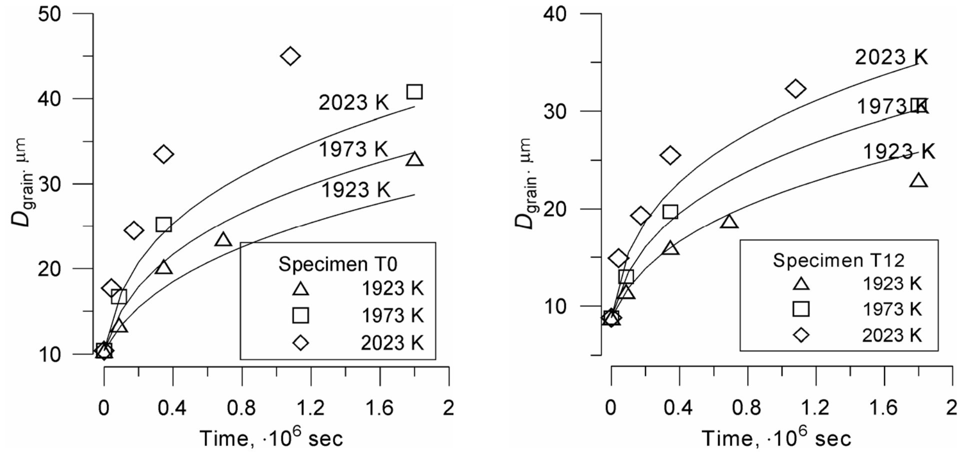

Fig. 8. MFPR simulations of Bourgeois' tests [16].
New model for normal grain growth controlled by intergranular pores

In Fig. 9 calculated curves for fuel density, Eq. (5.1), are compared with experimental data. The attained agreement between simulated porosity evolution and experiment data is also quite satisfactory.

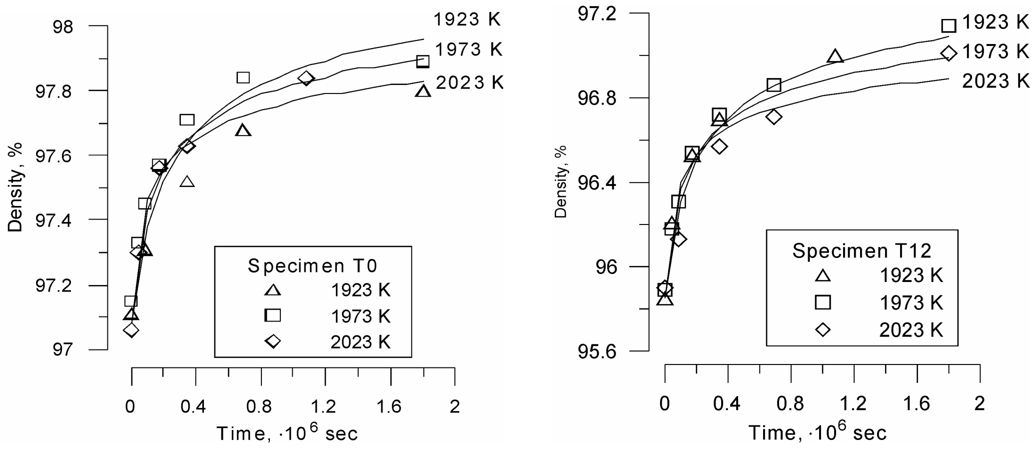

Fig. 9. MFPR simulation of porosity evolution in Bourgeois' tests [16]

5.3. Tests of MacEwan and Hayashi

The MFPR code with the new advanced model was applied to simulation of the grain growth during post-irradiation annealing of uranium dioxide observed in the MacEwan and Hayashi tests [23]. In these tests the effect of prior exposure to irradiation at temperature below 400 °C on subsequent grain growth of UO_2 samples with densities from 94 to 96 % of theoretical density at 1800 °C during 24 hours was studied. Grain growth was reduced in all irradiated specimens, with nearly complete inhibition occurring by $4{\cdot}10^{19}$ fissions/cm^3.

In order to reveal competitive influence of bubbles and pores on grain growth kinetics in pre-irradiated UO_2 samples, calculations were performed with two code versions, respectively including:

- Grain growth model controlled only by bubbles migration presented in Section 1 of the current paper;
- Grain growth controlled by migration of both intergranular pores and bubbles (final version).

The simulation results in comparison with experimental data are presented in Table 1.

It is evident from the simulation results that under irradiation exposure lower than $4{\cdot}10^{18}$ fissions/cm^3 grain growth is limited mainly by intergranular pores, and for exposures greater than $4{\cdot}10^{18}$ fissions/cm^3 migration of intergranular bubbles becomes the rate controlling mechanism.

The grain growth kinetics exponents (presented in Table 1 in parentheses), evaluated from calculated curves using the least-squares method, differ from exponent $n \approx 2.5$ measured in [23], however, they are in a reasonable agreement with the normal grain growth exponents, $3 < n < 4$, measured in the tests of Bourgeois et al. [16].

Table 1. Simulation of the MacEwan and Hayashi tests [23]

Irradiation exposure, fiss./cm^3	Final grain size, μm	Predicted grain size, μm (estimated value of grain growth exponent)	
		Grain growth controlled by bubbles	Grain growth controlled by bubbles and pores
0	16.0	38.5 (2.006)	16.75 (3.675)
$3.8{\cdot}10^{15}$	14.2	38.3 (2.013)	16.75 (3.626)
$3.6{\cdot}10^{16}$	13.8	35 (2.225)	16.74 (3.671)
$2.8{\cdot}10^{17}$	10.8	21.9	16.3 (3.711)
$4.4{\cdot}10^{18}$	–	9.8	10.2
$4.4{\cdot}10^{19}$	8.2	7.2	7.2

Conclusions

A new model for the grain growth in irradiated and non-irradiated UO_2 pellets is developed. As the first step of the new model development, Nichols' approach [4] to consideration of the drag force exerted by attached bubbles and pores on migrating grain boundaries is combined with supplementary consideration of grains coalescence within Hillert's mean field approach [5]. It is shown that the boundary migration rate becomes controlled by the movement of the second-phase particles with significantly smaller sizes than predicted in the simplified approach [4]. An additional consideration recommended by Rest [3] of various types of grain boundary pores and bubbles (i.e., grain face, edge and corner) which exert different drag forces owing to their different shapes and sizes, was performed.

However, Nichols' analysis [4] is based on consideration of retarding effect of bubbles on moving boundary using the standard (surface diffusion) mechanisms of bubble mobility derived for intragranular bubbles. This mechanism was re-considered in the present paper taking into account a more complicated, lenticular, shape of the grain face bubbles. Furthermore, migration mechanism of the grain face bubbles might be essentially different from the intragranular bubbles, owing to their specific location on and interaction with a grain boundary. The new mechanism of the lenticular grain face bubble migration is associated with vacancy fluxes over the grain boundary surfaces to the bubble, which afford coherent relocation of the grain boundary-bubble complex. The calculated mobility of the grain face bubble is characterised by a slower dependence on its projected radius, $\propto \rho_b^{-3}$, in comparison with the surface diffusion mechanism, $\propto \rho_b^{-4}$, which sustains its steady-state lenticular shape in the course of bubble migration. For this reason, the new mechanism becomes the rate controlling step for bubbles migration in a wide range of their radii from ~ 1 nm to ~ 1 μm, and correspondingly, determines the drag force exerted by bubbles on the grain boundary.

The new mechanism of the grain boundary bubbles migration which controls the bubble mobility and determines the drag force exerted on the grain boundary, is further developed in application to the peripheral (edge and corner) intergranular bubbles. As a result, the growth kinetics of grains with different types of intergranular bubbles is calculated. It is shown that contribution of the peripheral bubbles to the retarding effect can be significant, especially under irradiation conditions with high fission rates in UO_2 fuel.

The new model for the grain growth was further extended to consideration of as-fabricated porous fuel on the base of self-consistent simulation of grain growth and fuel densification, which occurs under annealing conditions owing to thermal evaporation of vacancies from (empty) pores. Under irradiation conditions the pore shrinkage is increased owing to vacancy knockout from pores by fission particles, on the one hand, and intergranular bubbles growth takes place owing to sinking of fission gas atoms from grains, on the other hand. Simultaneous consideration of intergranular bubbles and pores evolution allows further improvement of the model predictions for grain growth under irradiation conditions.

The new model was implemented in the integral code MFPR and validated against various test under irradiation [16] and annealing [22, 23] conditions with various types (dense and porous) fuel pellets with and without pre-irradiation. The code predictions for these tests are essentially improved and are in a satisfactory agreement with observations.

Acknowledgments

The original publications of parts of this article in the *Journal of Nuclear Materials* [7, 10] and *Multi-discipline Modeling in Materials and Structures* [9] are greatly acknowledged.

Appendix A. Solution of the continuity equations

In this Appendix will be searched the solution of Eq. (2.4):

$$\frac{D_{gb} w}{kT} \vec{\nabla}_S^2 \mu_{1,2} \pm u_{gb} \left(\mu_2 - \mu_1\right) / \Omega \mp v_{gb} \mp S = 0\,, \tag{A.1}$$

with the boundary conditions, Eq. (2.5):

$$\mu_{1,2}(r=\rho_b)=\left(\frac{2\gamma_S}{R_{1,2}}-p_f\right)\Omega, \qquad \left(\frac{\partial\mu_{1,2}}{\partial r}\right)_{b\to+\infty}=0. \tag{A.2}$$

Superposition of Eqs. (A.1) and (A.2) yields

$$\begin{gathered}\Delta\left(\mu_1+\mu_2\right)=0,\\ \frac{D_{gb}w}{kT}\Delta\left(\mu_1-\mu_2\right)-\frac{2u_{gb}}{\Omega}\left(\mu_1-\mu_2\right)-2v_{gb}-2S=0.\end{gathered} \tag{A.3}$$

System of equations (A.3) can be written in the following form:

$$\begin{gathered}\Delta\left(\mu_1+\mu_2\right)=0,\\ \Delta\eta-\chi^2\eta-B=0,\end{gathered} \tag{A.4}$$

with a new variable $B=\frac{2kT}{D_{gb}w}\left(S+v_{gb}\right)$, where $\chi^2=\frac{2u_{gb}kT}{\Omega D_{gb}w}>0$.

After substitution $N=\chi^2\eta+B$ one obtains the Laplace and Helmholtz type equations for variables $\left(\mu_1+\mu_2\right)$ and N, respectively:

$$\begin{gathered}\Delta\left(\mu_1+\mu_2\right)=0,\\ \Delta N-\chi^2 N=0,\end{gathered} \tag{A.5}$$

which have general solutions:

$$\begin{gathered}\mu_1(r)+\mu_2(r)=C_3+C_4\ln r,\\ N(r)=C_1I_0\left(\chi r\right)+C_2K_0\left(\chi r\right),\end{gathered} \tag{A.6}$$

where constants $C_{1,2,3,4}$ are found from the boundary conditions Eq. (A.2).

The solution is searched in the area $0<r<e$. Since $\ln(r\to 0)\to-\infty$ and $K_0(r\to 0)\to+\infty$, this results in $C_4=0$ и $C_2=0$. After determination of the constants $C_{1,3}$ from the boundary conditions, the final solution takes the form

$$\mu_{1,2}(r)=\frac{\left(\mu_{e1}+\mu_{e2}\right)}{2}\mp\frac{\mu_{e2}-\mu_{e1}-\left(v_{gb}+S\right)\Omega/u_{gb}}{2I_0\left(\chi s\right)}I_0\left(\chi r\right)\mp\left(v_{gb}+S\right)\frac{\Omega}{2u_{gb}}. \tag{A.7}$$

Appendix B. Validity of the mean-field approximation

In calculation of the vacancy flux to the grain face periphery, the distributed sink strength of face bubbles, Eq. (2.3), was used in the mean field approximation. The validity of such consideration will be checked in this Appendix. First of all one should check self-consistency of the sink strength calculations. For this purpose, the sink strength into a face bubble located in the center of the infinite grain face with uniformly distributed face bubbles surrounding this central bubble, should be evaluated.

The solution of the continuity equations for this system of bubbles with the pre-determined distributed sink strength *S*:

$$D_{gb} w \vec{\nabla}_S^2 \tilde{\mu}_{1,2} / kT \pm u_{gb} \left(\tilde{\mu}_2 - \tilde{\mu}_1 \right) / \Omega \mp v_{gb} \mp S = 0 \tag{B.1}$$

is similar to the general solution of Eqs. (2.4) and (2.5), presented in Appendix A, but has different boundary conditions:

$$\tilde{\mu}_{1,2}(r = \rho_b) = \left(\frac{2\gamma_S}{R_{1,2}} - p_f \right) \Omega, \quad \left(\frac{\partial \tilde{\mu}_{1,2}}{\partial r} \right)_{r \to +\infty} = 0 . \tag{B.2}$$

Hence, the terms with $I_0(\chi r)$ in the general solution, Eq. (A.6), must be excluded, since they become infinitely large as $r \to +\infty$. Therefore, the solution takes the form

$$\tilde{\mu}_{1,2}(r) = \left(\frac{\gamma_S}{R_1} + \frac{\gamma_S}{R_1} - p_f \right) \Omega \pm \frac{K_0(\chi r)}{2K_0(\chi \rho_b)} \left(\frac{2\gamma_S \Omega}{R_1} - \frac{2\gamma_S \Omega}{R_2} + \frac{v_{gb}\Omega}{u_{gb}} + \frac{S \cdot \Omega}{u_{gb}} \right) \pm \frac{v_{gb}\Omega}{2u_{gb}} \pm \frac{S \cdot \Omega}{2u_{gb}}, \tag{B.3}$$

where $R_{1,2}$ are the curvature radii of the two surface segments of the central bubble that obey the geometrical relationship:

$$R_1 \cdot \sin\theta_1 = R_2 \cdot \sin\theta_2 = \rho_b . \tag{B.4}$$

From this solution one obtains the vacancy flux to the central bubble:

$$\tilde{J}_{1,2}(r = \rho_b) = \left. \frac{D_{gb} w \nabla \tilde{\mu}_{1,2}(r)}{kT} \right|_{r=\rho_b} = \frac{D_{gb} w \chi}{2kT} \left(\Delta G + 2\varepsilon_f - \frac{v_{gb}}{u_{gb}} - \frac{S}{u_{gb}} \right), \tag{B.5}$$

where $\varepsilon_f = 2\gamma_S / R_2 - p_f$. From Eq. (1.14) the boundary mobility is equal

$$u_{gb} = \frac{D_{gb}\Omega}{2kTw}, \tag{B.6}$$

and the additional relationship between the boundary velocity v_{gb} and $\Delta G + 2\varepsilon_f$ is

$$v_{gb} = \left(\Delta G + 2\varepsilon_f \right) \frac{D_{gb}\Omega}{kT\rho_b} . \tag{B.7}$$

Hence, from Eq. (B.6) one obtains $\chi = \sqrt{2u_{gb}kT / D_{gb}w\Omega} = w^{-1}$. On the other hand, the distributed sink strength into face bubbles is determined by Eq. (2.2) as

$$S = \frac{J_{1,2}(r = \rho_b) \cdot 2\pi\rho_b\Omega}{\pi R_c^{\,2}} . \tag{B.8}$$

Substituting Eq. (B.5) in Eq. (B.7) and taking into account Eq. (B.8) one obtains the equation with unknown value *S*:

$$S \cong \frac{D_{gb}\pi\rho_b\Omega}{kT\pi c^2 u_{gb}} \left(\frac{v_{gb}u_{gb}}{\pi\rho_b^2 b_f} - v_{gb} - S \right), \tag{B.9}$$

which has the solution (using Eq. (B.6)):

$$S = \frac{2w\pi\rho_b v_{gb}}{\pi R_c^2}\left(\frac{\rho_b}{2w}-1\right)\left(1+\frac{2w\pi\rho_b}{\pi R_c^2}\right)^{-1}, \tag{B.10}$$

that coincides with Eq. (2.3) in the limit $w \ll \rho_b$:

$$S \approx \rho_b^2 v_{gb} \big/ R_c^2 . \tag{B.11}$$

Therefore, self-consistency of the sink strength calculation is confirmed.

Secondly, the self-consistency of the chemical potential distribution calculations has to be checked. On the one hand, it is straightforward to see that the chemical potential distribution around a face bubble, Eq. (B.3), steeply varies in a narrow vicinity $\approx \chi^{-1} \approx w$ of each face bubble and is practically constant in between the bubbles. This constant value is equal to

$$M_{\text{face}}^{(1,2)} = \left(\frac{2\gamma_S}{R_1}+\frac{2\gamma_S}{R_1}-2p_f\right)\Omega \pm \frac{v_{gb}\Omega}{2u_{gb}} \pm \frac{S\Omega}{2u_{gb}} \tag{B.12}$$

with except of the region near the face bubbles.

On the other hand, solution of the equation for the vacancy diffusion to the edge of the grain face, Eq. (2.7), has a similar form with the constant value outside a narrow zone ($\approx \chi^{-1} \approx w$) around peripheral toroid:

$$M_{\text{edge}}^{(1,2)} = \left(K_{e1}\gamma_S + K_{e2}\gamma_S - 2p_{tor}\right)\Omega \mp \left(v_{gb}+S\right)\frac{\Omega}{2u_{gb}}. \tag{B.13}$$

Comparison Eqs. (B.12) and (B.13) with account of Eq. (2.15) and its analogue for face bubbles, Eq. (1.9), gives $M_{\text{face}}^{(1,2)} = M_{\text{edge}}^{(1,2)}$. Hence, calculation of the chemical potential distribution is completely self-consistent, as schematically represented in Fig. B.1.

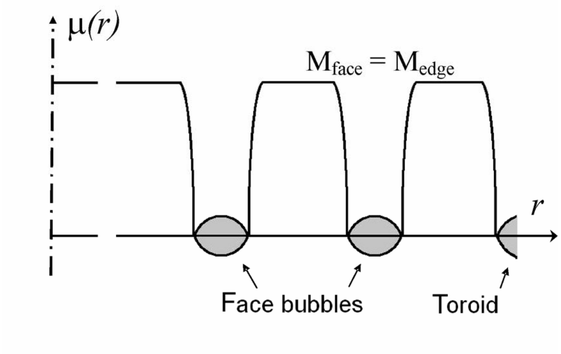

Fig. B.1. Chemical potential distribution

References

1. *Speight M.V., Greenwood G.W.* // Philosophical Magazine. 1964. Vol. 9. P. 683.
2. *Heames T.J., Williams D.A., Bixler N.E., Grimley A.J., Wheatley C.J., Johns N.A., Domogala P., Dickson L.W., Alexander C.A., Osborn-Lee I., Zawadzki S., Rest J., Mason A., Lee R.Y.* VICTORIA: A Mechanistic Model of Radionuclide Behaviour in the Reactor Coolant System under Severe Accident Conditions. NUREG/CR-5545. 1992.
3. *Rest J.* // J. Nucl. Mater. 1985. Vol. 131. P. 291.
4. *Nichols F.A.* // J. Am. Ceram. Soc. 1968. Vol. 51. P. 468.
5. *Hillert M.* // Acta Metall. 1965. Vol. 36. P. 469.
6. *Veshchunov M.S.* Modelling of grain growth kinetics in irradiated and non-irradiated UO$_2$ fuel pellets in framework of the MFPR code / *M.S. Veshchunov and V.I. Tarasov.* (Preprint / Nuclear Safety Institute (IBRAE) RAS, no IBRAE-2002-24). Moscow: NSI (IBRAE) RAS, 2002.
7. *Veshchunov M.S.* // J. Nucl. Mater. 2005. Vol. 346. P. 208–219.
8. *Shewmon P.G.* // Trans. AIME. 1964. Vol. 230. P. 1134.
9. *Antropov D.S., Veshchunov M.S.* Development of model for grain growth in UO$_2$ fuel // Multidiscipline Modeling in Materials and Structures. 2007. (*Accepted for publication*).
10. *Veshchunov M.S.* // J. Nucl. Mater. 2005. Vol. 346. P. 220–225.
11. *Cole D.G., Feltham P., Gilliam E. //* Proc. Phys. Soc. 1954. Vol. B67. P. 131.
12. *Burke J.E., Turnbull D.* // Prog. Metal Phys. 1952. Vol. 3. P. 220.
13. *Speight M.V., Beere W.* // Met. Sci. 1975. Vol. 8. P. 190.
14. *White R.J., Tucker M.O.* // J. Nucl. Mater. 1983. Vol. 118. P. 1.
15. *Tucker M.O.* // Ibid. 1979. Vol. 79. P. 199–205, 206–213.
16. *Bourgeois L., Dehaudt Ph., Lemaignan C., Fredric J.P.* // Ibid. 2001. Vol. 295. P. 73.
17. *Dollins C.C., Nichols F.A.* // Ibid. 1978. Vol. 78. P. 326.
18. *Kingery W.D., Francois B.* // J. Am. Ceram. Soc. 1965. Vol. 48. P. 546.
19. *Veshchunov M.S., Ozrin V.D., Shestak V.E., Tarasov V.I., Dubourg R., Nicaise G.* // Nucl. Eng. Des. 2006. Vol. 236. P. 179–200.
20. *Veshchunov M.S., Dubourg R., Ozrin V.D., Shestak V.E., Tarasov V.I.* // J. Nucl. Mater. 2007. Vol. 362. P. 327–335
21. *Alcock G.B., Hawkins R.J., Hills A.W.D., McNamara P.* // IAEA, Symp. Thermodynamics. Vienna. 1965. Paper SM-66/36. P. 57.
22. *Turnbull J.A.* // J. Nucl. Mater. 1974. Vol. 50. P. 62.
23. *MacEwan J.R., Hayashi J.* // J. Am. Ceram. Soc. 1962. Vol. 4. P. 37.
24. *Mikhlin Ya.* // J. Nucl. Mater. 1979. Vol. 87. P. 405.

Fuel Oxidation in Steam/Hydrogen/Air Mixtures

V.D. Ozrin, M.S. Veshchunov

Introduction

The oxidation state is generally acknowledged as one of the most important chemical properties of UO_2 nuclear fuel during both irradiation and accident conditions because the chemical potential of oxygen and the related oxygen-to-metal molar ration of the fuel affect significantly diffusion controlled processes such as grain growth [1], fission gas release [1 — 4], thermal conductivity [5], chemical states and thus the behaviour of the fission product elements [6].

The MFPR module includes modelling of two phenomena accompanying interaction of oxide fuel with an oxidising gas environment and affecting essentially the fission product behaviour and release. Those are fuel oxidation resulting in increase of urania stoichiometry and changes in chemical states of fission product elements, and fuel volatilisation. The aim of modelling is to evaluate the average fuel stoichiometry and the fuel mass losses as functions of time at given initial and external conditions which include the sample geometry, gas composition and flow rate, temperature and total pressure in the system.

The oxygen/uranium phase diagram [7] shows that at temperatures above 1500 K a single phase of non-stoichiometric UO_{2+x} exists in a wide range of stoichiometry with the lower phase boundary defined approximately as [8]

$$x_{\mathrm{low}} = -2 \times 10^{1.63-6270/T} .$$

Above 1950 K the upper boundary for this phase is $x_{\mathrm{up}} \le 1$ because UO_3(c) is generally not formed at atmospheric pressure. At temperatures $1500\,\mathrm{K} < T < 1950\,\mathrm{K}$ the highest oxide is U_3O_8/U_8O_{21} and the upper phase boundary for the UO_{2+x} single phase is approximately described by [9]

$$x_{\mathrm{up}} = -172/T + 0.316 .$$

The UO_{2+x} phase stability is governed by the oxygen partial pressure in the gas environment. For instance, in atmosphere of pure steam at 1 bar UO_{2+x} is stable above 1320 K. On the other hand, the stability in air at 1 bar is restricted by the temperature of about 1800 K. In the models included in the current version of MFPR code only the single phase (UO_{2+x}) region of the phase diagram is considered.

Significant fuel vaporization in high oxidising conditions of steam or steam/air mixtures accompanied by intensive fission product releases has been observed in a number of experiments [10–17]. Thermochemistry calculations show that urania vaporization in steam-hydrogen mixtures should be dominated by formation of gaseous uranium trioxide, UO_3, and oxyhydroxide, $UO_2(OH)_2$.

The model implemented in MFPR for high temperature fuel oxidation/reduction in O_2–H_2–H_2O–Inert gas mixtures includes description of the processes of solid state diffusion of oxygen within UO_2 matrix, kinetic effects of oxygen exchange at the gas/solid interface, fuel vaporization and mass transfer in the multicomponent gas phase [18]. In the real geometry of the fuel pellet with diameter about 1 cm, the rate of the solid state oxygen diffusion might be comparable with that at the gas/solid interface and thus should be considered self-consistently with the other kinetic processes.

1. Oxygen diffusion in solid urania

In the MFPR model, the solid state diffusion of oxygen is described in a simplified manner in terms of the surface and average stoichiometric deviations, x_s and $\bar{x}$. The effect of oxygen participation in solid state chemical reaction is approximately taken into account through a one step iteration scheme discussed below.

In accordance with typical experimental conditions, symmetric annular flow geometry is considered. A fuel specimen takes the shape of a cylinder with the radius R and height h. It is assumed that only the lateral surface of the cylinder is in contact with an oxidising gas environment, and due to the axial symmetry the surface stoichiometric deviation is a function of time only. Under the condition of slow vaporization kinetics (adiabatic approximation), integrating of the diffusion equation for the oxygen concentration (or stoichiometry) yields

$$\frac{1}{2} R \frac{d\bar{x}}{dt} = j_{\mathrm{O(sol)}}(x_s), \qquad (1)$$

where $\bar{x}(t)$ is the average stoichiometric deviation, $j_{O(\mathrm{sol})}(x_s)$ is the oxygen flux to solid at the gas/solid interface which, in general, depends on the composition of oxidising atmosphere in the vicinity of the surface. Explicit form of this function is discussed below in connection with the problem of mass transfer in the gas phase. Slow decrease of the sample radius caused by fuel vaporization is governed by the uranium conservation,

$$\frac{d}{dt} N_{\mathrm{UO_2}} = A \rho_{\mathrm{UO_2}} \frac{dR}{dt}, \qquad (2)$$

where $N_{\mathrm{UO_2}}$ is the number of moles in the fuel specimen, A is the surface area of the sample in contact with the oxidising gas, $\rho_{\mathrm{UO_2}}$ is the molar density of UO_2.

The oxygen flux to solid is a slowly varying function of x_s for sufficiently small deviations from the initial stoichiometry, x_0. Therefore, the initial stage of the diffusion process can be described by the asymptotic solution of the one-dimensional diffusion equation for a half-space with the constant boundary flux, which yields

$$\bar{x} - x_0 = \frac{D}{R\, j_{\mathrm{O(sol)}}(x_s)} \left(x_s - x_0\right)^2. \qquad (3)$$

Here D is the solid state diffusion coefficient of oxygen calculated using the Meachen correlation [19] presented in Appendix.

Following [20], for the late stage of diffusion when the oxygen flux to solid is small enough, the difference between the average and boundary stoichiometric deviations is approximately proportional to the flux and, in the considered cylindrical geometry, takes the form

$$\bar{x} = x_s - \tfrac{1}{4} R\, j_{\mathrm{O(sol)}}(x_s) / D. \qquad (4)$$

It is further supposed that the relation between $\bar{x}$ and x_s can be approximately represented by the asymptotic solution (3) within the initial time intervals when $x_s \le x_{s1}$, and by Eq. (4) for $x_s \ge x_{s1}$. The joining point, x_{s1}, is determined by

$$x_{s1} - x_0 = \frac{R}{2D} j_{\mathrm{O(sol)}}(x_{s1}).$$

Thus, since $j_{O(\mathrm{sol})}(x_s)$ is a monotonic function of x_s, Eqs. (3) and (4) are used respectively within the regions

$$\left|x_s - x_0\right| \le \frac{R}{2D} \left|j_{\mathrm{O(sol)}}\right| \text{ and}$$

$$\left|x_s - x_0\right| > \frac{R}{2D} \left|j_{\mathrm{O(sol)}}\right|. \qquad (5)$$

Solving of Eqs. (1), (3)–(5) with $\bar{x}(0) = x_0$ provides approximate solution of the diffusion boundary problem. Note that Eqs. (3)–(5) describe both the fuel oxidation process when $j_{\mathrm{O(sol)}} > 0$ and $\bar{x} < x_s < x_{\lim}$, and the reduction when $j_{\mathrm{O(sol)}} < 0$ and $\bar{x} > x_s > x_{\lim}$. Here $x_{\lim}$ is the limiting (steady-state) stoichiometric deviation that satisfies the equation

$$j_{\mathrm{O(sol)}}(x_{\lim}) = 0 \qquad (6)$$

and depends only on the sample geometry, initial gas composition and temperature.

2. Kinetics of surface oxidation

In steady-state regime, the oxygen partial pressure in the vicinity of the gas/solid interface, $P^{s}_{O_2}$, determines the equilibrium surface stoichiometry, x_{eq}, through the equation

$$P^{s}_{O_2} = \overline{P_{O_2}}(x_{eq}), \qquad (7)$$

where $\overline{P_{O_2}}(x)$ is the equilibrium oxygen pressure over uranium oxide with the stoichiometry x. This function is represented by the correlation proposed by Lindemer and Besmann [21] discussed in Appendix.

Kinetics of the exchange of oxygen at the solid/gas interface can be characterised by the specific rate constant α included into a general equation of the form

$$j_{O(sol)} = \alpha F(x_s, x_{eq}), \qquad (8)$$

where the function $F(x_s; x_{eq})$ depends on deviation of the actual stoichiometry from the equilibrium one ($F=0$ for $x_s = x_{eq}$,) and is determined by the surface exchange mechanism.

The current version of the MFPR code includes semi-phenomenological model that is based on the results by Gala and Grabke applied to the case of steam-hydrogen atmospheres by Abrefah et al. [16]. More detailed description of the model with a Langmuir-type generalization on wide range of gas compositions (from air to pure hydrogen) is presented in Ref. [18, 20]. In this model the driving force is given by

$$F(x_s, x_{eq}) = \sqrt{P^{s}_{H_2O}}\left(1 - \sqrt{\overline{P_{O_2}}(x_s)/P^{s}_{O_2}}\right). \qquad (9)$$

The rate constant in Eq. (8) is represented in the Arrhenius form

$$\alpha = K_{ox}/\rho_{UO_2},$$

$$K_{ox} = \exp(-E/T + E_1) \ \text{(mol/cm}^2\text{/s)}. \qquad (10)$$

Constants E and E_1 are presented in Table 1, where the fourth and fifth columns include the modified values found by the self-consistent treatment of the test data [17] using the gas transfer model of fuel oxidation implemented in the MFPR code [18, 20].

In contrast to the case of steam, the kinetics of high-temperature fuel behaviour in a gas environment as air or hydrogen-inert gas mixture is not well studied. For description of such situations, the model of instantaneous surface relaxation with $\alpha \to \infty$ is used in which the surface stoichiometry coincides with the equilibrium one, $x_s = x_{eq}$.

3. Thermodynamics of UO_2 vaporization in oxidising conditions

Under the condition of equilibrium between the non-stoichiometric urania and the gas phase with given partial pressures of oxygen, the deviation from stoichiometry is a function of the oxygen pressure found from Eq. (7). Since UO_3 gas is formed in the reaction

$$UO_3(g) = UO_{2+x}(c) + 0.5\,(1 - x)\,O_2(g),$$

the equilibrium variations of the Gibbs free energy in this reaction satisfy the equation

$$\Delta_f G^0_{UO_3(g)} + RT \ln P^{eq}_{UO_3} = \Delta G_{UO_{2+x}} + 0.5(1-x)\Delta G_{O_2},$$

where P_i^{eq} denotes the equilibrium partial pressure, $\Delta_f G_i^0$ is the Gibbs energy of formation of a mole of pure gaseous species 'i' in the standard state. Variations in the oxygen and urania Gibbs energies are defined as

$$\Delta G_{O_2} = RT \ln \overline{P_{O_2}}(x, T),$$

$$\Delta G_{UO_{2+x}} = \Delta_f G^0_{UO_2} + \tfrac{1}{2} RT \int_0^x \ln \overline{P_{O_2}}(x', T)\, dx',$$

where $\Delta_f G^0_{UO_2}$ is the Gibbs free energy of the formation of a mole of pure UO_2(c). Superposition of these equations yields

$$P^{eq}_{UO_3} = a_{UO_2}(x)\, C_{UO_3} \sqrt{P_{O_2}} \tag{11}$$

where x depends on the oxygen pressure P_{O_2} as determined by Eq. (7), C_{UO_3} is the equilibrium constant defined below, the function $a_{UO_2}(x)$ interpreted as the activity of UO_2 in the solid solution "UO_2 – O(sol)" [21, 22] can be represented in an explicit form by use of Lindemer—Besmann correlation (see Eq. (A.9) in the Appendix).

Reactions of formation of gaseous uranium oxyhydroxide, $UO_2(OH)_2$, and steam dissociation can be written as

$$UO_2(OH)_2(g) = UO_3(g) + H_2O(g),$$

$$H_2O(g) = H_2(g) + (1/2)\, O_2(g).$$

For the equilibrium partial pressures, the mass action law yields

$$P^{eq}_{UH_2O_4} = P^{eq}_{UO_3}\, P_{H_2O}\, C_{UH_2O_4} / C_{UO_3}\ ,$$

$$P_{H_2O} = C_{H_2O} P_{H_2} \sqrt{P_{O_2}}\ . \tag{12}$$

The equilibrium constants, $C_{UH_2O_4}$, C_{UO_3} and $C_{H_2O(g)}$, are given by

$$RT \ln C_{UO_3} = G^0_{UO_2(c)} + 0.5 G^0_{O_2(g)} - G^0_{UO_2(g)},$$

$$RT \ln C_{UH_2O_4} = G^0_{UO_2(c)} + 0.5 G^0_{O_2(g)} + G^0_{H_2O(g)} - G^0_{UH_2O_4(g)}$$

$$RT \ln C_{H_2O(g)} = G^0_{H_2(g)} + \tfrac{1}{2} G^0_{O_2(g)} - G^0_{H_2O(g)} \tag{13}$$

with Gibbs free energies of pure species, $G^0(T)$, taken from IVTAN Thermo database [24].

4. Mass transfer in gas phase

In the problem of fuel oxidation, the gas environment consists, in general, of O_2–H_2–H_2O–N_2 mixture and includes the low-concentration components of uranium-bearing vapours, UO_3 and $UH_2(OH)_2$, formed at the gas/solid interface due to the reactions of fuel vaporization.

Under typical experimental conditions [10, 15 — 17] (annular geometry of the flow channel and flow rate ~ 10 cm/s, total pressure ~ 1 bar, Reynolds number $\sim 1 - 10$) the laminar regime of the gas flow in the channel occurs. In this case, the problem of the gas mass transfer can be reduced to the problem of quasi-stationary multi-component diffusion at constant total pressure through the boundary gas layer at the gas/solid interface [23]. The stationary conditions follows from that the characteristic time of fuel oxidation determined by the solid state diffusion or surface exchange of oxygen exceeds significantly the characteristic time of diffusion relaxation in the gas phase. Since the diffusion time, in its turn, exceeds the characteristic time of the gas phase reactions, it is also assumed that the gas mixture is in the local chemical equilibrium state.

The consideration is restricted by the cases when the gas composition is dominated by an arbitrary pair of the four main constituents of the gas phase, those are H_2O, H_2, O_2, N_2. The molar densities of the other gas components including uranium-bearing vapours are assumed to be much smaller than that of the dominating pair.

A. Diffusion fluxes

The quasi-stationary flux densities, J_i (i = H_2O, H_2, O_2, N_2, UO_3, UH_2O_4), at the gas/solid interface are represented in the form

$$J_1 = K_1\left(X_2\Delta P_1 - X_1\Delta P_2\right) - X_1\sum_{i=3}^{6} K_i\,\Delta P_i + K_{\mathrm{cnv}}P_1^{\mathrm{s}},$$

$$J_2 = K_1\left(X_1\Delta P_2 - X_2\Delta P_1\right) - X_2\sum_{i=3}^{6} K_i\,\Delta P_i + K_{\mathrm{cnv}}P_2^{\mathrm{s}} \qquad (14)$$

for the dominating pair of the gases, and

$$J_i = K_i\,\Delta P_i + K_{\mathrm{cnv}}P_i^{\mathrm{s}}, \quad i = 3,\dots,6 \qquad (15)$$

for the other low-concentration components. Here $\Delta P_i = P_i^{\mathrm{s}} - P_i^{\mathrm{b}}$ and

$$X_1 = \frac{P_1^{\mathrm{s}}}{P_1^{\mathrm{s}} + P_2^{\mathrm{s}}}, \quad X_2 = \frac{P_2^{\mathrm{s}}}{P_1^{\mathrm{s}} + P_2^{\mathrm{s}}},$$

where P_i is the partial pressure of the gas 'i', the superscripts s and b designate values in the vicinity of the solid surface and in the bulk of the gas phase (or at the outer boundary of the diffusion boundary layer), respectively. The partial pressures satisfy the conditions

$$\sum_i P_i^{\mathrm{s}} = P_{\mathrm{tot}}, \quad \sum_i P_i^{\mathrm{b}} = P_{\mathrm{tot}}, \qquad (16)$$

where P_{tot} is the total pressure assumed to be constant.

In Eqs. (14)–(15), the mass transport coefficients, K_i, are given by

$$K_i = \frac{p_0}{RT}\cdot\frac{D_i}{d_h}\mathrm{Sh},$$

where $p_0 = 1.01325\cdot10^5$ kg/(m·s^2·bar), R is the universal gas constant, d_h is the hydraulic diameter of the flow channel, Sh is the Sherwood number. The diffusion coefficient D_1 ($=D_2$) is very close to the binary diffusivities in the '1–2' mixtures, whereas the diffusion coefficients of low-concentration components, D_i, $i = 3,\dots,6$, are defined as binary diffusion coefficients in mixtures of the type '(1–2) – i'. In general, the Sherwood number, Sh, depends on the channel geometry. In the current version of the MFPR model, the Sherwood number is introduced as a user defined parameter.

The last terms in the right hand side of Eqs. (14)–(15) describes the convective (Stefan) flux with the rate constant given by

$$K_{\mathrm{cnv}} = p_0 v/RT,$$

where the convection velocity v is defined as the net velocity of the gas mixture appearing due to the condition of constant total pressure. Note that the expressions for K_{cnv} and K_i are obtained with use of the ideal gas equation of state.

B. Balance (conservation) equations

Under the stationary conditions, the local conservation laws at the gas/solid interface for oxygen, hydrogen and nitrogen take the form

$$J_{\mathrm{H_2O}} + 2J_{\mathrm{O_2}} + J_{\mathrm{UO_3}} + 2J_{\mathrm{UH_2O_4}} + J_{\mathrm{O(sol)}} = 0, \qquad (17)$$

$$J_{\mathrm{H_2O}} + J_{\mathrm{H_2}} + J_{\mathrm{UH_2O_4}} = 0, \qquad (18)$$

$$J_{\mathrm{N_2}} = 0, \qquad (19)$$

where the fluxes are determined by Eqs. (14)–(15), and J_O(sol) is the oxygen flux to solid in mol/cm^2/s related to that introduced in Eq.(1) by $j_O(\mathrm{sol}) = J_O(\mathrm{sol})/\rho_{UO_2}$. Note that Eq. (17) is related to the uranium balance represented below by Eq. (25).

C. Local chemical equilibrium and conditions in the bulk of the gas phase

It is assumed that the kinetics of formation of the uranium-bearing gases at the gas/solid interface is a relatively rapid process in the time scales of both the oxygen solid state diffusion and gas diffusion. This assumption along with the condition of the local chemical equilibrium allows using of equations of chemical equilibrium (11) and (12), which yield

$$P^{s}_{UO_3} = a_{UO_2}(x_{eq})\, C_{UO_3}\sqrt{P^{s}_{O_2}}\ , \tag{20}$$

$$P^{k}_{UH_2O_4} = P^{k}_{UO_3}\, P^{k}_{H_2O}\, C_{UH_2O_4}\big/C_{UO_3}\ , \tag{21}$$

$$P^{k}_{H_2O} = C_{H_2O} P^{k}_{H_2}\sqrt{P^{k}_{O_2}}\ , \tag{22}$$

where $k = s,\ b$, the equilibrium constants are given by Eqs. (13), x_{eq} is defined by Eq. (7) as a function of the oxygen surface pressure. The elemental composition of the gas phase outside the diffusion layer is determined, as assumed, by the composition of the input gas flow only. Therefore, using the ideal gas law and elemental conservation we find that

$$\frac{P^{b}_{H_2O} + P^{b}_{H_2} + P^{b}_{UH_2O_4}}{P^{b}_{H_2O} + 2P^{b}_{O_2} + P^{b}_{UH_2O_4}} = \frac{f_{H_2O} + f_{H_2}}{f_{H_2O} + 2f_{O_2}}\ , \tag{23}$$

$$\frac{P^{b}_{N_2}}{P^{b}_{H_2O} + 2P^{b}_{O_2} + P^{b}_{UH_2O_4}} = \frac{f_{N_2}}{f_{H_2O} + 2f_{O_2}}\ . \tag{24}$$

Here f_i with $i = H_2O,\ H_2,\ O_2,\ N_2$ is the mole fraction of the i-th gas phase constituent in the initial composition (before mixing). The right-hand sides of Eqs. (23) and (24) represent respectively the hydrogen-to-oxygen and nitrogen-to-oxygen molar ratios characterising the initial gas composition.

D. Gas mass transfer and effects of saturation

Bulk pressures of the uranium-bearing gases depend strongly on the gas flow rate and geometry of the flow channel. For instance, the condition of negligibly small bulk pressures, $P_i^b = 0$, seem to be appropriate in the case of high flow rates and relatively thin boundary layers occurring in Abrefah et al. experiments [16]. On the contrary, estimations for the conditions of Cox et al. experiments [10, 17] on fuel oxidation in air show that the bulk and near-surface equilibrium pressures can be close to each other.

Both situations can be approximately described in the following way. The rate of mass losses caused by fuel vaporization kinetics is given by

$$-\frac{d}{dt}N_{UO_2} = A\left(J_{UO_3} + J_{UH_2O_4}\right). \tag{25}$$

On the other hand, in the case of steady-state laminar flow, the rate of mass losses is proportional to the gas flow rate and the uranium fraction in the outlet gas which is considered as a small impurity. Hence,

$$-\beta\frac{d}{dt}N_{UO_2} = AK_{fl}\left(P^{b}_{UO_3} + P^{b}_{UH_2O_4}\right), \tag{26}$$

where

$$K_{\mathrm{fl}} = \dot{N}_{\mathrm{gas}} / \left(P_{\mathrm{tot}} A \right),$$

$\dot{N}_{\mathrm{gas}}$ is the inlet gas flow rate (in mol/s) in the channel. Combining Eqs. (15), (25), (26) and the conditions of equilibrium given by Eqs. (21) and (22) one can obtain the following relation between the UO_3 bulk and surface pressures,

$$P^{\mathrm{b}}_{\mathrm{UO_3}} = \gamma P^{\mathrm{s}}_{\mathrm{UO_3}}, \tag{27}$$

where the saturation factor is defined by

$$\gamma = \beta \frac{K_{\mathrm{UO_3}} + K_{\mathrm{cnv}} + \left(K_{\mathrm{UH_2O_4}} + K_{\mathrm{cnv}} \right) P^{\mathrm{s}}_{\mathrm{H_2O}} C}{K_{\mathrm{fl}} \left(1 + P^{\mathrm{b}}_{\mathrm{H_2O}} C \right) + \beta \left(K_{\mathrm{UO_3}} + K_{\mathrm{UH_2O_4}} P^{\mathrm{b}}_{\mathrm{H_2O}} C \right)}, \tag{28}$$

with $C = C_{\mathrm{UH_2O_4}} / C_{\mathrm{UO_3}}$. In the current version of MFPR, the parameter β determined by the boundary conditions for the gas mass transfer problem is introduced as the user-defined parameter ranged from 0 to 1.

5. Model formulation

Thus, the model is based on the following equations:

1. Equations (1), (3–6) for the average and surface stoichiometric deviations, $\bar{x}(t)$ and x_s(t), describing the solid state oxygen diffusion caused by the boundary oxygen flux $j_{O(sol)}$.
2. Equations (8) and (9) which describe the surface kinetics and represent the boundary oxygen flux in terms of the surface stoichiometry, x_s, and the partial pressures of steam and oxygen in the vicinity of the gas/solid interface.
3. Equations (18)–(24) and (27)–(28) which describe mass transfer in the gas phase under condition of the local chemical equilibrium, formation of UO_3 and $UO_2(OH)_2$ vapour and the effects of saturation. Solution of these equations allows representing the bulk and surface partial pressures of all gases and the boundary oxygen flux in terms of the oxygen surface pressure and the initial gas composition.

For each time step, the initial conditions for the average stoichiometry $\bar{x}(\mathrm{t})$ are determined by the fission product chemistry model which takes into account changes in the fuel oxygen potential related to oxygen bonding in UO_2 solid solution and formation of solid precipitates within fuel. This provides approximate self-consistency in description of FP chemistry—release—oxidation processes. Equating of the expressions for the oxygen flux found from the gas mass transfer problem and the surface kinetics yields $j_{O(\mathrm{sol})}$ as a function of x_s that provides the boundary condition for the oxygen diffusion problem. Equations (2) and (25) describe the vaporization kinetics, fuel mass losses and changes in the fuel specimen sizes.

Table 1. Data for oxidation rate constants

Surface model	Simplified model		Gas transfer model	
	E	*E*$_1$	*E*	*E*$_1$
Gala —Grabke	21200	–2.52	22974	–1.1527

Conclusions

A general model for oxidation of UO_2 fuel in steam/hydrogen/air gas mixtures is presented. The model includes self-consistent description of solid state oxygen diffusion, adsorption processes of oxygen exchange at the gas/solid interface accompanied by UO_2 evaporation in the form of UO_3 and $UO_2(OH)_2$ gases, gas mass transfer in the boundary layer of multi-component gas mixture and the fuel mass losses. Effects of the fission product chemistry within the fuel on formation of the oxygen potential are also taken into consideration.

Appendix

The Lindemer—Besmann correlation [21] for the equilibrium pressure of oxygen over UO_{2+x} is based on a model of solid solution of different uranium oxides such as UO_2, U_4O_9, $U_{10}O_{23}$, U_3O_7, and so on. It is assumed that in the case of high hyperstoichiometry, non-stoichiometric urania can be represented in the form of $[UO_2]$–$[U_3O_7]$ solid solution with the oxygen potential given by

$$\ln P_1(x,T) = E_1 + 2\ln\left(\frac{x(1-2x)^2}{(1-3x)^3}\right), \qquad E_1 = -37621/T + 15.5\,. \tag{A.1}$$

For low hyperstoichiometry in UO_{2+x}, the best approximation corresponds to $[UO_2]$–$[U_4O_9]$ solid solution that gives

$$\ln P_2(x,T) = E_2 + 4\ln\left(\frac{2x(1-2x)}{(1-4x)^2}\right), \quad E_2 = -43298/T + 15.74\,. \tag{A.2}$$

Thus, the oxygen potential in a hyperstoichiometric urania is defined as

$$\overline{P_{O_2}}(x) = \begin{cases} P_1(x) & \text{for} \quad x_1 < x \le x_0, \\ P_2(x) & \text{for} \quad x_0 \le x, \end{cases} \tag{A.3}$$

where x_0 is a root of equation $P_1(x) = P_2(x)$ which can be well approximated by

$$x_0 \cong \exp\left(E\cdot z - 6.66838\right), \quad z = 1000/T\,,$$
$$E = 2.69835 + 0.19577z - 0.204792z^2. \tag{A.4}$$

Lindemer and Besmann found that hypostoichiometric fuel can be well represented by solid solution of $[U_{1/3}]$–$[UO_2]$ with the oxygen potential given by

$$\ln\overline{P_{O_2}}(x) = E_3 - 3\ln\left(\frac{-1.5x}{(1-x)^{2/3}(1+0.5x)^{1/3}}\right), \qquad E_3 = -156355/T + 27.15\,, \tag{A.5}$$

where $x < -x_1$. In the narrow interval near $x = 0$,

$$|x| \le x_1, \quad x_1 = \exp\left(1 + \tfrac{2}{7}\left(E_3 - E_2\right)\right), \tag{A.6}$$

the oxygen potential is represented by

$$\ln\overline{P_{O_2}}(x) = E_4 + \alpha x/x_1, \quad E_4 = \tfrac{1}{7}\left(3E_2 + 4E_3\right), \tag{A.7}$$

where $\alpha = 4$ for $x > 0$ and $\alpha = 3$ for $x < 0$.

The function $a_{UO_2}(x)$ included in Eq. (2.4.11) for equilibrium UO_3 pressure is defined by

$$\ln a_{UO_2}(x) = -\tfrac{1}{2}\int_0^x x(c)dx' \,\frac{d\ln\overline{P_{O_2}}(x(c),T)}{dx(c)}\,. \tag{A.8}$$

Using Eqs. (A.1)–(A.3) the UO_2 activity can be represented in the explicit form

$$a_{\mathrm{UO}_2}=\begin{cases}\dfrac{1-4x}{1-2x} & \text{for} \quad x\le x_0,\\ \dfrac{1-4x_0}{1-3x_0}\cdot\dfrac{1-3x}{1-2x} & \text{for} \quad x_0\le x,\end{cases} \qquad (A.9)$$

where $x_0(T)$ is defined in (A.4).

Density of the oxygen diffusion flux in solid urania caused by concentration gradients is described in terms of the chemical diffusion coefficient defined by

$$D=D^*\frac{2+x}{2RT}\frac{d\Delta G_{\mathrm{O}_2}(x,T)}{dx}. \qquad (A.10)$$

where D^* is usually referred to as the oxygen self-diffusion coefficient, $\Delta G_{\mathrm{O}_2}(x,T)$ is the chemical potential of oxygen. There is a number of experimental evidences that D shows a little change with changing stoichiometric deviation. Meachen [19] presented the following expression for the oxygen chemical diffusion coefficient

$$D=2.5\exp(-16400/T) \text{ (cm}^2\text{/s)}, \qquad (A.11)$$

obtained by averaging over the stoichiometric range $10^{-5} \le x \le 10^{-1}$ and valid for $700 \le T \le 1800$ K.

Unfortunately, the available data for the oxygen chemical diffusivity are sufficiently scattered (and sparse). For instance, measurements performed by Bittel et al. [7] for oxidation in steam at temperatures ranging from 1200 to 2100 K yielded the chemical diffusion coefficient

$$D=99.0\exp(-28640/T) \text{ (cm}^2\text{/s)},$$

which is lower than that of Eq. (A.11) by approximately an order of magnitude for $1800<T<2100$ K. According to data presented in review by Matzke [25], D is ranged from 10^{-4} to $8\cdot10^{-4}$ cm^2/sec at 2270 K. In the MFPR module the Meachen correlation given by Eq. (A.1) is used.

References

1. *Mansouri M.A., Olander D.R.* // J. Nucl. Mater. 1998. Vol. 254. P. 22.
2. *Matzke Hj.* // Radit. Eff. 1980. Vol. 53. P. 219.
3. *Turnbul J.A., Friskney C.A., Findlay J.R., Johnson F.A., Walter A.J.* // J. Nucl. Mater. 1982. Vol. 107. P. 168.
4. *Hirai M., Davies J.H., Williamson R.* // Ibid. 1995. Vol. 226. P. 238.
5. *Lucuta P.G., Matzke Hj., Verall R.A.* // Ibid. 1995. Vol. 223. P. 51.
6. *Kleykamp H. J.* // Ibid. 1985. Vol. 131. P. 221.
7. SCDAP/RELAP5 MOD2 CODE: Manual. Vol. 4: MATPRO — A Library of Material Properties for Light Water Reactor Accident Analysis. NUREG/GR-5273, EGG-255. 1990.
8. *Wang W., Olander D.R.J.* // Amer. Ceramic Soc. 1993. Vol. 76. P. 76.
9. *Anthony A.M., Kiyoura R., Sata T.* // J. Nucl. Mater. 1963. Vol. 10. P. 8.
10. *Cox D.S., Hunt C.E.L., Liu Z., Iglesias F.C., Keller N.A., Barrand R.D., O'Connor R.F.* A model for the release of low-volatility fission products in oxidising conditions: AECL report // Proc. of 12 Annual Conference of the Canadian Nuclear Society (Saskatchewan, Canada, 1991, June 9–12). AECL-10440. 1991.
11. *Powers D.A., Kmetyk L.N., Schmidt R.C.* A Review of the Technical Issues of Air Ingression During Severe Reactor Accidents. NUREG/CR-6218, SAND94-0731. Sandia National Laboratories. Albuquerque, NM, 1994.
12. *Alexander C.A., Ogden J.S.* Vaporization of UO_2 at high temperatures and pressures. A generic relation for volatilization // High Temp.-High Pres. 1990. Vol. 21. P. 149.
13. *Cox D.S., Iglesias F.C., Hunt C.E.L., Keller N.A., Barrand R.D., Mitchell J.R. O'Conner R.F.* Oxidation of UO_2 in air and steam with relevance to fission product releases // Proc. 192nd ACS Symp. on Chemical Phenomena Associated with Radioactivity During Severe Nuclear Accidents (Anheim, California, 1986, September 7–12). NUREG/GP-078. P. 2-35–2-39.

14. *Iglesias F.C., Hunt C.E.L., Cox D.S., Keller N.A., Barrand R.D., O'Conner R.F., Mitchell J.R.*. UO_2 oxidation and fission product release // Workshop on Chemical Reactivity of Oxide Fuel and Fission Product Release (Berkeley, England, 1987, April 7–9).
15. *Lewis B.J., Andre B., Morel B., Dehaudt P., Maro D., Purdy P.L., Cox D.S., Iglesias F.C., Osborne M.F., Lorenz R.A.* Modelling the Release Behaviour of Caesium during Severe Fuel Degradation // J. Nucl. Mater. 1995. Vol. 227. P. 83–109.
16. *Abrefah J., Aguiar Briad A.de, Wang W., Khalil Y., Olander D.R.* High Temperature Oxidation of UO_2 in Steam-Hydrogen Mixtures // Ibid. 1994. Vol. 208. P. 98–110.
17. *Lewis B.J., Corse B.J., Thompson W.T., Kaye M.H., Iglesias F.C., Elder P., Dickson R., Liu. Z.* Low volatile fission-product release and fuel volatilization during sever reactor accident conditions // Ibid. 1998. Vol. 252. P. 235–256.
18. *Ozrin V.D., Veshchunov M.S.* Improvement of fuel oxidation/volatilisation modelling / Nuclear Safety Institute (IBRAE) RAS. Report NSI-SARR-92-99. June 1999.
19. *Meachen J.A.* Oxygen diffusion in uranium dioxide: a review // Nucl. Ener. 1989. Vol. 28.P. 221–226.
20. *Dobrov B.V., Likhanskii V.V., Ozrin V.D., Solodov A.A., Kissane M.P., Manenc H.* Kinetics of UO_2 oxidation in steam atmosphere // J. Nucl. Matter. 1998. Vol. 255. P. 59–66.
21. *Lindemer T.B., Besmann T.M.* Chemical thermodynamic representation of $<UO_{2\pm x}>$ // J. Nucl. Mater. 1985. Vol. 130. P. 473–488.
22. *Blackburn P.E.* Oxygen pressure over fast breeder reactor fuel ((1) A model for UO_2+x) // Ibid. 1973. Vol. 46. P. 244–252.
23. *Levich V.G.* Physical-Chemical Hydrodynamics. Moscow: FisMatGIS, 1959.
24. *Gurvich L.V., Iorish V.S.* et al. IVTANTHERMO — A Thermodynamic Database and Software System for Personal Computer: User's guide. CRC Press, Inc., Boca Raton, 1993.
25. *Matzke Hj.* // J. Chem. Soc., Faraday Trans. 1987. Vol. 83. P. 1121.

Validation of the MFPR Code against Integral Tests

V.D. Ozrin

Introduction

Validation of the MFPR code models against various analytical tests was presented in various papers of this issue. This paper is devoted to analysis of the results obtained with the MFPR code in simulations of integral experiments with irradiated fuel.

Several series of integral tests on fission product (FP) releases have been performed in CRL, ORNL and CEA-CENG to create a realistic data bank for computing the behaviour of FP and to validate and improve the models (codes) describing the risk of FP transfer into environment during a severe accident. The measurements performed during the tests were aimed to characterise the release kinetics and total release of fission products, actinides and structural materials as a function of fuel burn-up, temperature and oxidising/reducing conditions of the gas environment.

For the MFPR validation the following tests were chosen: UCE9-1 and MCE1-5 experiments from CRL series; VERCORS 1, 2, 4 and 5 tests (CEA-CENG) using respectively oxidising and oxidising/reducing gas mixtures, two groups of high-temperature tests from HI-VI series (ORNL), VI-1, VI-2, VI-3 and VI-4, VI-5, performed respectively in steam and hydrogen atmospheres; one of the Dimitrovgrad series of tests on the WWER-1000 fuel with burn-up of 15.8 MWd/kg using inert gas flow with step-by-step temperature increase. The validation test grid and brief summary of experimental conditions are shown in Table 1.

Table 1. Summary of experimental conditions for integral tests

Test conditions	**Test**											
	UCE 9-1	**MCE 1-5**	**VERCORS**				**VI**					**Dimitrov-grad**
			1	**2**	**4**	**5**	**1**	**2**	**3**	**4**	**5**	
Fuel	UO_2	UO_2	UO_2 Zr	UO_2 Zr	UO_2 Zr	UO_2 Zr	UO_2 Zr	UO_2 Zr	UO_2 Zr	UO_2 Zr	UO_2 Zr	UO_2 Zr
UO_2 weight, g	2.4	0.3	23.1	23.1	23.1	23.1	109	82	81.1	78.2	80.8	~5
Burn-up, %	2.4	1.2	4.7	4.2	4.1	4.1	4.4	4.8	4.6	5.2	4.6	1.7
Grain diameter, μm	≤ 12.2	7	8	15	15	15	9.2	12	12	12	12	~5
Temperature ramp, K/s	0.4	0.2	1	~1	~1	~1	1−0.6	0.8	0.3–0.3	0.7–1.1	1.1–1.2	13–20
Temperature at plateau, K	1963	2073	2130	1050, 1250, 1500, 1750, 2150	773, 1523, 2573	673, 1075, 1273, 1573, 2573	1410, 2020, 2300	1273, 2300	2000, 2700	1660, 2440	1620, 2015, 2720	1573, 1773, 1973, 2123, 2273
Time at plateau, min	200	30	17	25, 10, 30, 25, 13	25, 67, 30	75,35, 25, 80, 30	20, 20, 20	5, 60	20, 20	23, 20	20, 20, 20	15, 15, 15, 15, 15
Gas composition at annealing	H_2O, Ar	H_2, Ar	H_2O, H_2	H_2O, H_2	H_2O, H_2	H_2O	H_2O, He	H_2O, He	H_2O, He	H_2, He	H_2, He	Ar

The integral tests are characterised by some specific features of experimental conditions that are of significant importance for modelling.

- In all tests the fragments of spent fuel were used with burn-up from 1 to 5-6 percent.
- Fuel samples were heated up to high temperature ranged from 1900 to 2700 K and held at a constant temperature during a period from about 0.5 to 3 hours. In the majority of the experiments the early heating-up stage was performed in inert gas environment, while during the late stage of heating and annealing the inert gas was switched to oxidising/reducing gas mixtures of varied compositions consisting of steam and hydrogen.
- In the majority of experiments, the fuel specimens included fragments of original Zircaloy cladding. Due to extensive steam/zirconium interaction, in such oxidising experiments as first three VERCORS and VI tests, the compositions of the gas environments in contact with the UO_2 surface differed significantly from that in the input gas flow during the first stage of annealing up to completion of cladding oxidation.

Thus, simulation of integral tests should be separated into two parts: modelling of the pre-test period and modelling of the experiment itself. The following peculiarities of the modelling related to the uncertainties in the input data should be pointed out.

In the conditions of normal PWR operating, the state of fuel rods is characterised by great radial temperature gradients with difference about 500–600 K along the pellet radius and by significant spatial inhomogeneity of radiation fields. Since the MFPR model does not include description of such situations, the pre-test periods for all experiments considered are modelled identically using the following typical average conditions [1]:

- fuel temperature is set a constant of 1100 K,
- fission rate is set a constant of 10^{19} fission/$m^3 \cdot s$,
- duration of the irradiation period is calculated using the above fission rate and the standard burn-up units in which 1 % burn-up corresponds to 9.6 MWd/kg or $2.49 \cdot 10^{26}$ fission/m^3 [1].

The approach to modelling of the pre-test periods for each integral experiment can be illustrated by consideration of VERCORS-1 as an example. Since the fuel used in this experiment was characterised by burn-up of 42.9 MWd/kg, calculation of the irradiation time yields $t_{rad} = 11.117 \cdot 10^7\,s$. Thus, the temperature pre-test scenario is assumed to be as follows:

- normal operating at $T = 1100\,K$ in irradiation field characterised by the fission rate of 10^{19} fiss/($m^3 \cdot s$) during the period from $t = -11.127 \cdot 10^7\,s$ to $t = -10^5\,s$,
- cooling (without irradiation) from $T = 1100\,K$ to $T = 300\,K$ during the interval from $t = -10^5\,s$ to $t = -9.6 \cdot 10^4\,s$,
- steady-state (without irradiation) at $T = 300\,K$ from $t = -9.6 \cdot 10^4\,s$ to $t = -1.8 \cdot 10^3\,s$,
- temperature increase from 300 K to the initial test temperature of 2130 K during the period from $t = -1.8 \cdot 10^3\,s$ to $t = 0$.

Note that duration of the low temperature steady-state period does not affect the results of calculations because the FP release rates at 300 K are negligibly small. The duration of the final pre-test stage depends on the initial test temperature and the heating rate.

In the experiments with the fuel/cladding samples in oxidising environment provided by steam/hydrogen gas mixtures, the conditions of UO_2 oxidation are determined by the oxygen partial pressure which, in turn, is defined by interaction of the input gas (with the composition presented in the literature) with the Zr cladding. Although the value of the real (but not input) oxygen partial pressure is of significant importance for the description of the behaviour and release of FP elements, the results of direct measurements of the gas composition in contact with the fuel surface are unknown (unpublished, or not available). There exist an approach [2 — 4] to restore the near-surface oxidation conditions basing on the average gas composition in the reaction crucible (tube) that can be calculated with the published data for hydrogen generation during steam-zirconium interaction measured during, for instance, VERCORS-2, VERCORS-4, VI-1, VI-2, VI-3. However, in complicated geometry of the experiments, this gas composition can hardly characterise the conditions within the gap and in the vicinity of the fuel surface. A more realistic assumption is that during the stage of cladding oxidation the atmosphere within the gap varied from slightly oxidising or inert to slightly reducing. This approach described in details in the following sections is used, in the present report, for estimation of the fuel oxidation conditions for all VI and VERCOR.

1. Initial grain boundary inventory and releases of FP elements

Grain boundary inventory at the end of the irradiation stage and before the beginning of the temperature ramp calculated with the MFPR code for VERCORS-4 conditions and typical for all integral tests is shown in Table 2. According to MFPR predictions at the beginning of the test the most parts of non-soluble, chemically active FP elements, that is Cs, I, Mo, Ru, Ba, Sr are in the solid precipitates at the grain boundary whereas well soluble elements as Zr and lanthanides are located in the solid solution phase.

Table 2. Initial phase distribution of FP elements for VERCORS-4 and VI-3 tests

Element	**Grain**	**Grain Boundary: solid precipitates, gas in face and edge bubbles**				**Release**
		Metal	Grey	CsI	Gas	
Xe	**0.88**	0.00	0.00	0.00	0.11	**0.01**
Cs	0.003	0.00	**0.95**	0.04	6.E-5	1.E-05
I	**0.27**	0.00	0.00	**0.73**	1.9E-4	0.4E-4
Mo	**0.17**	**0.83**	6.E-4	0.00	0.00	0.00
Ru	0.09	**0.91**	0.00	0.00	0.00	0.00
Ba	0.09	0.00	**0.91**	0.00	0.00	0.00
Zr	**1.00**	0.00	0.00	0.00	0.00	0.00
Te	**0.96**	0.00	0.00	0.00	0.01	**0.03**

Table 3 represents the results for releases of FP elements during the stage of normal reactor operation calculated with MFPR for two groups of experiments: VI–VERCORS tests with high burn-up fuel (≥ 4 %), and CRL tests with relatively low burn-up fuel, 1–2.4 %. Data presented in the table demonstrate that for the first test group, total Xe release during the irradiation phase (about 3 year) is predicted on the level of 1–6 % that is in agreement with experimental data of ~ 2–5 % [5]. Comparison with the standard experimental (estimated) data taken from [5] shows that MFPR underestimates releases of all chemically active FP elements by more than order of magnitude. In contrast, release of tellurium considered, in MFPR model, as inert element is significantly higher than expected.

In contrast to input data for VI–VERCORS tests and to other experimental data, MFPR predicts no FP releases during the irradiation phase for low burnup fuel used in CRL (and Dimitrovgrad) tests. Note, that in the MFPR code the main part of FP releases is described by the percolation model of intergranular transport. More detailed consideration shows that, for the parameters of typical irradiation regime used (that is fission rate of $\sim 10^{19}$ fissions/m^{3}s and $T \sim 1100$ K), this model predicts the beginning of releases after relatively high FP accumulations corresponding to burn-up of approximately 2–3 % (depending on the grain diameter).

Table 3. Comparison of measured and calculated initial fractional releases

Element	**Experiment**	**MFPR**				
		VI-3	**VI-4**	**VR-4**	**UCE9–1**	**MCE1–5**
Xe	2.0E-02	3.94E-02	5.63E-02	9.06E-03	0.00	0.00
Cs	1.0E-03	5.46E-05	8.26E-05	1.26E-05	0.00	0.00
I	5.0E-03	1.87E-04	2.72E-04	4.28E-05	0.00	0.00
Ba	1.0E-04	5.44E-16	8.32E-16	1.25E-16	0.00	0.00
Te	1.0E-04	1.19E-01	1.60E-01	3.25E-02	0.00	0.00

2. Modelling of VI tests

2.1. Experiment description and results

A series of annealing tests were conducted in vertical induction (VI) facility at ORNL [5] with the high-burnup LWR fuel. Fission gas release from the fuel during the normal reactor operation was estimated to be lower than 5 %. In these tests the fuel specimens consisted of 15-cm sections cut from full-length rods. Zircaloy end caps were fabricated and press-fit onto the fuel specimens to prevent any loss of fuel during handling. A small 1.6-mm hole was drilled in the cladding at the midlength of the section to permit gas release during heating.

The temperature history of the tests was the following:

- VI-1 — 300 K; 1 K/s; 2020 K, 20 min; 0.6 K/s; 2300 K, 20 min; 0.8 K/s; 300 K;
- VI-2 — 500 K; 0.8 K/s; 2300 K, 60 min; 0.5 K/s; 300 K;
- VI-3 — 300 K; 0.3 K/s; 2000 K, 30 min; 0.3 K/s; 2700 K, 30 min; 0.5 K/s; 300 K;
- VI-4 — 500 K; 0.7 K/s; 1660 K, 23 min; 1.1 K/s; 2440 K, 20 min; 0.6 K/s; 300 K;
- VI-5 — 500 K; 0.25 K/s; 2000 K, 20 min; 1.2 K/s; 2720 K, 20 min; 1.1 K/s; 300 K.

First three VI tests were performed in oxidising conditions of H_2O/He mixtures, while tests VI-4 and VI-5 used reducing atmosphere of hydrogen. The gas environments during annealing (the middle and high temperature plateaux) were characterised by the following parameters:

- VI-1 — H_2O/He ≈ 3.8, flow rate = 1.94 L/min;
- VI-2 — H_2O/He ≈ 5.1, flow rate = 1.84 L/min;
- VI-3 — H_2O/He = 4, flow rate = 1.84 L/min;
- VI-4 — H_2/He = 1, flow rate = 0.81 L/min;
- VI-5 — H_2/He = 1, flow rate = 0.80 L/min.

As an example, scenario and main results of VI-3 test are shown in Figs. 1–4.

As noted in [2, 6], in the 'steam' tests VI-1, VI-2, and VI-3, the fuel specimens had remained intact during entire experiments. However, fuel collapse was observed in the hydrogen tests above the melting temperature of the Zircaloy cladding: approximately at $T \sim 2150$ K in VI-4 test and between 2400 and 2700 K in VI-5. A summary of experimental conditions is given in Table 1. The results of the HI-VI test measurements of total released fraction of volatile and low volatile FP elements are presented in Ref. [5]. The measured release kinetics of volatile caesium for VI-3 test is shown in Fig. 3 [2, 3].

2.2. Comparison to experimental data

Modelling of oxidising/reducing conditions

Since the first three VI experiments used the fuel specimens including original Zr cladding, the gas composition in the reaction tube differed significantly from the input composition. Due to generation of hydrogen in the steam-zirconium reaction, the real partial pressure of oxygen was essentially lower than that could be in the case of the input steam dissociation. In Refs. [2, 3, 6, 4], the conditions of fuel oxidation in the presence of zirconium cladding were accepted to be the same as on average in the reaction tube and calculated using the experimental data for the rates of hydrogen production during the test. However, if complicated geometry of the experiments (intact cladding around UO_2, a small hole for gap/environment gas transfer) is taken into account, this gas composition can hardly characterise the conditions within the gap and in the vicinity of the fuel surface. It seems to be more realistic to assume that during the stage of cladding oxidation the atmosphere within the gap was from slightly oxidising or inert to slightly reducing. Basing on this assumption the scenarios for all oxidising VI tests (VI-1,2,3) is formulated as follows: extremely low (with some ambiguity) steam oxidation during the period of cladding oxidation, then — oxidation conditions as given by the input gas composition. The cladding oxidation time is estimated using experimental data on hydrogen generation [2, 3].

Typical sequence of oxidation events along with the fuel stoichiometry calculated by MFPR oxidation models for VI–3 test is shown in Fig. 1.

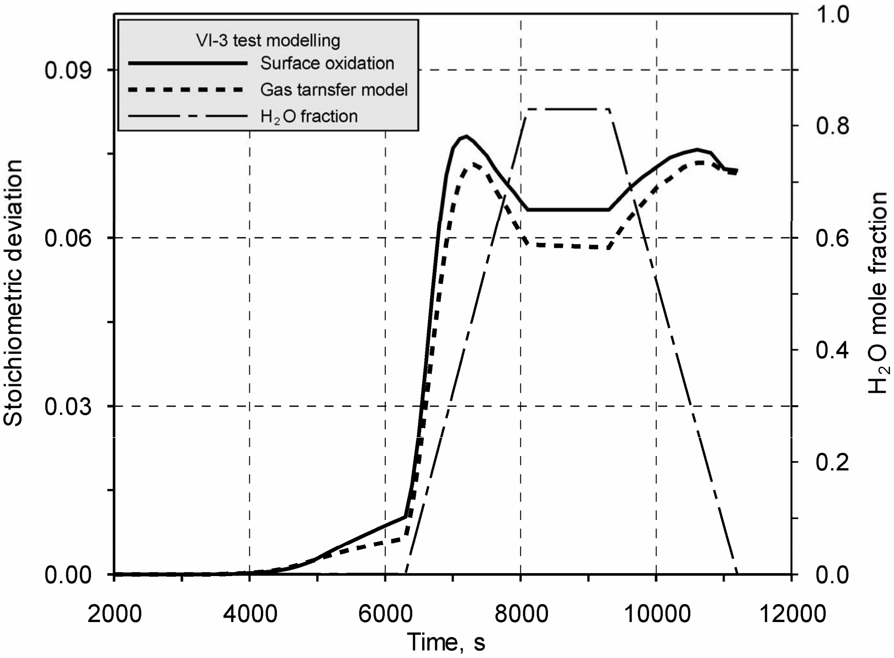

Fig. 1. VI-3 test. Modelling of oxidising conditions and predicted fuel stoichiometry

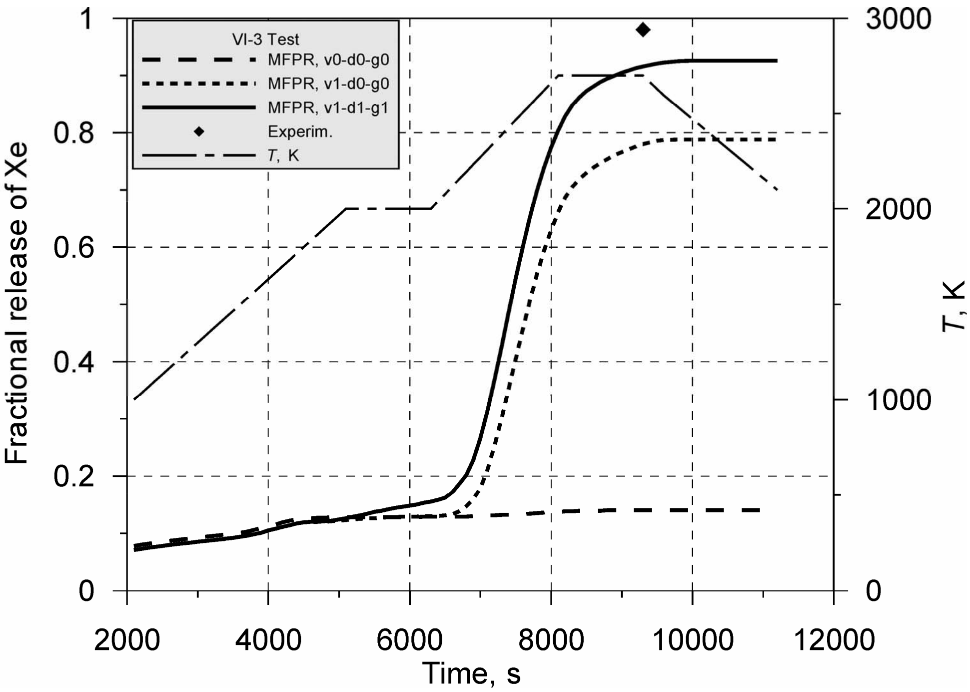

Fig. 2. VI-3 test. Comparison of calculated and measured release kinetics of Xe
Abbreviations: "v0–d0–g0" — vacancy, dislocation and grain growth models switched off,
"v1–d0–g0" — vacancy model activated, dislocation and grain growth models switched off,
"v1–d1–g1" — all three groups of the models are activated

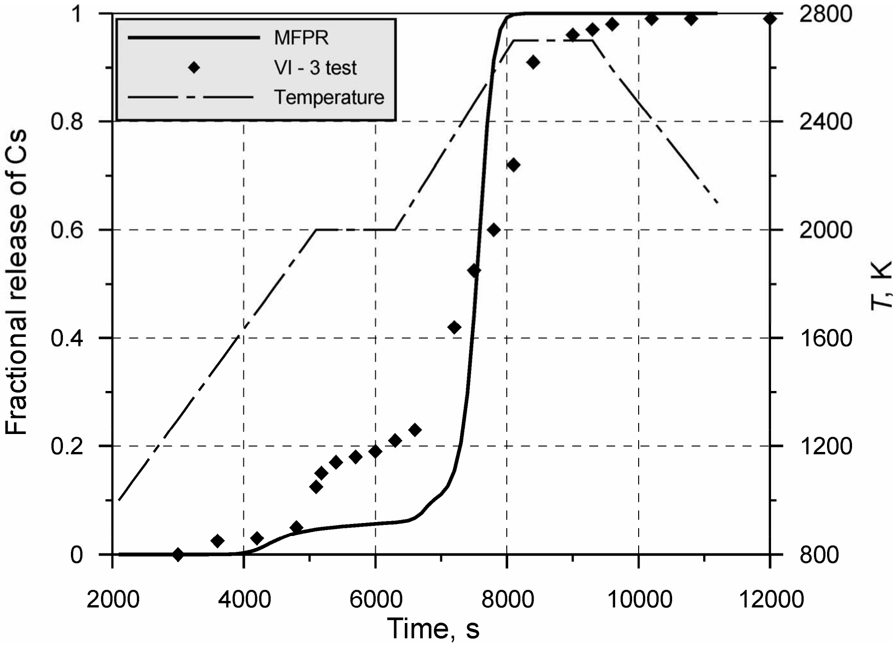

Fig. 3. VI-3 test. Comparison of calculated and measured release kinetics of Cs

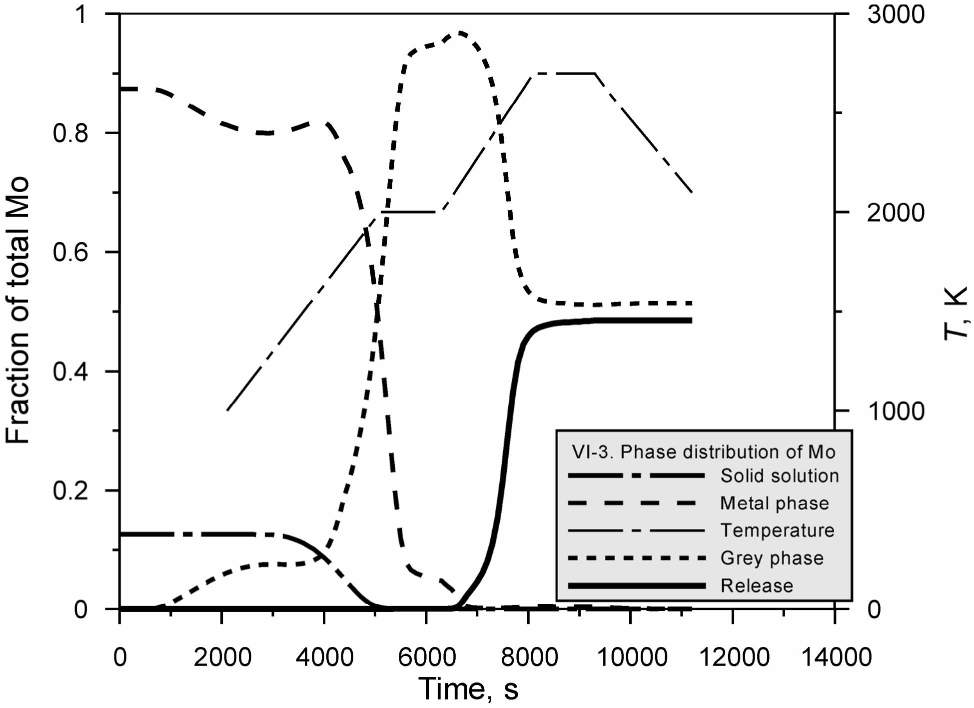

Fig. 4. VI-3 test. Phase distribution of Mo

Release kinetics and total releases

Release kinetics of Xenon calculated for VI-3 test with the different combinations of models is compared with that measured in the test in Fig. 2, where the following abbreviations are used: “**v0–d0–g0**” — vacancy, dislocation and grain growth models switched off, “**v1–d0–g0**” — vacancy model activated while dislocation and grain growth models switched off, and “**v1–d1–g1**” — all three groups of the models are activated. It is evidently seen that inclusion of the vacancy/thermal-resolution mechanism (discussed in detail in paper of this Collection on p. 87) increasing the effective mobility intragranular bubbles solves, in part, the problem of Xe release connected strong diffusion sinking of gas atoms into the bubbles. The best fit to experimental data is provided by simultaneous activation of the complete defect model along with the grain growth mechanism implemented in the code.

Typical release kinetics of caesium calculated with MFPR chemistry model for VI-3 test is compared with that measured experimentally in Fig. 3 The data are in reasonable qualitative and quantitative agreement with the test measurements. In the MFPR description of tests VI-1 through VI-5 there are common features: relatively high starting release rate at temperature of about 1700 K, and quasi-plateau in Cs release during the middle temperature plateau (if exists) at $T \sim 1800–2000$ K up to the beginning of the temperature rise and intensive fuel oxidation/reduction.

The main mechanism of the quasi-plateau formation and the caesium release kinetics, as predicted by the chemistry model, can be understood by analysis of the phase distribution of FP elements. Due to low solid solubilities of barium and strontium, the most part of Ba and about a half of Sr are in the grey phase during the entire test. These phase distributions are determined mainly by two reactions,

$$\begin{aligned} BaUO_4(c) &= BaO(c) + UO_2(c) + 0.5\ O_2\ , \\ SrUO_4(c) &= SrO(c) + UO_2(c) + 0.5\ O_2\ , \end{aligned} \qquad (1)$$

which are significantly ‘shifted’ to the left. As a consequence, and the fuel stoichiometric deviation is on the level of $\sim 10^{-3}–10^{-4}$, and in the high temperature conditions of VI tests the Cs release is dominated by the reaction of decomposition of caesium molybdate with transfer of molybdenum to the metal phase,

$$Cs_2MoO_4(c) = Cs(g) + Mo(c) + 2\ O_2\ , \qquad (2)$$

along with redistribution between barium and strontium molybdates in the grey phase. This channel is more effective in the conditions of lower oxygen potential. At temperatures higher than 2200–2300 K the Cs release is dominated by the reaction of direct vaporization of caesium molybdate,

$$Cs_2MoO_4(c) \rightarrow Cs\ MoO_4\ (g)\ , \qquad (3)$$

that provides another essential channel for Cs (and Mo) release. For this stage of test, MFPR predicts very high release rates of Cs exceeding noticeably the experimental values.

Table 4 represents the results of measurements [5, 6] and MFPR predictions for total FP releases during VI–3 and VI–4 tests (the values in brackets are taken from Ref. [2]). Comparison of the results shows that the calculated releases of Cs and Mo are in reasonable agreement with experimental data with a tendency to overestimate releases of iodine and to underestimate the molybdenum releases, especially in oxidising experiments.

Typical release kinetics of Mo in such conditions is illustrated in Fig. 4 which represents the results for evolution of the phase distribution of this element during VI-3 test. It is seen that, in the MFPR description, during the middle temperature plateau (2000 K) and in the conditions of weak external oxidation (stoichiometric deviation $\sim 10^{-3}$) the phase of metallic molybdenum becomes unstable, and almost total molybdenum passes to the grey phase. The Mo release then proceeds along with the high temperature decomposition of the grey phase and is dominated by caesium molybdate, $Cs_2MoO_4(g)$, and gaseous molybdenum trioxides, $MoO_3(g)$, $(MoO_3)_2(g)$, $(MoO_3)_3(g)$. Note that, in general, formation of gaseous molybdenum trioxides is a significantly efficient channel for release of Mo from the metallic phase. However, as shown in Fig. 4, this channel is not included because total molybdenum is rapidly transferred from the metallic to the grey phase before the beginning of the high-temperature oxidation stage. Therefore, the tendency to underestimate the Mo release can be explained, in part, by simplified description of inter-phase transport of FP elements considered in MFPR as an instantaneous process governed by the equilibrium thermochemistry only.

Significant releases of barium and strontium were observed in both oxidising, VI-2 and VI-3, and reducing, VI-4 and VI-5 tests. The data presented in Table 4 show that the results obtained with MFPR for VI-4 test, where annealing was performed in reducing conditions of hydrogen atmosphere, are in agree with the measurements with overestimation by a factor of ~ 1.5. However, the current MFPR model can not explain relatively high release of Ba and Sr in such steam tests as VI–3.

Note that the released fraction of Eu calculated with MFPR for VI-4 test is lower than 10^{-14}, whereas the test measurements yielded the value of about 70 %. Such an extremely high release of europium is related, as assumed [5] to significant fuel reduction during interaction of melted Zircaloy with the fuel and some of the fission products.

Table 4. Comparison of measured and calculated fractional releases for VI-3 and VI-4 tests

VI–3 Test			**VI–4 Test**		
Element	**Experiment**	**MFPR**	**Element**	**Experiment**	**MFPR**
Xe	0.995	9.05E-01	Xe	0.944 (0.85)	6.94E-01
Cs	0.999	1.00E+00	Cs	0.9587	1.00E+00
I	0.790	1.00E+00	I	0.868 (0.71)	1.00E+00
Mo	0.770	4.78E-01	Mo	0.069	1.65E-03
Ru	0.050	1.72E-04	Ru	0.	3.99E-08
Ba	0.297	1.99E-03	Ba	0.268	6.65E-01
Sr	0.027	5.84E–07	Sr	–	2.92E-01
Zr	–	1.90E–09	Zr	–	1.05E-11
La	–	3.47E–08	La	–	2.26E-07
Ce	<0.002	1.67E–08	Ce	–	1.87E-07
Eu	<0.0001	3.16E–08	Eu	0.1863	1.99E-05
Nd	–	2.06E–08	Nd	–	1.28E-07
Nb	–	1.20E–09	Nb	–	5.03E-09
Sb	0.992	6.80E–01	Sb	0.0636	4.03E-02
Te	0.988	1.00E+00	Te	–	1.00E+00

3. Modelling of VERCORS tests

3.1. Experiment description and results

The VERCORS test series of annealing experiments was performed at CEA-Grenoble as an extension of the HEVA (HElium and VApor) program in order to investigate the release behaviour of fission products in the conditions of great fuel deterioration at high temperature.

For each test the fuel sample comprised a small section of a spent PWR fuel rod consisted of three pellets in their original Zr cladding. Since the samples were maintained vertically, to prevent fuel loss during experiment, two half-pellets of depleted urania were placed on each side of the test sample and held in place by crimping the cladding. In order to recreate the most important short-lived FP elements (including Xe, Te, I, Mo, Ba, La, Ru, Ce, Zr, etc.) after the long cooling periods, the fuel samples were re-irradiated in an experimental reactor. During the tests the fuel temperature was increased with the rate of about 1 K/s through a series of plateaux to the highest value ranged from 2100 to 2600 K. Temperatures and duration of the plateaux are presented in Table 1 [2, 7].

Each VERCORS test was made under total pressure of about 1 atmosphere at a gas flow of steam/hydrogen mixture the input composition of which varied, as a rule, during the heating and annealing period:

- VERCORS-1 — oxidising mixture with $H_2O/H_2 \cong 50/1$ at the high temperature plateau;
- VERCORS-2 — oxidising mixture with $H_2O/H_2 \cong 6/1$ at the high temperature plateau and $H_2O/H_2 \cong 50/1$ at lower temperatures;
- VERCORS-4 — H_2/He atmosphere at the high temperature plateau after oxidation in H_2O/H_2 mixture at lower temperatures;
- VERCORS-5 — H_2O/He atmosphere at the high temperature plateau after oxidation in H_2O/H_2 mixture at lower temperatures.

Details of the experimental conditions are briefly summarised in Table 1.

Typical temperature and oxidation scenario of VERCORS tests is shown in Figs. 5–7.

The results of the VERCORS test measurements are presented in literature in the form of total released fraction of volatile and low volatile FP elements [7]. The results of measurements of the release kinetics are available for caesium in the case of VERCORS-2 [2] and VERCORS-4,5 [7, 8]) and for low volatile FP for VERCORS-4,5 [7, 8].

3.2. Comparison to VERCORS experimental data

Modelling of oxidising/reducing conditions

Similar to VI series, VERCORS tests used the fuel specimens including Zr cladding interacting intensively with the oxidising atmosphere and affecting the gas composition. Since in these two series of experiments almost the same geometry was applied, modelling of the VERCORS tests was based on the simplified approach discussed in the previous section.

In VERCORS-4 test, high temperature (2573 K) annealing in pure hydrogen atmosphere followed the clad pre-oxidising phase in steam/hydrogen mixture. It is known that cladding was oxidised completely approximately by the end of the middle temperature plateau (1523 K). Therefore, the following scenario is use for modelling of the high temperature phase of the test:

- steam/hydrogen mixture with the ratio $H_2/H_2O \sim 10^5–10^6$ during the middle temperature plateau (1523), steam/hydrogen mixture with the ratio $H_2/H_2O \sim 0.1–0.001$ during the temperature ramp, and pure hydrogen during the high temperature plateau.

This oxidation/reduction scenario is illustrated by Fig. 5, where the results of calculations of fuel stoichiometry are shown. It is seen that the fuel is in almost stoichiometric state (slightly hypostoichiometric with the stoichiometric deviation $x \sim \pm(10^{-4}–10^{-5})$) before the temperature ramp. The state of the fuel changes to strongly hypostoichiometry during the plateau 2573 K in the reducing (hydrogen) atmosphere.

Modelling of the VERCORS-5 conditions are performed in similar manner, that is steam/hydrogen mixture with the ratio $H_2/H_2O \sim 10^5–10^6$ during the middle temperature plateau, and pure steam at the high temperature plateau.

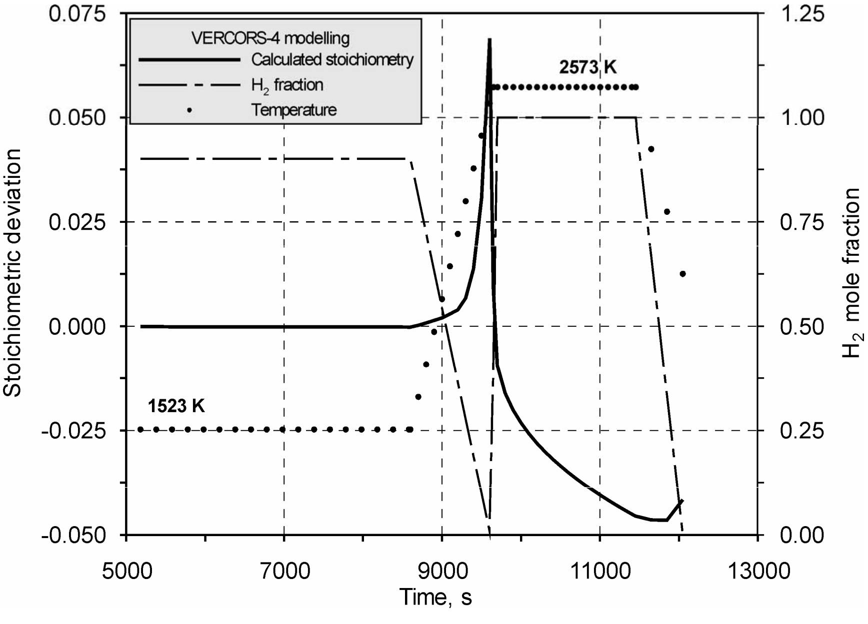

Fig. 5. VERCORS-4 test. Modelling of oxidising conditions and predicted fuel stoichiometry

Release kinetics and total releases

Release kinetics of xenon calculated for VERCORS-4 test with the different combinations of models is compared with that measured in the test in Fig. 6. As for VI tests, the best fit to experimental data is provided by simultaneous activation of the complete defect model along with the grain growth mechanism implemented in the code.

Release kinetics of caesium calculated for VERCORS–4 test with the current chemistry–release models is compared with the experimental data in Fig. 7. As in the case of tests VI-3, 4, 5, the model overestimates significantly the release rate of caesium during the rise to the high temperature plateau.

Evolution of the phase distribution of Cs calculated for VERCORS-2, 4, 5 tests illustrates that during the low-temperature plateaus the most part of Cs is in the grey phase which is predicted to be stable even in the weakly reducing conditions with small hypostoichiometry of $x \sim -10^{-4}$. Intensive release of Cs begins simultaneously with very rapid decomposition of Cs-bearing components of the grey phase at temperatures $T \sim 2100$–2200 K, that is before the beginning of the strong reduction stage of experiment.

Total released fractions calculated for VERCORS-4, 5 tests are compared with the experimental data [7, 8] in Table 5 (the values in brackets are taken from Ref. [2]).

Data presented in Table 5 show that the chemistry models underestimate releases of Mo. Similar to VI tests, this can be explained, in part, by a simplified approach to description of inter-phase transport of FP elements considered, in the MFPR model, as an instantaneous process (without any kinetic limitations). In Fig. 8 representing the evolution of the phase distribution and the release kinetics of molybdenum in VERCORS-4 test, it is seen that according to the oxidation scenario shown in Fig. 5, the molybdenum release occurs during a very short period of fuel oxidation. When steam is switched to hydrogen, the Mo release is terminated simultaneously with almost instantaneous and complete decomposition of the molybdenum-bearing components of the grey phase from which molybdenum is transferred to the metal phase.

In oxidising VERCORS-5 test, the Mo release is dominated by two, practically instantaneous processes at the beginning of the strong high temperature oxidation: that is transfer of metallic molybdenum to the grey phase and evaporation through the reactions Mo → MoO_3, $(MoO_3)_2$. Additionally, decomposition of the molybdenum-bearing components of the grey phase completed.

Another point in VERCORS-4 description is related to the MFPR fuel oxidation model which represents the high-temperature reduction of fuel in hydrogen atmosphere as very rapid process (see Fig. 5) determined by the solid state diffusion of oxygen only. This problem is discussed in more details below in Section 5.

The MFPR model underestimates significantly (by several orders of magnitude) releases of Ba and Sr in oxidising tests as VERCORS-1, 2 and VERCORS-5 (and also VI-3 as shown in Table 4). Probably such underestimation can be explained by non-homogeneity of the oxygen potential, however, in general, this problem is not yet understood.

On the other hand, the MFPR chemistry provides reasonable agreement with experimental data for the barium and strontium releases in the case of VERCORS-4 test including the high-temperature reducing phase. The predicted release of Ba as a function of time shown in Fig. 9 along with the phase distribution of this element demonstrates an instantaneous-like kinetics of the same type as for Mo. The release rate of Ba is calculated to be large during a short period at the beginning of the reducing stage of the test when the barium-bearing components of the grey phase are partially (but almost instantaneously) decomposed.

The MFPR model underestimates the releases of antimony within a factor of 10, and the ruthenium releases by 2 to 3 orders of magnitude.

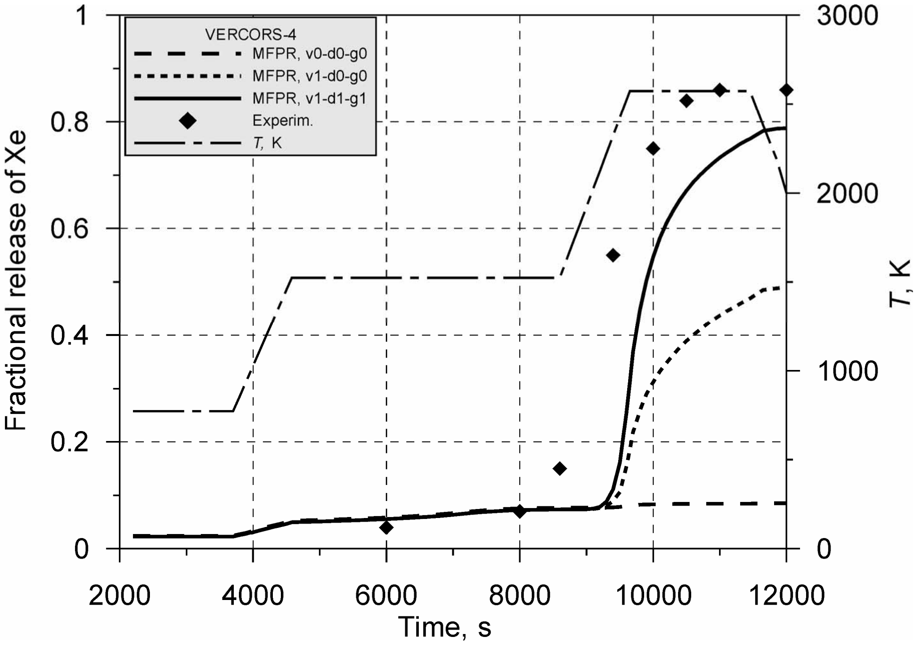

Fig. 6. VERCORS-4 test. Comparison of calculated and measured release kinetics of Xe Abbreviations: "v0–d0–g0" — vacancy, dislocation and grain growth models switched off, "v1–d0–g0" — vacancy model activated, dislocation and grain growth models switched off, "v1–d1–g1" — all three groups of the models are activated

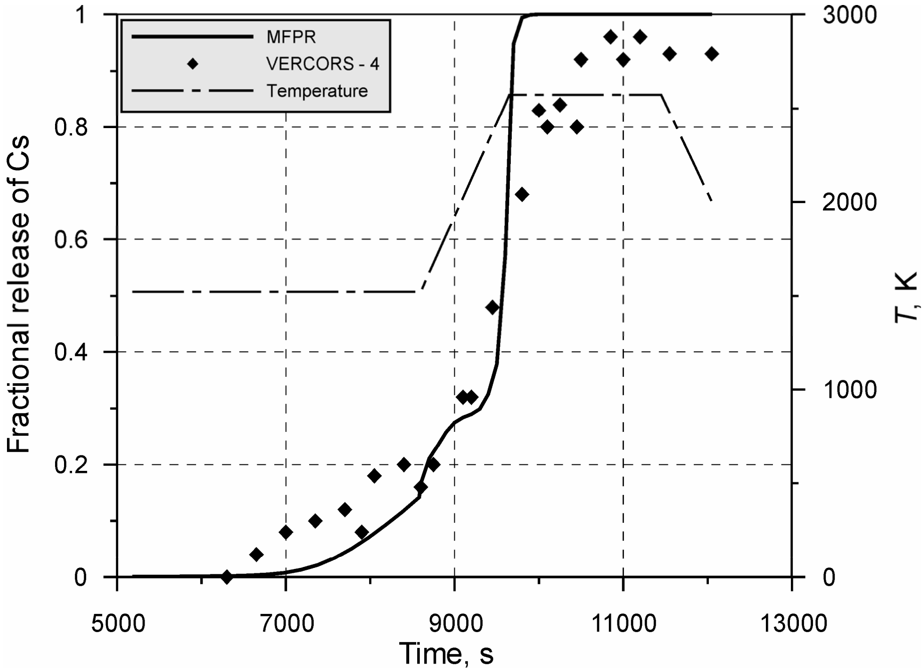

Fig. 7. VERCORS-4 test. Comparison of calculated and measured release kinetics of Cs

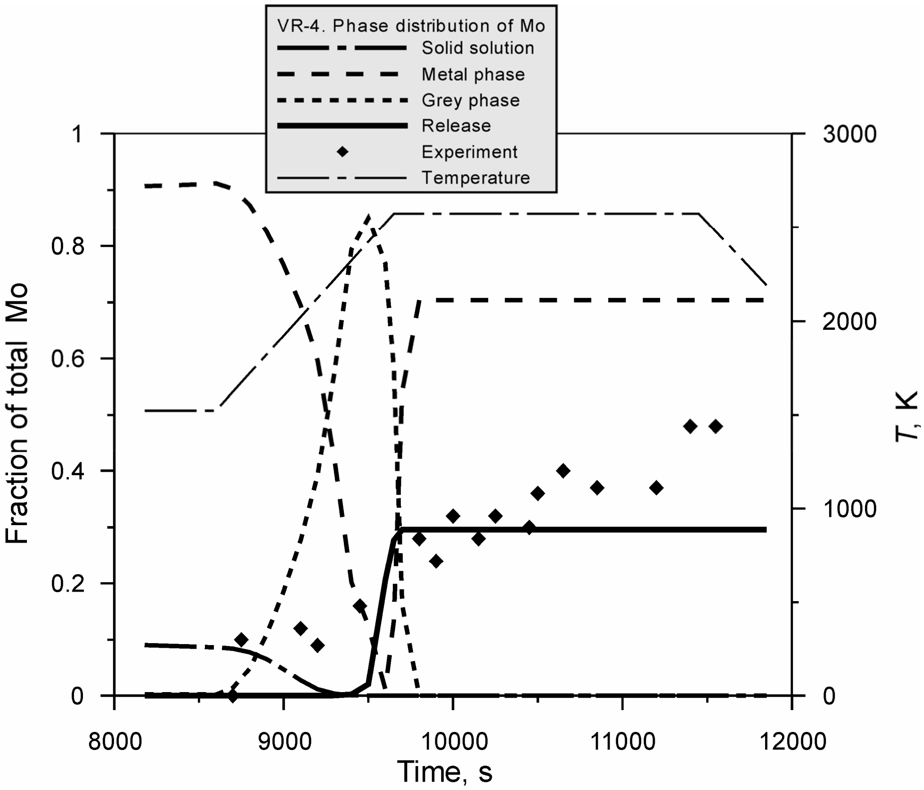

Fig. 8. VERCORS-4 test. Phase distribution and comparison of calculated and measured release kinetics of Mo

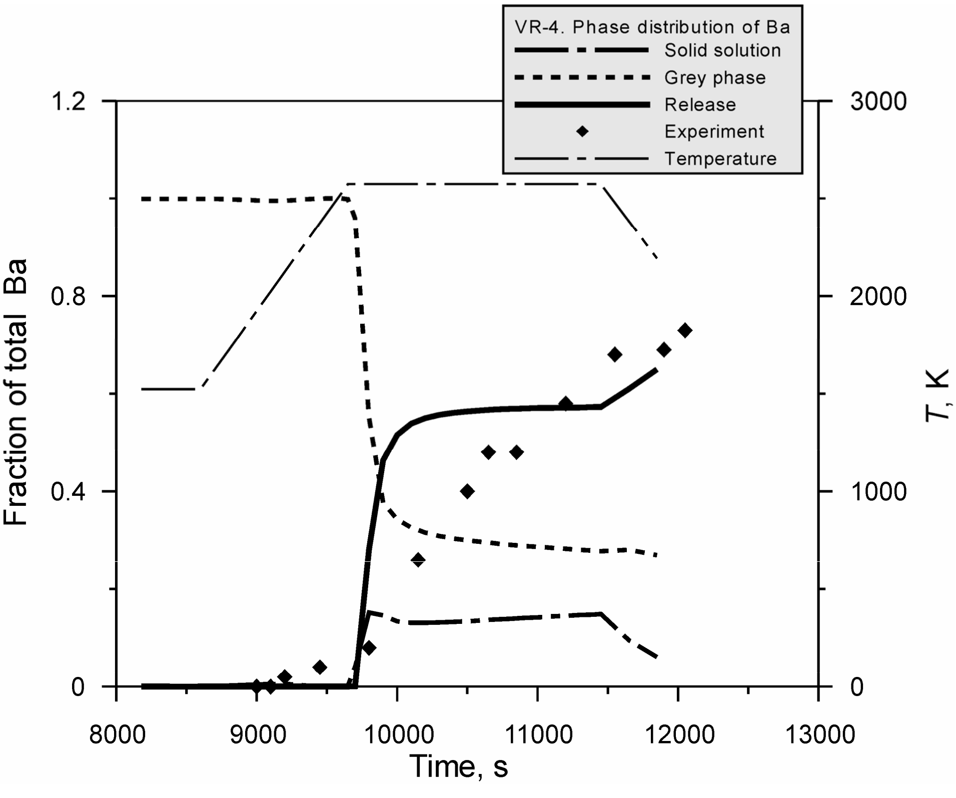

Fig. 9. VERCORS-4 test. Phase distribution and comparison of calculated and measured release kinetics of Ba

Table 5. Comparison of measured and calculated fractional releases for VERCORS-4, 5

VERCORS–4			**VERCORS–5**		
Element	**Experiment**	**MFPR**	**Element**	**Experiment**	**MFPR**
Xe	0.86	7.52E-01	Xe	0.87	7.47E-01
Cs	0.93	1.00E+00	Cs	0.93	1.00E+00
I	0.87	1.00E+00	I	0.93	1.00E+00
Mo	0.47	2.96E-01	Mo	0.92	4.85E-01
Ru	0.07	6.36E-06	Ru	0.06	1.76E-04
Ba	0.66	6.76E-01	Ba	0.55	1.37E-03
Sr	<0.08	3.14E-01	Sr	< 0.06	2.08E-07
Zr	<0.02	3.81E-09	Zr	< 0.04	5.94E-10
La	<0.02	1.20E-06	La	< 0.03	1.29E-08
Ce	0.03	9.38E-07	Ce	< 0.03	5.48E-09
Eu	<0.05	1.02E-04	Eu	< 0.05	1.18E-08
Nd	–	7.12E-07	Nd	–	7.46E-09
Nb	–	1.66E-08	Nb	–	3.19E-10
Sb	0.97	1.81E-01	Sb	0.98	6.90E-01
Te	1.0	1.00E+00	Te	0.98	1.00E+00

4. Summary of integral test simulation

In this section the results of modelling of integral tests are discussed with focus on analysis of chemistry effects and total FP releases, kinetics of FP releases and effects of oxidation on the predictions of FP releases.

4.1. Chemistry effects and total FP releases

Comparison of the calculation of total FP releases with the experimental data through all integral tests considered is presented in Table 6 which shows the order of magnitude deviation between measured and calculated fractional release for each of elements included in MFPR scheme. The order of magnitude deviation (OMD) is defined as

OMD = $\log_{10}$ (Calculated Released Fraction / Measured Released Fraction).

In the table, the symbol '–' is used in the cases when a finite release of an element is calculated whereas the measurements yielded zero release.

Table 6. Comparison of the order of magnitude deviations between measured and calculated fractional releases for integral tests

Test	**VRC–1**	**VRC–2**	**VRC–4**	**VRC–5**	**VI–1**	**VI–2**	**VI–3**	**VI–4**	**VI–5**	**UCE**	**MCE**	**Dmtr**
Xe	0.04	–0.3	–0.06	–0.07	0.2	0.3	–0.04	–0.1	–0.04	–	–	–
Cs	–0.1	0.2	0.03	0.03	–0.03	0.05	0.00	0.02	0.00	–0.1	–0.1	0.2
I	0.5	0.6	0.06	0.03	0.3	0.3	0.1	0.06	0.2	–	–	–
Mo	–	–1.9	–0.2	–0.3	–0.2	–0.4	–0.2	–1.6	–0.6	–	–	–
Ru	–	–	–4.0	–2.5	–	–	–2.5	–	-	–	–	–
Ba	–3.7	–3.4	0.01	–2.6	–	–3.1	–2.2	0.4	–0.2	–	–	–
Sr	–	–	0.6	–5.5	–	–	–4.7	–	–0.2	–	–	–
Zr	–	–	–6.7	–7.8	–	–	–	–	–	–	–	–
La	–	–	–4.2	–6.4	–	–	–	–	–	–	–	–
Ce	–	–	–4.5	–6.7	–	–	–5.1	–	–3.6	–	–	–
Eu	–	–	–2.7	–6.6	–	–	–3.5	–4.0	–3.5	–	–	–
Sb	0.02	–2.1	–0.7	–0.2	–0.4	–1.0	–0.2	–0.2	0.2	–	–	–
Te	1.3	0.7	0.00	0.01	–	–	0.01	–	0.09	–	–	–

Noble gases and volatile FP elements, Xe, Cs, I, Te

In Table 6 it is seen that total releases of Xe, Cs and I are satisfactorily described by MFPR: throughout all tests under/over predictions are within a factor of 2–1.5. Besides the uncertainties of measurements these deviations from the test data can be related to the following causes:

- High temperature ($T > 2000$ K) thermodynamics of ternary compounds composing the grey phase is not well established.
- The solid state diffusion coefficients for the majority of elements included into the MFPR chemistry are not well measured especially in the high temperature range. This problem is of great importance for the dissolved oxygen and, in general, for the FP thermochemistry in oxide fuel.
- There are some uncertainties in description of the equilibrium oxygen pressure over UO_{2+x} and the fuel oxidation kinetics with different models.
- There is some ambiguity in modelling of the pre-test period of normal operating and, that is of more importance, in the fuel oxidation conditions discussed throughout the report.

Note, that the above comments are also related to description of behaviour of the other FP elements.

The problem of Te and I

Discussion on the iodine release kinetics in Section 2.4.2 as well as the data presented in Table 6 indicate that in almost all tests, both oxidising and reducing, the MFPR model overestimates release rates and total releases of iodine. To remove this problem the possible importance of the iodine species other than caesium iodide and gaseous monatomic I should be assessed.

Although for the majority of the tests, the MFPR predictions for total releases of tellurium are in reasonable agreement with the test data with tendency to overestimation, typical kinetics of tellurium release differs noticeably from that measured in experiments. This concerns, in particular, to a high level of the initial (low-temperature) release and too rapid release at high temperatures. Since MFPR does not include any tellurium chemistry, it would probably be appropriate to include (assessed for inclusion) Te(c) along with some tellurium compounds such as caesium tellurides, tellurium oxides, Cs—Te—(O) compounds and possibly tellurium iodides in the MFPR database if the corresponding thermodynamic data are available.

Semi-volatile Mo, Ru, Sb

Analysis of data presented in Table 6 shows that current chemistry model describes satisfactorily the behaviour of fission molybdenum and antimony with some tendency of underestimation of total releases. Most essential underestimation of Mo release is observed for tests VI-4 and VI-5 with pure hydrogen atmosphere in which, according to equilibrium thermochemistry, this element is known to be extremely low volatile.

Releases of ruthenium are, as a rule, underpredicted: by several orders of magnitude. This element (as well as molybdenum) is known to have a relatively high volatility in the conditions of high temperature oxidation and high oxygen potential. For all experiments considered, MPFR predicts that a dominant part of Ru is in the metal phase during the entire tests. Nevertheless, the calculated releases of Ru are underestimated by several orders of magnitude even in the conditions of oxidation.

Possible and most reliable way to remove the problem of antimony is related to re-analysis of phase distribution of this element with inclusion of new solid phases.

Semi-volatile Ba, Sr

The results presented in Table 6 show that the problems with description of behaviour of Ba and Sr are inverse to those for Mo: the MFPR chemistry describes satisfactorily the releases of these elements in reducing (hydrogen) environment of tests VI-4, VI-5 and VERCORS-4 and underestimates the releases by several orders of magnitude in oxidising and inert tests. Note that this problem of Ba and Sr behaviour in oxidising and inert conditions is not yet understood.

Low volatile Zr, La, Ce, Eu, Nd, Nb

Reliable data for releases of Ce and Eu were obtained in the tests VERCORS-4, VI-4 and VI-5. For these tests, the MFPR chemistry model underestimates the releases of fission cerium and europium by several orders of magnitude. This can be explained, in part, by MFPR incapability to describe extensive fuel reduction occurred in these experiments: according to Lorenz and Osborne [5], in VI-4, 5 tests the release of europium was dramatically increased when melted Zircaloy reacted with the fuel and some of the fission products.

Experimental data for releases of the other low volatile FP elements are scarce if known.

4.2. Release kinetics and effects of oxidation

Comparison of calculated and measured release kinetics of Cs, Mo and Ba presented in the report shows that for the majority of tests, the MFPR description of the FP behaviour is in qualitative agreement with experimental results. The following pronounced difference between the results of calculations and measurements should be pointed out:

- the predicted release rates are lower than that observed in the tests on the temperature plateaux and significantly higher during the temperature rises, especially at temperatures $T \geq 2200–2300$ K;
- similar ‘jumps’ in the release rates, in particular, for Ba, Sr and Mo are calculated, but not observed, for sharp changes in oxidation conditions, for instance, from oxidising to reducing.

To remove these inconsistencies the models responsible for the description of bubble dynamics (formation of grain boundary bubbles, grain face channel and grain edge-open porosity interlinkage) should be re-analysed and improved. Additionally, the problem of inter-phase transport of FP elements such as Mo, Ba and Zr discussed in detail in connection with VI-3 and VERCORS-4 modelling should be analysed.

Conclusions

The present validation of MFPR code against integral tests allows formulation of the following conclusions:

1. The MFPR model somewhat underestimates FP releases during the irradiation phase of tests or the stage of normal reactor operation. Besides possible corrections to the diffusion coefficients of FP elements affecting the FP behaviour, additional models are needed for adequate description of releases of chemically active elements during low temperature irradiation stage.
2. The obtained results have demonstrated that implementation of the extended defect and grain growth models provides good agreement with experimental data for both release kinetics and total releases of Xe during annealing phase of the tests.
3. Comparison of calculated and measured release kinetics of Cs (and also Mo and Ba) shows that the MFPR description of the FP behaviour is in qualitative agreement with experimental data for the majority of tests. Nevertheless, the following pronounced differences between the results of calculations and measurements should be pointed out:

- The predicted release rates are significantly higher than that observed for the phases of the temperature rise, especially at high temperatures $T \geq 2200–2300$ K.
- In contrast to observations, similar ‘jumps’ in the release rates are calculated for sharp variations in composition of gas environment even at relatively low temperatures of ~ 1700–1800 K, in particular, for transition from oxidising to reducing conditions (as in VI-4 test).

To remove these inconsistencies the models responsible for the description of the release kinetics (intergranular FP transport through the net of channels to open porosity) should be re-analysed and improved.

As shown by modelling of VERCORS-4, 5 and VI-3, 4, 5 tests, the most significant problems are related to description of molybdenum behaviour (and high releases) in the reducing (hydrogen) experiments, and barium behaviour (and high releases) in the oxidising (steam) experiments. These effects can hardly be understood with the standard thermochemical approach used in MFPR code.

In future development of the MFPR code, it seems reasonable extending of application of the MFPR chemistry to all intergranular bubble similar to that is done for the face bubbles.

References

1. *Degaltzev Yu.G., Ponomarev-Stepnoj N.N., Kuznetzov V.F.* Behaviour of high-temperature nuclear fuel under irradiation. Moscow: Energoatomizdat, 1987. (in Russian).
2. *Lewis B.J., Andre B., Morel B., Dehaudt P., Mari D., Purdy P.L., Cox D.S., Iglesias F.C., Osborne M.F., Lorenz R.A.* Modelling the release behaviour of caesium during severe fuel degradation // J. Nucl. Mater. 1995. Vol. 227. P. 83–109.
3. *Harnden-Gillis A.C., Lewis B.J., Andrews W.S., Purdy P.L., Osborne M.F., Lorenz R.A.* Modeling of cesium release from light water reactor fuel under severe accident conditions // Nucl. Techn. 1995. Vol. 109. P. 39–53.
4. *Ozrin V.D., Shestak V.E., Tarasov V.I., Veshchunov M.S.*. MFPR Module. Vers. 1.4. Validation Study / Nuclear Safety Institute (IBRAE) RAS. Report NSI-SARR-166-04. December 2004.
5. *Lorenz R.A., Osborne M.F.* A summary of ORNL fission product release tests with recommended release rates and diffusion coefficients. NUREG/CR-6261, ORNL/TM-12801. 1995.
6. *Osborne M.F., Lorenz R.A.* ORNL Studies of Fission Product Release Under LWR Severe Accident Conditions // Nucl. Safety. 1992. Vol. 33. P. 344.
7. *Ducros G., Andre B., Tourasse M., Maro D.* The fission product and actinide release at high temperature in PWR fuel rods: the VERCORS safety programme // IAEA Tech. Committee Meeting (Dimitrovgrad, Oct. 1995).
8. *Ducros G., Andre B., Ferroud-Plattet M.P., Boulaud D., Tourasse M.* Atmosphere dependence of fission product release: the VERCORS-4 and 5 experiments // CSARP Meeting (Bethesda, May 1996).

Научное издание

Труды ИБРАЭ РАН

Под общей редакцией чл.-кор. РАН Л. А. Большова

Выпуск 5

МОДЕЛИ ВЫХОДА ПРОДУКТОВ ДЕЛЕНИЯ ИЗ ОБЛУЧЕННОГО ТОПЛИВА

(на английском языке)

Утверждено к печати Ученым советом
Института проблем безопасного развития атомной энергетики
Российской академии наук

Издательство «Наука»
117997, Москва, Профсоюзная ул., 90
Зав. редакцией *М. В. Грачева*

Оригинал-макет подготовлен издательством ООО «Комтехпринт»
Иллюстрации приведены в авторской редакции

Сдано в набор 17 октября 2008 г. Подписано в печать 15 ноября 2008 г.
Формат 60 х 90$^1/_8$. Бумага офсетная 80 г/м^2. Печать офсетная. Гарнитура «Таймс»
Уч.-изд. л. 16,5. Тираж 500. Заказ 17735

Заказное

Отпечатано с готовых диапозитивов типографией ООО «Инфолио-Принт»